Ph.D. in "*Scienze*"

INNOVATIVE METHODOLOGIES FOR THE PURIFICATION OF POLLUTED WATER

SSD AGRI-06/B and CHEM-01

Coordinator

Prof. Patrizia FALABELLA

Ph.D. Candidate

Dr. Angelica Rebecca ZIZZAMIA

Supervisor

Prof. Filomena LELARIO

Co-supervisors

Prof. Sabino Aurelio BUFO

Prof. Giuliana BIANCO

Cycle XXXVIII

ABSTRACT- English

Pharmaceuticals constitute a major class of Emerging Contaminants due to their extensive global consumption, intrinsic chemical stability, and limited removal in conventional wastewater treatment plants. Their persistence and bioactivity raise considerable environmental and toxicological issues, necessitating the development of efficient, scalable, and sustainable remediation strategies.

This thesis first provides a systematic review of heterocyclic pharmaceuticals, synthesizing current knowledge on their sources, environmental occurrence and fate, physicochemical persistence, transformation pathways, and documented toxicological profiles, including neurotoxicity, genotoxicity, mutagenesis, and carcinogenicity. Examples of targeted experimental studies employing Advanced Oxidation Processes and adsorptive materials are also presented. The analysis identifies substantial gaps in the understanding of long-term ecological risks and highlights pressing limitations in existing remediation technologies.

Sildenafil and tadalafil are heterocyclic pharmaceuticals used to treat erectile dysfunction that, in recent years, have gained considerable attention due to their widespread legal and illegal use, including increasing recreational consumption among young people. Their high stability and environmental persistence, together with the generation of potentially hazardous phototransformation products, pose risks to human health and ecosystems. Conventional wastewater treatment plants are largely ineffective at removing these compounds, resulting in their continuous release into effluents and subsequent contamination of surface waters. This study evaluated photooxidation processes under simulated solar irradiation for removing sildenafil and its derivatives from water using three oxidants (hydrogen peroxide, peroxymonosulfate, and persulfate), as well as photocatalytic processes employing a TiO_2 catalyst. Potential transformation products were assessed and tentatively identified using liquid chromatography coupled to mass spectrometry with electrospray ionization and multiple-stage mass spectrometry. The Sunlight/peroxymonosulfate system proved most effective, achieving complete degradation in distilled water after 80 minutes and in synthetic wastewater after 130 minutes. Acute toxicity tests on *Vibrio fischeri* confirmed the non-toxicity of treated solutions, demonstrating the environmental compatibility of the Sunlight/peroxymonosulfate system.

The global rise in depressive disorders has led to increased prescription of venlafaxine, a serotonin–norepinephrine reuptake inhibitor. Its physicochemical stability, limited biodegradability, and incomplete removal in wastewater treatment have resulted in its frequent detection in effluents and surface waters. The persistence and biological activity of venlafaxine underscore the need for effective, sustainable treatment technologies, including Electrochemical Advanced Oxidation Processes, which employ reactive species such as

hydroxyl (•OH) and sulfate (SO_4^{-}•) radicals to achieve the mineralization of pollutants. While most studies employ boron-doped diamond anodes, these present practical challenges, including delamination, high cost, limited scalability, and short service life. In this thesis, platinum was used as a stable alternative for galvanostatic electrochemical degradation. Experiments conducted in 0.1 M Na_2SO_4 at pH 9 under a current density of 25 mA cm^{-2} achieved 94% degradation of 25 mg L^{-1} venlafaxine within 7 hours, following first-order kinetics (k = 0.0084 min^{-1}). LC-MS (Liquid Chromatography-Mass Spectrometry) analysis identified key transformation intermediates, revealing predominant degradation pathways involving demethylation, hydroxylation, and aromatic ring modification. *In silico* toxicity predictions confirmed that these intermediates pose significantly lower ecological risks than the parent compound.

To complement oxidative treatments, sustainable adsorption-based approaches were investigated. Activated carbons were synthesized from spent brewery grains using K_2CO_3 as an activating agent, with both conventional and microwave-assisted pyrolysis employed to assess the effect of thermal treatment on adsorbent properties. Microwave-assisted activated carbon exhibited higher surface areas, enhanced porosity, and improved surface functionalization, as confirmed by Scanning Electron Microscopy and BET (Brunauer-Emmett-Teller) analysis. Adsorption experiments showed that, with microwave-derived activated carbon, equilibrium was reached within 2 hours, achieving removal efficiencies of 62% ± 3% in ultrapure water and 49.5% ± 0.6% in wastewater at a dose of 50 mg L^{-1}. Kinetic modeling indicated pseudo-second-order behavior, suggesting chemisorption as the dominant mechanism, while equilibrium isotherm fitting supported monolayer adsorption on a homogeneous surface with identical adsorption sites. The superior performance of the microwave-derived activated carbon is attributed to its enhanced porosity and improved textural properties resulting from rapid and uniform heating during microwave-assisted pyrolysis. The results support the viability of transforming agro-industrial waste into high-value adsorbents and contribute to the development of greener, circular, and robust solutions for addressing emerging pharmaceutical contaminants.

The removal of sildenafil and tadalafil was similarly investigated using activated carbons and natural and organo-modified montmorillonite with didodecyldimethylammonium bromide (DDAB). Microwave-derived activated carbons achieved equilibrium in 2 hours with removal efficiencies of 90.3% ± 0.1% for sildenafil and 95% ± 2% for tadalafil at a dose of 50 mg L^{-1}. DDAB-modified montmorillonite reached equilibrium within 60 minutes, removing 84.9% ± 0.1% of sildenafil and 91% ± 3% of tadalafil using a dose of 250 mg L^{-1}. Isotherm analyses and kinetic modeling confirmed that chemisorption and specific interactions with

active sites govern adsorption, while differences in surface heterogeneity explain variations in capacity across the different materials. Collectively, this investigation demonstrates that bio-derived activated carbons and engineered clay minerals are effective and sustainable adsorbents for removing sildenafil and tadalafil from aqueous matrices.

This study advances sustainable and economically viable water-treatment strategies aligned with circular-economy principles. By evaluating technology and resource-recovery, it offers a scientific framework for designing systems that reduce waste, save energy, and encourage material reuse. The research provides a solid foundation for mitigating pharmaceutical contaminants in water, promoting ecosystem health, and resilient management practices.

ABSTRACT- Italiano

I prodotti farmaceutici costituiscono una delle principali classi di contaminanti emergenti, a causa del loro elevato consumo a livello globale, della loro stabilità chimica intrinseca e della limitata rimozione negli impianti convenzionali di trattamento delle acque reflue. La persistenza e l'attività biologica di questi composti sollevano rilevanti preoccupazioni ambientali e tossicologiche, rendendo necessaria la definizione di strategie di bonifica efficienti, scalabili e sostenibili.

La tesi si apre con uno studio sistematico dei farmaci eterociclici, che raccoglie e sintetizza le conoscenze attuali sulle loro fonti, sulla presenza e sul destino nell'ambiente, sulla persistenza fisico-chimica, sui principali processi di trasformazione e sui profili tossicologici documentati (inclusi neurotossicità, genotossicità, mutagenesi e cancerogenicità). Sono inoltre riportati esempi di studi sperimentali mirati che impiegano processi di ossidazione avanzata e di adsorbimento su materiali naturali. L'analisi di tali evidenze mette in luce rilevanti lacune nella conoscenza dei rischi ecologici a lungo termine e le limitazioni delle tecnologie di bonifica attualmente in uso.

Nell'ambito dei farmaci eterociclici, il sildenafil e il tadalafil rivestono un interesse particolare. Si tratta di composti impiegati per il trattamento della disfunzione erettile che, negli ultimi anni, hanno attirato crescente attenzione a causa dell'ampio uso legale e illegale, incluso l'impiego ricreativo tra i giovani. La loro elevata stabilità e persistenza ambientale, unitamente alla formazione di prodotti intermedi della fototrasformazione del farmaco potenzialmente pericolosi, rappresentano un rischio per la salute umana e per gli ecosistemi. Gli impianti di trattamento delle acque reflue risultano in gran parte inefficaci nella rimozione, determinandone il continuo rilascio negli effluenti e la conseguente contaminazione delle acque superficiali. In questa tesi è stata valutata l'efficacia di processi per la rimozione del sildenafil e dei suoi derivati in acqua, con particolare attenzione alla fotoossidazione sotto irradiazione solare simulata, impiegando tre diversi ossidanti, perossido di idrogeno, perossimonosolfato e persolfato, e ai processi fotocatalitici mediante l'uso del catalizzatore TiO_2. I potenziali prodotti di trasformazione sono stati valutati e identificati mediante cromatografia liquida accoppiata a spettrometria di massa con ionizzazione elettrospray e spettrometria di massa tandem. Il sistema radiazione solare/perossimonosolfato è risultato il più efficace, raggiungendo la completa degradazione in acqua distillata dopo 80 minuti e in acque reflue sintetiche dopo 130 minuti. Test di tossicità acuta su *Vibrio fischeri* hanno confermato la non tossicità delle soluzioni trattate, dimostrando la compatibilità ambientale del sistema radiazione solare/perossimonosolfato.

L’aumento globale dei disturbi depressivi negli ultimi anni ha comportato una crescente prescrizione di un farmaco antidepressivo, la venlafaxina, appartenente alla classe degli inibitori della ricaptazione di serotonina e noradrenalina. La sua stabilità fisico-chimica, la limitata biodegradabilità e la rimozione incompleta negli impianti di trattamento ne hanno determinato la frequente rilevazione negli effluenti e nelle acque superficiali. La persistenza e l’attività biologica della venlafaxina rendono necessaria l’adozione di trattamenti efficaci e sostenibili, tra cui i processi elettrochimici di ossidazione avanzata, che impiegano specie reattive quali radicali idrossilici (•OH) e solfato ($SO^{\bullet -}$) per la mineralizzazione degli inquinanti.

Poiché la maggior parte degli studi utilizza anodi in diamante drogato con boro, che presentano criticità pratiche quali la delaminazione, l'elevato costo, la limitata scalabilità e la ridotta durata operativa, in questo studio è stato impiegato il platino come alternativa stabile alla degradazione elettrochimica galvanostatica. Gli esperimenti condotti in Na_2SO_4 0,1 M a pH 9, con densità di corrente pari a 25 mA cm^{-2}, hanno permesso di ottenere una degradazione del 94% della venlafaxina (25 mg L^{-1}) in 7 ore, con cinetica del primo ordine (k = 0,0084 min^{-1}). Le analisi LC-MS (cromatografia liquida accoppiata a spettrometria di massa) hanno consentito l’identificazione dei principali intermedi di trasformazione, evidenziando percorsi di degradazione dominati dalla demetilazione, dall’idrossilazione e dalle modificazioni dell’anello aromatico. Studi di previsione di tossicità *in silico* hanno confermato che tali intermedi presentano rischi ecotossicologici significativamente inferiori rispetto a quelli del composto precursore.

A integrazione dei trattamenti ossidativi, sono stati sviluppati approcci sostenibili basati sull’adsorbimento. A partire da scarti di produzione della birra, sono stati sintetizzati carboni attivi mediante attivazione con K_2CO_3 e utilizzando pirolisi convenzionale e pirolisi assistita da microonde, per valutare l’effetto del trattamento termico sulle proprietà dei materiali prodotti. Il carbone attivo ottenuto tramite pirolisi a microonde è risultato avere migliori proprietà adsorbenti di quello ottenuto tramite pirolisi convenzionale. Gli esperimenti di adsorbimento hanno evidenziato, per il carbone derivato da pirolisi a microonde, il raggiungimento dell’equilibrio in 2 ore, con efficienze di rimozione della venlafaxina pari al 62% ± 3% in acqua ultrapura e al 49,5% ± 0,6% in acque reflue, con una dose di adsorbente pari a 50 mg L^{-1}. Studi cinetici hanno indicato un comportamento di pseudo-secondo ordine, suggerendo la predominanza del chemisorbimento, mentre l’analisi delle isoterme ha evidenziato un adsorbimento monostrato su una superficie omogenea con siti attivi equivalenti. Le prestazioni superiori del carbone ottenuto mediante pirolisi a microonde sono attribuibili alla maggiore porosità e alle migliori proprietà strutturali, dovute al riscaldamento rapido e uniforme tipico di tale tecnologia. I risultati supportano la fattibilità di trasformare i residui agro-industriali in

adsorbenti ad alto valore aggiunto, contribuendo allo sviluppo di soluzioni sostenibili, coerenti con i principi dell'economia circolare e ad alta robustezza per la rimozione dei contaminanti farmaceutici emergenti.

A conferma di ciò, anche la rimozione di sildenafil e tadalafil è stata studiata su carboni attivi oltre che su altri adsorbenti naturali, in particolare montmorilloniti naturali e modificate con bromuro di didodecil-dimetil-ammonio. L'adsorbimento su carboni attivi ottenuti tramite microonde ha raggiunto l'equilibrio in 2 ore, con efficienze di rimozione del 90,3% ± 0,1% per il sildenafil e del 95% ± 2% per il tadalafil, con una dose di 50 mg L^{-1}. La montmorillonite modificata con bromuro di didodecil-dimetil-ammonio ha raggiunto l'equilibrio in 60 minuti, rimuovendo l'84,9% ± 0,1% di sildenafil e il 91% ± 3% di tadalafil, a una dose di 250 mg L^{-1}. L'analisi cinetica e delle isoterme ha confermato che l'adsorbimento è governato da interazioni specifiche con siti attivi e da meccanismi di chemisorbimento, mentre le differenze nelle proprietà superficiali determinano le variazioni di capacità tra i diversi materiali.

Nel complesso, questo studio può contribuire in modo rilevante allo sviluppo di strategie integrate per il trattamento delle acque, caratterizzate da sostenibilità ambientale, fattibilità economica e coerenza con i principi dell'economia circolare. La valutazione congiunta delle prestazioni tecnologiche e del potenziale di valorizzazione delle risorse delinea un quadro scientifico completo per la progettazione di sistemi finalizzati alla riduzione degli inquinanti emergenti, al contenimento dei consumi energetici e alla promozione del riutilizzo dei materiali. Tale approccio pone basi solide per l'implementazione di misure efficaci di mitigazione dei contaminanti farmaceutici negli ambienti acquatici, favorendo la tutela a lungo termine degli ecosistemi e pratiche di gestione delle acque più resilienti.

LIST OF ABBREVIATIONS AND ACRONYMS

ADME/Tox: absorption, distribution, metabolism, excretion and toxicity

AC: activated carbon

AO: anodic oxidation

AOPs: Advanced Oxidation Processes

AU: arbitrary units

BDD: boron-doped diamond

BET: Brunauer-Emmett-Teller

BSEs: backscattered electrons

CE: capillary electrophoresis

CID: collision-induced dissociation

CP: conventional pyrolysis

CV: cyclic voltammetry

cGMP: cyclic guanosine monophosphate

DAD: photodiode-array detection (detector)

DDA: data-dependent acquisition

DDAB: didodecyldimethylammonium bromide

DI: direct injection

DPV: differential pulse voltammetry

D-A: Dubinin–Astakhov

D-R Dubinin–Radushkevich

DW: distilled water

EAOPs: Electrochemical Advanced Oxidation Processes

ECOSAR: Ecological Structure-Activity Relationship

ECs Emerging Contaminants

ED: erectile dysfunction

EDS: Energy Dispersive X-ray Spectroscopy

EF: Electro-Fenton

EMA: European Medicines Agency

EPR: Electron Paramagnetic Resonance

EQS: Environmental Quality Standards

ESI: electrospray ionization

FAB: Fast Atom Bombardment

FAT: Fixed Analyzer Transmission

FDA: Food and Drug Administration

FIA: flow injection analysis

FLD: fluorescence detection (detector)

FRR: Fixed Retard Ratio

FT-ICR: Fourier transform ion cyclotron resonance

FWHM: full width at half maximum

GC: glassy carbon

HCD: higher-energy collisional dissociation

HEPT: theoretical equivalent plate height

HPLC: High Performance Liquid Chromatography

HRMS: High-Resolution Mass Spectrometry

IARC: International Agency for Research on Cancer

ICSM: International Consultation on Sexual Medicine

IE: ionization energy

LC-MS: Liquid Chromatography-Mass Spectrometry

LIT: linear ion trap

LOD: limit of detection

LOQ: limit of quantification

LR: low resolution

LSIMS: liquid secondary ion mass spectrometry

LTQ: linear trap quadrupole

MALDI: matrix-assisted laser desorption ionization

MET: methanogenic

MMT: montmorillonite

MP: microwave-assisted pyrolysis

MRM: Multiple Reaction Monitoring

MS^n or MS/MS: tandem mass spectrometry

NET: norepinephrine transporters

PDE-5i: Phosphodiesterase Type 5 inhibitors

PMS: peroxymonosulfate

PNEC: predicted no-effect concentration

POPs: Persistent Organic Pollutants

PS: persulfate or peroxydisulfate

PZC: point of zero charge

Q: quadrupole

QSAR: Quantitative Structure-Activity Relationship

QSPR: Quantitative Structure–Property Relationship

RSD: relative standard deviation

RF: radiofrequency

SBG: spent brewery grains

SCE: saturated calomel electrode

SD: standard deviation

SEs: secondary electrons

SEM: Scanning Electron Microscopy

SERT: serotonin transporters

SILD: sildenafil

SIM: Selected Ion Monitoring

SNRIs: serotonin–noradrenaline reuptake inhibitors

SRM: Selected Reaction Monitoring

SWW: synthetic wastewater

TAD: tadalafil

TIC: Total Ion Current Profile

TOC: Total Organic Carbon

ToF: Time of Flight

UV: ultraviolet

UVA: near-ultraviolet

VFX: venlafaxine

VIS: visible

WFD: Water Framework Directive

WHO: World Health Organization

WWTP: wastewater treatment plant

XIC: eXtracted Ion Chromatogram

XPS: X-ray Photoelectron Spectroscopy

Index

1. INTRODUCTION

Environmental pollution is now among the most pressing global challenges, with profound implications for ecosystem integrity, biodiversity, human health, and sustainable development. Rapid industrialization, urban expansion, intensive agriculture, and the ever-growing use of pharmaceuticals have significantly increased the input of synthetic chemicals into aquatic, terrestrial, and atmospheric systems. Among these pollutants, pharmaceuticals and other Emerging Contaminants (ECs) have attracted particular attention because they often remain biologically active even at trace concentrations, resist conventional treatment, and accumulate in the environment, thereby posing novel and complex risks [1].

Although most pharmaceuticals are not inherently highly persistent, their continuous release from multiple sources, even in small but significant amounts, renders many effectively pseudo-persistent. These contaminants can exert both acute and chronic effects on aquatic flora and fauna, yet their long-term consequences and potential impacts on human health remain poorly understood. Recent studies indicate that pharmaceuticals may accumulate in aquatic invertebrates, which are then consumed by fish and ultimately by humans. This process, known as biomagnification, contaminates the food chain [2]. These substances can enter the aquatic environment through multiple pathways: direct or indirect discharges from pharmaceutical manufacturing wastewater treatment plants (WWTPs), human excretion into domestic wastewater, or animal excretion from agricultural sources (**Figure 1.1**).

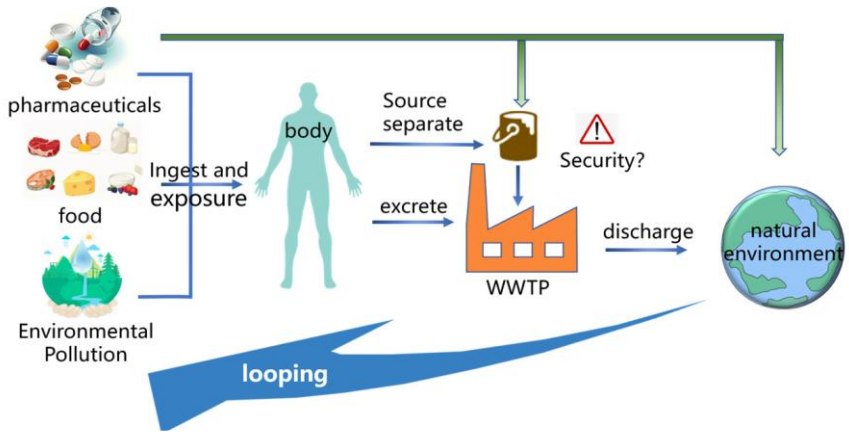

Figure 1.1 *Major pathways through which pharmaceuticals enter the environment* [2].

Pharmaceutical active compounds are detected in surface waters, groundwater, and even drinking-water supplies around the world; they are not yet strictly regulated in most jurisdictions and thus escape full monitoring [3]. Pharmaceuticals pose a particular challenge as environmental contaminants because they are designed to be biologically active. Even at trace concentrations, they can interfere with endocrine systems, disrupt development, promote antibiotic resistance, and impact non-target organisms. As a result, these substances are

increasingly concerning for environmental safety and public health [4]. Because traditional WWTPs were largely designed to remove conventional pollutants (e.g., nutrients, suspended solids, pathogens), many micropollutants persist and are released into downstream environments [5]. Moreover, the fate and behaviour of these compounds in engineered and natural water cycles remains poorly understood in many contexts: their persistence, transport, transformation, and potential to generate more toxic by-products pose serious gaps in our knowledge [6].

Given the complexity of these ECs, the urgency of developing innovative and sustainable remediation technologies cannot be overstated. It is essential not only to remove these pollutants effectively, but also to do so in ways that are environmentally efficient, economically feasible, and scalable. In this context, the present thesis aims to evaluate and compare advanced physical and chemical treatment methods specifically targeting pharmaceuticals such as sildenafil (SILD), tadalafil (TAD), and venlafaxine (VFX), assessing each method's removal efficiency, ecological footprint, cost-effectiveness, and potential for scale-up. By explicitly linking the environmental challenge to treatment strategy development, this research contributes to the broader objective of mitigating pharmaceutical pollution and safeguarding aquatic ecosystems, groundwater resources, and human health.

The following sections provide an overview of the literature on advanced water treatment methods, highlighting the advantages and limitations of the most widely adopted degradation and removal strategies. A concise description of the chemical and physical properties of key contaminant classes is also presented, with particular attention to the factors influencing their persistence and reactivity in natural environments. Among the available treatment strategies, Advanced Oxidation Processes (AOPs) and adsorbent-based approaches are examined in detail, as these technologies remain central to the effective mitigation of ECs.

1.1 Definition and classification of Emerging Contaminants (ECs)

Environmental pollution is one of the most pressing global challenges of the 21st century, affecting air, water, and soil systems and posing significant risks to ecosystems, human health and sustainable development. Along with "classic" pollutants (Persistent Organic Pollutants, POPs), ECs are now considered. ECs are natural or synthetic chemicals that are present or transformed into new chemical compounds in water bodies across the globe [7]. These contaminants are classified and categorized as follows [8-10]:

- Pharmaceuticals (illicit and prescribed drugs);
- Personal care products (cosmetic, surfactants, disinfectants, domestic biocides, food additives);

- Industrial chemicals (food additives, pesticides, polychlorinated biphenyls, flame retardants, antimicrobial substances);
- Disinfection byproducts (from water treatment plant: nitrosamine, halonitromethanes, haloacetonitriles, trihalomethanes, haloacetic acids);
- Algal toxins (toxic compounds released from some algae: cyanotoxins, microcystin);
- Biocides and their metabolites (plants and agricultural preventive agents, the well-known pesticides);
- Bioterrorism and disruption devices (biological and chemical weapons).

The term "emerging" does not necessarily imply that these substances are newly synthesized; rather, it reflects recent detection in environmental matrices due to advances in analytical techniques, increasing awareness of their potential toxicity, persistence, bioaccumulation, adverse ecological or human health effects, and insufficient regulatory frameworks to control their presence in water, soil or air [11]. ECs are characterized by [12-13]:

- low concentrations (often ng L^{-1} to μg L^{-1} in water);
- potential for bioaccumulation and biomagnification;
- resistance to conventional wastewater treatment;
- sub-lethal or chronic effects on organisms, including endocrine disruption, genotoxicity and neurotoxicity.

Although present at low concentrations, they are continuously released into the environment, leading to so-called pseudo-persistence and a steadily increasing and continuous presence. Therefore, the presence of ECs in our environments is a global issue that requires urgent attention. Aquatic ecosystems are highly vulnerable to pollution, as they are critical components of the Earth's biosphere and essential for biodiversity, the human water supply, and food production. More than 700 ECs have been detected in European surface waters alone, including metabolites and degradation products. Their monitoring has only become possible through the development of advanced analytical techniques such as liquid chromatography coupled with high-resolution mass spectrometry (LC-HRMS). The sources of ECs are diverse and include pharmaceuticals released from manufacturing effluents, domestic wastewater and veterinary use in agriculture; personal care products and cosmetics; pesticides and fertilizers from agricultural runoff; household chemicals and industrial discharges (**Figure 1.2**) [14].

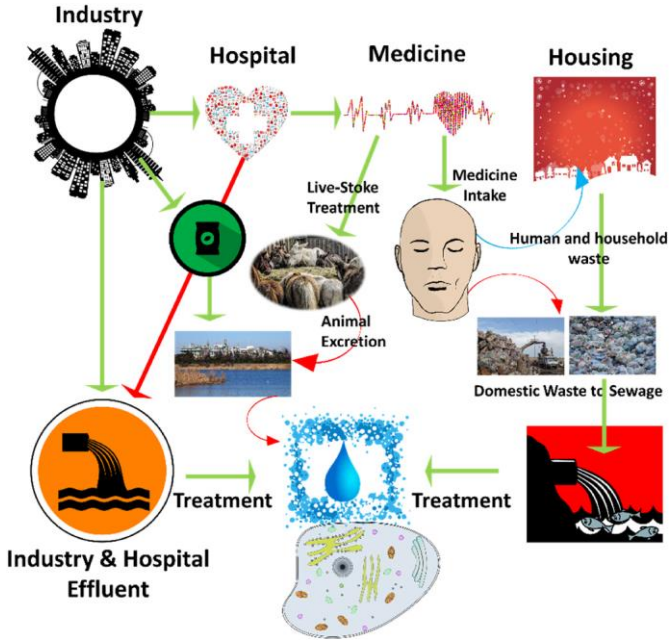

Figure 1.2 *Primary sources of ECs in the environment* [14].

To assess their ecological impact, ecotoxicological bioassays are employed using species from different trophic levels, including unicellular algae (*Pseudokirchneriella subcapitata*), freshwater crustaceans (*Daphnia magna*), and bioluminescent bacteria (*Vibrio fischeri*) [15]. Among these, *Daphnia magna* tests are widely used due to their sensitivity. Results are expressed as mortality/immobilization percentages or EC_{50} values, which indicate the concentration that causes a 50% effect in the test population (European Commission, 1996) [16-17]. Substances are classified as very toxic (<1 mg L^{-1}), toxic (1–10 mg L^{-1}), harmful (10–100 mg L^{-1}), or not classified (>100 mg L^{-1}). The growing prevalence and pseudo-persistent nature of these contaminants, coupled with their bioactive properties and potential for biomagnification, underscores the urgent need for advanced monitoring, remediation, and regulatory strategies. Addressing these challenges requires identifying methods that are not only effective in removing pollutants but also eco-friendly, economically feasible and scalable, ensuring the protection of aquatic ecosystems, groundwater resources, and human health.

1.2 What are Watch Lists?

In environmental policy, a Watch List is a regulatory and monitoring tool used to identify and prioritize substances that may pose a risk to ecosystems or human health, particularly when information is limited. These Watch Lists track water quality, availability, and risks such as pollution or overuse, supporting sustainable water management and fair distribution. The first Watch List was established in 2015 as a cost-effective and dynamic way of ensuring that the Commission can keep the EU legislation on water pollutants up-to-date by

gathering evidence, in particular on contaminants of emerging concern. To date, five Watch Lists have been published under the Water Framework Directive (WFD).

The Watch List acts as an early-warning system, allowing authorities to monitor ECs, assess their prevalence in environmental matrices, and generate data to guide future regulatory decisions. Substances are typically selected based on scientific evidence of potential toxicity, persistence, bioaccumulation, or widespread occurrence, as well as their relevance to public health or ecological protection. Monitoring programs collect standardized data across regions, enabling trend analysis and comparisons over time.

Under the WFD (Directive 2000/60/EC), the Watch List includes emerging pollutants such as pharmaceuticals, industrial chemicals, and endocrine-disrupting compounds, and it is periodically updated based on scientific risk assessments. Data from the Watch List inform whether substances should be added to the priority substances list, potentially leading to legally binding environmental quality standards (EQS) and stricter control measures. This proactive approach bridges the gap between emerging scientific evidence and formal regulation, helping policymakers anticipate risks, prioritize research, and implement effective monitoring and mitigation strategies before contaminants become widespread.

The latest version, the 5th Watch List, was published in February 2025 [18]. It adds new substances suspected of posing risks to aquatic environments and human health and mandates their monitoring across EU Member States. According to the 5th Watch List, these substances, along with other compounds, are targeted for removal in the next update, highlighting the urgent need to identify effective techniques for their elimination from aquatic environments.

1.3 Venlafaxine

The antidepressant VFX and its metabolite O-desmethylvenlafaxine were first included in the 3rd Watch List (EU/2020/1161) [19] and retained in the 4th Watch List (EU/2022/1616). Since VFX is a substance of environmental concern, it was selected as one of the target pharmaceuticals for this study. Chemically known as 1-[2-(dimethylamino)-1-(4-methoxyphenyl)ethyl]cyclohexanol hydrochloride, VFX has the molecular formula $C_{17}H_{27}NO_2$ and molecular weight of 313.86 $g \cdot mol^{-1}$ (its chemical structure is shown in **Figure 1.3**).

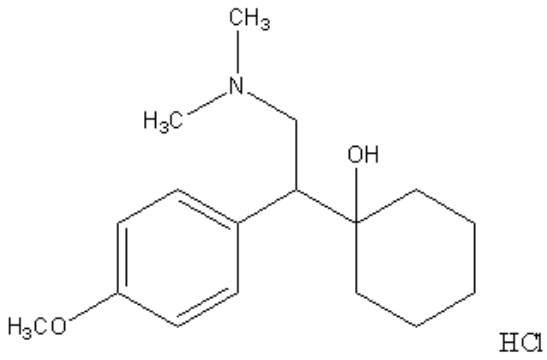

Figure 1.3 *Chemical structure of venlafaxine hydrochloride*.

VFX is an antidepressant belonging to the class of serotonin–noradrenaline reuptake inhibitors (SNRIs). It acts by blocking the serotonin (SERT) and norepinephrine (NET) transporters, thereby preventing the reuptake of these neurotransmitters into the presynaptic terminal and increasing their availability in the synaptic cleft. This mechanism enhances neurotransmission and alleviates the symptoms of psychiatric disorders associated with deficits in serotonin and norepinephrine. VFX exhibits dose-dependent selectivity. At low doses (≤150 mg/day), it primarily inhibits serotonin reuptake, whereas at moderate doses (150–300 mg/day), it also inhibits norepinephrine reuptake. At higher doses (>300 mg/day), it shows weak inhibition of dopamine reuptake. The recommended therapeutic dose ranges from 75 to 375 mg/day. Overdoses can lead to serious adverse effects, including cardiac arrhythmias, serotonin syndrome, hypertension or hypotension, coma, and, in extreme cases, death. [20].

Pharmacokinetically, most of the VFX (approximately 87% of the administered dose) is not metabolized and is excreted unchanged in urine. Consequently, VFX enters the environment primarily through human excretion, and via waste streams from hospitals, pharmaceutical production, and improper disposal (**Figure 1.4**). Its high excretion rate, combined with widespread therapeutic and off-label use, makes VFX a persistent EC in aquatic systems, where it can be detected in wastewater influents, effluents and surface waters worldwide [21].

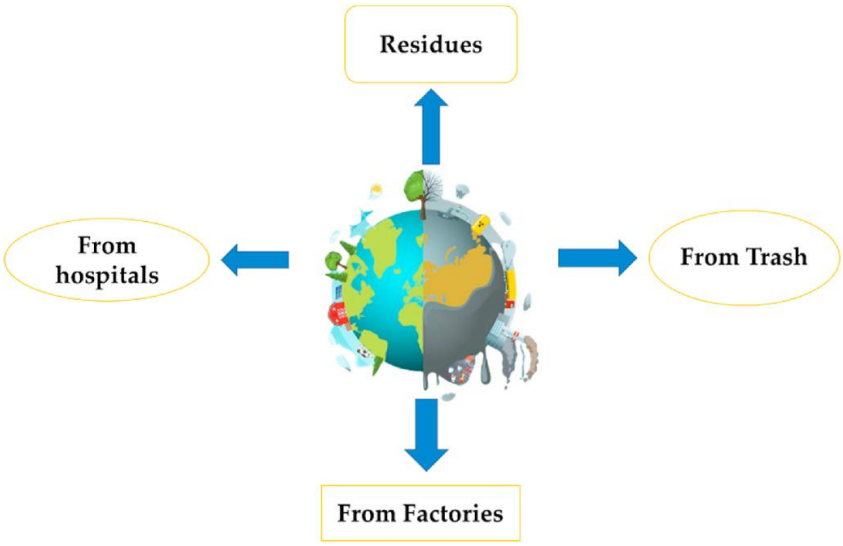

Figure 1.4 *Primary environmental entry pathways of VFX* [21].

Chemically, VFX has a p*Ka* of 9.6, meaning that at natural waters or wastewater pH (6.5-8.5) values, it predominantly exists in a cationic form due to protonation of its tertiary amine group. Its aqueous solubility is relatively high (572 mg mL^{-1} at 25°C), contributing to its mobility in aquatic environments and persistence in water systems. Its logK_{ow} value of 3.2 indicates moderate hydrophobicity and potential for bioaccumulation [21]. Its presence in aquatic environments results primarily from human excretion and the discharge of untreated or partially treated wastewater [22]. The continuous input of VFX, even at low concentrations (typically in the ng L^{-1} to low µg L^{-1} range), classifies it as a "pseudo-persistent" contaminant, as repeated releases maintain steady environmental levels despite partial biodegradation [21]. The most commonly detected metabolite of VFX, O-desmethylvenlafaxine, is also commonly detected and contributes to the overall pharmacological load in the environment [23]. The persistence and potential biological activity of VFX and its metabolite raise concerns about long-term ecotoxicological effects, including endocrine disruption and behavioral alterations in aquatic organisms [24]. As a non-volatile, poorly degradable compound in natural waters, VFX exhibits high environmental persistence and potential toxicity to aquatic life. Recent ecotoxicological studies have demonstrated that exposure to VFX can significantly reduce serotonin levels in the brains of fish, such as European seabass (*Dicentrarchus labrax*), impairing their hunting abilities and altering reproductive mechanisms in aquatic organisms [25]. In zebrafish (*Danio rerio*), for example, a six-week exposure to a pharmaceutical mixture containing VFX led to a substantial decrease in embryo production, highlighting potential long-term reproductive effects [26]. Data from the German Federal Environment Agency reported over 400 detections of VFX in various water bodies, with concentrations ranging from 0.02 ng·L^{-1} to 400 ng·L^{-1}. The highest levels, exceeding 1 µg·L^{-1}, were observed in surface waters

and WWTP effluents. These effluents are considered the primary entry points of VFX into the aquatic environment, due to its incomplete removal during conventional treatment processes. Such findings underscore the need to develop advanced remediation strategies. [27].

1.4 Phosphodiesterase Type 5 inhibitors (PDE-5i)

Phosphodiesterase type 5 inhibitors (PDE-5i), such as SILD and TAD, are increasingly detected in surface waters, groundwaters and wastewater effluents worldwide [28-29]. Despite their rising environmental relevance, these compounds are not included in any of the five Watch Lists for priority monitoring. However, mounting evidence of their persistence and ecological risk has led several authors to recommend their inclusion in future monitoring programmes [28-29]. For this reason, in addition to VFX, SILD and TAD were also considered ECs and selected as target compounds in this study.

PDE-5i are primarily used for the treatment of erectile dysfunction (ED). ED has been defined by the Fourth International Consultation on Sexual Medicine (ICSM) as "the constant or recurrent inability to achieve and maintain a penile erection sufficient for sexual satisfaction" [30]. The etiology of ED is multifactorial. It can be neurological, due to impaired nerve signalling to the corpora cavernosa; psychological, including depression, stress, and anxiety; or endocrinological, such as low testosterone or other hormonal imbalances [31]. PDE-5i are structurally similar to cGMP (cyclic guanosine monophosphate) and can block the enzyme's degradative action on cGMP by occupying its catalytic site [32]. By maintaining high cGMP levels in the smooth muscle cells of the corpora cavernosa, PDE-5i prolong the physiological mechanism of penile erection. In addition to treating ED, these drugs are approved for other therapeutic indications, such as pulmonary arterial hypertension and lower urinary tract symptoms, as well as experimental applications in cardiovascular and neurological disorders (**Figure 1.5**) [33].

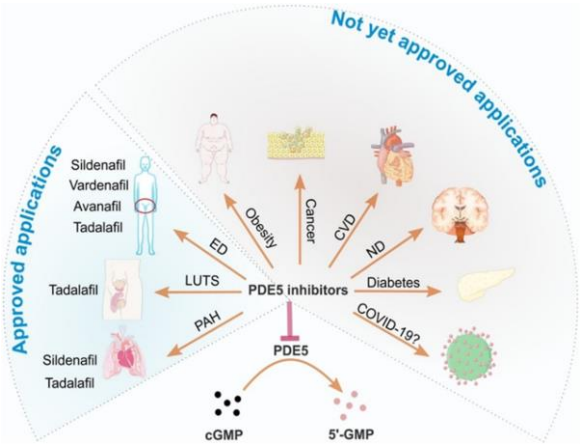

Figure 1.5 *Therapeutic uses of PDE-5 inhibitors* [33].

However, a concerning aspect is that these drugs are not only used for medical purposes but also recreationally. According to a 2023 study, SILD sales are extremely high among young adults aged 20–30 years [34]. This suggests that PDE-5 inhibitors are often used recreationally rather than for legitimate medical purposes, resulting in unregulated and potentially elevated environmental loads [35].

1.4.1 Sildenafil (SILD) and tadalafil (TAD)

SILD, known as 1-{[3-(6,7-dihydro-1-methyl-7-oxo-3-propyl-1H-pyrazolo [4,3-d] pyrimidin-5-yl)-4-ethoxyphenyl] sulfonyl}-4-methylpiperazine, belongs to the class of PDE-5i. It was first discovered in 1989 by the Cardiovascular Research and Development group at Pfizer (Sandwich, UK) during studies aimed at identifying selective PDE-5i for the treatment of *angina pectoris*. Although the compound proved ineffective in relieving *angina* symptoms, researchers observed an unexpected side effect, penile erection, which led to a new therapeutic application [36]. This serendipitous finding laid the foundation for the use of SILD in the treatment of ED. In 1998, SILD was approved by the USD Food and Drug Administration (FDA) for ED therapy, and later, in 2005, by the European Medicines Agency (EMA) for the treatment of pulmonary arterial hypertension in patients classified in functional classes II and III.

Chemically, SILD has the molecular formula $C_{22}H_{30}N_6O_4S$, a molecular mass of 474.6 g mol^{-1} and exhibits poor aqueous solubility (5–10 mg L^{-1}) [37]. Its logK_{ow} value of 0.93 indicates very high hydrophobicity and potential for bioaccumulation [38]. The molecular structure of SILD is shown in **Figure 1.6**.

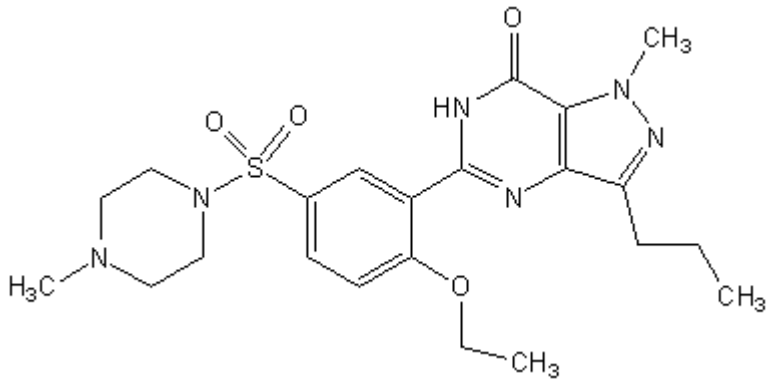

Figure 1.6 *Chemical structure of SILD.*

TAD, whose IUPAC name is (2R,8R)-2-(1,3-benzodioxol-5-yl)-6-methyl-3,6,17-triazatetracyclo[8.7.0.0^{3},^{8}.0^{11},^{16}]heptadeca-1(10),11,13,15-tetraene-4,7-dione, is another member of the PDE-5i class. It was developed in the late 1990s by ICOS Corporation in

collaboration with Eli Lilly & Co. as part of a research program to identify selective PDE-5 inhibitors with longer-lasting pharmacological effects. [39].

Chemically, TAD (**Figure 1.7**) has the molecular formula $C_{22}H_{19}N_3O_4$, with a molecular weight of 389.41 g mol^{-1}. It appears as a white-to-off-white crystalline powder, with poor water solubility (approximately 5 mg L^{-1} at 25°C) and high lipophilicity, which contribute to its slower elimination and a prolonged duration of effect, up to 36 hours, earning it the nickname "the weekend pill" [40]. A logK_{ow} value of 1.42 for TAD classifies it as very lipophilic [41].

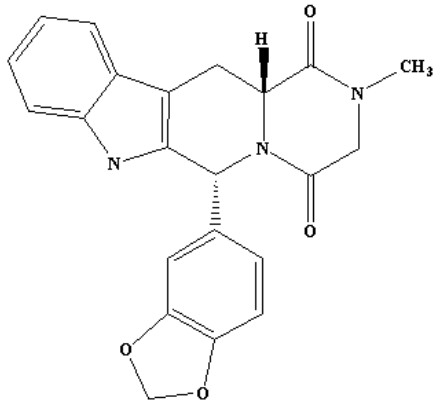

Figure 1.7 *Chemical structure of TAD.*

Unlike SILD, TAD demonstrated a markedly longer half-life (17.5 hours) and duration of action, allowing for greater flexibility in dosing and extended therapeutic coverage [39-40]. The compound was approved by the USD FDA in 2003 for the treatment of ED and later, by the EMA for benign prostatic hyperplasia and PAH. The compound acts by selectively inhibiting PDE-5 in the corpus cavernosum, thereby enhancing the nitric oxide–cGMP pathway, promoting smooth muscle relaxation, and increasing blood flow.

Because of its wide use and persistence, TAD, like SILD, has been detected in wastewater and surface waters worldwide, raising concerns about its environmental persistence and ecotoxicological effects [43]. In recent years, SILD has received particular attention from the scientific community due to its high sales volume and frequent detection in the environment, particularly in wastewater [41-43]. For instance, Nieto et al. (2010) detected SILD in wastewater influents, effluents, and sludge in Spain at ng L^{-1} concentrations [44], while Schroeder et al. (2010) reported ~35 ng L^{-1} in municipal wastewater in Germany [45]. Similarly, Causanilles et al. (2017) found a threefold increase in SILD levels in Korean urban wastewater between 2012 and 2015, following the drug's patent expiration and the market introduction of over 60 generic versions [46]. A small but insightful study published in a British medical journal highlighted the detection of unexpectedly high concentrations of SILD in wastewater samples collected from three Dutch cities. The measured levels were significantly higher than those

predicted based on official prescription data. According to the national database, this discrepancy suggests that the illegal supply and unregulated use of SILD are widespread. These findings reinforce concerns about the growing non-prescribed consumption and illicit market distribution of PDE-5 inhibitors, which may contribute not only to public health risks but also to their continuous release into the aquatic environment [47]. Over the past decade, environmental monitoring studies have increasingly detected PDE-5 inhibitors in WWTP influents, effluents, and sludge, with concentrations typically in the low ng L^{-1} range [28].

Their very low removal during conventional wastewater treatment, combined with their chemical stability, results in their accumulation and pseudo-persistence in aquatic environments; for this reason, SILD and TAD are now recognized as ECs of growing concern, underscoring the need for very effective monitoring and new removal strategies.

1.5 Conventional treatment methods and their limitations

Conventional WWTPs are primarily designed to remove biodegradable organic matter, nutrients and suspended solids. However, they are not specifically equipped to eliminate trace ECs such as pharmaceuticals. Standard biological processes, including activated sludge, trickling filters, and membrane bioreactors, often fail to fully degrade these compounds due to their chemical stability, low biodegradability, and relatively high solubility, as well as their continuous input into the system [26, 45]. Many pharmaceuticals, such as antidepressants and ED drugs, resist biodegradation and persist through conventional treatment steps, leading to their accumulation in effluents and eventual release into aquatic environments. Moreover, some compounds may undergo incomplete transformation, generating intermediate products that can be equally or even more toxic than the parent compounds [49].

Physical and chemical processes such as coagulation, flocculation, sedimentation and filtration may contribute to partial removal but are often ineffective for highly soluble and stable molecules. Additionally, adsorption onto activated sludge or suspended solids only temporarily transfers contaminants to the solid phase without achieving real degradation [50]. In fact, the technologies commonly applied in WWTPs have proven insufficient for the complete removal of pharmaceuticals and other ECs. As a result, these substances are continuously released into surface waters, where they can reach concentrations in the μg L^{-1} range [51]. Therefore, while conventional methods can mitigate some pollutants, they remain insufficient for the complete removal of ECs, underscoring the need to apply advanced treatment technologies, such as AOPs, adsorption on novel materials, and electrochemical degradation, to ensure environmental protection and water safety [50].

Conventional wastewater purification processes generally include the following stages (**Figure 1.8**):

- Pre-treatment: large solid materials (plastics, metals, paper) are removed using screens or bar racks. The wastewater is then collected in an equalization tank and pumped to the next stage of treatment.
- Primary treatment: wastewater flows slowly through a grit chamber, allowing sand and coarse particles to settle. The flow then passes to a sedimentation tank, where solids settle at the bottom while oils and greases float to the surface.
- Secondary treatment: the clarified water undergoes biological treatment to remove biodegradable organic matter. Air is bubbled into the aeration tank to promote the growth of aerobic bacteria, which degrade organic pollutants such as food residues and fecal matter. The sludge produced is further treated in anaerobic digesters.
- Tertiary treatment: this final step often involves disinfection (typically chlorination) and nutrient removal (nitrogen and phosphorus) before the treated effluent is discharged into surface waters [52].

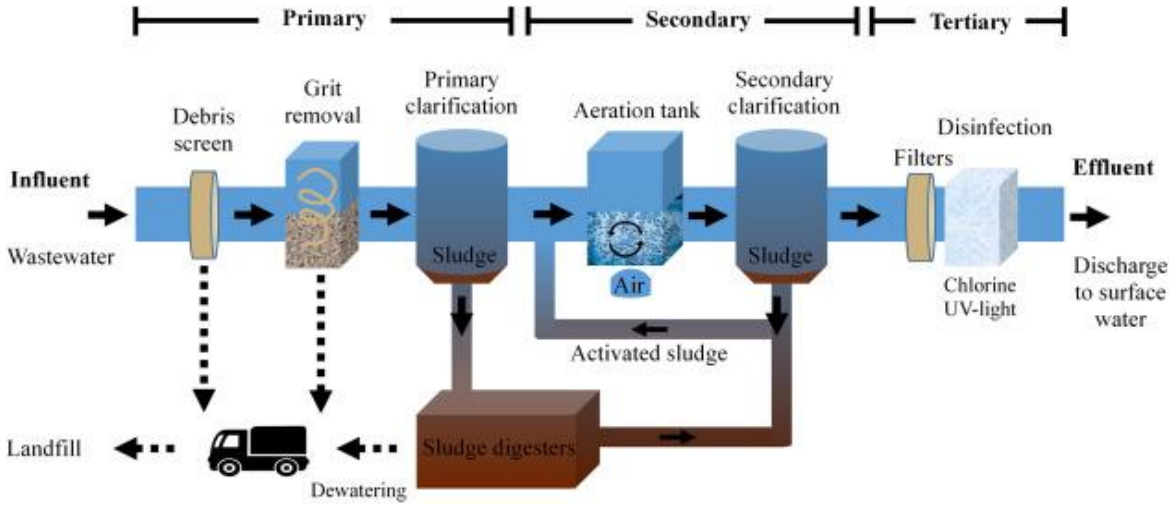

Figure 1.8 *Schematic representation of a WWTP* [52].

The removal efficiency depends on various factors, including the physicochemical properties of the pollutants, the type of treatment process, operational parameters and seasonal variations. Moreover, many pharmaceuticals present in wastewater in conjugated forms may regenerate their active components during treatment. Some compounds can also inhibit the activity of microorganisms within biological systems, further reducing process efficiency. The fraction of compounds that are not effectively removed eventually reaches surface and groundwater and, in some cases, even drinking water sources [53].

In recent years, several advanced treatment technologies have been developed and tested to overcome the limitations of conventional methods and to achieve complete removal of ECs, paving the way for more efficient remediation strategies [54].

1.6 Advanced Treatment Methods

Advanced treatment methods have emerged as critical solutions for effectively addressing pharmaceutical contaminants in water, given the limitations of conventional wastewater treatment. These removal methods can be classified into the following categories (**Figure 1.9**) [55]:

- Biological treatments: These involve removing pharmaceuticals through biodegradation, specifically via nitrification and anaerobic digestion. Nitrification is the oxidation of reduced inorganic nitrogen compounds by autotrophic bacteria, which use inorganic carbon to convert ammonia to nitrites and nitrites to nitrates. Anaerobic digestion treats wastewater treatment sludge by employing microorganisms that break down pollutants into methane and carbon dioxide [56]. Biological treatments are often insufficient for effectively removing ECs from the environment.
- Chemical treatments: This category includes AOPs, such as photodegradation and electrochemical oxidation, which are among the most promising wastewater treatment methods. Indeed, AOPs generate highly reactive species, including hydroxyl and sulfate radicals, which efficiently degrade persistent contaminants in wastewater [57].
- Physical treatments: These are the most common and include membrane filtration and adsorption. Adsorption removes contaminants using various adsorbent materials such as activated carbon, biochar, and zinc oxide nanoparticles. Membrane processes, on the other hand, offer the advantage of removing microorganisms and viruses without chemical disinfection while reducing the concentration of organic substances in wastewater. Membranes primarily retain pharmaceuticals through size-exclusion and charge-repulsion mechanisms [58]. However, a limitation of physical methods is that they only separate contaminants from water rather than fully degrade them, thereby leaving potential environmental risks.

Figure 1.9 *Different technologies used for wastewater treatment* [59].

1.7 Advanced Oxidation Processes (AOPs)

The limited efficiency of conventional degradation methods, coupled with increasing water pollution, has driven the development of new technologies for removing organic ECs. AOPs represent a promising alternative to traditional water treatment approaches [56]. The main classes of AOPs are illustrated in **Figure 1.10**.

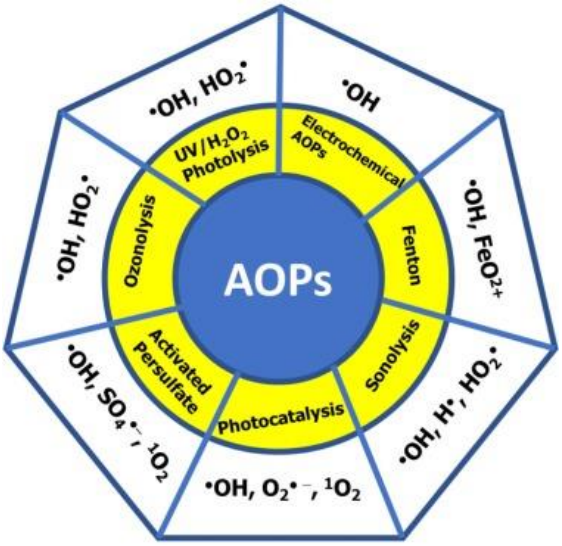

Figure 1.10 *Primary categories of AOPs* [56].

AOPs involve various reaction systems but share a common feature: the generation of hydroxyl radicals (•OH), highly reactive species that can attack a wide range of organic molecules. These water treatment approaches include Fenton processes, photocatalysis and photolysis, ozone-based systems and Electrochemical Advanced Oxidation Processes (EAOPs).

Although AOPs are relatively costly, they are widely used because the production of •OH radicals ensures high removal efficiency for contaminants resistant to conventional treatments [60]. However, conventional AOPs require the use of potentially hazardous

chemicals such as H_2O_2 or O_3 and may produce toxic transformation by-products. In contrast, EAOPs generate oxidizing species directly at the electrode surface, thereby eliminating or significantly reducing the need for chemical oxidants and providing a greener, potentially safer alternative to conventional AOPs. EAOPs also allow fine control over the degradation process by adjusting parameters such as current density, electrode material, and electrolyte composition, thereby improving efficiency and minimizing the formation of toxic intermediates. Overall, while conventional AOPs remain effective and widely used, EAOPs represent a promising evolution toward more sustainable, controllable, and selective degradation of contaminants in water.

1.7.1 Photodegradation and Photocatalysis

AOPs represent an innovative and promising alternative for treating wastewater containing recalcitrant organic compounds [61], such as pesticides, pharmaceuticals, surfactants, dyes, and endocrine-disrupting chemicals. The application of AOPs is gaining importance because these processes can oxidize a wide range of biologically persistent compounds, achieving either complete mineralization or the formation of more biodegradable intermediates [62]. Among the most widely used AOP technologies for water purification and wastewater treatment, heterogeneous photocatalysis using semiconductors and oxidation with reagents such as hydrogen peroxide (H_2O_2), peroxymonosulfate (PMS), and persulfate (PS) have proven particularly effective [60-62]. AOPs are based on the *in situ* generation of highly reactive oxidizing species at concentrations sufficient to decontaminate water effectively. They are generally classified according to the method of radical generation into chemical, photolytic and photocatalytic processes (**Figure 1.11**):

- Chemical AOPs generate radical species solely through reactions between oxidants, without using any physical promoters.
- Photolytic AOPs produce radicals by combining ultraviolet (UV) or visible (VIS) light with chemical reagents.
- Photocatalytic AOPs operate in a heterogeneous phase, using semiconductor materials such as titanium dioxide (TiO_2), which generate radicals upon irradiation with UV light of the appropriate wavelength.

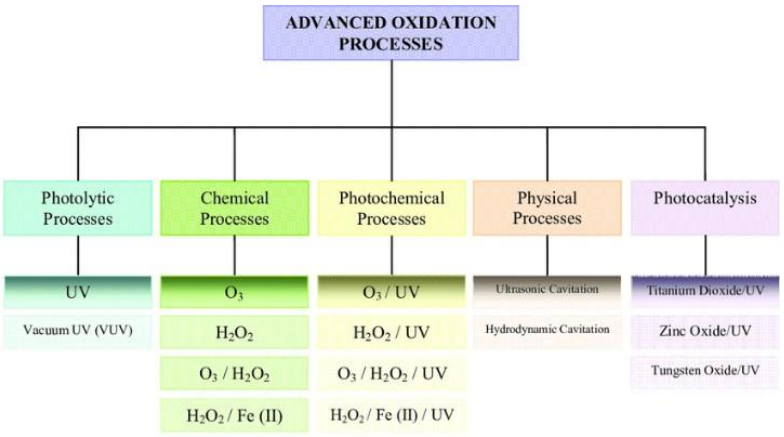

Figure 1.11 *Typology of AOPs* [61].

AOPs are characterized by two main stages: the first involves the *in situ* generation of highly reactive oxidizing species, while the second corresponds to the oxidative degradation of organic contaminants. Radicals are molecules with an unpaired electron in their outermost orbital; this unpaired electron enables them to react rapidly with electron donors, such as organic pollutants in wastewater. Among these, the hydroxyl radical (•OH) is the most commonly used oxidant due to its high reactivity, low selectivity, and ability to react with a wide range of compounds, exhibiting a rate constant of 10^6–10^{10} M^{-1} s^{-1}. Moreover, •OH possesses a very high oxidation potential (2.8 V). Although hydroxyl radicals have an extremely short lifetime of approximately 10 µs, this is sufficient to ensure their oxidative action. They react with organic compounds to produce ·R–OH radicals, which are subsequently converted to organic peroxyl radicals (ROO·) in the presence of oxygen. These radical species continue to react with one another, generating additional highly reactive compounds, such as hydrogen peroxide, which ultimately leads to the complete chemical degradation of the organic contaminants. The generation of hydroxyl radicals is typically catalyzed by the combination of oxidizing agents, such as hydrogen peroxide, or specific catalysts, including titanium dioxide or Fe^{2+} ions, in the presence of Sunlight. In this study, both photodegradation with H_2O_2, PS and PMS, as well as photocatalysis with titanium dioxide, were investigated.

An important AOP relies on the combination of Sunlight and hydrogen peroxide. In this system, reactive radical species are generated via the photolysis of hydrogen peroxide [66]. The reaction involves the cleavage of a chemical bond in a molecule upon exposure to electromagnetic radiation. When H_2O_2 absorbs Sunlight, it reaches an excited electronic state with higher energy than its ground state. If this excitation leads to a dissociative state whose energy decreases monotonically with bond distance and lacks a minimum, the molecule tends to dissociate.

In most cases, this dissociation is homolytic, producing two hydroxyl radicals. These radicals can subsequently initiate chain reactions, leading to the oxidation and degradation of organic pollutants. Sunlight interacts with hydrogen peroxide molecules, leading to the dissociation of the O–O bond and the consequent formation of two hydroxyl radicals [67]:

$$H_2O_2 + hv \rightarrow 2{\bullet}OH$$

The hydroxyl radicals produced are extremely reactive and immediately interact with other species in solution, resulting in the following possible reaction mechanisms [68]:

$$\bullet OH + \bullet OH \rightarrow H_2O_2$$

$$\bullet OH + \bullet O_2 \rightarrow O_2 + OH^-$$

$$\bullet OH + HO_2\bullet \rightarrow O_2 + H_2O$$

$$HO_2\bullet + HO_2\bullet \rightarrow O_2 + H_2O_2$$

$$O_2\bullet + HO_2\bullet \rightarrow O_2 + HO_2^-$$

$$OH\bullet + \text{organic compound} \rightarrow \text{oxidation products}$$

H_2O_2 is a strong oxidizing agent (standard potential 1.70 V), and its application for the removal of various inorganic and organic pollutants is well documented [66-67].

Persulfate, or peroxydisulfate, is a colourless or white crystalline solid characterized by high stability. It is easily soluble in water (solubility of 730 g L^{-1}) and its aqueous solution is acidic. The PS molecule has a symmetric structure, with an O–O bond length of 1.497 Å and a bond dissociation energy of 140 kJ mol^{-1} [71]. The persulfates most used in experimental studies are sodium persulfate ($Na_2S_2O_6$) and potassium persulfate ($K_2S_2O_6$). PS is stable at pH values below 6 and around 12; however, at pH 9, it exhibits the lowest stability, where approximately half of HSO_5^- decomposes into SO_5^{2-} [72].

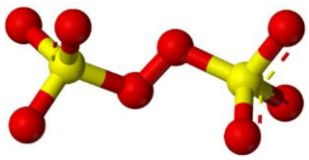

Figure 1.12 *Structure of PS: the sulfur atom is depicted in yellow and the oxygen atoms are shown in red. The dashed line indicates the O–O bond that undergoes cleavage to generate sulfate radicals.*

PS (**Figure 1.12**) can react directly with various organic substances by accepting electrons through a direct oxidation process, according to the following reaction:

$$S_2O_8^{2-} + 2e^- \rightarrow 2SO_4^{2-}$$

Indirectly, PS can also generate highly reactive radical species, mainly sulfate and hydroxyl radicals [73], as shown by the following reactions:

$$O_8^{2-} + 2e^- \rightarrow SO_4^{2-} + \bullet SO_4^-$$

$$\bullet SO_4^- + OH^- \rightarrow SO_4^{2-} + \bullet OH$$

At high pH, PS tends to self-activate, generating sulfate radicals. Once initiated, the reaction propagates through hydroxyl radical formation. Under strongly alkaline conditions (pH > 11), base-induced activation is particularly effective in generating both persulfate and hydroxyl radicals. The main operational challenge is activating PS, which may require adding a base to the system, depending on the aqueous phase's specific characteristics.

PMS, also known as Oxone (**Figure 1.13**), is a triple salt ($2KHSO_5 \cdot KHSO_4 \cdot K_2SO_4$) and serves as the precursor of the PMS ion (HSO_5^-). Its standard redox potential (+1.81 V) is higher than that of H_2O_2. Compared to H_2O_2, PMS is a solid compound stable at room temperature and highly soluble in water (>250 g L^{-1}). It has an asymmetric molecular structure with an O–O bond length of 1.453 Å and a bond energy estimated in the range of 140–213.3 kJ mol^{-1}.

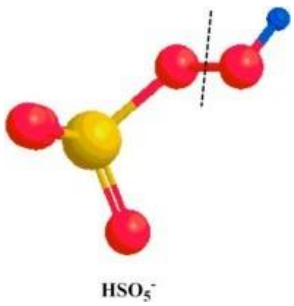

Figure 1.13 *Structure of PMS: the sulfur atom is shown in yellow, the oxygen atoms in red. The dashed line represents the position of the O-O bond cleavage to form sulfate radicals.*

The half-reaction leading to hydrogen sulfate formation can be represented as follows:

$$HSO_5^- + H^+ + 2e^- \rightarrow HSO_4^- + H_2O$$

The degradation of Oxone may proceed through the following reactions:

$$HSO_5^- + e^- \rightarrow \bullet SO_4^- + \bullet OH^-$$

$$HSO_5^- + e^- \rightarrow \bullet SO_4^- + \bullet OH$$

$$HSO_5^- \rightarrow \bullet SO_5^- + H^+ + e^-$$

The reactions of Oxone with organic compounds are generally slow at ambient temperature. However, PMS can be efficiently activated by photolysis or thermolysis, leading to the generation of reactive radicals ($\bullet SO_4^-$ and •OH). Compared with hydroxyl radicals, sulfate radicals exhibit an equal or even higher redox potential (2.5–3.1 V), depending on the activation

method [74]. Several stimuli, including heat, alkaline conditions, light, ultrasound and various catalysts, can activate them.

AOPs using Sunlight as an energy source for POP degradation offer the significant advantage of low operational costs, as they can exploit abundant, readily accessible solar radiation. Sunlight is unevenly distributed across the globe due to factors such as solar altitude, which depends on latitude and season, and atmospheric conditions, influenced by cloud cover and pollution levels. Therefore, in regions with high solar irradiation, the photolytic degradation of organic compounds in wastewater effluents can be enhanced either through direct phototransformation via an excited-state reaction or through indirect phototransformation via photosensitized processes. Two main AOPs utilize Sunlight as an energy source: heterogeneous photocatalysis, which employs semiconductors, and homogeneous photocatalysis, such as Fenton processes [72-73]. Heterogeneous photocatalysis activated by Sunlight primarily uses the near-ultraviolet (UVA) portion of the solar spectrum (wavelengths below 380 nm), whereas homogeneous Fenton photocatalysis utilizes a broader portion of the solar spectrum (up to 580 nm). Both approaches are effective for the photodegradation of POPs. These methods represent innovative ways to harness renewable energy and are highly promising for wastewater treatment [74-75].

Photocatalysis is the combination of photochemistry and catalysis, a process in which light and catalysis are simultaneously used to promote or accelerate a chemical reaction. It can thus be defined as the "catalysis-driven acceleration of reaction rates in chemical processes via light." One of the main advantages of photocatalysis over thermally activated catalytic processes is the direct absorption of light by the system, which enhances efficiency and selectivity. Heterogeneous photocatalysis is a process based on the direct or indirect absorption of VIS or UV radiant energy by a solid [79]. The overall reaction involves catalysis between an oxidant and a reductant, for example, between O_2 and organic matter. Various materials are known to act effectively as photocatalysts, including TiO_2, ZnO, CdS, iron oxides, WO_3, and ZnS, among others. These materials are readily available, and most can be excited by light with wavelengths in the solar spectrum ($\lambda > 310$ nm).

To date, the most extensively studied photocatalysts are metal oxides, particularly titanium dioxide. In its anatase form, TiO_2 exhibits the most favorable properties, such as high stability and strong photocatalytic activity. It can be employed over a wide pH range and can undergo electronic transitions upon absorption of light in the UVA region. Therefore, TiO_2 demonstrates excellent performance at low cost, making it one of the most attractive materials for photocatalytic applications [80]. The main disadvantage of the catalyst, which is generally available as nanoparticles, is the need to separate it from the solution at the end of the process.

Heterogeneous photocatalysis using TiO_2 can also be combined with other advanced oxidation technologies. For instance, the addition of Fe(III) and H_2O_2 integrates the Sunlight/TiO_2 system with the Photo-Fenton process, thereby enhancing the removal efficiency of certain recalcitrant pollutants. As an example, oligocarboxylic acids are mineralized more rapidly in the presence of Fe (III)/H_2O_2 than when TiO_2 alone is used [78-79].

1.7.2 Electrochemical Advanced Oxidation Processes (EAOPs)

EAOPs represent a valid alternative to traditional AOPs as they are characterized by simplicity, low cost, safety, and environmental compatibility. In EAOPs, the electric current is the main reagent, and no harmful chemicals are required to produce strong oxidants [83]. EAOPs are mainly divided into two categories:

Electro-Fenton (EF): this process is based on the formation of •OH radicals, strong oxidants, resulting from the reaction between H_2O_2, generated at the cathode, and Fe^{2+} (2). The obtained •OH radicals oxidize organic contaminants (3):

$$O_2+2H^++2e^-\rightarrow H_2O_2 \text{ (1)}$$

$$Fe^{2+}+H_2O_2\rightarrow Fe^{3+}+\bullet OH+OH^- \text{(2)}$$

$$RH+\bullet OH \rightarrow H_2O+\cdot R \cdots H_2O+CO_2 \text{ (3)}$$

$$Fe^{3+}+e^-\rightarrow Fe^{2+} \text{ (4)}$$

This technique is a variant of the Fenton process, which instead requires the addition of H_2O_2. EF is therefore more advantageous than the Fenton process because H_2O_2 is produced *in situ* (1), avoiding the potential risks associated with the transport and storage of this substance. Moreover, in EF, Fe^{2+} is regenerated at the cathode (4), thereby significantly reducing iron sludge production. Voltage and pH are two important factors that influence the evolution of iron ions and the production of H_2O_2. For the degradation to proceed, an acidic environment (pH = 4) is essential for H_2O_2 formation. The higher the pH, the lower the H^+ concentration in solution, leading to less H_2O_2 formation and, consequently, a gradual decrease in degradation efficiency.

Anodic oxidation (AO): This process consists of the oxidation of contaminants near the anode. Compared to EF, AO does not require the addition of iron, making the technique simpler to execute. AO is further subdivided into direct oxidation and indirect oxidation (**Figure 1.14**):

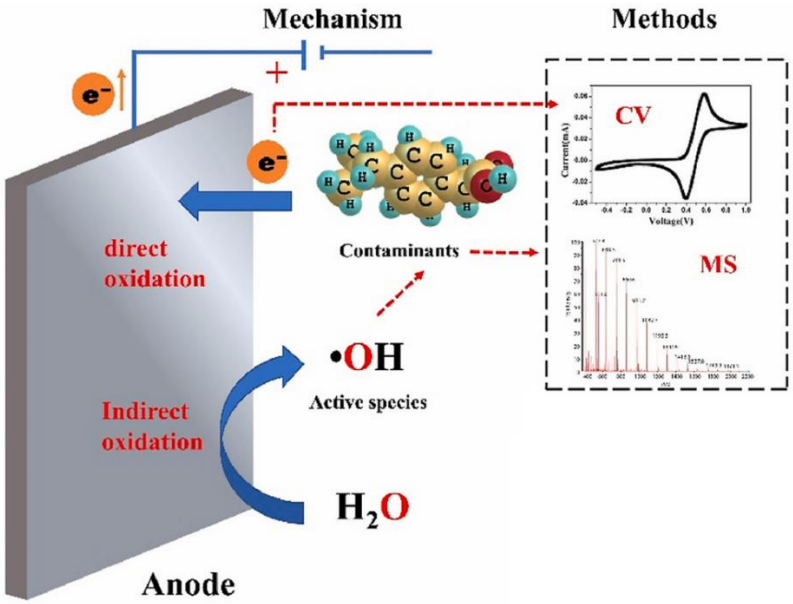

Figure 1.14 *Classification of AO processes* [83].

Direct oxidation involves the direct oxidation of organic matter at the anode without the involvement of radical species. The following processes occur:

$$M + Organic \rightarrow M(Organic_{ads}) \quad (5)$$

$$M(Organica_{ds}) \rightarrow M(Products_{ads}) + e^{-} \quad (6)$$

$$Products_{ads} \rightarrow M + Products \quad (7)$$

The contaminant (*Organic*) approaches the anode surface (*M*) and is adsorbed (*ads*) onto the electrode (5). Electron transfer then occurs, resulting in the oxidation of the pharmaceutical (6), and finally, the oxidation products desorb from the electrode (7) [84]. The nature of the contaminants produced can be determined using various detection techniques, particularly mass spectrometry or voltammetric methods.

Indirect oxidation, on the other hand, uses radical species to oxidize organic contaminants and can be divided into type I and type II. In type I indirect oxidation (**Figure 1.15**), the generation of •OH radicals occurs via the oxidation of water:

$$H_2O \rightarrow \bullet OH + H^{+} + e^{-} \quad (8)$$

The •OH radicals generated on the anode surface (M) are denoted as M(•OH). These radicals are highly reactive and can attack organic compounds, leading to rapid degradation into harmless final products.

$$M(\cdot OH) + R \rightarrow M + \text{oxidation intermediates} \quad (9)$$

$$\text{Intermediates} + M(\cdot OH) \rightarrow M + CO_2 + H_2O + \text{inorganic ions} \quad (10)$$

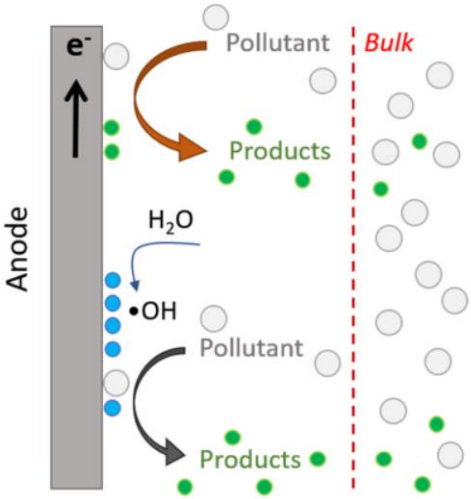

Figure 1.15 *Contaminant degradation mediated by OH radicals* [84].

Type II indirect oxidation is based on the degradation of pollutants by radical species other than OH•, derived from compounds specifically added to the solution. The most used oxidizing agents are the Cl· radical, derived from Cl^-, and sulfate radicals ($SO_4^{\bullet -}$) and persulfate ($S_2O_8^{2-}$), which can be electro-generated according to the following mechanism:

$$HSO_4^- + {\bullet}OH \rightarrow {\cdot}SO_4^- + H_2O \quad (11)$$

$$H_2SO_4 + {\bullet}OH \rightarrow SO4{\cdot}^- + H_2O + H^+ \quad (12)$$

$$SO{\cdot}_4^- + SO{\cdot}_4^- \rightarrow S_2O_8^{2-} \quad (13)$$

Several factors can influence the nature and quantity of reactive species formed during the AO process, including the type of contaminant, the electrode material, the electrolyte type, and the externally applied current or voltage [85].

1.8 Adsorption: Fundamental Principles and Mechanisms

Physical treatment methods for water's remediation mainly include adsorption and membrane-based filtration [83-84]. In this study, adsorption processes for the removal of ECs from aqueous matrices were investigated. Over the past few decades, adsorption has emerged as an efficient and versatile technique, characterized by low initial investment and the absence of harmful by-products in treated water, enabling the effective removal of pharmaceuticals even at trace concentrations [85-86].

Adsorption is a surface phenomenon of molecular attraction that occurs when two phases come into contact: a solid phase (the adsorbent) and a liquid or gaseous phase (the solvent), which contains adsorbate molecules. The adsorption process in a solvent–adsorbate–adsorbent system takes place as a result of two factors:

• low affinity between adsorbate and solvent;

• high affinity between adsorbate and adsorbent.

The degree of hydrophilicity of a substance dissolved in the liquid is certainly the most significant parameter in determining the level of affinity between solute and solvent. It is clear that the greater the affinity a substance has for the solvent — in the case of an aqueous solution, this is called hydrophilic — the lower its adsorption at the solid interface will be. Conversely, a hydrophobic substance will be more readily adsorbed.

With reference to the second factor, relating to the affinity between the adsorbate and the adsorbent, three different types of attractive forces must be considered:

• electrostatic forces;

• Van der Waals forces;

• forces of a chemical nature.

In the first case, the process is referred to as ion exchange. Adsorption occurs, in fact, as a result of electrostatic forces that allow the bonding between the ions of the adsorbate and the charges present on the surface of the adsorbent. Adsorption that occurs due to Van der Waals forces is generally called physisorption (**Figure 1.16**) [90]. It takes place at low temperatures (with values essentially close to ambient conditions) and is not 'site-specific': the adsorbate molecules do not bind to a specific site but are instead free to undergo translational movements on the interface. Van der Waals forces are weak intermolecular forces, and for this reason, the process is considered reversible. If the adsorbate undergoes chemical interactions with the adsorbent, then the process is referred to as chemisorption (**Figure 1.16**) [90]. Molecules that are 'chemically adsorbed,' unlike in the previous case, are not free to move on the surface because the adsorbate forms very strong, localized bonds with the adsorbent sites. The chemical interaction between the adsorbent and the adsorbate is irreversible and favored by high temperatures: chemical reactions, in fact, proceed faster at high temperatures than at low ones.

Anyway, most adsorption phenomena result from interactions among the three mechanisms. It is therefore not easy to distinguish between physical and chemical adsorption.

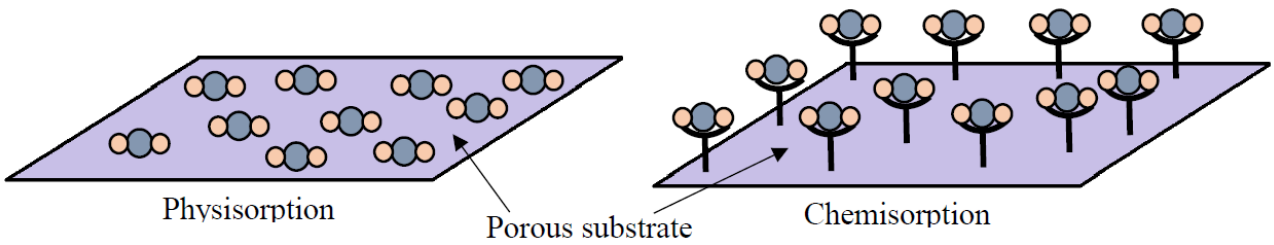

Figure 1.16 *Schematic of the interactions between adsorbate and the adsorbent surface (porous substrate) during physisorption and chemisorption* [90].

For an effective adsorption process in a liquid–solid system, the solute (or solutes) must be removed from the solution and subsequently immobilized on the adsorbent surface. The system reaches equilibrium when the solute concentration in the liquid phase is in dynamic balance with that on the solid surface. At this point, the adsorption rate equals the desorption rate, thereby defining the system's thermodynamic equilibrium. Reaching this condition indicates that the adsorptive capacity of the material has been exhausted.

Determining the equilibrium is essential for evaluating a material's adsorption capacity toward a specific contaminant. This theoretical capacity is typically described by adsorption isotherms, which relate, at constant temperature, the amount of solute adsorbed per unit mass of adsorbent to the equilibrium solute concentration remaining in solution. In general, the amount of solute adsorbed per unit mass of adsorbent increases with increasing the equilibrium concentration of the solute remaining in solution, although not in a directly proportional manner. Before proceeding with the construction of adsorption isotherms, it is necessary to investigate how the concentration of the adsorbate varies over time until the equilibrium condition, as a function of both the initial concentration of the species of interest and the amount of adsorbent used. Once the adsorption kinetics of a given compound are known, the equilibrium concentration of the adsorbate remaining in solution can be determined, and then the corresponding equilibrium adsorption capacity can be calculated. After evaluating these two parameters, it becomes possible to construct the adsorption isotherm. Different types of adsorption isotherms exist, distinguished by whether a single monolayer of adsorbed molecules forms on the adsorbent surface or multiple layers are generated. The most widely used models for studying adsorption isotherms are the Langmuir and the Freundlich models.

The Langmuir model assumes monolayer adsorption onto a homogeneous surface with a finite number of identical sites [91], whereas the Freundlich model is an empirical equation that accounts for multilayer adsorption on heterogeneous surfaces [92].

The Langmuir equation is based on four key assumptions. It is assumed that:

1. Adsorption occurs at specific sites on the adsorbent surface.
2. Each site can bind only a single adsorbate molecule.
3. The adsorption energy (i.e., the strength of the bond formed between the surface and the adsorbate species) is the same for all sites.
4. No interactions occur between adjacent adsorbed molecules.

Since the number of specific sites per unit mass of adsorbent is fixed, adsorption continues until all these sites are fully occupied. This generally corresponds to the assumption of a single monolayer of adsorbed molecules on the surface. A representation of the Langmuir isotherm behavior is shown in **Figure 1.17**.

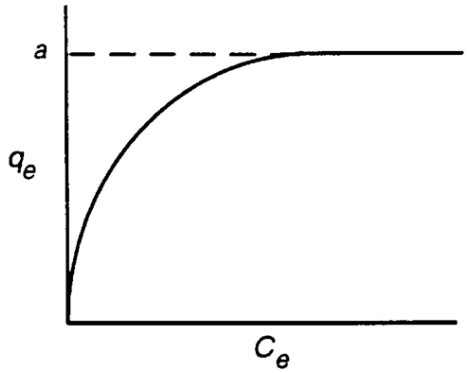

Figure 1.17 *Langmuir isotherm (In this figure,* a *indicates the Langmuir maximum adsorption capacity, q_m)* [91].

The Freundlich isotherm assumes a heterogeneous surface with sites where the heat of adsorption decreases exponentially with the degree of coverage. **Figure 1.18** shows the behavior of the Freundlich isotherm.

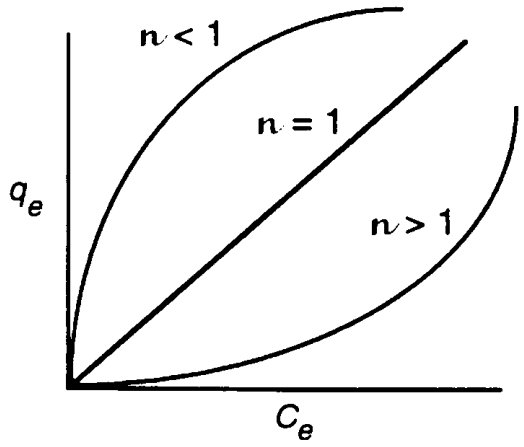

Figure 1.18 *Freundlich isotherm* [92].

Once the characteristic parameters of the Freundlich and Langmuir isotherms have been determined, the equilibrium model that best describes the adsorption process is evaluated.

1.8.1 Adsorption onto natural and functionalized materials

The most important properties that an adsorbent should possess to achieve high adsorption efficiency are a porous structure that provides a high surface area and a large concentration of adsorption sites and/or functional groups capable of optimal interactions with pollutants. In this context, numerous types of adsorbents are available, including clays modified with organic surfactants [1, 90-91] and carbon-based materials, particularly activated carbons (ACs) derived from industrial or agricultural waste [92-95].

In the recent years, functionalized clay-based materials as montmorillonite (MMT) were developed, tested and employed for the effective removal of various organic pollutants [96-97] MMT is a natural 2:1 layered clay [$(Na, Ca)_{0.3}(Al, Mg)_2Si_4O_{10}(OH)_2 \cdot nH_2O$] characterized by a high cation exchange capacity and a strong affinity for polar molecules [101]. However, its hydrophilic nature results in minimal interactions with nonpolar or weakly polar contaminants, thereby reducing adsorption efficiency. The hydrophilic surface of MMT can be made more hydrophobic by intercalating cationic surfactants, such as DDAB, thereby forming vesicle–clay complexes that serve as powerful sorbing materials for water purification from organic contaminants [1].

On the other hand, adsorption onto ACs represents one of the most promising strategies, thanks to their high surface area, well-developed porosity, and versatile surface chemistry [102]. To address sustainability concerns and reduce the environmental footprint of AC production, attention has shifted toward the valorization of agro-industrial residues as AC precursors. Agro-industrial by-products, particularly lignocellulosic wastes, represent a sustainable and valuable source for the production of ACs. Utilizing such environmentally friendly precursors not only helps mitigate solid waste management challenges but also lowers the cost of feedstock for AC production. Spent brewery grains (SBG), a by-product of the brewing industry, consist of the residual barley malt after the mashing process and represent approximately 85% of total brewery by-products. SBG is mainly composed of polysaccharides (hemicellulose and cellulose), along with lignin, proteins, and lipids [100-101]. Its high lignocellulosic fiber content makes it an attractive precursor for AC production [105]. AC can be obtained by physical or chemical activation of various waste materials, combined with thermal decomposition (carbonization) [106]. Traditionally, the carbonization step involves conventional pyrolysis (CP), which requires prolonged operation times and high temperatures, making it highly energy-intensive and costly [107]. Microwave-assisted pyrolysis (MP) offers a promising alternative, providing rapid and uniform heating that reduces production time and energy consumption [105-106].

1.9 Ecotoxicity assessment of transformation products

The degradation of pharmaceuticals can lead to the formation of transformation products that may be more or less toxic than the parent compound. It is therefore important to assess the ecotoxicity of these degradation products using specific techniques, including in vivo, in vitro, and *in silico* methods.

In vivo tests are performed on living animals, whereas *in vitro* tests use a cell line. Consequently, a series of acute and chronic toxicity bioassays has been developed to establish

the toxicity levels of compounds for aquatic organisms, including microorganisms, plants, invertebrates, and fish. The biological response to a chemical varies across different living organisms and depends on their sensitivity to toxic products. Therefore, for the assessment and monitoring of water quality, a range of methodologies can be applied using a variety of bioindicators. Toxicity bioassays can be classified according to the species under study, including bacterial bioassays such as the *Vibrio fischeri* test and invertebrate bioassays such as the *Daphnia magna* test [110].

In this study, *Vibrio fischeri* tests have been conducted to evaluate the toxicity of SILD and its photoproducts. This test is based on the inhibition of bioluminescence of the luminescent bacterium *Vibrio fischeri* [111]. *V. fischeri* naturally emits light thanks to an enzyme, bacterial luciferase, which catalyzes the following reaction:

$$FMNH_2 + O_2 + R\text{-}CO\text{-}H \rightarrow FMN + R\text{-}COOH + H_2O + light$$

The light emission is directly proportional to the microorganism's metabolic activity; therefore, any inhibition of this activity results in a decrease in bioluminescence, expressed as a percentage (*I%*). Toxicity is expressed as *the EC50,* the effective concentration of a toxic substance that causes a 50% reduction in light. This test has the advantage of being sensitive and reproducible, but it also has a limitation: *V. fischeri* is a marine bacterium, so the test works only in saline solution. Additionally, the solution must be filtered before testing, as salinity can affect the solubility of some organic substances, leading to turbid solutions [112]. Several commercial devices based on the same principle are available, such as Microtox from Azur Environmental [113].

In vivo and *in vitro* approaches are not widely used to evaluate the ecotoxicity of pharmaceutical degradation products because these products are often not available as commercial standards and cannot be directly tested. In contrast, *in silico* analysis has gained prominence in the scientific field in recent years. It involves applying computational algorithms to predict the properties of substances, such as toxicity, based on their structures and experimental data from similar compounds. Among the well-established models for predicting ecotoxicity using this type of analysis is the ECOSAR (Ecological Structure-Activity Relationship) software (V 2.2) [114]. ECOSAR can estimate the short- and long-term toxicity of transformation products by calculating the LC50 (median lethal concentration), the concentration (mg L^{-1}) that causes the death of 50% of individuals in toxicity assays. In this thesis, the toxicity assessment of VFX and its degradation products was carried out using the ECOSAR software. In the program, the structures of VFX and its main degradation products were drawn, and LC50 values were obtained for each relative to the species *Daphnia magna*.

1.10 General aim of the Ph.D. project

This Ph.D. thesis evaluates and compares advanced chemical and physical remediation strategies for removing pharmaceuticals from aquatic environments. The assessment is based on original experimental data generated throughout the doctoral research, comprising peer-reviewed publications and manuscripts currently in preparation. The overarching objective is to identify treatment approaches that maximize removal efficiency while ensuring environmental sustainability, cost-effectiveness, scalability, and minimizing toxic by-products.

Heterocyclic pharmaceuticals have recently attracted significant attention as ECs due to their toxicity, persistence, and potential ecological risks. These compounds, widely used in medical therapy, are characterized by stable heterocyclic structures containing heteroatoms such as nitrogen, oxygen, and sulfur. While their structural stability enhances pharmacological activity, it also leads to low biodegradability and high environmental persistence, resulting in accumulation across various environmental compartments. Continuous release into aquatic environments through wastewater discharges, industrial effluents, and improper disposal contributes to their pseudo-persistent nature. Chronic exposure to these compounds has been associated with neurotoxic, genotoxic, endocrine, and reproductive effects, raising concerns for both aquatic organisms and human health. In response to these issues, this Ph.D. research first focused on the identification and environmental assessment of selected heterocyclic pharmaceuticals as model ECs (CONTRIBUTION 1, Chapter 3). This investigation aims to improve understanding of their environmental occurrence, physicochemical behavior, and potential risks, providing a scientific foundation for the development of effective remediation and monitoring strategies. In particular, the objectives of this comprehensive review were:

- to assess the chemical persistence and the environmental entry pathways;
- to evaluate multi-systemic ecotoxicity and long-term health risks;
- to analyze and optimize remediation and mitigation frameworks.

One of the most widely recognized pyrazole derivatives is SILD. Commonly prescribed for ED, SILD has recently garnered significant scientific interest due to its extensive legal and illicit use worldwide. Its chemical stability and persistence in environmental conditions, combined with its potential for accumulation and phototransformation in the aquatic environment, raise substantial ecological and human health concerns. Consequently, innovative and sustainable methods are needed to ensure its complete removal from water matrices while minimizing the formation of toxic transformation products. The study reported in CONTRIBUTION 2 (Chapter 4) accordingly focused on three main objectives:

- to evaluate the efficiency of AOPs for the degradation of SILD (in particular, different AOP systems were compared, including Sunlight/TiO_2, Sunlight/H_2O_2,

Sunlight/PS, and Sunlight/PMS) in both distilled water (DW) and synthetic wastewater (SWW);

- to identify degradation pathways and intermediate by-products using LC-HRMS and LC-MS^n;
- to assess the ecotoxicological safety of treated effluents through bioassays.

By integrating these approaches, the work aims to ensure not only pollutant removal but also the environmental safety of treated waters.

Pharmaceuticals, particularly antidepressants, are a primary concern due to their environmental persistence and neurobehavioral impacts on aquatic life. VFX, a serotonin and norepinephrine reuptake inhibitor, has been officially recognized as a priority pollutant under the Commission Implementing Decision (EU) 2022/1307, which incorporated it into the 3rd EU Watch List, due to its widespread use, persistence in aquatic environments, and potential ecotoxicological effects. CONTRIBUTION 3 (Chapter 5) investigated the electrochemical degradation of VFX based on galvanostatic oxidation with a Pt anode. The aim of this study was:

- to compare Pt and glassy carbon (GC) anodes for the electrochemical degradation of VFX and to investigate the role of indirect oxidation mechanisms mediated by hydroxyl and sulfate radicals in improving the overall degradation efficiency;
- to identify optimal operational conditions, particularly in terms of current density and pH, and to investigate the degradation kinetics of VFX, to promote its transformation into lower-molecular-weight products through electrochemical treatment;
- to identify and evaluate the ecotoxicity of the transformation products generated during the electrochemical degradation process and to reconstruct the possible degradation pathways**.**

Despite their effectiveness, these chemical approaches may, in some cases, require substantial energy and reagent consumption and can generate transformation products that are more toxic than the parent compound. To address this issue, sustainable water treatment strategies are required. In this context, adsorption has emerged as a promising, environmentally friendly alternative, enabling the removal of recalcitrant pharmaceuticals without generating toxic transformation products. ACs and MMT-based clays are widely recognized as highly effective adsorbent materials due to their large specific surface areas, well-developed porosity, surface functional groups, and cation-exchange capacity, which enable strong interactions with a wide range of organic pollutants. Within this context, CONTRIBUTION 4 (Chapter 6) and CONTRIBUTION 5 (Chapter 7) focused on the development and evaluation of sustainable and

efficient adsorbent materials derived from waste resources and modified clay minerals. In particular, these studies aimed to:

- promote the sustainable valorization of agro-industrial waste, specifically SBG, as a precursor for the production of activated carbons;
- investigate and compare different pyrolysis approaches (conventional and microwave-assisted pyrolysis) in order to identify the most suitable technique for producing high-performance ACs from SBG;
- evaluate MMT and DDAB-MMT as potential alternative or complementary adsorbent materials, assessing their capability to enhance pollutant removal through surface modification and improved adsorption properties;
- perform a comprehensive physicochemical characterization of the prepared adsorbent materials to understand better their structural, morphological, and surface properties and their relationship with adsorption performance;
- assess the removal efficiency of VFX, SILD, and TAD from both ultrapure water and real wastewater matrices to evaluate the practical applicability of these materials in water treatment scenarios.

Chapter 2 provides a detailed description of the methodologies used in this study, while Chapters 3–7 present and discuss the results, and Chapter 8 outlines the conclusions.

2. METHODOLOGIES

The current chapter presents the methodologies applied in this research for the detection of SILD, TAD, and VFX and their transformation products, as well as the characterization of the adsorbent materials employed. The concentration of target pharmaceuticals was monitored using high-performance liquid chromatography coupled with photodiode-array detection (HPLC-DAD) or fluorescence detection (HPLC-FLD).

Because retention time and UV spectra alone are insufficient for the correct identification of unknown compounds, a study of the transformation products of SILD and VFX was performed using liquid chromatography coupled to linear ion trap mass spectrometry with electrospray ionization (LC–ESI–LIT–MS) and liquid chromatography coupled to Orbitrap mass spectrometry with electrospray ionization (LC–ESI–Orbitrap–MS), allowing identification of individual compounds by considering both retention time and mass values. Low-resolution multiple mass spectrometry experiments were conducted to elucidate the fragmentation pathways of transformation products and to obtain further information on their chemical structures. These MS^n experiments were performed via collision-induced dissociation (CID). The application of fragmentation studies and tandem mass spectrometry (MS^n or MS/MS) provided essential support for the comprehensive analytical characterization of unknown compounds.

In addition to these chromatographic and mass spectrometric techniques, the electrochemical behavior and degradation of VFX were investigated using an EAOP. A series of electrode materials, including GC modified with graphene oxide, graphite, graphite felt, and platinum, was tested. Cyclic voltammetry (CV) was first employed to study the electrochemical behavior of VFX at each electrode, providing insights into the degradation mechanism and distinguishing between direct electrode-surface oxidation and indirect oxidation mediated by radical species generated in solution during electrolysis. Subsequently, differential pulse voltammetry (DPV) was used to evaluate the electrochemical stability and degradation efficiency of VFX under the EAOP conditions.

To ensure a thorough understanding of the adsorbents' properties, the ACs were characterized through surface area measurements (S_{BET}), Scanning Electron Microscopy (SEM), and point of zero charge (PZC) determination, while natural and modified montmorillonites were analyzed using X-ray Photoelectron Spectroscopy (XPS) to investigate their surface composition and functionalization. This methodological framework enables a comprehensive evaluation of both the removal efficiency and the performance of the adsorbent materials under the applied treatment conditions.

2.1 Chromatography

Chromatography is an analytical technique suitable for separating components of a mixture that are differentially distributed between two immiscible stationary and mobile phases. The stationary phase is fixed either in a column or on a planar surface; it can be solid or liquid and may be adsorbed onto an inert support. The mobile phase, on the other hand, moves along or through the stationary phase carrying the analyte with it; it can be a gas (gas chromatography), a liquid (liquid chromatography), or a supercritical fluid (supercritical chromatography). The components of the mixture have different affinities for the two phases, establishing a dynamic equilibrium in which substances continuously move from the mobile phase to the stationary phase and vice versa. Components that are more similar to the stationary phase will be retained more in the chromatographic column and will therefore have higher retention times than components that are more similar to the mobile phase and have shorter retention times. The different interactions between the stationary and mobile phases result in the separation of the sample components into discrete bands, which can be analyzed qualitatively and/or quantitatively by placing a detector at the column outlet to measure the solute concentration in the eluate. The graph produced by the detector is called a chromatogram, in which a more or less intense peak is observed depending on the concentration of the eluted component. The parameters used to determine separation efficiency are the partition coefficient, retention time, capacity factor, selectivity factor, chromatographic efficiency, and resolution [115].

- *Partition coefficient*

  The partition coefficient *K'* is the equilibrium constant for the following reaction:

$$A_{mobile} \leftrightarrow A_{stationary}$$

The equation gives the equilibrium constant of this reaction and thus the partition coefficient:

$$K' = \frac{Cs}{Cm} \tag{2.1}$$

where *Cs* is the molar concentration of the analyte in the stationary phase and *Cm* is the concentration of the analyte in the mobile phase.

- *Retention time and dead time*

Retention time (t_r) is the time between the injection of a sample and the appearance of the solute peak at the detector of a chromatographic column, so it is a measure of the time spent by the solute in the stationary phase. Dead time, on the other hand, is the time taken by an unretained

species to pass through the column and is therefore an estimate of the average velocity of the mobile phase.

- *Capacity factor*

The capacity factor *k'* is a parameter that defines the rate of migration of the analyte along the chromatographic column. It is defined as the ratio between the time spent by the solute in the stationary phase (t_s) and the time spent in the mobile phase (t_m):

$$k' = \frac{t_r - t_m}{t_m} = \frac{t_s}{t_m} \tag{2.2}$$

A capacity factor less than unity indicates that the solute leaves the column at a time comparable to the dead time; this indicates that the components of the mixture have not been separated. A capacity factor value above 20-30 indicates that elution times are too long, resulting in a very broad chromatographic peak. Under ideal conditions, the capacity factor should be between 1 and 5. In gas chromatography, capacity factors are optimized by varying temperature and column packing; in liquid chromatography, they are improved by varying the composition of the mobile and stationary phases, i.e., by performing gradient elution.

- *Selectivity factor*

The selectivity factor *α* is a measure of the column's ability to separate two analytes A and B, with the first being the species most retained by the chromatographic column and the second being the least retained; it is defined as the ratio of the partition coefficients k' between the two analytes:

$$\alpha = \frac{k'_A}{k'_B} \tag{2.3}$$

According to this definition, α is always greater than unity. A column with higher selectivity ensures greater separation in retention times of the two solutes: by selecting the stationary phase so that it interacts preferentially with one of the two solutes, its retention time can be increased, and it can be better separated from the other.

- *Efficiency*

The efficiency of a chromatographic column is related to peak width and depends essentially on factors such as flow rate, packing, and diffusion, which affect the theoretical equivalent plate height (HEPT, *H*) and the number of theoretical plates (*N*):

$$N = \frac{L}{H} \tag{2.4}$$

where *L* is the length (usually in centimeters) of the column packing, *H* is the height of the theoretical plate, and *N* is the number of theoretical plates. In particular, the efficiency of the column increases as the number of theoretical plates increases and the height of the theoretical plate decreases. Experimentally, by measuring the retention time of a peak, *tr*, and the amplitude of the peak at half height, *W* (expressed in units of time) on a chromatogram, *N* can be estimated from the simple relationship:

$$N = 5.4\left(\frac{t_r}{W}\right)^2 \tag{2.5}$$

In a column, at high flow rates and where flow effects prevail over diffusion, the efficiency can be approximated by the following relationship:

$$H = A + \frac{B}{u} + C_S u \tag{2.6}$$

where *H* is the height of the theoretical plate expressed in centimeters; *u* is the linear velocity of the mobile phase expressed in cubic centimeters; *A* is a coefficient describing the effects of multiple paths; *B* is the longitudinal diffusion coefficient; and *Cs* is a coefficient describing the mass transfer contribution. This equation is the well-known van Deemter equation, often used to describe the efficiency of a chromatographic column [115].

- *Resolution*

The resolution *R* of a chromatographic column is a quantitative measure of its ability to separate two analytes A and B. It is defined as:

$$R = 2\frac{t_{rB} - t_{rA}}{W_B + W_A} \tag{2.7}$$

where W_A and W_B are the peak widths at the base. A zero value of *R* provides coincident peaks, while values of 1.5 provide complete separations with overlapping peaks of only 0.3%. Achieving 1.5 resolution requires increasing efficiency and/or selectivity, but as these parameters are incompatible with retention times, a compromise is sought to achieve the highest resolution in the shortest total analysis time. In **Figure 2.1,** two chromatographic peaks are shown, with indications of the parameters described, such as dead time, retention times, and base widths.

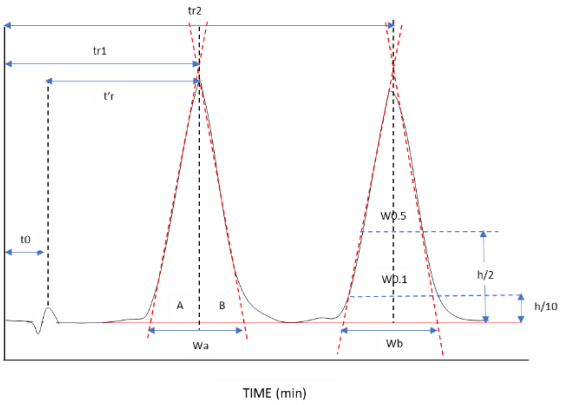

Figure 2.1 *Graphic scheme of the dead time (t0), the corrected retention time (t'r), the width at the base, at 10 and 50% of the height of a chromatographic peak (w, w0.1 and w0.5). A and B are the half-widths at the base of the peak.*

2.1.1 High Performance Liquid Chromatography (HPLC)

The most versatile and widely used type of liquid chromatography (LC) is high-performance liquid chromatography (HPLC, or simply LC). LC techniques are divided into partition chromatography (liquid-liquid), adsorption chromatography (solid-liquid), ion-exchange chromatography (liquid-resin-exchange), and size-exclusion chromatography (porous liquid-solid), depending on the type of stationary phase and separation mechanism [115]. In liquid chromatography, elution is performed by forcing the mobile phase to pass through the packing material by gravity, with uncontrolled particle size. Columns for HPLC are filled with microparticles ranging in size from 2.7 to 10 μm: a stationary phase with such a fine particle size ensures a large contact surface area between the mobile and stationary phase, but in this case, since the flow of the mobile phase is too low, or even zero, high pressure is required to allow the mobile phase to move. This is achieved with the aid of pumps capable of generating pressures up to 6000 psi (1psi = 0.069 bar), allowing flows ranging from 0.1 to 10 ml min^{-1}. There is often a guard column (pre-column) at the head of the analytical column, which is useful for increasing the 'life' of the analytical column by preliminary removal of particulate impurities contained in the solvents. In addition, in partition chromatography, the guard column serves to saturate the mobile phase with the stationary phase, thereby minimizing the risk of stationary-phase loss from the analytical column. The packing composition of the guard column is generally similar to that of the analytical column, while the particle size is larger to reduce pressure drop. Other important components of the chromatographic system are the sample introduction system, the injection valve, which ensures high reproducibility of injected volumes, and, finally, the degassing device (vacuum pump, distillation system, or bubbling system), which removes dissolved gases, avoiding bubble production, band broadening in the column, and detection problems.

2.1.2 Reverse Phase LC

The most commonly used LC technique is partition chromatography, in which the stationary phase is a second liquid immiscible with the mobile phase. It includes liquid-liquid chromatography and bound-phase chromatography [115]. The difference between the two techniques lies in the way the stationary phase is attached to the solid inert support: in liquid-liquid chromatography, the liquid is held by physical adsorption, whereas in bonded-phase chromatography, it is held by chemical bonds. Bounded-phase packings offer greater stability than adsorbed phases: there is no need to periodically reset the stationary phase, as the liquid is held tightly and cannot be dissolved by the mobile phase ('bleeding'). The bonded-phase packing is prepared, as shown in **Figure 2.2**, by the reaction of an organochlorosilane with the silanolic groups (Si-OH) of the solid support, resulting from the hydrolysis of the siloxane groups (Si-O-Si) of the silica.

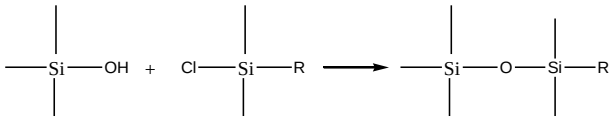

Figure 2.2 *Silanization reaction of the silanolic groups.*

In addition, partition chromatography can be distinguished by the relative polarities of the mobile and stationary phases: in normal-phase chromatography, the stationary phase is polar and the mobile phase non-polar; in reversed-phase chromatography, the polarity of these phases is reversed. For such a separation to be successful, it is necessary to choose a stationary phase of comparable polarity to that of the analyte and a mobile phase that is considerably different.

2.2 HPLC detectors

2.2.1 Photodiode-array detection (DAD)

In chemical analysis, there is often a need to measure the intensity of many points in an optical image. So, in recent years, array detectors based on semiconductor principles have been developed, enabling measurements to be made simultaneously at many points along a line or, in some cases, over a whole area comprising many thousands of image points. All these devices are based on integrated circuit technology and fall into three main categories: photodiode arrays, charge-coupled devices, and charge-injection devices [116].

A DAD is a widely employed chromatographic tool in LC. Its primary function is to simultaneously detect and quantify various sample compounds that absorb light within the UV-Vis range. The detector principle is shown in Figure 2.3, where it can be seen that the transmitted light from the sample continuously illuminates the array detector, enabling rapid

acquisition of spectral data. The innovative use of both UV and VIS source lamps allows simultaneous illumination of the sample across all wavelengths from 190 nm to 1100 nm.

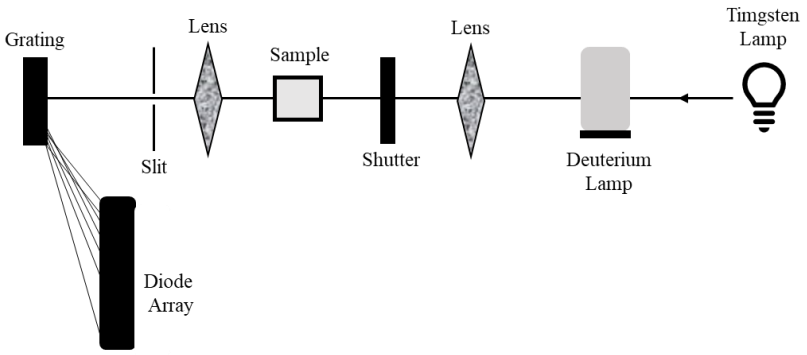

Figure 2.3 *A DAD principle.*

A photodiode array consists of an array of microscopic photodiodes, each equally charged; when exposed to a light image, the elements at the points of highest intensity discharge, losing most of their charge. The output signal is obtained by connecting each element in turn to the signal line and measuring the charge required to restore each element to its original charge potential. Parameters such as the scan time and repetition rate are set based on the number of elements [116].

2.2.2 Fluorescence detection (FLD)

A FLD is a device commonly used for techniques like high-performance liquid chromatography [116]. It operates on the principle of measuring the fluorescence emitted by certain compounds when they are excited by light (**Figure 2.4**).

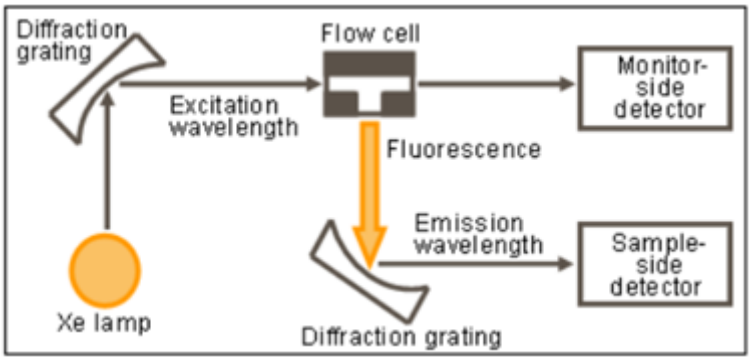

Figure 2.4 *Schematic drawing of FLD.*

The detector starts with an excitation light source, often a high-energy light source such as a xenon lamp. This light emits a light beam at a specific wavelength, known as the excitation wavelength. The chosen wavelength depends on the specific absorbance properties of the compounds of interest. The sample, which contains analytes with fluorescent properties, is

introduced into the detectors' flow cell. As the sample flows through the cell, it encounters the excitation light. Compounds in the sample that have inherent fluorescence, known as fluorophores, or those that have been labeled with fluorescent tags (derivatization), absorb the energy from the excitation light at the excitation wavelength. This absorption elevates the fluorophores' electrons to a higher energy state.

After absorbing energy, the excited electrons return to their lower energy state, releasing the excess energy as fluorescence. This emitted light occurs at a longer wavelength than the excitation light and is characteristic of the specific fluorophores present in the sample. A detector, typically equipped with a photomultiplier tube or a photodiode array, captures and measures the intensity of the emitted fluorescence. The detector is set to emission wavelength, allowing selective detection of the fluorescent signal. The detected fluorescence signal is converted into an electrical signal, processed, and recorded as a chromatogram. The chromatogram shows the intensity of fluorescence relative to compound concentration at different wavelengths as the sample components elute from the chromatographic column [116].

2.3 Mass spectrometry

Mass spectrometry is an analytical technique commonly used in combination with separative techniques such as gas chromatography, liquid chromatography, and capillary electrophoresis (CE), due to its high sensitivity and ability to identify a wide range of substances. A mass spectrometry experiment consists of ionizing the sample in the gas phase, separating the ions produced on the basis of their m/z ratios, detecting them, and recording the corresponding mass spectrum. The components of a mass spectrometer are:

- a sample introduction system that allows the sample to be transferred into the spectrometer;
- an ion source or ionization source, where ionization of the analyte and/or production of charged fragments takes place;
- an analyzer, which separates ions according to their *m/z* ratio;
- a detector, which converts the ion beam into an electrical signal;
- a vacuum system, which is required to prevent loss of ionization through collision and/or chemism with atmospheric gases;
- a data-acquisition and processing system that allows mass spectra to be recorded.

The mass spectrum is displayed as a set of vertical lines of different intensity, each corresponding to the *m/z* value of a single ion. The signal with the highest *m/z* value corresponds to the molecular ion. Typically, the ion current is normalized to 100; that is, the highest peak (base peak) has a value of 100, regardless of its absolute value. As already underlined at the

beginning of the paragraph, the combination of liquid chromatography with mass spectrometry represents an ideal fusion between separation and detection [115]. The intrinsic incompatibility between these two techniques, i.e., LC operates in the liquid phase at high pressures while mass spectrometry operates in the gaseous phase under vacuum, is overcome by using interfaces capable of reducing the eluent flow and vaporizing the solvent before entering the mass spectrometer. LC-MS interfaces can be divided into two categories:
- interfaces that evaporate and transfer the sample from the LC system to the mass spectrometer;
- interfaces that play an active role in the ionization itself.

Atmospheric-pressure ionization interfacing systems are the best approach for mass spectrometry interfaced with liquid chromatography; among these, electrospray ionization (ESI) is currently the preferred ionization method. Atmospheric-pressure ionization interfaces are the best combination for solving the problem of mass spectrometry coupled to liquid chromatography; among these, ESI is currently the preferred ionization modality.

2.3.1 Sample injection system

In the ESI ion source mass spectrometer, two modes of sample introduction are available: direct infusion with a syringe pump and coupling to an LC system. In the first case, the sample solution is introduced directly into the source via a capillary with a microsyringe (250-500 μL) (Direct Injection, DI). Alternatively, the solution contained in the microsyringe can be introduced into the mobile phase flow of the LC (Flow Injection Analysis, FIA). This introduction can take place discontinuously, filling the injection valve loop, or continuously via a T-junction, allowing only a small quantity of eluent to be sent into the mass spectrometer (200 μL min^{-1}).

2.3.2 Ionization source: electrospray ionization (ESI)

The mass analyzer of any mass spectrometer can only handle charged species, i.e., ions generated from atoms or molecules, and occasionally from radicals, zwitterions, or clusters. The ion source performs this crucial step, and a wide range of ionization methods is used to achieve this goal across the full range of analytes. The classical procedure of ionization involves shooting energetic electrons at a gaseous neutral, a process called electron ionization [117]. When a neutral is hit by an energetic electron carrying several tens of electronvolts (eV) of kinetic energy, some of the energy of the electron is transferred to the neutral. If the electron, in terms of energy transfer, collides very effectively with the neutral, the energy transferred can exceed the ionization energy (IE) of the neutral. Then, ionization by ejection of one electron can occur, generating a molecular ion, a positive radical ion [117]:

$$M + e^- \rightarrow M^{+\bullet} + 2e^-$$

A less effective interaction brings the neutral into an electronically excited state without ionizing it. As the energy of the primary electrons increases, the abundance and variety of the ionized species will also increase, i.e., electron ionization may occur via different channels, each of which gives rise to characteristic ionized and neutral products. This includes the production of the following types of ions: molecular ions, fragment ions, multiply charged ions, metastable ions, rearrangement ions, and ion pairs [118]. Ionization energies of most molecules are in the range of 7–15 eV. Removal of an electron from a molecule can formally be considered to occur at a σ-bond, a π-bond, or at a lone pair, with the σ-bond being the least favored and the lone pair being the most favored position for charge localization within the molecule. The more atoms there are in a molecule, the easier it is to find a way to stabilize the charge, e.g., by delocalization or hyperconjugation. Once the molecular ion is formed, the electron charge is never really localized in a single orbital, although this assumption is often a good working hypothesis for mass spectrum interpretation [114-115].

However, IE cannot ionize the most valuable and thermally unstable polar biological compounds. Subsequently, additional soft ionization methods were developed and replaced older techniques. These include fast atom bombardment (FAB), liquid secondary ion mass spectrometry (LSIMS), matrix-assisted laser desorption ionization (MALDI), and ESI [116-118]. Remarkably, the latter ionization techniques have revolutionized the usage of mass spectrometers and enabled researchers to easily study biological substances, such as glycoconjugates, proteins, and DNA [116-117, 119]. Development of ESI started with the study of Dole and co-workers, who successfully introduced a polystyrene polymer (average MW = 51,000 Da) into the gas phase as a charged species [123]. Surprisingly, this ionization technique is among the simplest to understand. Samples are usually dissolved in a buffer or solvent, which is then introduced into the mass spectrometer as a spray. In ESI-MS, the sample should be soluble in a preferably polar solvent, which can be infused, under atmospheric pressure, into the ionization source via a thin needle. As the sample is continuously sprayed, a high electrical potential is applied to the needle (3–4 kV), resulting in the formation of highly charged droplets (i.e., nebulization). These droplets are then driven electrically and are vaporized with the aid of a warm neutral gas (usually nitrogen). A schematic representation of the ESI source is shown in **Figure 2.5**:

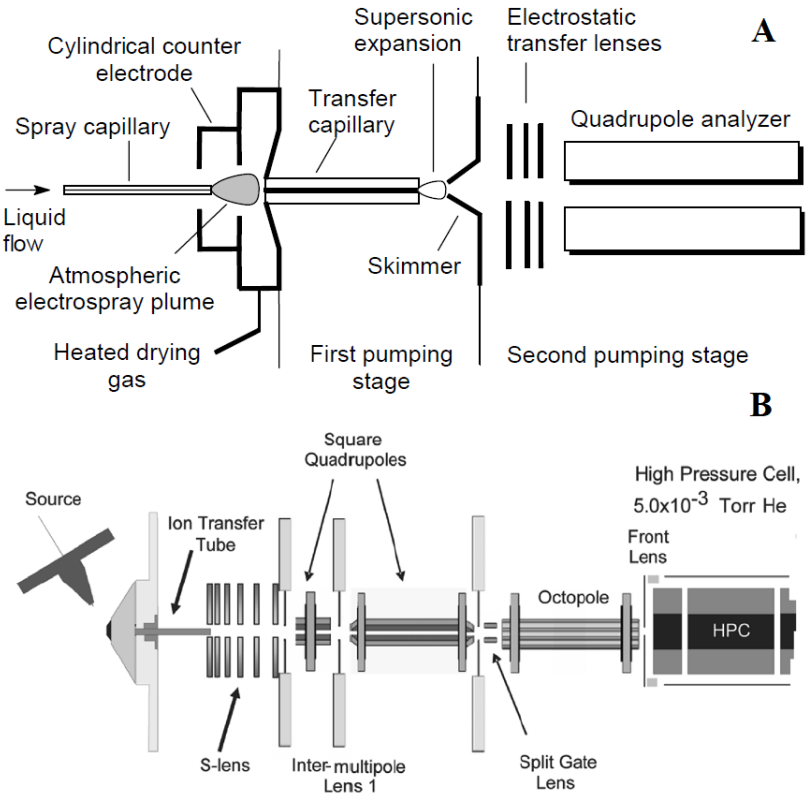

Figure 2.5 *Representation of an early ESI source (A). In more recent configurations (B), the spray capillary is set at a 45° angle to the transfer capillary, preventing the clogging of capillaries and skimmers caused by the deposition of non-volatile impurities, such as buffer salts* [124].

Under these conditions, the droplets break down and, as they shift within the source, their size is continuously reduced. Eventually, the repulsive forces, also called Coulombic forces, among the ions on the surface of the shrinking droplets become very high. These forces will ultimately exceed the solvent's surface tension, leading to ion desorption into the gas phase. This theory of ESI ion formation, termed the ion evaporation method [125], is believed to favor ions with relatively low *m/z* values. An alternative theory, which is supposed to be dominant in the case of ions with very high *m/z*, is the charge residue model [125], which involves continuous evaporation of the solvent accompanied by droplet fragmentation so that a single ion (probably multiply charged) is formed at the end of this process (i.e., solvent is completely evaporated). $[M+H]^+$ and $[M-H]^-$ are mainly produced during the process. However, other types of ions may form, such as clusters, multi-charged ions (resulting from the gain or loss of more than one proton), or metal adducts [116, 119].

2.3.3 Resolution and Mass Accuracy

The peak separation observed in a mass spectrum is called *mass resolution*, *R*, or simply *resolution*. Mass resolution is the smallest difference in *m/z* ($\Delta m/z$) that can be separated for a given signal, i.e., at a given *m/z* value:

$$R = \frac{m}{\Delta m} = \frac{m/z}{\Delta m/z} \tag{2.8}$$

This parameter is dimensionless [123-124]. The instrument's ability to resolve neighboring peaks is called mass resolving power, or simply *resolving power*. It is given by the peak width at a specific percentage of the peak height expressed as a function of mass (**Figure 2.6**). Two neighboring peaks are considered sufficiently separated when the valley between their maxima has decreased to 10% of their intensities [121, 123]. Hence, this is known as 10% valley definition of resolution, R10%. The 10% valley conditions are fulfilled if the peak width at 5% relative height equals the mass difference of the corresponding ions, because then the 5% contribution of each peak to the same point of the *m/z* axis adds up to 10%. With the advent of linear quadrupole analyzers, the full width at half maximum (FWHM) definition of resolution became widespread, especially among instrument manufacturers. In principle, resolution is always determined from the peak width of some signal at a certain relative height, and therefore, any peak can serve this purpose. Increasing resolution does not affect the relative intensities of the peaks, but higher resolving power settings are usually obtained at the cost of the analyzer's transmission, thereby reducing the absolute signal intensity [126].

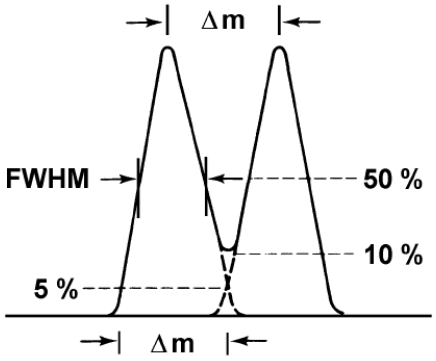

Figure 2.6 *The 10% valley and FWHM definitions of resolution* [124].

Resolution is closely related to another important aspect of mass spectra: mass measurement accuracy. In detail, the *absolute mass accuracy, Δm/z,* is defined as the difference between measured mass and *calculated exact mass*, i.e., the sum of monoisotopic masses of every atom of a chemical species [127]:

$$\Delta m/z = m/z_{Observed} - m/z_{Exact} \tag{2.9}$$

In general, mass accuracy is reported as relative accuracy, expressed as the absolute accuracy divided by the calculated exact mass. This quantity is thus expressed in parts-per-million (ppm). Accuracy describes the deviation of the experimental value from the true value; however, in

practice, one never deals with exact values but rather with reference values. Accuracy is high if the values from several measurements are close to the reference value.

Higher mass measurement accuracies enable the assignment of chemical formulas to observed ionic species [118]. With infinite accuracy, for example, one can assign a unique formula to each observed MS signal to obtain important chemical information about identified analytes, such as the presence of unsaturations and/or heteroatoms. In practice, it is highly probable to encounter errors in the order of several mg L-1, depending on the instrument used, thereby increasing the number of possible formula candidates per MS signal [118].

High-resolution, accurate mass measurements are closely related and depend on each other, because mass accuracy tends to improve as peak resolution improves. Nevertheless, they should not be confused, as measuring high resolution alone does not equally imply measuring the accurate mass [127].

2.3.4 Tandem mass spectrometry (MS^n or MS/MS)

To obtain information on the molecular structure of an unknown compound, the coupling of two mass analysis stages (tandem mass spectrometry, or MS/MS) is very useful. In a typical MS/MS experiment, structural data are obtained by isolating the ion of interest, exciting (and thus dissociating) it, and finally analyzing the ions generated by mass spectrometry.

A tandem mass spectrometer consists of two analyzers arranged in series. The first analyzer (Ms1) selects (filters) the desired ion from the various ions in a spectrum. The selected ion (precursor ion) is then collided with a suitable collision gas (He, Ar) in a collision cell, and the fragments (produced ions), generated by the dissociation of the precursor ion due to the collisions with the gas, are separated by the second analyzer according to their *m/z* ratio. For sector, quadrupole, and time-of-flight instruments, each stage of mass analysis requires a separate analyser (in this case, all three types of scanning are possible). In ion trap or ICR mass spectrometers, MS/MS experiments can be conducted sequentially over time within a single mass analyzer. With the latter, the selection of the ion, its induced dissociation, and the analysis of the fragments generated are performed in the same space, but at successive times. Specifically, in the ion trap it is possible to trap all the ions present in the primary spectrum initially, then isolate the desired ion (ejecting the others from the trap), then induce dissociation of the isolated ion by collision with atoms or molecules (helium, neon, argon and nitrogen have been used as collision gases), and finally analyse the fragments generated within the trap itself. The ions produced can be analyzed in a new mass spectrometry experiment. In principle, the process can be repeated by isolating and fragmenting the ions obtained in an MS^2, $MS^{3,}$ and so

on in a multiple mass spectrometry (MS^n) experiment. Theoretically, many systems are capable of performing MS^n experiments, but the value of n is typically limited to 3 or 4, due to the decrease in ion abundance that occurs as n increases [128].

Ion-trap CID and higher-energy collisional dissociation (HCD, a beam-type CID) are fragmentation techniques in which molecular ions are accelerated by an electrical potential, thereby gaining additional kinetic energy. This increase in energy causes the ions to collide with inert gas molecules in the trap (typically helium, nitrogen, or argon). During the collision, part of the kinetic energy is converted into internal energy, leading to bond breaking and the fragmentation of molecules into smaller ions, which can then be analyzed. There are, therefore, two stages: activation by collision, where ions, accelerated by an electric potential, collide with inert neutral molecules in the gas phase, and molecular dissociation, where excess kinetic energy is converted into internal energy, so that one or more bonds are broken. The collision can occur at high (of the order of keV) or low (1-100 eV) energy. HCD is generally better than CID for peptide sequencing in the negative ion mode, since HCD generates more backbone cleavage products, whereas CID produces predominantly neutral loss peaks of precursors [129].

2.4 Mass Analyzers

A mass analyzer is the part of the instrument that separates ions based on their *m/z* values. In a mass spectrometer, ion isolation is usually electrically driven, although traditional analyzers, such as magnetic sectors, employ a magnetic field to influence ion separation. From the very beginning to the present, almost any physical principle, ranging from time-of-flight to cyclotron motion, has been employed to construct mass-analyzing devices. Some were extremely successful at the time of their invention; for others, it took decades for their potential to be fully recognized. Currently, many analyzers are widely used, namely, quadrupole (Q), linear trap quadrupole, Time of Flight (ToF), Fourier transform ion cyclotron resonance (FT-ICR), and Orbitrap. These analyzers vary in terms of size, price, resolution, mass range, and the ability to perform MS^n experiments.

2.4.1 Linear trap quadrupole (LTQ) analyzers

The linear trap quadrupole (LTQ) analyzer consists of a set of quadrupole electrodes to confine the ions radially and a static electric potential on the end electrodes to trap the ions axially, two *endcap* electrodes, and a central ring electrode (*ring electrode*) arranged in a "sandwich" geometry (**Figure 2.7**). Together, these electrodes form a cavity in which ions can be trapped and analyzed; both dome electrodes have a small hole through which ions enter and exit. This device traps ions in the space between the electrodes with a given range of *m/z* ratios,

determined by the applied potentials. In fact, a potential of constant frequency (radiofrequency, RF) and variable amplitude is applied to the ring electrode in such a way as to create a three-dimensional quadrupole field inside the trap. In this way, the ions will begin to move along oscillating trajectories confined within the analyzer cavity. The trajectory will depend on both the potential applied to the ring electrode and the *m/z* ratio of the ions. By varying the potential applied to the electrodes, it is possible to destabilize the ions' trajectories in the cavity, leading to their expulsion from the ion trap [130]. The mass spectrum is produced by sequentially varying the potential to expel ions in order of increasing m/z ratio.

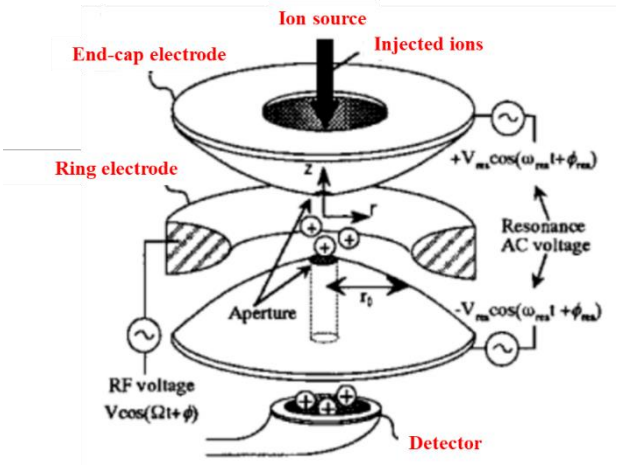

Figure 2.7 *Schematic representation of a LIT analyzer* [131].

2.4.2 Quadrupole analyzers

Since the Nobel Prize-awarded discovery of the mass-analyzing and ion-trapping properties of two- and three-dimensional electric quadrupole fields and the concomitant construction of a quadrupole mass spectrometer [129-130], this type of instrument has steadily gained importance. Modern quadrupole instruments cover m/z values up to 2000 or higher, with good resolving power, and are a standard device in LC-MS [134]. Among the advantages of quadrupoles are high transmission, light weight, compactness, comparatively low prices, low ion acceleration voltages, and high scan speeds, since scanning is achieved solely by sweeping electric potentials. A linear quadrupole mass analyzer consists of four hyperbolically or cylindrically shaped rod electrodes extending in the z-direction and mounted in a square configuration (xy-plane) [135], as shown in **Figure 2.8**:

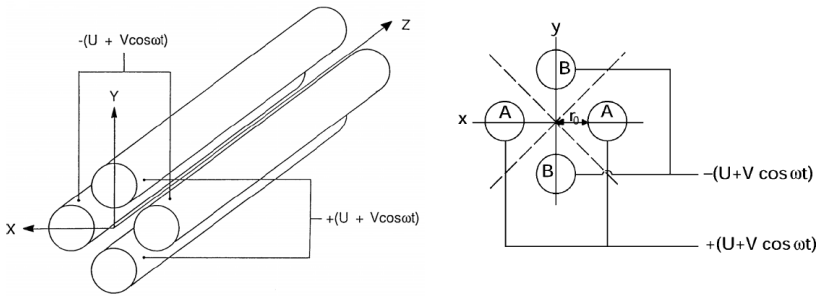

Figure 2.8 *Schematic representation of a linear quadrupole mass analyzer* [124].

The pairs of opposite rods are each held at the same potential, which is composed of a DC and an AC component. As an ion enters the quadrupole assembly in the z-direction, an attractive force is exerted on it by one of the rods with its charge opposite to the ionic charge. If the voltage applied to the rods is periodic, attraction and repulsion in both the x- and y-directions will alternate in time, because the sign of the electric force also changes periodically in time [135]. If the applied voltage is composed of a DC voltage *U* and an RF voltage *V* with the frequency ω, the total potential φ_0 is given by:

$$\varphi_0 = U + V coscos\ \omega t \tag{2.10}$$

Thus, the equations of motion are:

$$\frac{d^2x}{dt^2} + \frac{e}{mr_0^2}\varphi_0 x = 0 \tag{2.11}$$

$$\frac{d^2y}{dt^2} + \frac{e}{mr_0^2}\varphi_0 y = 0 \tag{2.12}$$

where r_0 is the distance between the center of the quadrupole and the rod surface. In the case of an inhomogeneous periodic field, such as the above quadrupole field, there is a small average force that is always in the direction of the lower field. The electric field is zero along the asymptotes for hyperbolic electrodes. It is therefore possible that an ion may traverse the quadrupole without hitting the rods, provided its motion around the z-axis is stable with limited amplitudes in the xy-plane. For a given set of *U*, *V*, and ω, the overall ion motion can result in a stable trajectory, allowing ions of a specific m/z value or m/z range to pass through the quadrupole. Ions oscillating within the distance $2r_0$ between the electrodes will have stable trajectories. These are transmitted through the quadrupole and detected thereafter. The path stability of a particular ion is defined by the magnitude of the RF voltage *V* and by the ratio *U/V*. From here, it is possible to obtain a stability diagram, useful to evaluate the xy-plan trajectory stability, by plotting parameters *a* and *q*, defined as the time invariant and variant fields, respectively, and obtained from the equation of motion:

$$a_x = -a_y = \frac{4eU}{m^2 r_0^2 \omega^2} \tag{2.13}$$

$$q_x = -q_y = \frac{2eV}{m^2 r_0^2 \omega^2} \tag{2.14}$$

The plot, shown in **Figure 2.9**, reveals the existence of regions where both x- and y-trajectories are stable, either x- or y-trajectories are stable, and no stable ion motion occurs:

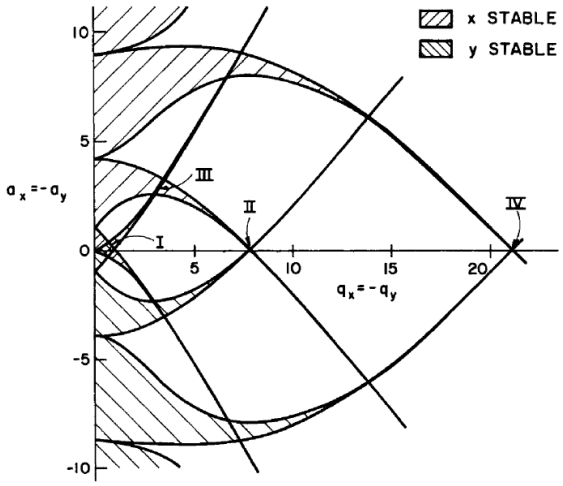

Figure 2.9 *Stability diagram for a linear quadrupole analyzer* [124].

Among the four stability regions of the first category, region I is of special interest for the normal mass-separating operation of the linear quadrupole [131-132]. If the ratio *a/q* is chosen so that *2U/V* = 0.237/0.706 = 0.336, the xy-stability region shrinks to one point, the apex, of the diagram. By reducing *a* constant *q*, i.e., reducing *U* relative to *V*, an increasingly wider *m/z* range can be transmitted simultaneously. Enough resolving power is achieved as long as only a small *m/z* range remains stable, e.g., one specific *m/z* ± 0.5 for unit resolution. Thus, the width (*Δq*) of the stable region determines the resolving power. By varying the magnitudes of U and V at a constant U/V ratio, a U/V = constant linked scan is obtained, allowing ions of increasing m/z to pass through the quadrupole. Overall, the quadrupole analyzer acts more like a mass filter. Quadrupole analyzers are generally operated at so-called unit resolution, which normally restricts their use to typical low-resolution (LR) applications [135]. At unit resolution, adjacent peaks are just separated from each other over the entire *m/z* range, i.e., *R* = 20 at *m/z* 20, *R* = 200 at *m/z* 200, and *R* = 2000 at *m/z* 2000. Setting the DC voltage *U* to zero transforms the quadrupole into a wide-band pass filter for ions. In the stability diagram, this mode of operation is represented by an operation line equivalent to the q-axis. Such devices are commonly known as RF-only quadrupoles; RF-only hexapoles and octopoles are used analogously [133-134]. Generally, higher-order RF 2N-multipoles differ from quadrupoles in that they do not exhibit a sharp *m/z* cut-off in transmission. Higher-order multipoles exhibit

increasingly steep potential wells, offer better ion-guiding capabilities, and exhibit better wide-band pass characteristics, i.e., a wider *m/z* range acceptance. This property led to the widespread application of electric quadrupoles, hexapoles, and octopoles as ion guides and collision cells [138]. From the ions' viewpoint, they act like a hose or pipe, fully permeable to neutrals. Thus, the RF ion guide allows residual gas to effuse through the gaps between the rods into the vacuum pumps, whereas ions are escorted into the mass analyzer. RF-only quadrupole, hexapole, or octopole collision cells are part of so-called triple quadrupole mass spectrometers, which essentially represent QqQ, QhQ, or QoQ instruments, respectively, depending on the type of RF-only collision cell actually in place [139].

2.4.3 Orbitrap analyzers

As the name suggests, the Orbitrap (invented by Makarov in 1999) is an ion-trapping device. A thorough description of the Orbitrap is available elsewhere; a brief description is provided here. The actual design was based on the Kingdon Trap of the 1920s, which comprised a small filament or wire electrode, pulled along a horizontal axis and enclosed by an outer barrel-shaped casing, which also served as an electrode (Figure 2.10) [115]. The space between the two electrodes is linked to the vacuum pumping system to provide high vacuum conditions.

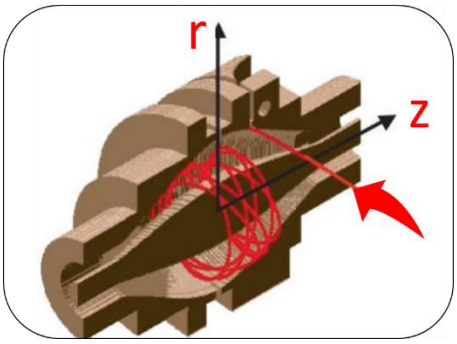

Figure 2.10 *Cutaway view of the Orbitrap mass analyzer. Ions are injected into the trap at the point indicated by the red arrow. Once trapped, the ions orbit around the central filament and also oscillate in the horizontal (z) direction* [128].

Ions are injected into the trap in a perpendicular direction in a pulse. In the original Kingdon design, a direct current voltage applied between the inner and outer electrodes produced a radial potential that trapped the ions; these days, the design is such that the ions are also confined axially. Once trapped, the ions adopt a stable orbit around the central filament (orbital trapping) but also oscillate along the horizontal axis. In this device, the oscillation frequency is related to the ion's m/z ratio. Ions are detected by measuring the image current from axial motion around the central electrode. The ions move along spiral trajectories induced by the electrostatic field generated by applying a potential difference between the two

electrodes. The spiral trajectory has two components: radial (along *r*) and axial (along *z*). It can be shown that the axial oscillation frequency is given by:

$$\omega = \sqrt{\left(\frac{z}{m}\right) k} \tag{2.15}$$

So it is inversely proportional to the square root of *m/z*; *k* is a constant that incorporates the characteristics of the electric field due to the particular shape of the two concentric electrodes. The measurement of the *m/z* ratio of each ion present in the trap is done using the Fourier transform, as for FT-ICR, although in this case it is not necessary to apply an AC before the measurement, since it is the electric field that aligns the trajectories of the ions at the same distance from the central electrode, while maintaining a different axial oscillation frequency dependent on *m/z*.

The electric field is defined as a quadrilogarithmic field:

$$U(r,z) = \frac{k}{2}\left(z^2 - \frac{r^2}{z}\right) + \frac{k}{2}\, x\, (R_m)2\, x\, ln\left[\frac{r}{R_m}\right] + C \tag{2.16}$$

where *r* and *z* are cylindrical coordinates, *k* denotes the curvature of the field, and R_m is the characteristic radius. The axial oscillation frequency can be determined by detecting the image current with a differential amplifier connected to the middle of the outer electrode. A sine wave is produced for each *m/z* value. The electrostatic attraction towards the middle electrode is compensated by the centrifugal force resulting from the initial tangential velocity of the ions.

As with TOF analyzers, the Orbitraps can exist as MS-only systems or as hybrids, for example, with a quadrupole mass filter to perform mass selection before fragment analysis by the Orbitrap. This filter enables additional experiments, such as MS/MS or MS^n [128].

2.5 Acquisition and processing of mass spectrometry data

In hyphenated techniques that couple mass spectrometry with chromatographic systems (LC-MS), the data consist of a series of mass spectra acquired sequentially. To obtain this type of information, the spectrometer scans the selected mass range repetitively during the course of the chromatographic analysis. This information can then be represented in different ways:

• By summing up all the currents generated by the various ions with different mass-to-charge ratios, which reach the spectrometer's detector, the classic mass chromatogram is obtained, known as the 'Total Ion Current Profile' (TIC), in which the intensity as a function of retention time is recorded; each chromatographic peak on the TIC represents an eluted compound, which can be identified through interpretation of the corresponding mass spectrum.

• By plotting only the intensities of ions that fall within a narrow mass-to-charge ratio window, commonly referred to as a 'segment', an eXtracted Ion Chromatogram (XIC) current profile is obtained, which is sought from the data set obtained by performing a full scan. This mode highlights only the compounds of interest in a complex mixture.

• By setting up the mass spectrometer manually or using the computer, it is also possible to select only the ions of interest. This results in 'Selected Ion Monitoring' (SIM): only the ion currents of the selected ions are displayed during analysis. SIM differs from XIC mode, in which profiles of individual ions are extracted from a set of complete mass spectra. The SIM mode, unlike the TIC and XIC modes, is not a full-scan MS experiment because the analyzer does not transmit all the masses formed in the source to the detector, but only the selected ones: instead of obtaining the entire mass spectrum of the eluted compounds, only the selected ions are monitored, thus increasing the sensitivity, i.e. the signal strength of the substances under investigation.

• A further mode that can be used for ion detection when performing MS/MS experiments is the SRM (Selected Reaction Monitoring) or MRM (Multiple Reaction Monitoring) mode. In this type of analysis, the precursor ion and one or more fragment ions are monitored at higher intensities. This significantly reduces chemical noise and increases the specificity of the analysis.

2.6 Electrochemical detection methods

In recent years, electrochemical techniques have been used to determine pharmaceuticals in water [25]. The electrochemical approach enables the identification of analytes in pharmaceutical compounds with remarkable selectivity and sensitivity, without the need for sample pretreatment or preliminary separation of components. Furthermore, electrochemical techniques offer advantages such as low cost, shorter analysis times, broader linear response, acceptable stability, and accuracy and reproducibility. Electrochemical methods allow relationships to be obtained between electrical measurements and the analyte concentration. This information can be acquired by monitoring electron transfer during a redox process involving the analyte:

$$Ox + ne^{-} \rightleftharpoons Red$$

where Ox and Red refer to the oxidized and reduced forms of the redox pair, respectively.

The measurement of current as a function of applied potential is carried out by employing an electrochemical cell (**Figure 2.11**) consisting of three electrodes immersed in the

solution containing the analyte: a working electrode, a reference electrode, and a counter or auxiliary electrode.

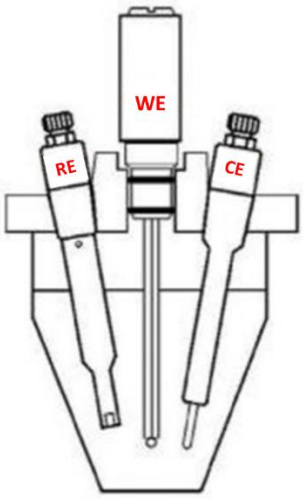

Figure 2.11 *Schematic representation of a conventional electrochemical cell.*

The electrochemical reaction under investigation takes place at the working electrode. The potential change is calculated between the working electrode and the reference electrode, whose potential is known and constant. The auxiliary electrode, typically a platinum wire, conducts current from the generator to the working electrode through the solution. The current passing through the reference electrode is negligible, and its potential is not affected by ohmic drop, polarisation, or overvoltage effects, thus remaining constant. The potential between the working electrode and the reference electrode, as well as the current circulating between the working electrode and the counter electrode, are controlled by a potentiostat connected to the electrochemical cell. A current/potential converter measures the current circulating as a result of the application of the potential so that curves of the current variation can be constructed as a function of the potential change (voltammetry) or as a function of time (chronoamperometry) [140].

A generic electrode/solution interphase process consists of the following steps:

- mass transport of the redox species to and from the electrode;
- associated chemical reactions, i.e., reactions by which there is a transformation of the species involved in the redox process into intermediates that actively take part in the electron transfer process;
- change in the physical state of the involved species by adsorption, desorption, or crystallization on the electrode surface;
- electron transfer.

One of these steps, depending on the experimental conditions, may be the slowest stage of the reaction, i.e., the rate-determining step of the electrochemical process, thereby limiting

the current at the electrode. When the rate-determining step is mass transfer, the electrode process is called reversible or Nernstian. Mass transport in electrochemical systems occurs in three different ways: migration, convection, and diffusion. Migration is the movement of charged species under the influence of an electric field: all charged species in solution will move towards the opposite charged electrode, which will instead exert an electrostatic repulsion towards the species with the same charge. This phenomenon is the mechanism by which current flows through the electrolyte solution: the current in the external circuit must be balanced by the flow of ions through the solution between the electrodes. Since the migration phenomenon is due solely to electrostatic forces, it affects not only electroactive species but also any other ionic species present in solution. Convection is the movement of the analyte together with the solvent by mechanical stirring of the solution. Convective motions are also generated as a result of the formation of density or temperature gradients. Finally, diffusion constitutes the spontaneous movement of a given species in solution following the establishment of a concentration gradient. During the reduction of an electroactive species, the portion of the solution in contact with the electrode is progressively depleted of the oxidized form relative to the rest of the solution. The concentration gradient that is established draws the distant electroactive species towards the electrode, and they move with a diffusion rate directly proportional to the gradient.

Of the mass transfer processes described, only diffusion is linearly correlated with the concentration of the electroactive species under investigation, so the control and or reduction of the other two phenomena is of fundamental importance during an electrochemical analysis. In particular, the effects of the migration process are limited by adding an excess of an inert supporting electrolyte (usually alkali metal salts) to the solution, which does not interfere with the electrode process but allows the migration of a negligible amount of the electroactive species. Convection can be minimized by working under thermostated conditions and without agitation or vibration.

2.6.1 Cyclic voltammetry (CV)

Voltammetry is an electrochemical technique that studies the relationship between current and potential during an electrochemical process. In particular, CV is a widely used analytical technique that is extremely versatile because it allows rapid observation of the redox behavior of a given system over a wide range of potentials.

In CV experiments, the potential between the reference and working electrodes, immersed in a quiescent solution, is cycled first to induce oxidation and then reduction (or vice versa) of an electroactive species, and the resulting current is measured. The excitation signal

is a linear potential scan with a triangular waveform (**Figure 2.12**). The potential varies from an initial value at which no faradic current is flowing to a value at which the polarity of the scan is reversed.

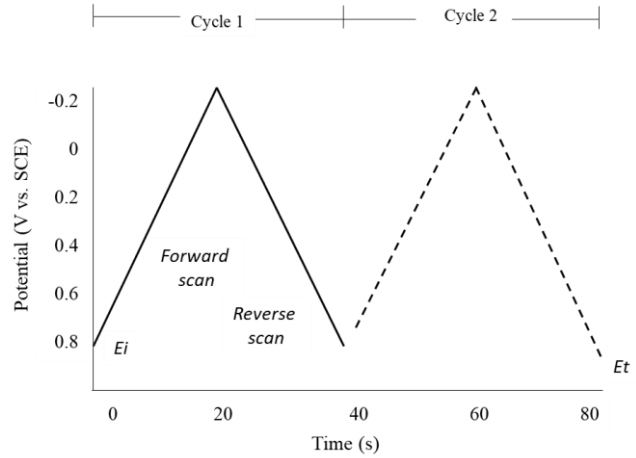

Figure 2.12 *Potential waveform.*

A voltammogram is a graph of current versus applied potential (**Figure 2.13**). The voltammogram profile depends on the nature of the redox reaction at the working electrode involving the electroactive species in solution. Therefore, each electroactive species is characterized by a specific voltammogram profile and a characteristic peak potential, *E*p.

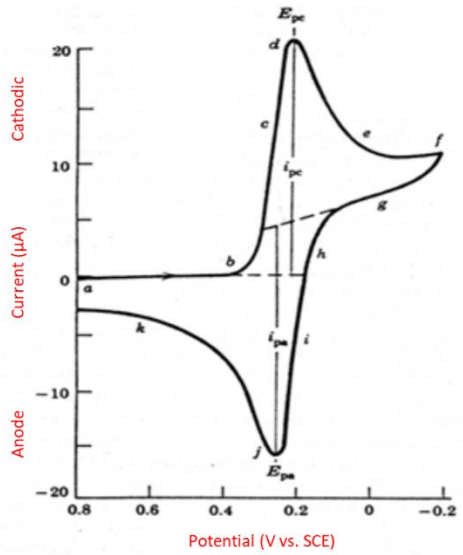

Figure 2.13 *Cyclic voltammogram.*

In a typical voltammogram for a reversible redox reaction, once a potential sufficient for the faradic process to occur is reached, the current increases rapidly, passes through a maximum (peak current), and then decreases. Reversing the potential scan direction, a return peak is observed with a current of the opposite sign. The voltammogram profile shown in the

figure can be rationalized as follows: no electrolysis of the analyte occurs when the initial potential is applied; when the potential becomes sufficiently negative to reduce the electroactive species, a cathodic current is observed which increases until reaching the so-called peak potential, at which the concentration of analyte that can be reduced at the electrode becomes negligible; the cathodic current then decreases because the solution surrounding the electrode has been depleted of the oxidized form as a result of its electrochemical conversion; when the scan is reversed, the potential is still sufficiently negative to reduce the analyte and therefore a cathodic current continues to flow even though the scan is in the positive direction; the reduced analyte begins to oxidize again, giving rise to an anodic current of opposite polarity which increases rapidly until the surface concentration of oxidized analyte is practically negligible, giving rise to the appearance of the anodic peak; finally, the current decays due to the low level of oxidized substance in the solution surrounding the electrode. The peak current for a reversible process is given by the Randles-Sevcik equation:

$$I_p = (2.69 * 10^5) n^{3/2} A C_0 D^{1/2} v^{1/2} \quad (2.17)$$

where C_0 is the analyte concentration in solution (mol cm^{-3}), v is the potential scan rate (V s^{-1}), D is the analyte diffusion coefficient (cm^2 s^{-1}), A is the electrode area (cm^2), n is the number of transferred electrons, and I_P is peak current intensity (A). The peak current, as described by the equation, is directly proportional to the concentration of the species present in the bulk of the solution and varies with the square root of the scan rate.

2.6.2 Differential pulse voltammetry (DPV)

DPV is an electrochemical pulse technique that involves applying both a linear potential scan and a periodic series of pulses of constant duration and amplitude. The basis of this technique is the measurement of current when the difference between the faradaic and capacitive (non-faradaic) currents is large. Two types of excitation signals can be applied:

- The first signal, shown in **Figure 2.14 (a)**, results from superimposing a periodic voltage pulse of constant duration and amplitude onto a linear potential scan.
- The second signal, shown in **Figure 2.14 (b)**, is obtained by adding a staircase signal to a pulse signal.

A small pulse, usually on the order of 50 mV, is applied in the final moments of the excitation signal in both of the signals depicted.

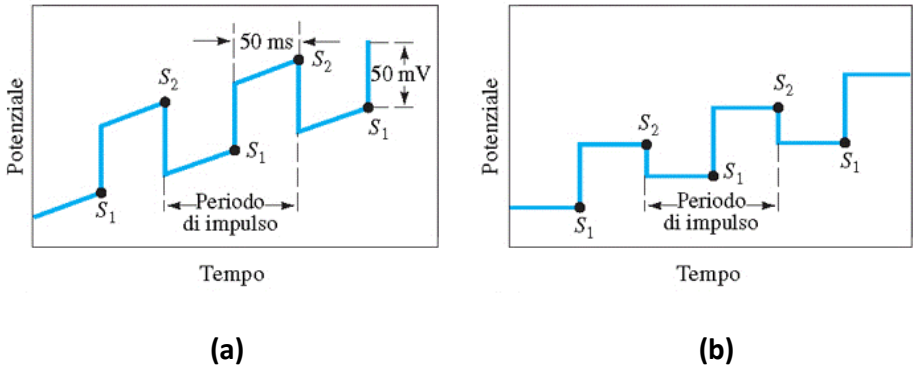

Figure 2.14 *Excitation signals for DPV.*

The DPV technique involves a first current measurement taken before the pulse (*iS1*) and a second measurement taken at the end of the pulse, during the final milliseconds (*iS2*). By recording, for each pulse, the difference between the two current measurements ($\Delta i = iS2 - iS1$) as a function of the excitation voltage, a differential pulse voltammogram is obtained, which appears as a peak (**Figure 2.15**).

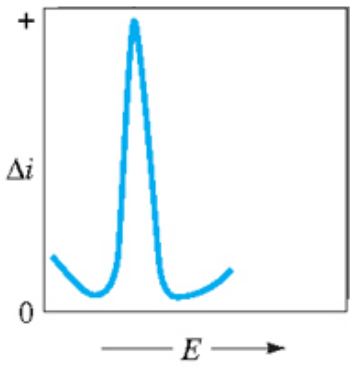

Figure 2.15 *Graph of the current variation as a function of the application of differential potential pulses.*

The resulting peak is symmetric and centered at a potential approximately equal to the standard potential of the half-reaction in reversible processes. The peak height is a quantitative parameter because it is directly proportional to the concentration. One of the main advantages of DPV is the significant improvement in method sensitivity compared to linear sweep voltammetry: it provides well-defined peaks at concentration levels that are 2×10^{-3} times lower than those required to obtain the classical voltammetric wave, and detection limits 2–3 orders of magnitude lower than classical methods, reaching a concentration range between 10^{-7} and 10^{-8} M. The increase in sensitivity can be attributed to the fact that the capacitive current is at its maximum when the pulse is applied and then decreases rapidly. At the end of the pulse, essentially only the faradaic current is sampled.

2.7 Methods for the Characterization of Adsorbent Materials

The final section of Chapter 2 provides a brief overview of the characterization methods used in this study to analyze the adsorbent materials.

2.7.1 Scanning Electron Microscopy (SEM)

SEM is based on the interaction between an electron beam and a sample. Specifically, the electron beam is generated by a source, typically a tungsten filament, located at the top of a vacuum-maintained column (electron column). Before reaching the sample, the beam follows a precise path regulated by a system of electromagnetic lenses. These lenses consist of a coil of wires inside magnetic poles made of metal, through which an electric current is applied. Since electrons are sensitive to magnetic fields, varying the current intensity applied to each lens allows the beam to follow a defined trajectory before striking the sample (**Figure 2.16**).

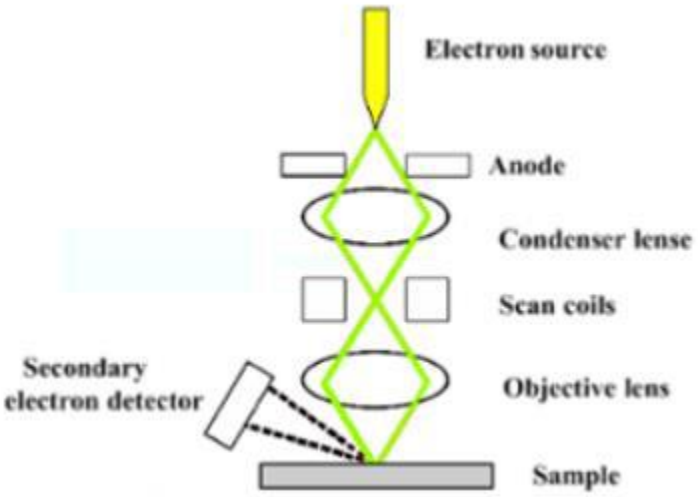

Figure 2.16 *Diagram of the path followed by an electron beam in the SEM.*

The electromagnetic lenses used in SEM can be classified as follows:

1. Condenser lenses, which are the closest to the electron source and therefore the first encountered by the electron beam along its path toward the sample. These lenses provide an initial convergence of the electron beam.
2. Objective lenses, which allow further convergence of the electron beam before it reaches the sample. They are responsible for focusing the beam onto the sample.

When the electron beam strikes the sample, the latter emits a signal in the form of electrons, which can be classified as follows:

- Backscattered electrons (BSEs): BSEs are produced through elastic collisions between the atoms in the sample and the electrons from the primary beam generated by the instrument. Their production depends strongly on atomic number, as heavier atoms

scatter electrons more efficiently than lighter ones. BSEs are particularly useful for analyzing chemical composition and crystallography.

- Secondary electrons (SEs): SEs are generated by interactions between the primary electron beam and the sample surface and have lower energy than BSEs. SEs are particularly useful for morphological analysis of the sample surface.
- X-rays: These are emitted when electrons excite the atoms in the sample, providing information about the elemental composition.

After the electron beam reaches the sample, it is scanned using a dedicated scanning unit within the lens system (scan coils). The presence of three distinct detectors allows the collection and analysis of the signal emitted by the sample [141]. The Everhart–Thornley detector primarily detects SEs and generates high-resolution images of the sample surface. It is positioned with its front end facing the sample and inclined at approximately 30° relative to the surface. The front end is enclosed within a Faraday cage. Since SEs have low energies (0–50 eV), applying a current of 200–300 V to the Faraday cage ensures that these electrons are attracted toward the detector, including those initially emitted in directions away from it. The backscattered electron detector is positioned above the sample to improve BSE collection efficiency. Most BSEs are emitted along the direction of the incident electron beam (upward), while lateral scattering is less probable. The geometric configuration of the E-T detector makes it less efficient at collecting BSEs. Finally, the Energy-Dispersive X-ray Spectroscopy (EDS) detector measures X-rays emitted by the sample, including background radiation. By analyzing the energy distribution and intensity of the detected X-rays, the EDS detector enables the identification of elements and their concentrations within the analyzed region of the sample.

The result is a high-resolution black-and-white image with a large depth of field, exhibiting characteristics similar to those of a standard photographic image. For this reason, SEM images are immediately intuitive and easy to interpret [142].

2.7.2 X-ray Photoelectron Spectroscopy (XPS)

XPS traces its origins to Hertz's 1887 experiment on the photoelectric effect, in which X-rays were used as the excitation source; however, the first XPS spectrum recorded on a NaCl sample dates only to 1954 [143]. The physical principle underlying the technique is as follows: a photon emitted by the source with sufficient energy is absorbed by an atom in the sample, which can then emit an electron from one of its core levels [144]. By analyzing the various photoemitted electrons (photoelectrons), it is possible to identify the elements present on the

surface under investigation and to quantify their relative abundance. The kinetic energy E_k of the photoelectron, by energy conservation, will be

$$E_k = h\nu - E_B \tag{2.18}$$

If emitted from a solid, its equation becomes

$$E_k = h\nu - E_B - \varphi \tag{2.19}$$

where $h\nu$ is the energy of the incident photon (h is Planck's constant and ν is the frequency), E_B is the binding energy of the electron in the atom, and φ is the work function.

The position of the peaks in the energy spectrum is characteristic of each atomic species present in the sample. Following the emission of a photoelectron, the system relaxes through two competing processes: fluorescence emission and Auger emission. Fluorescence occurs when an electron from an outer shell relaxes to fill the vacancy left by the expelled photoelectron. During this relaxation, the electron releases energy in the form of a photon. In Auger emission, a second electron also fills the primary vacancy, but its relaxation energy is transferred to a third electron, which is subsequently ejected (**Figure 2.17**).

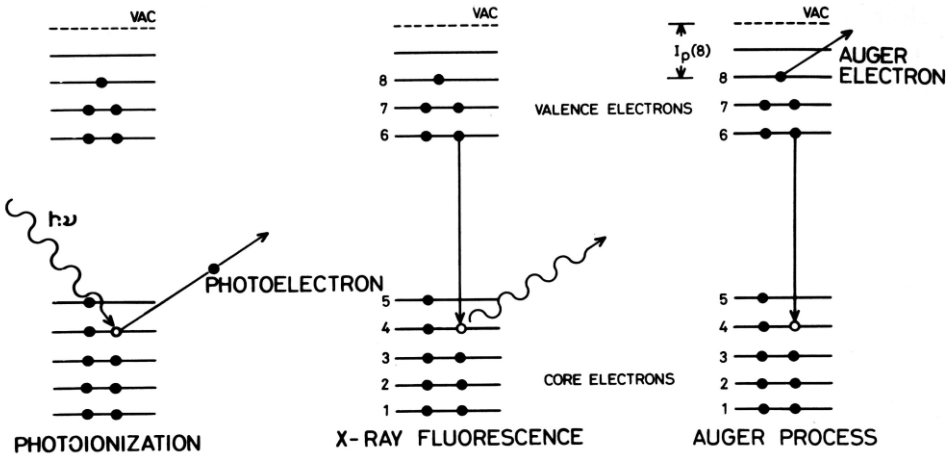

Figure 2.17 *Diagrams of the emission processes resulting from photoionization.*

The kinetic energy of the Auger electron, $E_{k,Auger}$ is given by

$$E_{k,Auger} = E_B - E_2 - E_3 \tag{2.20}$$

where E_B is the binding energy of the first-level electron that is photoemitted, E_2 is the binding energy of the second electron that relaxes, and E_3 is that of the third electron that is expelled [145]. As shown in Eq. 2.20, the energy of the initial photon does not appear; this means that $E_{k,Auger}$ depends solely on the electronic structure of the excited atom. It therefore becomes important to distinguish Auger peaks from photoelectron peaks in the spectrum. For this reason, a dual-anode system (Al and Mg) is used: by changing the energy of the incident photon, E_B

varies, but $E_{k,Auger}$ does not. In this way, the two types of emission can be clearly differentiated. Auger emission dominates over fluorescence for low atomic numbers (Z < 35).

The instrument is housed in an ultra-high vacuum chamber, where the source, sample, electrostatic lens system, analyzer, and detector are positioned as shown in **Figure 2.18**.

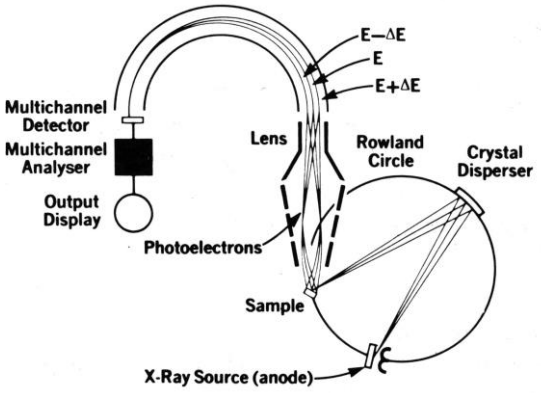

Figure 2.18 *XPS instrument* [145].

The low pressure is necessary to keep the sample clean (preventing unwanted adsorption) and to avoid attenuation of the photoelectron signal due to scattering with residual gas. The source usually consists of a dual anode of Al and Mg, as mentioned above, engineered to excite emission from either anode selectively. Next to the anodes are two incandescent filaments that emit electrons via thermionic emission, which then strike one of the anodes. The excited core levels are:

$$Al \quad K\alpha \quad 1486,6\ eV$$

$$Mg \quad K\alpha \quad 1253,6\ eV$$

These are the most intense lines, but not the only ones resulting from this excitation. To ensure accurate analysis, a quartz-crystal monochromator is used to allow only photons from the Kα lines to pass. The source assembly is finally cooled by water flowing through a tube near the anodes, preventing them from melting. Once the beam strikes the sample, photoelectron emission occurs. These photoelectrons are collected by an analyzer, which separates them according to energy and directs them toward the detector.

An XPS spectrum allows both qualitative and quantitative analysis of the elements present on a surface. First, the peak positions can be compared with tabulated values to identify the species present in the sample. However, it is important to note that XPS is sensitive to small variations in binding energy due to the chemical environment of the emitting species (a phenomenon known as chemical shift). Therefore, qualitative analysis is not straightforward but can distinguish between different chemical states, such as various oxidation states of the same element.

2.7.3 Brunsuer-Emmett-Teller (BET) analysis

The BET method is based on the BET theory, developed by S. Brunauer, P. Emmett, and E. Teller in 1938. It provides a way to determine the specific surface area S_{BET} (usually expressed in $m^2\ g^{-1}$) of a solid material — including both external surface and internal surface accessible via pores — by measuring how much gas is physically adsorbed onto the material's surface under controlled conditions. This technique is widely used in materials science, catalysis, powders, porous materials, adsorbents, nanoparticles, ceramics, etc.

Before adsorption measurements, the solid sample is typically degassed (i.e., heated under vacuum or in an inert atmosphere) to remove moisture or contaminants, ensuring the surface is "clean". The standard practice uses nitrogen gas (N_2) at cryogenic temperatures (liquid N_2, ~77 K) as the adsorbate. The gas is dosed incrementally, and at each dose, the amount adsorbed is measured once equilibrium is reached. The results yield an adsorption isotherm: a plot of adsorbed volume (or amount) vs. relative pressure (P/P_0, where P_0 is the adsorbate's saturation vapor pressure at that temperature). The data in a certain region of the isotherm — typically for relative pressures P/P_0 in the range ~0.05 – 0.35 — are transformed according to the BET equation [146]:

$$S_{BET} = \frac{V_p N_A \sigma}{Vmol} \tag{2.21}$$

where N_A is Avogadro's number; σ is the known cross-sectional area of the adsorbate molecule (for N_2, typically ~ 0.162 nm^2) and V_{mol} is the molar volume of the gas (expressed in $cm^3\ mol^{-1}$). A linear fit in the P/P_0 range ~0.05 – 0.35 yields two parameters (slope and intercept), from which one can determine the volume of gas Vp ($cm^3\ g^{-1}$) that would form a monolayer covering the surface. Once Vp is known, the S_{BET} of the sample is calculated by using Eq. 2.21.

Microporosity (W_0, $cm^3\ g^{-1}$) is evaluated from the low relative pressure region of the nitrogen adsorption isotherm using the Dubinin–Astakhov (D-A) equation. The D-A equation is based on micropore filling, not layer-by-layer adsorption as in the BET model. In microporous materials (pores < 2 nm), adsorption occurs mainly because of volume filling rather than surface coverage. Adsorbate molecules are "forced" into the tiny pores due to adsorption potential, creating a nearly saturated state in each micropore. Characteristic adsorption potential A is a measure of how strongly the adsorbate is attracted to the pore:

$$A = RT\ ln\frac{P_0}{P} \tag{2.22}$$

where R is the gas constant, T is the temperature, P_0 is the saturation pressure, and P is the equilibrium pressure.

The original Dubinin–Radushkevich (D–R) equation assumed a Gaussian distribution of adsorption energies in the micropores. However, real materials often have heterogeneous micropores, leading to deviations from the Gaussian assumption. The D-A equation introduces a variable exponent *n* to account for this [147]:

$$W = W_0 \, exp[-(A/E)^n] \tag{2.23}$$

- $n=2$ → Gaussian energy distribution (D–R equation);
- $n \neq 2$ → accommodates micropore heterogeneity; smaller *n* for broader energy distribution, larger *n* for narrower one.

W is the volume of the adsorbate at a given pressure; W_0 is the maximum adsorbate volume; *E* is the characteristic energy of adsorption (reflects adsorbate-adsorbent interaction strength); *n* is the pore heterogeneity exponent (describes how uniform or heterogeneous the pore structure is); *A* is the adsorption potential (given by Eq. 2.22).

The average micropore width (*L*, expressed in nm) is obtained from the Stoeckli–Ballerini equation [148]**:**

$$L = \frac{10.8}{E_0 - 11.4} \tag{2.24}$$

where E_0 is the characteristic adsorption energy (in kJ mol^{-1}), obtained from fitting the D-R (or D-A) isotherm to the experimental adsorption data.

2.7.4 Point of zero charge (PZC)

The PZC is determined to assess the net surface charge of the materials. The PZC is a fundamental physicochemical parameter that describes the electrical behavior of a solid surface in contact with an aqueous environment. It is defined as the pH at which the material's net surface charge is zero. At this pH, the total concentration of positively charged surface sites is exactly balanced by the concentration of negatively charged sites. Consequently, the solid exhibits no overall electrostatic charge, although individual functional groups may still participate in protonation–deprotonation equilibria. From a theoretical standpoint, the origin of surface charge derives primarily from the acid–base properties of materials' surface functional groups. These groups can undergo protonation or deprotonation depending on the activity of hydrogen ions in solution. For a generic amphoteric surface site, commonly represented as ≡R, the following protolytic equilibria may occur:

$$\equiv RH + H^+ \rightleftharpoons \equiv RH_2^+$$

$$\equiv RH \rightleftharpoons \equiv R^- + H^+$$

The distribution of these species is governed by the thermodynamic equilibrium constants for protonation and deprotonation, respectively.

For a generic acid-base reaction in aqueous solution

$$HA \rightleftharpoons H^+ + A^-$$

We can represent the acid dissociation as

$$Ka = \frac{[\mathbf{H}+][\mathbf{A}-]}{[\mathbf{HA}]}$$

Where *Ka* is the acid dissociation constant, when the solution pH is lower than p$K_{a,}$ the equilibrium shifts toward the formation of the protonated species; conversely, at pH values higher than pK_a, deprotonation is favored. The PZC corresponds to the pH at which the thermodynamic tendencies toward protonation and deprotonation are balanced, resulting in a zero net surface charge density. The relative distribution of positive and negative species varies with solution pH: at pH below the PZC, the surface is predominantly positively charged, exhibiting enhanced affinity for anionic species; at pH above the PZC, the negatively charged surface favors interactions with cationic solutes. Consequently, understanding the PZC is therefore essential for interpreting and predicting the physicochemical behavior of materials, because it strongly influences processes such as adsorption, electrostatic stabilization or destabilization of colloids, aggregation phenomena, ion exchange, and heterogeneous catalysis.

3. CONTRIBUTION 1

Environmental Fate, Ecotoxicity, and Remediation of Heterocyclic Pharmaceuticals as Emerging Contaminants: A Review of Long-Term Risks and Impacts

3.1 Abstract

Heterocyclic pharmaceuticals are ECs due to their toxic and carcinogenic properties and their detrimental impact on natural ecosystems. These compounds pose a significant environmental concern due to their widespread use in medical therapy, accounting for over 90% of new medications. Their unique chemical structures contribute to their persistence across diverse environmental matrices, underscoring the urgent need to mitigate associated risks. This review provides a comprehensive examination of the sources, environmental fate, toxicity, and long-term risks of heterocyclic pharmaceuticals and proposes potential remediation strategies. This contribution begins with an overview of the diverse types of heterocyclic pharmaceuticals and their applications, with particular focus on compounds containing heteroatoms such as nitrogen, oxygen, and sulfur. It then explores the sources and pathways by which these pollutants enter the environment, including wastewater discharge, agricultural runoff, improper disposal, resistance to biodegradation, and bioaccumulation. The toxic effects and long-term consequences of exposure are discussed, encompassing neurotoxicity, genotoxicity, mutagenesis, cardiovascular and metabolic toxicity, carcinogenicity, and teratogenesis.
Furthermore, the contribution summarizes various remediation strategies and treatment approaches to reduce the environmental impact of these compounds, drawing on evidence from the literature. The contribution concludes by identifying critical knowledge gaps and highlighting the urgent need for more effective remediation strategies to address the growing environmental threat posed by these ECs.

3.2 Introduction

Heterocyclic compounds are cyclic structures characterized by the inclusion of heteroatoms, elements other than carbon, notably oxygen, nitrogen, and sulfur, within five- or six-membered rings [149]. These compounds can also incorporate other ions, such as phosphorus, iron, magnesium, and selenium [148-149]. They are prevalent in nature and can be synthesized in significant quantities through industrial processes [152]. The pharmaceutical significance of heterocyclic compounds is profound, as they are integral to the formulation of a wide range of medicines, insecticides, and crop protection agents. Their design enables the

production of beneficial biological compounds, including hormones, antibiotics, and vitamins [151-152].

Heterocycles exhibit a wide range of biological activities, including antibacterial, antifungal, anti-inflammatory, anticancer, antiviral, anti-allergic, anthelmintic, antioxidant, anticonvulsant, antihistamine, antileprosy, and antihypertensive properties [153-155]. These compounds play a central role in modern drug development, as they enable modifications in physicochemical properties, thereby improving absorption, distribution, metabolism, excretion, and toxicity (ADME/Tox), which are crucial for effective pharmaceuticals [156-157]. The World Health Organization (WHO) reported that over 90% of new medications include heterocyclic structures [158-159].

In agriculture, heterocyclic compounds are also significant, used as synthetic growth promoters to boost crop yields and protect crops. However, their extensive presence and persistence in ecosystems, coupled with their toxic and carcinogenic properties, raise substantial environmental concerns [160-161]. Even trace amounts in drinking water can disrupt endocrine function and cause various health impairments, including effects on the thyroid and nervous systems [162-163]. Certain heterocyclic compounds have been categorized as priority pollutants by the United States Environmental Protection Agency, recognizing the environmental hazard posed by pharmaceutical pollution of surface and groundwater [166].

Heterocyclic substances are characterized by high polarity and solubility, which enable them to penetrate groundwater systems readily. They have been detected in environmental samples at concentrations that pose ecological risks; for instance, sulfonamides have been found in surface waters at concentrations of 0.13 to 1.9 μg L^{-1} [167]. The growing contamination of water sources, exacerbated by industrial growth and the emergence of high-tech sectors, is troubling. Studies estimate that around 38,000 chemicals are currently in use, with over 300 new compounds introduced each year, many of which end up in untreated wastewater discharges into the environment [166-167].

This chapter provides an in-depth exploration of the environmental impact, ecotoxicity, and long-term risks associated with heterocyclic pharmaceuticals. By identifying existing knowledge gaps and investigating innovative remediation strategies, it aims to develop sustainable methods to mitigate the harmful effects these compounds have on ecosystems and human health.

3.3 Overview of Heterocyclic Pharmaceuticals

Heterocyclic compounds are essential in medicinal chemistry and the pharmaceutical industry because of their biological activity and stability. These compounds are widely used in

drug design and production and serve as the fundamental structures of various pharmaceutical agents [170]. Common heterocyclic compounds include amino acids, vitamins, and enzyme precursors. Heterocycles with condensed ring structures exhibit diverse physiological functions and are classified according to their heteroatom composition [147, 149]. This document examines the most common pharmaceutical heterocyclic compounds, organized by heteroatom, and their uses in the pharmaceutical industry.

3.3.1 Nitrogen-Containing Heterocycles

Nitrogen-containing heterocycles are a crucial category of compounds in pharmaceuticals, accounting for nearly 50% of newly approved chemical entities [170]. Over 85% of bioactive molecules contain at least one nitrogen atom, which is pivotal to their diverse biological activities, owing to their structural similarity to naturally occurring substances [159]. Key nitrogen-containing heterocycles in medicinal chemistry include pyrroles, indoles, triazoles, pyrimidines, imidazoles, benzimidazoles, tetrazoles, and quinolines [162]. Among these, indole derivatives (**Figure 3.1**) are particularly significant due to their extensive therapeutic potential. They exhibit a wide range of pharmacological activities, including anti-inflammatory, antibacterial, anticonvulsant, and anticancer effects, making them invaluable for medicinal applications [163, 169-170].

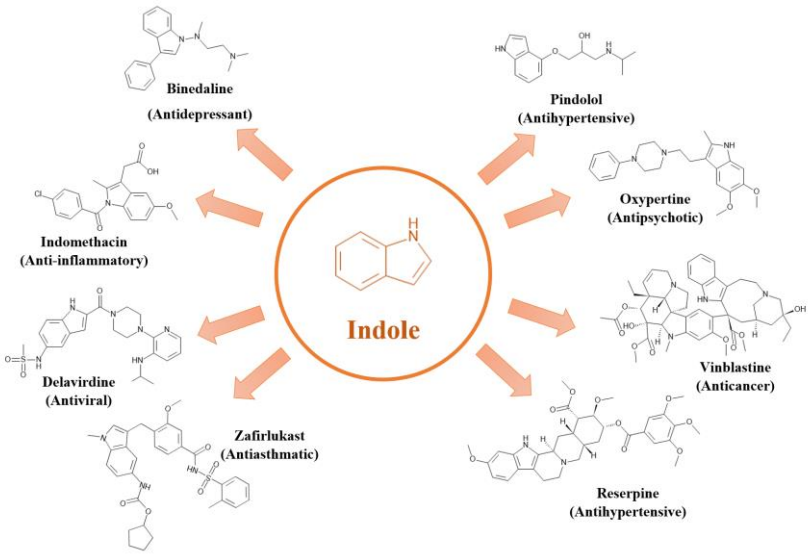

Figure 3.1 *Structure of common indole derivatives and their application in pharmaceutical chemistry.*

Benzimidazole and imidazole (**Figure 3.2**) are also well-established heterocycles that are used extensively in drug development [173]. Their structural versatility has resulted in various derivatives, including thiabendazole and albendazole, which have shown effectiveness against a range of diseases, including protozoal infections, cancer, and as anti-inflammatories [172-173].

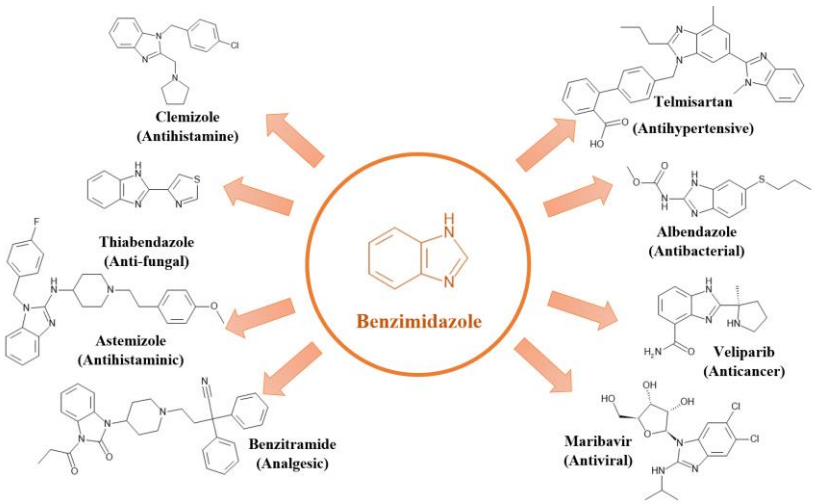

Figure 3.2 *Structure of common benzimidazole derivatives and their application in pharmaceutical chemistry.*

Additionally, pyrazole has emerged as a prominent scaffold in medicinal chemistry due to its ease of synthesis and chemical modification [176]. Pyrazole derivatives (**Figure 3.3**) display numerous therapeutic effects, particularly in oncology and infectious diseases, and exhibit functionalities such as anticancer and anti-inflammatory activities [177]. These nitrogen-containing heterocycles play a vital role in the development of new pharmaceuticals, underscoring their significance in medicinal chemistry [176-178].

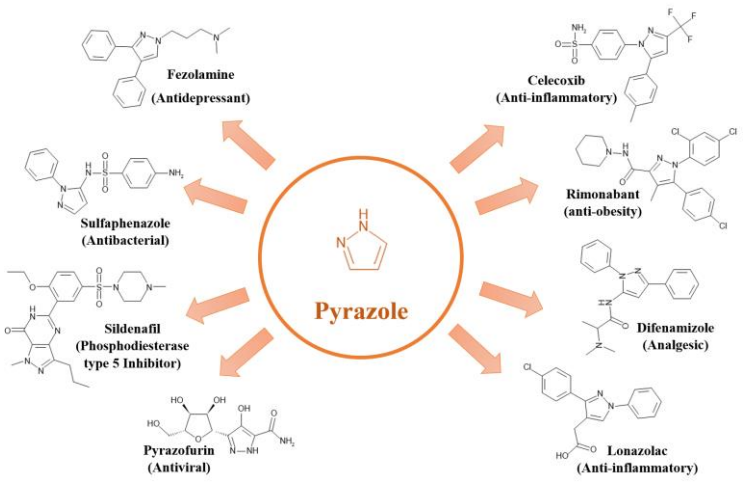

Figure 3.3 *Structure of common pyrazole derivatives and their application in pharmaceutical chemistry.*

3.3.2 Oxygen and Nitrogen-Containing Heterocycles

Oxygen- and nitrogen-containing heterocycles (**Figure 3.4**), such as oxazole and isoxazole, are notable for their unique properties, which enable them to participate in various noncovalent interactions with enzymes and biological receptors [181]. The distinction between oxazole and isoxazole lies in the arrangement of their heteroatoms (oxygen and nitrogen) within the ring structures, which results in different chemical characteristics [182]. These differences

confer versatile biological activities on these compounds, with many derivatives, including oxazoles, oxazolines, isoxazoles, oxazolidones, oxadiazoles, and benzoxazoles, being used as medicinal agents. These compounds have shown significant potential for treating a wide range of diseases, indicating promising development prospects for pharmaceutical applications [183]. Their biological activities span a multitude of therapeutic areas, including anti-inflammatory, antibacterial, antifungal, antiparasitic, anti-obesity, antitubercular, anticancer, antiviral, analgesic, anti-neuropathic, antidiabetic, and antioxidative properties, underscoring their broad applicability and value in drug discovery [179, 182].

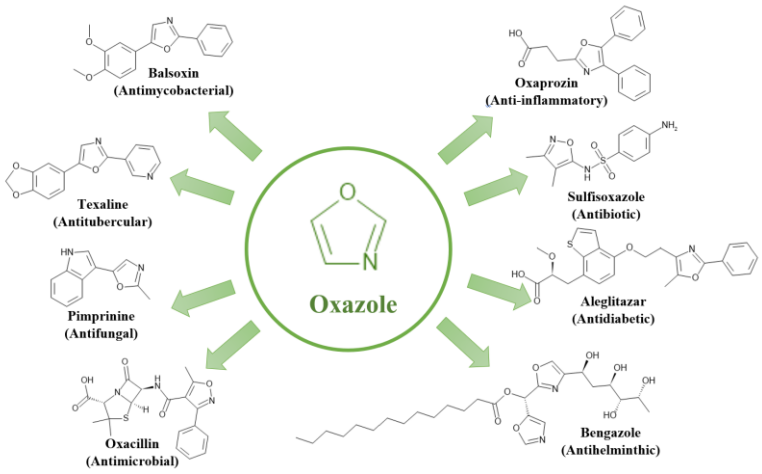

Figure 3.4 *Common oxazole-derived medicinal agents and their application in pharmaceutical chemistry.*

3.3.3 Sulfur-Containing Heterocycles

Sulfur-containing heterocycles (**Figure 3.5**), particularly thiophene and thiopyran, are crucial in medicinal chemistry and drug discovery [185]. These S-heterocycles serve as essential building blocks for synthetic analogs that exhibit various therapeutic activities, including anticancer, antiviral, antimicrobial, antidiabetic, antihypertensive, and anti-inflammatory properties [183-184]. Thiophene derivatives are widely used in FDA-approved drugs, while thiopyrans, despite being less studied due to the prevalence of oxygen heterocycles, have gained attention for their potential biological activities [186]. They are utilized in organic synthesis and pharmaceutical chemistry for their versatility as building blocks, with applications in antibacterial, anti-hyperplasia, anti-psychiatric, and anticancer treatments, exemplified by the diuretic Meticrane, derived from thiopyran [187].

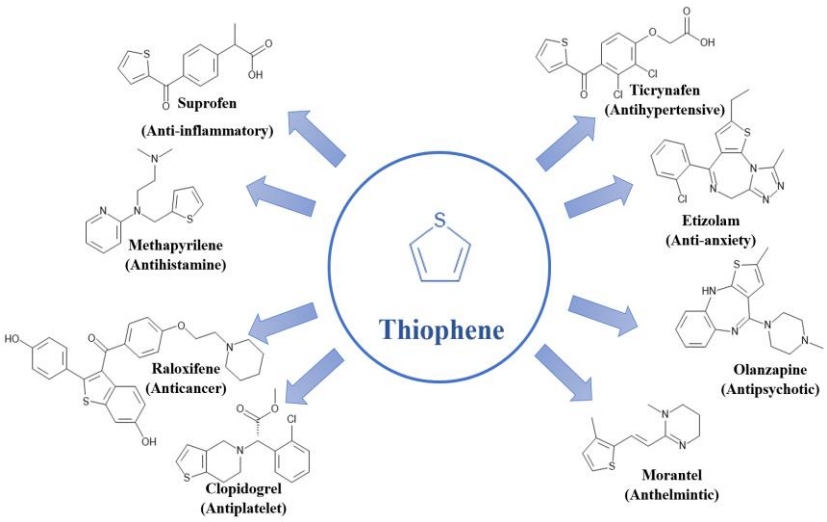

Figure 3.5 *Common thiophene derivatives and their application in pharmaceutical chemistry.*

3.3.4 Nitrogen and Sulfur-Containing Heterocycles

Significant advancements have been made in the development of heterocycles containing nitrogen and sulfur, particularly thiazole, isothiazole, and thiazolidine, leading to novel synthetic and natural agents [186-189]. Thiazole is particularly notable in pharmaceuticals for its anti-inflammatory, antibacterial, antiviral, anticancer, and antifungal properties. Its aromatic structure allows for electron delocalization and various reactive sites, making it valuable for donor-acceptor, nucleophilic, and oxidation reactions [190-192]. Multiple thiazole analogs are now approved for treating various diseases, as shown in the chemical structures of thiazole-containing drugs (**Figure 3.6**).

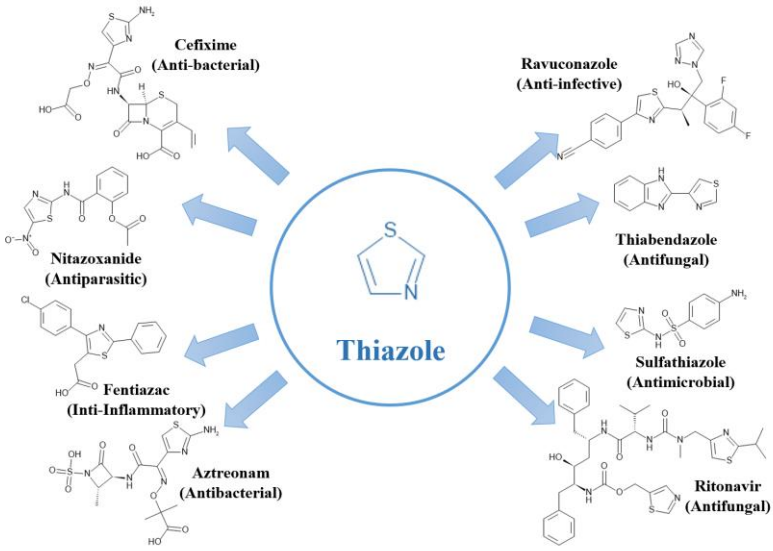

Figure 3.6 *Common thiazole derivatives and their application in pharmaceutical chemistry.*

3.4 Sources and Environmental Fate of Heterocyclic Pharmaceuticals

Numerous pharmaceuticals and compounds used in medicine are derived from heterocyclic compounds, which possess versatile chemical structures and therapeutic properties essential to modern healthcare. Annually, thousands of tons of pharmaceuticals are produced worldwide for human and veterinary applications, with domestic consumption being the primary source of environmental emissions [195]. Sources of pharmaceutical release into the environment include healthcare services, hospitals, industrial residues, veterinary practices, agriculture, and aquaculture[194-195]. Pharmaceuticals can infiltrate the environment during their manufacture, use, and disposal, and improper disposal practices, such as discarding unused drugs down sinks and toilets, contribute to 3-50% of pharmaceuticals becoming waste. Heterocyclic pharmaceuticals are particularly concerning due to their high toxicity and persistence in environmental matrices, leading to incomplete breakdown and potential accumulation of residues if not properly managed [196-197].

These nitrogen-containing heterocyclic compounds exhibit high solubility, allowing them to easily enter aquatic environments, including surface and groundwater, as well as industrial wastewater. Concentrations of these pharmaceuticals in various aquatic environments range from 0.03 to 11,000 ng L^{-1} [197]. A recent study by Zhang et al. (2023) found substantial levels of organic compounds, including pharmaceuticals, in WWTP effluents, with 33.6% of these compounds entering rivers, underscoring the environmental impact of wastewater treatment facilities on aquatic pollution and the urgent need for advanced treatment technologies [200].

In aquatic systems, heterocyclic pharmaceuticals may undergo several fates, including biodegradation, photolysis, and sorption. Microbial activity and photolytic processes can partially degrade these compounds; however, their sorption to various environmental matrices can affect their bioavailability and may lead to ecological toxicity [201]. The resistance of these pharmaceutical pollutants to traditional wastewater treatment methods represents a significant environmental challenge. **Figure 3.7** summarizes the pathways through which heterocyclic pharmaceuticals are released into the environment, emphasizing their environmental contamination. It focuses on sources and fate, including industrial waste, improper disposal of human and animal waste, and wastewater from domestic use and hospitals.

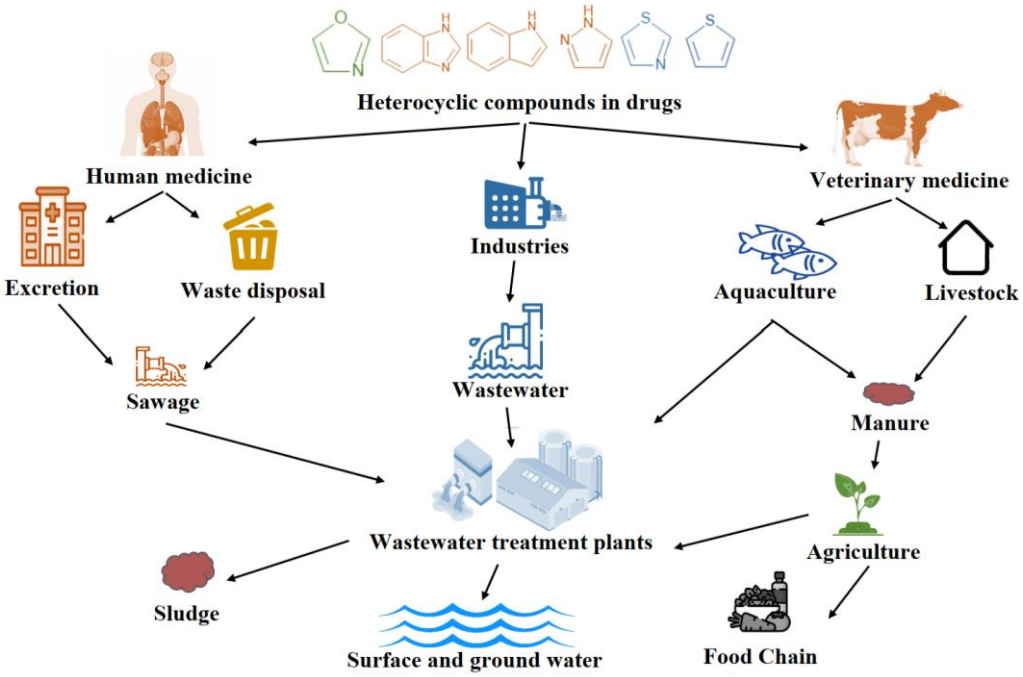

Figure 3.7 *Sources and fate of heterocyclic compounds in drugs into the environment* [199-201].

3.5 Toxicity, Long-Term Risks, and Impacts on Ecosystems of Heterocyclic Pharmaceuticals

Heterocyclic pharmaceuticals are crucial in healthcare due to their therapeutic benefits, significantly enhancing patients' quality of life. However, their extensive use raises environmental concerns, as these compounds exhibit recalcitrance and acute toxicity, as well as mutagenicity, carcinogenicity, teratogenicity, and genotoxicity in various species, including humans [202-204]. The risk escalates as they degrade into more harmful derivatives. These compounds have a strong persistence in environmental matrices, demonstrating high bioavailability and resistance to degradation, which can lead to groundwater contamination and subsequent ecological and human health risks, including aquatic and terrestrial toxicity and biomagnification [207].

Exposure to heterocyclic pharmaceuticals occurs through multiple pathways: water, soil, food ingestion, inhalation, and skin contact, leading to neurotoxicity, genotoxicity, cardiovascular toxicity, and carcinogenic outcomes [208]. Notably, nitrogen or oxygen-containing heterocycles can induce neurotoxicity, while specific compounds like pyrazole and thiophene may result in central nervous system depression, headaches, and other cognitive impairments [197]. DNA damage and mutations arise from genotoxic mechanisms, in which reactive metabolites may bind to DNA, posing long-term health risks due to oxidative stress and disrupted metabolic processes that can lead to insulin resistance and metabolic disorders [209].

Nitrogen-containing heterocycles are particularly hazardous, being classified as human carcinogens by the International Agency for Research on Cancer (IARC) due to their altered toxicological profiles and potential to cause various cancers [209]. Additionally, certain heterocycles can induce developmental defects during pregnancy. Despite their medical benefits, these pharmaceuticals pose significant risks of persistence and bioaccumulation, negatively impacting biological functions [207-208]. **Figure 3.8** summarizes the toxicological effects of these chemicals on human health.

The environmental impact of heterocyclic compounds extends to ecosystems, threatening aquatic life and soil organisms. Their mobility causes long-term harm and chronic toxicity, disrupting reproductive and developmental processes in species such as fish and invertebrates. Studies assessing aquatic toxicity reveal that many heterocycles are "very toxic" to freshwater organisms, with EC50 values indicating acute dangers [211]. Comparisons of toxicity reveal variations based on the heterocyclic core and haloegens present [212]. The multifaceted toxic effects of heterocycles necessitate robust monitoring and regulatory frameworks to address their environmental fate and health impacts. Ongoing risk assessments are critical for effectively managing the adverse consequences of heterocyclic pharmaceutical residues.

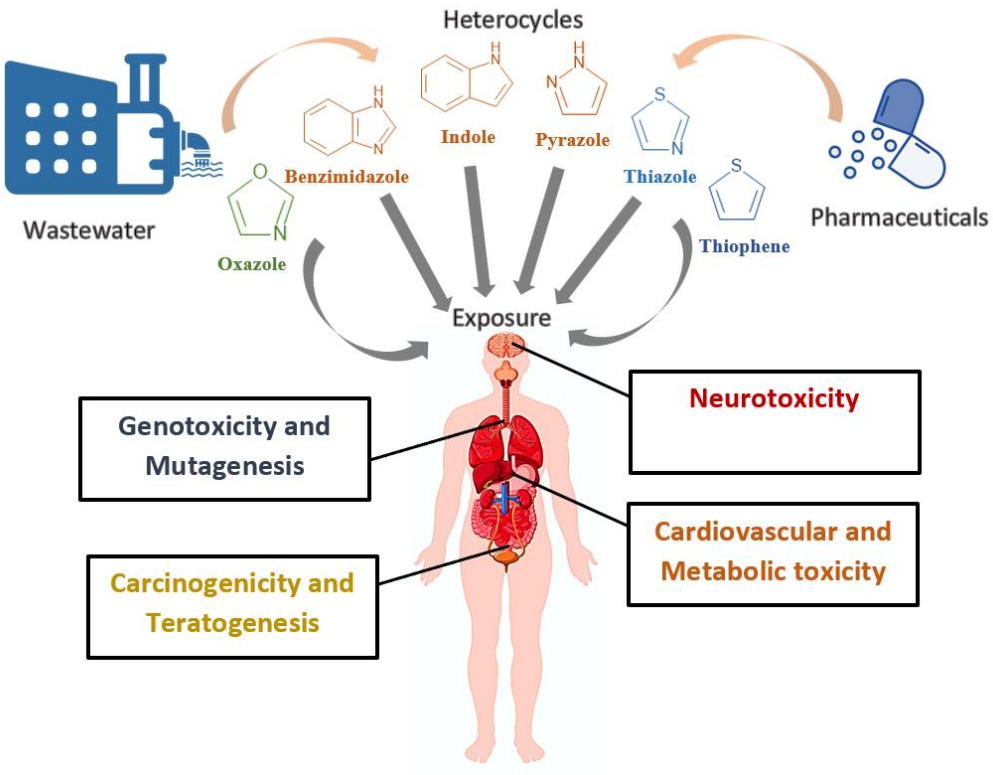

Figure 3.8 *Toxicological impacts of heterocyclic pharmaceuticals on human health.*

3.6 Remediation Technologies and Treatment Solutions for Heterocyclic Pharmaceuticals

Heterocyclic pharmaceuticals present considerable environmental challenges due to their persistence and potential toxicity in aquatic ecosystems. Addressing the ecological risks associated with these pollutants requires a comprehensive approach that includes source reduction, regulatory strategies, public awareness, safe disposal, monitoring methods, analytical detection, and environmental remediation measures [213]. Implementing international regulatory frameworks can help to minimize the release of pharmaceutical heterocycles into the environment and promote sustainable practices [214].

In the analysis and detection of these compounds, methods such as Quantitative Structure-Activity Relationship (QSAR) and Quantitative Structure–Property Relationship (QSPR) are pivotal for predicting risks based on the physicochemical properties of pollutants [215]. Developing sustainable production methods for pharmaceutical heterocycles can enhance remediation [216]. However, the bioactivity of these pharmaceuticals remains a significant concern, especially their long-term effects on health and the environment, due to their limited elimination by conventional WWTPs [217]. This inadequacy has led to the exploration of more efficient treatment systems.

A variety of remediation technologies have been developed to remove these contaminants, including biological treatments, AOPs (such as photo-Fenton and photocatalysis) [218], and filtration techniques [219]. Each method presents distinct advantages and challenges, notably the risk of hazardous by-product formation during photocatalytic degradation, which necessitates further research to understand and mitigate these risks. **Table 3.1** summarizes some relevant findings from the literature on the removal of pharmaceutical heterocyclic compounds. Studies have shown that degradation processes can increase toxicity, underscoring the need for more effective and sustainable degradation strategies. Future research should focus on innovative solutions that not only enhance the removal of heterocyclic compounds but also reduce potential toxicities associated with their degradation, ultimately promoting sustainability in pollution remediation practices.

Table 3.1 *Selected examples of pharmaceutical heterocycle compound removal methods.*

Pharmaceutical Compound	Heterocycle Type	Method Used	Operating Conditions	Efficiency (%)	Ref.
Indomethacin (Anti-inflammatory)	Indole	UV–vis/peroxydisulfate	pH = 7, [IM] = 20 μM and [PDS] = 20 μM	100% in 24 min	[220]

Indomethacin (Anti-inflammatory)	Indole	Adsorption using ACNF/Polypyrrole/MIL-100-Fe composites	[IM] = 1–25 mg/L, pH = 5.0, T = 298 K, adsorbent mass = 0.5 g/L	99.1% in 256 min	[221]
Pindolol (Antihypertensive)	Indole	Membrane filtration (Desal HL thin film composite membrane)	[DOM] = 2 μg/dm^3, Membrane from GE Osmonics, 98% Magnesium sulfate	74%	[222], [223]
Pindolol (Antihypertensive)	Indole	Photodegradation (photolysis)	River water with riverine [DOM] = 20 mg/L, [NO_3] = 1 mM	68% in 42 min	[224]
Telmisartan (Antihypertensive)	Benzimidazole	Photocatalytic Degradation (TiO_2)	UV light, pH 7.0, [TN] = 5.5×10^{-5} mol/L, TiO_2 mass = 20 mg	100% in 180 min	[225]
Albendazole (Antibacterial)	Benzimidazole	UV-C + H_2O_2 process	[ALB] = 1 mg/L, [O_3] = 1.5 mg/L, UV-C = 185/254 nm radiation peaks and incident photon flux Np = 1.033×10^{-6} Einstein/s	>99% in 120 min	[226]
Thiabendazole (Anti-fungal)	Benzimidazole	Cold Atmospheric Plasma	Voltage: 8 kV, Distance: 1 cm, Airflow rate: 0.5 slm	100% detoxification in 20 min	[227]
Sildenafil (Phosphodiesterase type 5 Inhibitor)	Pyrazole	UV/PMS	SWW (pH ±8), [PMS] = 800 μM, [SIL] = 3 mg/L	100% in 130 min	[29]
Sildenafil (Phosphodiesterase type 5 Inhibitor)	Pyrazole	Anaerobic Biological Treatment	Inoculum: Hydrolytic/acidogenic (H/A) and methanogenic (MET), [SIL] = 50 μg/L	43% (H/A inoculum), 41% (MET inoculum)	[228]
Celecoxib (Anti-inflammatory)	Pyrazole	Photochemical, UV Lamp	River water, pH = 7.8, [CLC] = 2.00 μg/L, irradiated UV = 254 nm	100% in 1 week	[229]
Nevirapine (Antiretroviral)	Pyrimidine	Bioremediation by microalgae	Cultivation modes: mixotrophic; pH 7.5; 25 °C,*Tetradesmus obliquus*, mixotrophic cultivation	80.13% in 8 days	[230]

Sulfisoxazole (Antibiotic)	Oxazole	Photodegradation, Fe_3O_4 Nanoparticles	Fe_3O_4 mass 1 g/L, [SSX] 10 mg L^{-1}, irradiated with 150 W UV lamp	60% in 120 min	[231]
Sulfisoxazole (Antibiotic)	Oxazole	Hydrogen-based membrane biofilm reactor	[SSX] = 5 mg/L, HRT: 48 h, 30 °C, Continuous H_2 feeding, H_2 headspace 20 mL	88% in 28 days	[232]
Oxaprozin (Anti-inflammatory)	Oxazole	Electrochemical Anodic Oxidation (Ti/IrO_2 anode)	[OXA] = 203 μmol/L, Current density: 30.25 mA/cm^2, [sodium chloride] = 0.225 mol/L	100% in 4 min	[233]
Olanzapine (Antipsychotic)	Thiophene	Photocatalytic degradation (TiO_2)	[OLA] = 5×10^{-5} mol/L, Solar simulated light (250 and 500 W/m^2), catalyst mass 1.56 g/L	100% in 120 min	[234]
Clopidogrel (Antiplatelet)	Thiophene	Aerobic biodegradation	[CPG] = 25 mg/L, pH: 8.5, Temperature: 30 °C, Mixed bacterial culture (*Pseudomonas aeruginosa* 1 M, *Pseudomonas putida* 5 M)	99.08% in 96 h	[235]
Clopidogrel (Antiplatelet)	Thiophene	Electrochemical advanced oxidation (Electro-Fenton Process)	[CPG] = 0.02 mM, [Fe^{2+}] = 0.7 mM, [Na_2SO_4] = 50 mM, pH = 3, I = 0.55 A and V = 0.3 L	70.4% in 8 h	[236]
Cefixime (Antibacterial)	Thiazole	Photocatalytic Degradation ($Bi_{12}TiO_{20}$)	[CFX] = 10 mg/L, pH = 6, catalyst dosage = 1.5 g/L	94.93% in 180 min	[237]
Thiabendazole (Antifungal)	Thiazole	Adsorption using *Cellana tramoserica* shells modified by copper (CT-Cu)	pH 5, [THB] = 50 mg L^{-1}, Adsorbent mass 20 mg	91% in 120 min	[238]
Nitazoxanide (Antiparasitic)	Thiazole	Photocatalytic Degradation (BiOI/$Bi_4O_5I_2$ heterostructure)	Photocatalyst mass 0.4 mg/L, [NTZ] = 10 mg/L, 150 W mercury lamp (500–550 nm, 7.31–7.53 mW cm^{-2})	100% in 60 min	[239]

3.7 Conclusions and Perspectives

Heterocyclic pharmaceutical pollutants pose a significant environmental threat due to their toxic and carcinogenic properties, their widespread use in medical therapies (accounting for over 90% of new medications), and their persistence in the environment. This contribution examines the sources, environmental fate, toxicity, and long-term risks of these compounds, and proposes potential remediation strategies. It provides an overview of the various types of heterocyclic pharmaceuticals, focusing on common heteroatoms such as nitrogen, oxygen, and sulfur, and explores their pathways into ecosystems through wastewater discharge, agricultural runoff, and improper disposal, highlighting their resistance to biodegradation and tendency for bioaccumulation.

The contribution also addresses the adverse health effects associated with these compounds, including neurotoxicity, genotoxicity, cardiovascular toxicity, carcinogenicity, and teratogenesis. To mitigate their environmental impacts, several remediation techniques are discussed, such as biological treatment, AOPs, and membrane filtration technologies suitable for wastewater treatment. The conclusion emphasizes the urgent need for continued research to develop effective strategies to reduce the toxicity of heterocyclic pharmaceuticals and prevent the formation of hazardous by-products, and recommends adopting combination approaches to enhance effectiveness.

Furthermore, the contribution highlights issues of global health and environmental justice, noting that marginalized communities often bear a disproportionate burden of pollution, thereby complicating potential solutions. It advocates implementing robust international regulations governing the production, use, and disposal of heterocyclic pharmaceuticals, alongside public awareness campaigns about the associated risks. Promoting responsible consumption and encouraging green chemistry practices in the pharmaceutical industry, with a focus on designing safer compounds, is also critical. Finally, continuous innovation in wastewater treatment technologies, including the exploration of nanomaterial-based solutions, will be essential for effectively addressing the environmental challenges posed by heterocyclic pharmaceutical pollutants.

The results presented in this contribution were published in the journal *Organics* (https://doi.org/10.3390/org6010001) and were selected as an Editor's Choice article.

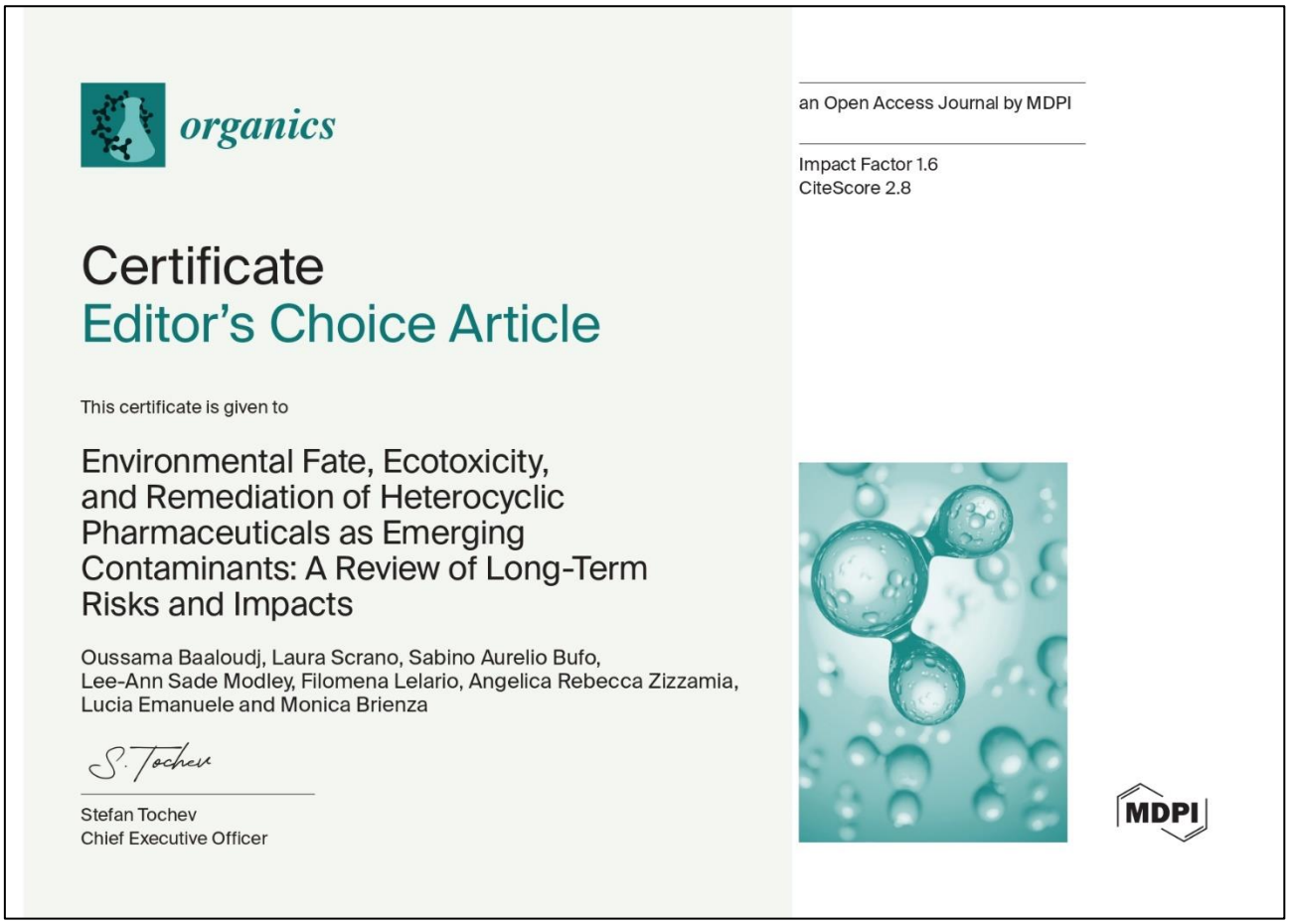

organics

an Open Access Journal by MDPI

Impact Factor 1.6
CiteScore 2.8

Certificate
Editor's Choice Article

This certificate is given to

Environmental Fate, Ecotoxicity, and Remediation of Heterocyclic Pharmaceuticals as Emerging Contaminants: A Review of Long-Term Risks and Impacts

Oussama Baaloudj, Laura Scrano, Sabino Aurelio Bufo, Lee-Ann Sade Modley, Filomena Lelario, Angelica Rebecca Zizzamia, Lucia Emanuele and Monica Brienza

S. Tochev

Stefan Tochev
Chief Executive Officer

MDPI

Overall, heterocyclic compounds play a crucial role in modern pharmacology due to their structural diversity and widespread use in therapeutic agents. In this context, SILD was selected as a representative compound to investigate its removal from aqueous matrices through AOPs, with particular focus on the phototransformation pathways and the identification of potentially toxic degradation products (Chapter 4).

4. CONTRIBUTION 2

Efficient Photooxidation Processes for the Removal of Sildenafil from Aquatic Environments: A Comparative Study

4.1 Abstract

SILD has gained considerable attention due to its widespread legal and illegal use, including increasing recreational use among young people. Its high stability and persistence in aquatic environments, along with the formation of potentially harmful phototransformation products, pose risks to human health and ecosystems. This study evaluated photooxidation processes for removing SILD and its derivatives from water. DW and SWW were treated using three oxidants: PS, PMS, and H_2O_2 and a TiO_2 catalyst. Potential transformation products were assessed and tentatively identified using LC-ESI-MS and MS^n. The Sunlight/PMS system proved most effective, achieving complete degradation in DW after 80 minutes and in SWW after 130 minutes. Toxicity tests with *Vibrio fischeri* showed that the resulting products were non-toxic. These findings highlight Sunlight/PMS photooxidation as a promising and environmentally friendly method for mitigating SILD contamination.

4.2 Introduction

Phosphodiesterase type-5 inhibitors are a primary therapeutic option for ED. According to the USD FDA, the four most widely used and approved PDE-5i are sildenafil (Viagra®), tadalafil (Cialis®), vardenafil (Levitra®), and avanafil (Spedra®) [240]. SILD is commercially available as the citrate salt of sildenafil ($C_{22}H_{30}N_6O_4S \cdot C_6H_8O_7$, **Figure 4.1**).

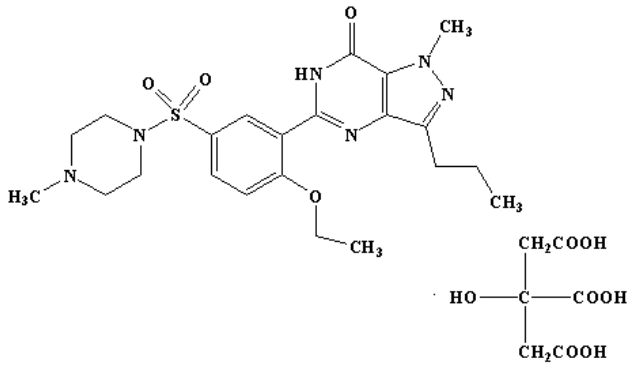

Figure 4.1 *Molecular structure of sildenafil citrate ($C_{22}H_{30}N_6O_4S \cdot C_6H_8O_7$).*

In recent years, SILD has received significant attention from the scientific community due to its high consumption and increasing detection in environmental matrices, particularly in wastewater [241]. These substances, classified as ECs, reach WWTPs in metabolized or

unmetabolized forms. Once released into the environment, these molecules undergo various abiotic (e.g., photolysis, hydrolysis) and biotic (e.g., biodegradation) processes, generating transformation products that may be more persistent or more toxic than the parent compound. Several studies have revealed potential toxic effects of SILD and its metabolites on aquatic organisms [242]. Although the predicted no-effect concentration (PNEC) has been estimated at 640 ng L^{-1} [243], further research is needed to fully assess environmental risks, particularly given unknown loads from non-prescribed use.

However, many such compounds are resistant to conventional activated-sludge treatments and pass through to surface waters, where they may accumulate at concentrations ranging from ng L^{-1} to μg L^{-1} [244]. For this reason, despite increasing awareness of WWTP limitations [245], many pollutants, including SILD, are insufficiently removed. Consequently, AOPs have been extensively studied as promising technologies for eliminating recalcitrant organic contaminants [58, 246].

Several studies have examined the photochemical degradation of SILD. Eichhorn et al. (2012) investigated the photolysis of SILD and its metabolite N-demethylsildenafil under simulated Sunlight and proposed potential intermediates and transformation products [247]. Herbert et al. (2015) confirmed similar results, observing Sunlight-induced degradation of SILD and vardenafil [248]. Medana et al. (2011) applied a TiO_2/Sunlight photocatalytic system to produce chemically modified products resembling those generated by equine metabolism, identifying key intermediates and proposing a degradation pathway [249]. These findings are relevant to the present study, as photocatalysis involves the formation of hydroxyl radicals, a mechanism also active in solar photodegradation systems using TiO_2 or hydrogen peroxide. Among AOP technologies, sulfate-radical-based processes, driven by PMS or PS, remain comparatively underexplored for SILD degradation.

Evaluating advanced treatments requires integrating chemical analysis with toxicity assessment to provide a comprehensive evaluation of water quality after purification [250]. Accordingly, various acute and chronic toxicity bioassays for aquatic organisms have been developed [251]. For analytical identification of SILD and its degradation products, high-performance liquid chromatography coupled with mass spectrometry is the preferred technique [41, 248].

This study investigates the effectiveness of several AOPs for removing SILD from aqueous solutions. Specifically, we examined solar phototransformation in DW and SWW in the presence of PMS, PS, H_2O_2, and TiO_2, with emphasis on identifying potentially toxic phototransformation products. LC–ESI–MS and MS^n were used to detect and characterize

SILD and its degradation products, while *Vibrio fischeri* bioluminescence assays were used to assess the ecotoxicity of transformation mixtures.

4.3 Materials and methods

4.3.1 Chemicals

The standard sildenafil (Certified Reference Material), potassium peroxymonosulfate (PMS, available as the triple potassium salt $KHSO_5 \cdot 0.5\ KHSO_4 \cdot 0.5\ K_2SO_4$ under the trade name of Oxone®), sodium persulfate (PS, reagent grade ≥ 98%), and hydrogen peroxide (H_2O_2, 30%) were purchased from Sigma Aldrich (St. Louis, USA). All chemicals were used as received without further purification. For heterogeneous photocatalysis, TiO_2 (Degussa P-25) was obtained as a gift from Evonik (Hanau, Germany). All the aqueous solutions were prepared with a Milli-Q grade ultrapure water system produced using a Milli-Q RG system from Millipore (Bedford, MA, USA).

The exact composition of SWW is as follows: $NaHCO_3$ (96 mg L^{-1}), NaCl (7 mg L^{-1}), $CaSO_4 \cdot 2H_2O$ (60 mg L^{-1}), urea (6 mg L^{-1}), $MgSO_4$ (60 mg L^{-1}), KCl (4 mg L^{-1}), K_2HPO_4 (0.28 mg L^{-1}), $CaCl_2 \cdot 2H_2O$ (4 mg L^{-1}), peptone (32 mg L^{-1}), and $MgSO_4 \cdot 7H_2O$ (2 mg L^{-1}) [252].

4.3.2 Experimental devices for oxidation processes

The photocatalytic experiments were conducted in a 250 mL cylindrical reactor covered with a quartz plate and placed inside a solar simulator (Heraeus-Atlas Suntest CPS+, Chicago, USA). The simulator was equipped with a 1.8 kW xenon arc lamp, providing an irradiance of 400 W m-2 over the spectral range of 290–800 nm. The reaction temperature was maintained at 26 ± 0.1 °C using an air-conditioning system, and the solutions were continuously stirred to ensure homogeneous mixing. Due to the quartz filter protecting the lamp and the filtration effect of the borosilicate reactor, the effective irradiation spectrum reaching the samples ranged from 300 to 580 nm.

Degradation experiments under Sunlight alone and in combination with PMS, PS, H_2O_2, and TiO_2 were performed to evaluate the effectiveness of AOPs in removing SILD and its transformation products from aqueous matrices. Parallel tests were also conducted in the dark under identical conditions to determine whether any degradation could be attributed to hydrolysis rather than photochemical processes. All experiments were conducted in triplicate, and irradiation was maintained long enough to ensure the complete disappearance of both SILD and its photoproducts.

All kinetic studies were performed with an initial SILD concentration of 3 mg L^{-1}, whereas experiments aimed at identifying transformation products were carried out at 10 mg

L^{-1}. These tests were conducted in DW and SWW at pH 8, and in buffer solutions at pH 7.3 and pH 5 to assess the influence of pH on degradation.

A 100 mM stock solution of PMS was prepared by dissolving approximately 1.5 g in 50 mL of DW. Similarly, a 100 mM PS stock solution was obtained by dissolving roughly 1.2 g in 50 mL of DW. Hydrogen peroxide solutions were prepared by diluting a 0.98 M stock. For each matrix, oxidation performance was evaluated using H_2O_2, PMS, and PS at concentrations of 400, 800, and 1600 μM, and TiO_2 at 0.2 g L^{-1}. The same PS, PMS, and TiO_2 concentrations were applied in SWW experiments.

Before analysis, samples collected during the photocatalytic treatment were filtered through a 0.2 μm PTFE membrane to remove TiO_2 particles.

4.3.3 Analytical procedures

The degradation profiles of SILD were obtained using an HPLC system (Agilent 1200 series, USA) equipped with a Luna C18 column (150 × 4.6 mm, 5 μm) and a DAD set at 254 nm. Chromatographic separation was achieved using a binary gradient elution consisting of ultrapure water containing 0.1% formic acid (solvent A) and acetonitrile (solvent B). The gradient program was as follows: 0–3 min, 20% B; 3–7 min, linear increase from 20% to 60% B; 7–13 min, 60% B; 13–15 min, ramp to 100% B; 15–20 min, 100% B; 20–22 min, decrease to 20% B; and 22–25 min, hold at 20% B. The flow rate was maintained at 0.800 mL min^{-1}, with an injection volume of 20 μL.

Mass spectrometric analyses were performed in positive-ion mode over an *m/z* range of 90–1200 using an LC system coupled to an LTQ mass spectrometer (Thermo Fisher Scientific, Bremen, Germany). Separation was performed on the same Luna C18 column under the described gradient conditions, operating at a flow rate of 0.8 mL min^{-1} with a post-column split ratio of 3:1.

Low-resolution MS^n experiments were conducted using CID. Mass spectra were processed and visualized using SigmaPlot 10.0 (Systat Software, Inc., London, UK), while chemical structures of detected compounds were illustrated using ChemDraw Ultra 12.0 (CambridgeSoft Corporation, Cambridge, MA).

A calibration curve for SILD quantification was constructed by injecting standard solutions ranging from 0.25 to 10 mg L^{-1} and fitting the resulting chromatographic data. The method exhibited a limit of detection (LOD) of 0.1 mg L^{-1} and a limit of quantification (LOQ) of 0.3 mg L^{-1}.

4.3.4 Toxicity tests

Toxicity assays using *Vibrio fischeri* were performed by exposing the bacteria to the test samples in microplate wells and measuring their response after 5, 10, and 30 minutes of contact. Three types of samples were evaluated: a non-irradiated control, a mixture containing SILD along with the maximum number of photoproducts generated during the investigated processes, and a fully photodegraded sample in which neither SILD nor its photoproducts were detected.

4.4 Results and discussion

4.4.1 Degradation tests

A comparison of the degradation profiles (**Figure 4.2**) indicates that SILD undergoes faster photolysis in DW than in buffered solutions. In DW, its concentration decreases rapidly, reaching 50% removal in approximately 90 minutes and becoming non-quantifiable after roughly 240 minutes. Conversely, in phosphate buffer (pH 7.3) and acetate buffer (pH 5), a markedly slower degradation is observed, with half-lives near 350 minutes and only about 80% degradation achieved after more than 420 minutes. In SWW, negligible SILD degradation is detected even after 6 hours of irradiation.

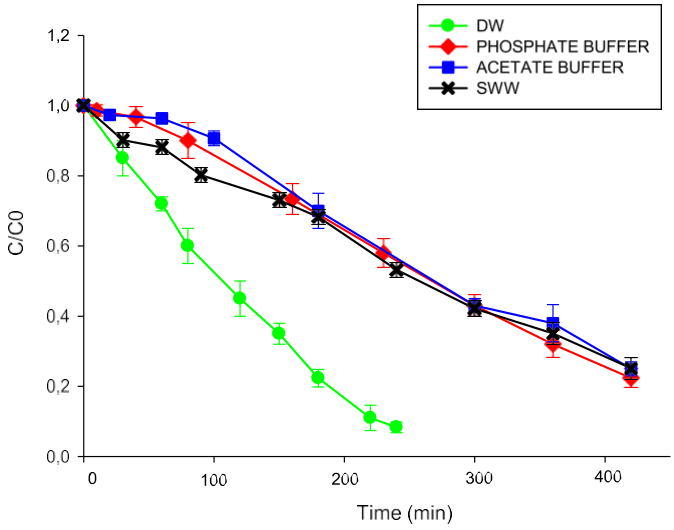

Figure 4.2 *Degradation curves of SILD subjected to photolysis in solutions with different pH: DW (pH 6), phosphate buffer (pH 7.3) and acetate buffer (pH 5), and SWW (pH ~8); C = concentration at time t, Co = initial concentration (3 mg L^{-1}).*

The strong resistance to degradation in SWW is likely attributable to dissolved ionic species, which may inhibit photochemical reactions by reducing SILD's effective absorption of incident radiation [248].

In the heterogeneous photocatalysis experiment with TiO_2, the initial step involved stirring the TiO_2 suspension in the dark for more than 24 hours. Under these conditions, the

concentration of SILD remained essentially unchanged, confirming that neither hydrolysis nor adsorption of the compound onto the TiO_2 surface occurred. Subsequently, a 3 mg L^{-1} SILD solution was irradiated in the presence of a 0.2 g L^{-1} TiO_2 suspension under continuous magnetic stirring. The photocatalytic process resulted in a rapid degradation of the molecule, with a half-life of approximately 50 minutes, consistent with previously reported data [249]. As shown in **Figure 4.3**, SILD concentrations fell below the LOD after roughly 120 minutes of irradiation. Under the same conditions in SWW, degradation reached about 80% after 120 minutes. The characteristic parabolic shape of the photocatalytic degradation curves reflects an initial adsorption step that does not significantly hinder the availability of SILD for rapid photoreaction.

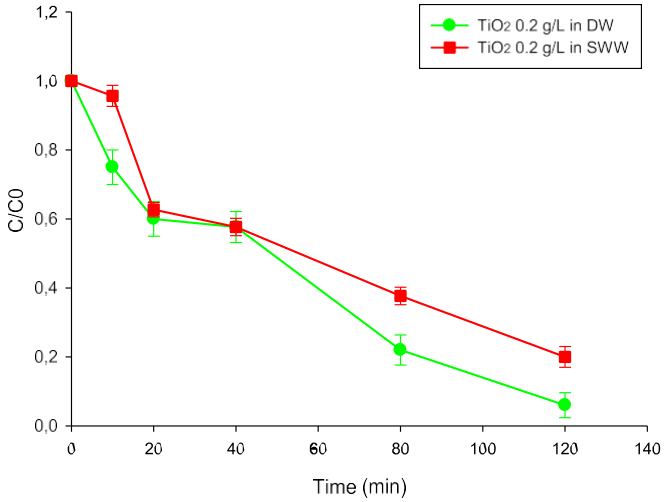

Figure 4.3 *Photodegradation curves of SILD in DW and SWW in the presence of the catalyst TiO_2 (data shown based on three replicates).*

As an effective, low-cost, and environmentally compatible alternative to TiO_2-based photocatalysis, photodegradation processes employing oxidants such as H_2O_2, PS, and PMS have gained increasing attention in recent years. Unlike heterogeneous photocatalysis, these processes do not require a catalyst recovery step. Despite differences between the methods, some of them substantial, the common feature is the *in situ* generation of reactive radical species capable of degrading oxidizable organic contaminants, including many emerging pollutants.

It is important to note that both the initial pollutant concentration and the amount of oxidant strongly influence the formation of reactive species. For this reason, the experiments in this study were performed at a constant SILD concentration (3 mg L^{-1}), while the concentrations of the three oxidants were varied between 100 and 1600 µM. All processes showed maximum efficiency at an oxidant concentration of 800 µM, although even 100 µM was sufficient to achieve partial degradation of SILD and its photoproducts. **Figure 4.4** shows the degradation curves of SILD obtained during photodegradation experiments conducted with 800 µM

solutions of H_2O_2, PS, PMS, and with a PS + PMS mixture (400 µM each). At this oxidant concentration, PMS demonstrated the highest efficiency in degrading SILD. Its half-life was below 50 minutes, and more than 90% of the compound was degraded within approximately 80 minutes. The performance of PS at 800 µM was comparable to that of the PS + PMS mixture.

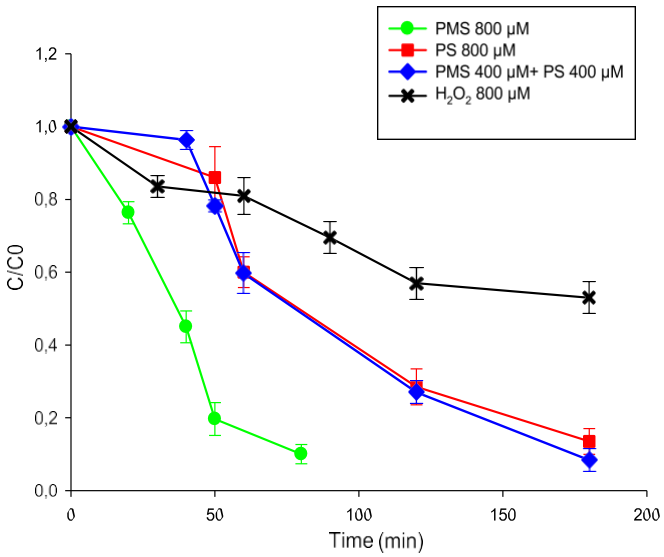

Figure 4.4 *SILD degradation curves under Sunlight/PMS, Sunlight/PS, Sunlight/(PMS+PS), and Sunlight/H_2O_2 systems.*

Figure 4.5 displays the chromatograms of selected samples collected during the photolysis experiments in DW **(a)**, in the presence of 800 µM PMS **(b),** and under dark conditions **(c)**. Under these conditions, the peaks corresponding to SILD and its main transformation product, N-oxide sildenafil, which elutes immediately after SILD, rapidly decreased between the 60 min and 90–120 min samples. During the Sunlight/PMS experiment, both oxidation and photooxidation reactions occur simultaneously, and the observed removal efficiency results from their combined effects. The most effective system was Sunlight/PMS at 800 µM (**Figure 4.5 (b)**). In comparison, heterogeneous photocatalysis with TiO_2 showed slightly lower degradation efficiency and requires an additional filtration step for catalyst removal. **Figure 4.5 (c)** shows that in the dark experiment with PMS (800 µM)**,** SILD was quantitatively converted to its N-oxide, an inactive metabolite and one of its well-known photoproducts [247]. No significant degradation of SILD was observed in the dark experiments with PS or H_2O_2.

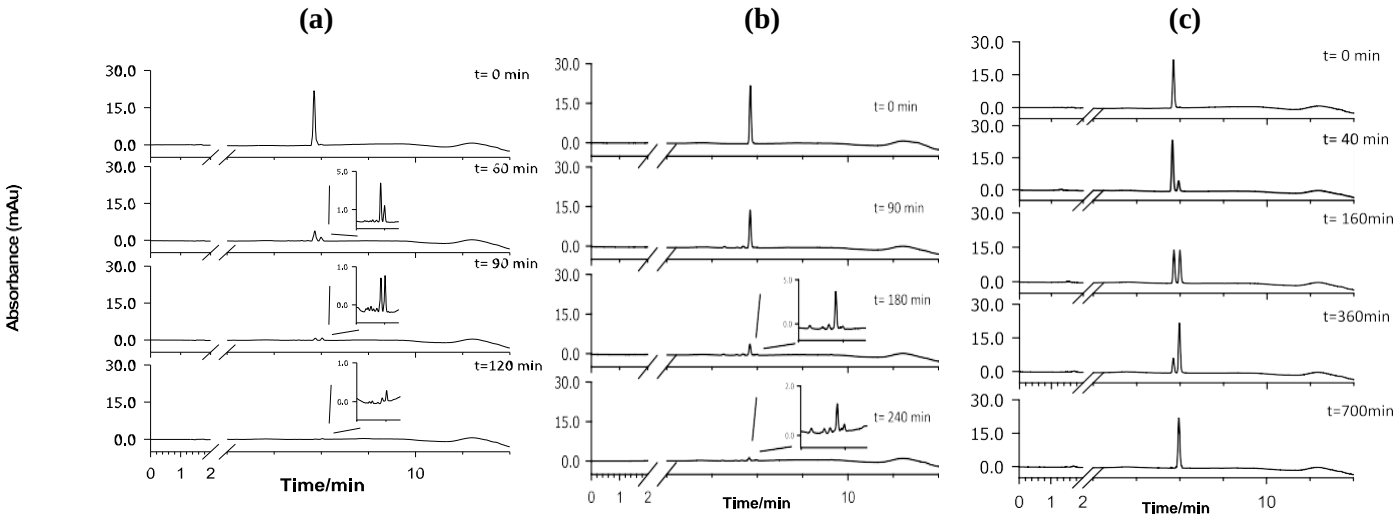

Figure 4.5 *Chromatograms of a 3 mg L^{-1} SILD solution at different times of degradation by Sunlight* **(a)**, *Sunlight/PMS 800 µM* **(b),** *and PMS 800 µM* **(c)**.

Further photodegradation tests were conducted in SWW until SILD was completely removed. Among the oxidizing agents tested, PMS at 800 µM proved far more efficient than PS at the same concentration. **Figure 4.6** shows that in the presence of 800 µM PMS, SILD became undetectable after 130 minutes, whereas complete degradation by 800 µM PS required 430 minutes. In the same timeframe, only about 70% of SILD was degraded using H_2O_2. Although the composition of SWW may have influenced these experiments, the results are consistent with those obtained in DW and confirm PMS as the most effective oxidant among the three tested.

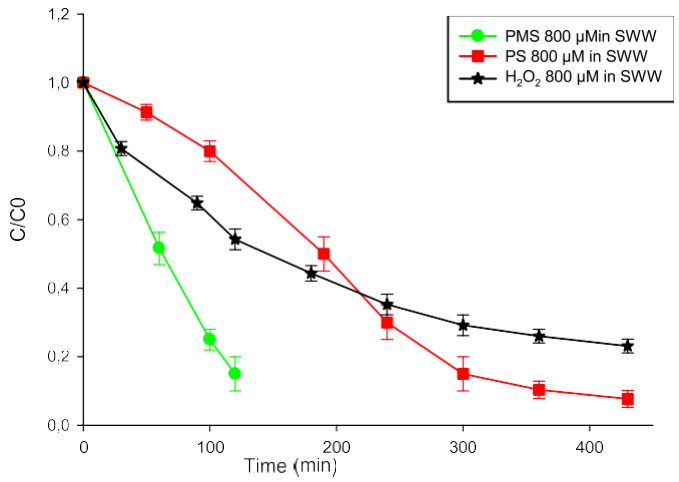

Figure 4.6 *SILD degradation curves in SWW subjected to photodegradation in the presence of 800 µM PMS, 800 µM PS, and 800 µM H_2O_2.*

4.4.2 Characterization of sildenafil and its photoproducts by LC-ESI-LTQ-MS and CID-MS^n

Retention time (t_r) and UV spectra alone are insufficient for the unambiguous identification of constituents in complex systems, particularly for unknown compounds. Therefore, part of this study focused on LC–ESI–MS analysis in an LTQ operating in full-scan mode with positive ionization, to investigate SILD and its photoproducts formed during photolysis and photocatalysis. MS^n experiments were also conducted to examine fragmentation patterns and provide additional structural information.

The MS^n spectra of the $[M+H]^+$ ion of SILD (*m/z* 475, $C_{22}H_{30}N_6O_4S$), obtained at collisional energies of 20–35% of the instrument maximum, are shown in **Figure 4.7**. As illustrated in **Figure 4.7 (a)**, fragmentation of the molecular ion produced ten major fragment ions at *m/z* 475, 447, 391, 377, 329, 313, 311, 299, 283, and 163. The most intense peak at *m/z* 377 ($[C_{17}H_{20}N_4O_4S + H]^+$) corresponds to the neutral loss of 98 Da, attributable to the cleavage of the methylpiperazine group ($C_5H_{10}N_2$) via the labile S–N bond. The identity of this fragment was confirmed through MS^3 of *m/z* 377 and MS^4 of *m/z* 331 (**Figures 4.7 (b)** and **4.7 (d)**), which generated characteristic secondary fragments. The MS^3 spectrum of *m/z* 311 (**Figure 4.7 (c)**) and the MS^4 spectrum of m/z 283 (**Figure 4.7 (e)**) indicate that the fragment at *m/z* 311 arises from C–S bond cleavage, while the fragment at *m/z* 283 results from the loss of the ethyl group on the phenyl ring's ethoxy substituent. These findings are consistent with Eichhorn et al. (2012), who identified these ions as lacking the piperazine and sulfonamide groups, with *m/z* 313 also originating from C–S bond cleavage [247].

Notably, fragments at *m/z* 311, 299, and 283 are common in the mass spectra of most photoproducts in this study and can serve as fingerprints for distinguishing structural modifications in the phenyl pyrazolopyrimidinone moiety from those occurring in the piperazine ring. The complementary ion of *m/z* 311 appears at *m/z* 163, formed by cleavage between the aromatic and sulfonamide groups. The fragmentation of the ion at *m/z* 299 ($C_{15}H_{15}N_4O_3$) is less straightforward but can be attributed to cleavage of the C–O bond in the ethoxy group, accompanied by rearrangement of the sulfonamide moiety, involving migration of an oxygen atom to the aromatic ring and transfer of a hydrogen atom to the departing fragment. A secondary fragmentation pathway of the *m/z* 475 ion involves the neutral loss of 28 Da (CO), producing a less intense fragment at *m/z* 447.

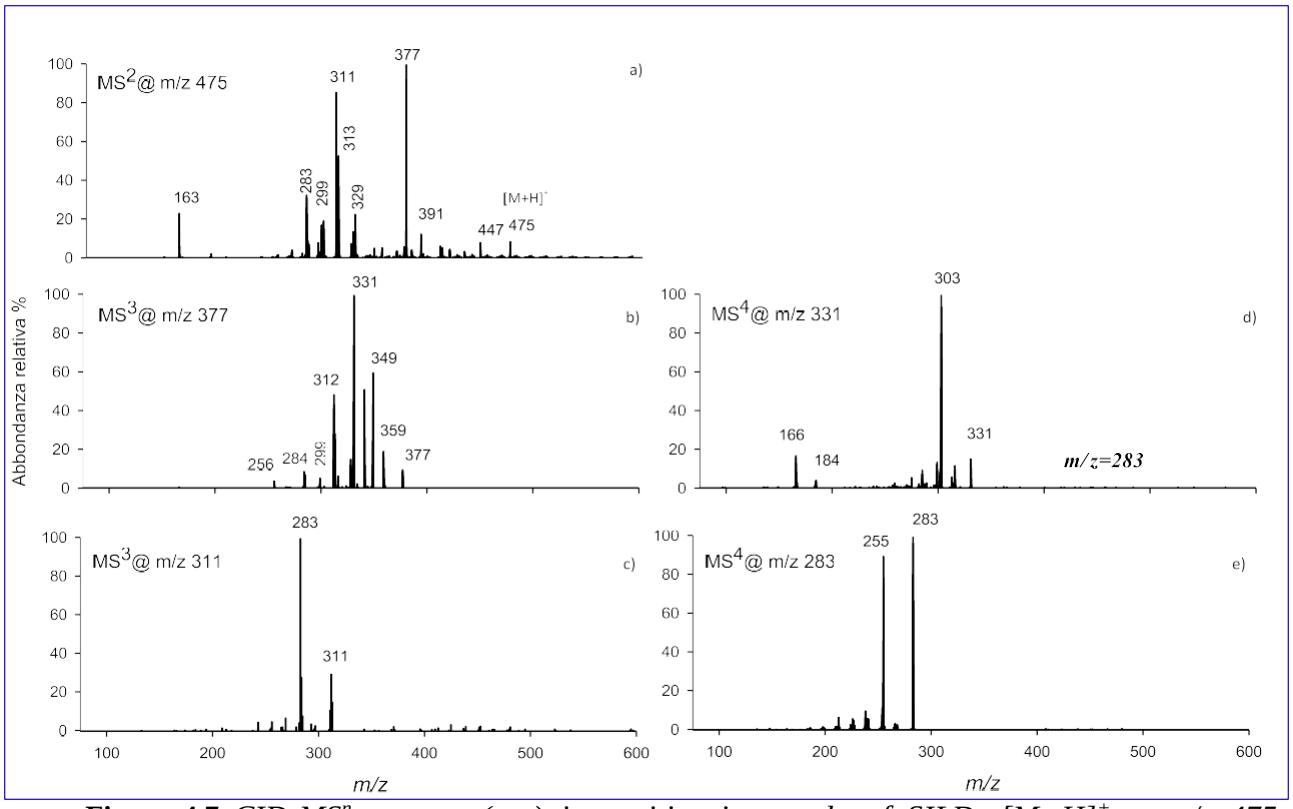

Figure 4.7 *CID-MS^n spectra (**a-e**) in positive ion mode of SILD, [M+H]$^+$ at m/z 475, generated by applying relative collisional energies between 20% and 35%.*

Table 4.1 summarizes the proposed structures of the photoproducts detected in the AOP experiments, along with their corresponding product ions.

Table 4.1 *Main photoproducts detected and corresponding product ions* [247].

Compound	Precursor ion [M+H]$^+$ (*m/z*)	Structure	Main MS/MS product ions (*m/z*)
1	475	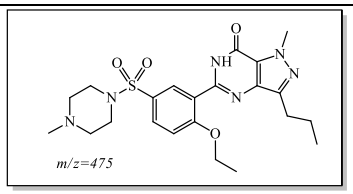	447; 377; 331: 329; 313; 311; 303; 299; 283; 255; 166; 163
2	491	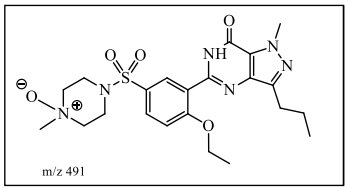	447; 473; 404; 377; 313; 311; 283; 255
3	491	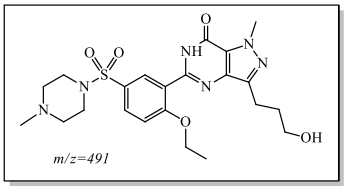	463; 445; 435; 420; 393; 377; 329; 311

4	461	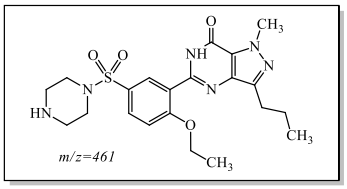	443; 377; 329; 313; 311; 299; 283
5	449	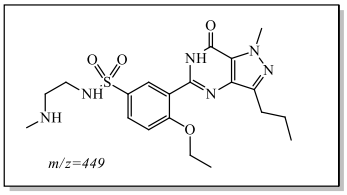	432; 418; 392; 377; 361; 313; 311; 285
6	477	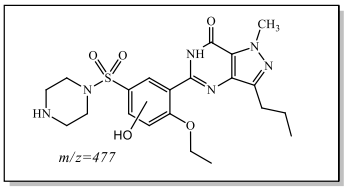	459; 434; 395; 390; 377; 362; 311; 298
7	477	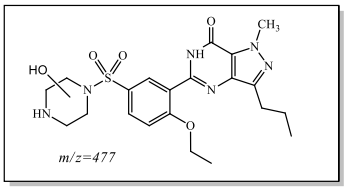	459; 449; 418; 392; 377; 311;
8	505	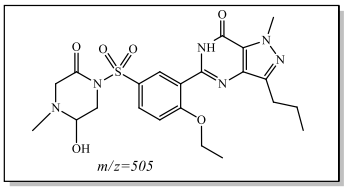	487; 477; 463; 418; 391; 377; 326; 311
9	505	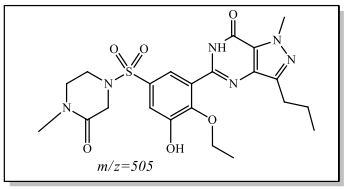	487; 477; 459; 393; 311; 299; 283
10	507	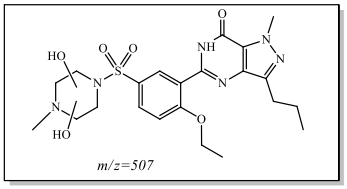	489;461; 447;377; 349
11	507	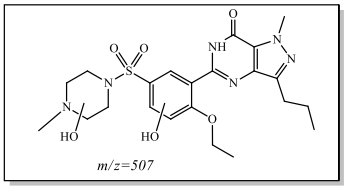	479; 461;395

Two isobaric compounds eluting after SILD were identified with an *m/z* of 491 (compounds 2 and 3, eluting at 8.1 min and 10.4 min, respectively). The 16 Da increase relative to SILD's *m/z* 475 is consistent with the formation of two isomeric hydroxy derivatives. This hypothesis is supported by analysis of the fragments observed in the MS^n spectra. The presence of specific characteristic fragments enables the determination of the OH group's position in

these molecules. Based on the fragmentation pathways and literature data [247], the proposed structures of the photoproducts, along with the most informative fragments identified from their MS^n spectra, are shown in **Figure 4.8**.

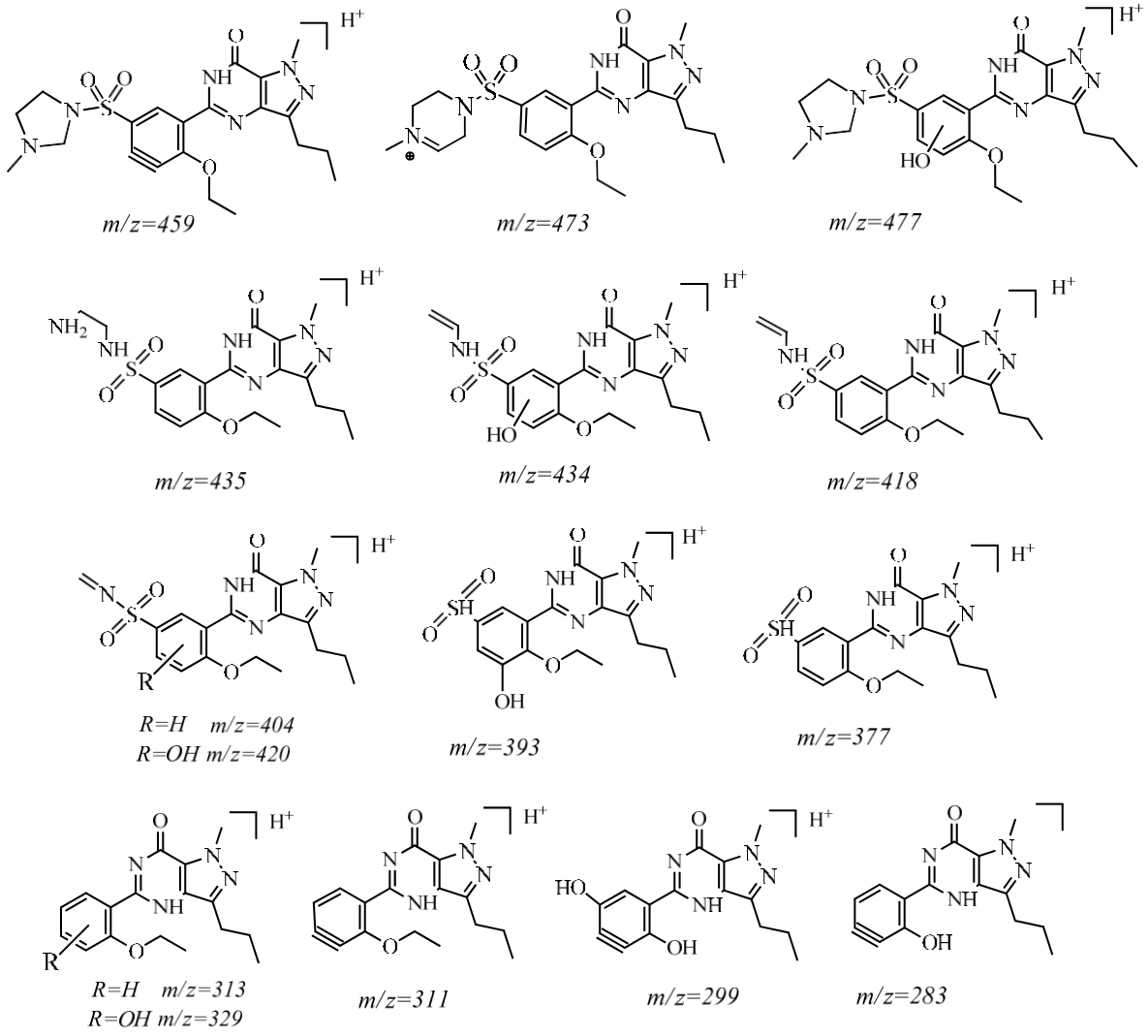

Figure 4.8 *Proposed structures for more informative fragments of photoproducts identified in this study, based on ESI-CID-MS^n spectra.*

According to the literature, several photoproducts identified during SILD photodegradation are also known products of human metabolism [253] and have been observed in in vivo studies in mice and horses [249]. Among these, N-desmethylsildenafil (**Table 4.1**, compound 4) arises from the loss of the methyl group attached to the nitrogen of the piperazine ring. Its MS^2 fragments in positive mode ($[M+H]^+$ at *m/z* 461, retention time 7.7 min) closely resemble those of SILD, supporting the proposed structure [254]. The most relevant ions correspond to cleavage of the piperazine moiety and the C–S bond. The presence of

characteristic peaks at *m/z* 377, 311, 299, and 283 indicates that Sunlight-induced structural modification occurs primarily on the piperazine ring.

Another notable photoproduct elutes at 7.1 min and has a molecular ion at *m/z* 449 (**Table 4.1**, compound 5), analogous to the major human metabolite detected in pharmacokinetic studies and also observed in raw and treated wastewater [249]. Its molecular mass is reduced by 26 Da relative to SILD, consistent with dealkylation (loss of C_2H_2). The MS^2 spectrum shows two characteristic ions at *m/z* 311 and 313, reflecting modification of the piperazine ring, while the base peak at *m/z* 418 and the peak at *m/z* 392 correspond to cleavage of the piperazine ring followed by neutral losses of NH_2CH_3 (31 Da) and C_2H_2 (26 Da). The MS^3 spectrum of *m/z* 418 further confirms the proposed structure, producing three intense ions at *m/z* 377, 361, and 311.

Table 4.1 also reports the fragments of two other isobaric photoproducts at *m/z* 477, eluting at 7.4 and 10.0 min (compounds 6 and 7). MS^2 analysis of the 7.4 min compound indicates that the Sunlight-induced structural change does not involve the piperazine ring. The key fragment is the one at *m/z* 434 (**Figure 4.8**), which is not present in the spectrum of the other compound at *m/z* 477, which elutes at 10 min, where instead the fragment appears at *m/z* 418. Both fragments result from cleavage of the piperazine ring with loss of a neutral 31 Da fragment (NH_2CH_3), but the 16 Da difference is due to the presence of an additional OH group in the 7.4 min compound.

Two other photoproducts, with protonated ions at *m/z* 505 ($C_{22}H_{29}N_6O_6S$) and a mass increase of 30 Da relative to SILD, are consistent with a combination of double hydroxylation and oxidation, forming a ketone group (**Table 4.1**, compounds 8 and 9). MS^2 (505) and MS^3 (418) spectra of compound 8 show characteristic SILD fragments at *m/z* 283, 311, 377, and 418 arising from loss of the piperazine moiety, indicating that both hydroxylation and oxidation involve the piperazine ring. The base peak at *m/z* 487 corresponds to loss of H_2O from the same ring.

In contrast, MS^2 (505) and MS^3 (459) spectra of compound 2 exhibit more intense fragments at *m/z* 459, corresponding to simultaneous loss of H_2O and CO, at *m/z* 393 due to cleavage of the ketopiperazine ring, and at *m/z* 477 due to CO loss associated with piperazine ring cleavage. Additionally, the presence of an ion at *m/z* 416 indicates the presence of a hydroxyl group on the aromatic ring.

Less intense but detectable in the mixture of photoproducts eluting before SILD, two isobaric compounds with $[M+H]^+$ at *m/z* 507 were observed, consistent with double hydroxylation of SILD. The proposed structures and fragmentations of these compounds, which

elute at 7.2 min and 7.7 min, are shown in **Table 4.1** (compounds 10 and 11) and have not been previously reported.

Compound 11 (t_r = 7.2 min) exhibits a fragmentation pathway similar to N-oxide sildenafil, producing fragments at *m/z* 479, 461, and 395, corresponding to the loss of CO, two H_2O molecules, and S–N bond cleavage with loss of the hydroxylated piperazine ring and formation of a sulfonic acid (**Figure 4.8**). These fragments indicate the presence of hydroxyl groups on both the piperazine ring and the aromatic moiety. The low intensity of this peak prevented acquisition of the MS^3 spectrum.

For compound 10 (t_r = 7.7 min), both MS^2 and MS^3 (*m/z* 489) spectra were obtained. The base peak at *m/z* 377 confirms the presence of two hydroxyl groups on the piperazine ring. Subsequent losses of H_2O (–18 Da) and CO (–28 Da), producing fragments at *m/z* 489 and 461, analogous to *m/z* 459, and contraction of the piperazine ring, further support this assignment. Additionally, the MS^3 peak at *m/z* 325 (data not shown) is consistent with a fragment analogous to SILD at *m/z* 299 plus a C_2H_2 group, likely resulting from sulfonamide rearrangement with oxygen transfer to the aromatic ring and hydrogen migration to the leaving group. All other photoproducts identified in this study have been previously reported [247, 253-254].

The photodegradation results demonstrate that the piperazine ring is highly susceptible to hydroxyl radical attack and readily degraded under simulated radiation. Importantly, under the experimental conditions used, and likely in natural aquatic environments, SILD, by the action of Sunlight, undergoes reactions partially analogous to human metabolism. Several human metabolites result from oxygenation and N-dealkylation of the piperazine ring, yielding structures similar to some of the observed photoproducts. These findings highlight the significance of studies aimed at removing SILD and its by-products released into the environment through wastewater discharges [35].

4.4.3 Toxicity tests

In this study, the ecotoxicity of SILD and its transformation products in the aquatic environment was evaluated using the Microtox® toxicity test. This assay provides a rapid method for determining the acute toxicity of aqueous samples by measuring the reduction in light emission from the luminescent bacterium *Vibrio fischeri*. Because light production is directly proportional to the bacterial metabolic activity, any inhibition of enzymatic processes results in a corresponding decrease in luminescence. Microtox® tests with *V. fischeri* are widely applied in ecotoxicology due to their high reproducibility and sensitivity to a broad range of contaminants [255]. In the presence of toxic agents, the natural bioluminescence of *V. fischeri*

decreases, and toxicity is expressed as an EC_{50} value calculated according to ISO 11348-3 standard procedures [256-257].

Table 4.2 reports the percentage inhibition (I%) values measured after 5, 15, and 30 minutes of exposure. Tests were performed on a freshly prepared aqueous SILD solution (T_0), on samples irradiated for 120 and 300 minutes (T_{120} and T_{300}, respectively), and on SILD solutions containing 800 μM PMS after 0, 40, and 100 minutes of irradiation.

Table 4.2 *Results of the Vibrio fischeri acute toxicity test* [256] *after 5, 15, and 30 minutes of contact with aqueous SILD samples photodegraded under light irradiation without oxidant or in the presence of PMS 800 μM.*

	Percentage inhibition *I%*		
SAMPLES	**5 min**	**15 min**	**30 min**
SILD 3mg/L T_0	19.4%	22.55%	23.1%
SILD 3 mg/L T_{120}	15.24%	15.37%	15.68%
SILD 3 mg/L T_{300}	13.67%	14.97%	15.62%
SILD 3mg/L + PMS 800 μM T_{PMS-0}	19.4%	22.55%	23.1%
SILD 3mg/L + PMS 800 μM T_{PMS-40}	16.5%	16.6%	16.7%
SILD 3mg/L + PMS 800 μM $T_{PMS-100}$	12.1%	12.2%	12.4%

Percentage inhibition *I%*	***EC*$_{50}$**	[a]**Judgment**
<20%		Absence of acute toxicity
>=20% < 50%		Weakly toxic
>=50%	100–10	Toxic
>50%	<10-1	Very toxic
>50%	<1	Extremely toxic

[a] Toxicity legend table according to UNI EN ISO 11348–3:2009.

The ecotoxicity results show low toxicity for the fresh SILD solution (T_0) after 15 and 30 minutes of exposure to *V. fischeri*. In contrast, the T_{120} sample, corresponding to the point at which the highest number of photoproducts is present, exhibits significantly higher toxicity, and the T_{300} sample, collected at the end of the degradation process when neither SILD nor its photoproducts were detectable, does not show acute toxicity.

Similar results were obtained for the Sunlight/PMS system: the samples collected at 40 minutes (T_{40}) and 100 minutes (T_{100}) also showed no acute toxicity. The progressive decrease in V. fischeri bioluminescence inhibition during irradiation further confirms the effectiveness of the proposed photodegradation processes.

An *in silico* toxicological assessment was also performed to evaluate SILD and its photoproducts using structure–toxicity relationships. The ECOSAR program was employed to estimate acute toxicity (LC_{50}) toward daphnids after 48 hours of exposure [258]. Preliminary results (data not shown) indicate that only SILD itself and two photoproducts, those with *m/z* 461 and *m/z* 449, are potentially toxic.

4.5 Conclusions and future perspectives

This study evaluated the performance of different photooxidation processes for the degradation of SILD, a pharmaceutical compound of growing environmental concern. Although simulated solar irradiation showed limited effectiveness, both Sunlight/TiO_2 and Sunlight/oxidant systems produced promising results. Among them, the Sunlight/PMS system proved to be the most efficient, achieving complete degradation of SILD in DW within 80 minutes and in SWW within 130 minutes. These findings highlight the strong potential of Sunlight/PMS photooxidation as a viable treatment technology for SILD removal.

LC-LIT-MS analyses confirmed the formation of several photoproducts, some structurally similar to human SILD metabolites, underscoring the need to assess their environmental relevance. Nevertheless, ecotoxicity tests using *Vibrio fischeri* verified the overall environmental safety of the proposed remediation strategy. Collectively, the results support the development of sustainable and effective approaches to reduce the environmental load associated with SILD contamination.

Future work should aim to optimize the Sunlight/PMS system by identifying more environmentally friendly catalysts and developing efficient, cost-effective recovery and disposal strategies.

The results presented in this contribution were published in the journal *Case Studies in Chemical and Environmental Engineering* (https://doi.org/10.1016/j.cscee.2024.100708).

In addition to photochemical methods, electrochemical approaches have proven effective alternatives for removing VFX from water. Techniques such AO processes operate under milder conditions (e.g., ambient temperature and pressure) and require fewer chemical reagents, enabling simpler, more controllable treatment systems. Furthermore, electrochemical processes often achieve high removal efficiencies with limited formation of secondary pollutants and can be optimized by adjusting key parameters such as current density, electrode material, and pH. Overall, their operational flexibility and environmental compatibility make them a promising option for VFX removal from aqueous environments. (Chapter 5).

5. CONTRIBUTION 3

Electrochemical degradation of venlafaxine on platinum electrodes: identification of transformation products by LC-MS/MS and *in silico* ecotoxicity assessment

5.1 Abstract

Antidepressants such as VFX have become ECs of global concern due to widespread use and misuse. VFX, a serotonin–norepinephrine reuptake inhibitor, can cause adverse and potentially toxic effects on aquatic organisms. EAOPs are increasingly explored as effective methods for degrading pharmaceutical pollutants. Most EAOP studies on VFX use boron-doped diamond (BBD) anodes, valued for their low background current and high oxygen overpotential. However, BBD electrodes present challenges, including delamination, limited scalability, and restricted service life. In this study, platinum was selected as the anode material for the galvanostatic degradation of VFX due to its high stability and a reliable surface-cleaning protocol, which ensured excellent reproducibility. The degradation experiments were conducted in 0.1 M Na_2SO_4 at pH 9 using a current density of 25 mA cm^{-2}. Under these conditions, a 25 mg L^{-1} VFX solution reached 94% degradation after 7 hours. Hydroxyl and sulfate radicals generated in the electrochemical system served as the primary oxidative species. The degradation followed first-order kinetics, with a rate constant of 0.0084 min^{-1}. LC-MS analysis revealed several key intermediates, including two isomers at m/z 276 and three at *m/z* 294. Toxicity assessment using an *in silico* prediction model confirmed that the degradation pathway is environmentally safe, supporting the sustainability of the proposed method.

5.2 Introduction

UNESCO has recognized pharmaceuticals as a major category of ECs [259]. Antidepressants, in particular, are increasingly detected in surface and groundwater at concentrations ranging from ng L^{-1} to mg L^{-1} [260]. VFX is one of the most widely found in aquatic environments worldwide [261]. Its persistence and limited biodegradability raise significant environmental concerns, as VFX has been shown to induce neurobehavioral and reproductive disruptions in aquatic organisms [262].

Conventional WWTPs are generally ineffective for completely removing VFX, with reported elimination efficiencies ranging from only 7.7% to 56% [3]. In contrast, AOPs offer a promising alternative to traditional treatment methods. These technologies generate highly

reactive hydroxyl radicals that can oxidize a broad spectrum of organic pollutants [263], including VFX.

Accordingly, multiple AOPs have been explored for VFX degradation [264-267]. Among these, EAOPs have attracted growing interest due to their simplicity, cost-effectiveness, safety, and environmental compatibility. These methods rely on the *in situ* electrochemical generation of powerful oxidants without requiring hazardous chemical reagents [268].

Regarding VFX, only a few studies have investigated its electrochemical degradation, all of which employed boron-doped diamond (BDD) anodes [269]. Comparative studies of electrochemical and photoinduced degradation have shown that both AOPs are effective, although photoinduced degradation proceeds more rapidly. Mechanistic analyses revealed that photoinduced degradation primarily follows an indirect pathway mediated by •OH radicals, whereas electrochemical oxidation involves both direct and indirect routes [270]. The influence of other radical species has also been assessed. In the presence of chloride ions, VFX degradation is significantly accelerated, achieving 98.5% removal of a 25 mg L^{-1} solution within 5 minutes [271]. Chlorine radicals (Cl•) promote benzene-ring opening, enabling rapid decomposition. Conversely, the addition of tert-butanol, a well-known •OH scavenger, slows the degradation, confirming the dominant role of hydroxyl radicals. Likewise, bicarbonate and phosphate ions act as radical scavengers and inhibit VFX degradation [272].

BDD anodes possess several advantageous physicochemical properties, including a wide potential window, low background current, high oxygen overpotential, and excellent corrosion resistance [273]. As inert electrodes, they exhibit weak adsorption of electrochemically generated hydroxyl radicals, thereby increasing the availability of these species for reaction with contaminants in solution. These features have contributed to the widespread use of BDD electrodes for the oxidation and mineralization of organic pollutants. Nevertheless, several limitations remain to be addressed [274].

BDD films are typically deposited onto substrates such as silicon, tungsten, molybdenum, titanium, niobium, or tantalum using chemical vapor deposition. Mechanical cleaning of BDD surfaces can cause physical damage and is therefore discouraged. Instead, electrochemical cleaning protocols are often employed, but these procedures can significantly alter electrode properties and lack standardization due to morphological variability among BDD electrodes [275]. Moreover, electrochemical pre-treatment frequently requires high current densities or potentials, which may damage adhesive layers used to secure the BDD coating and compromise electrode performance and reproducibility.

Another major concern is the susceptibility of BDD films to delamination. Selecting an appropriate substrate requires careful consideration of thermal expansion compatibility;

mismatches can introduce structural defects that permit electrolyte penetration and lead to substrate corrosion [276]. Although silicon and tantalum exhibit the most suitable thermal expansion characteristics, silicon is brittle and has low electrical conductivity, while tantalum is costly. Other potential substrates, such as nickel, tungsten, and titanium, exhibit satisfactory electrochemical performance but still experience delamination. Furthermore, materials such as silicon, tantalum, niobium, and tungsten are not ideal for industrial-scale deployment [277]. These challenges underscore the need to explore alternative anode materials to advance EAOP technologies.

The present study addresses these limitations by evaluating alternative electrode materials for the electrochemical degradation of VFX. A comparative analysis of platinum and GC anodes was performed, with particular emphasis on distinguishing between direct and indirect oxidation mechanisms. Although the CV revealed no direct VFX oxidation on platinum, this electrode showed higher degradation efficiency via indirect oxidation, a critical observation often overlooked in studies focused predominantly on BDD systems. Notably, even on electrodes capable of direct oxidation, such as GC, the degradation mechanism was largely governed by indirect pathways. Understanding these electrode-specific behaviors is essential for rational EAOP design.

In this context, platinum is proposed for the first time as a viable alternative to BDD for the electrochemical degradation of VFX. Platinum offers several advantages: a well-established and reproducible cleaning procedure, long-term stability, and suitability for extended operation [278]. The degradation process in this study was optimized under environmentally relevant conditions, including a near-neutral electrolyte pH and a moderate applied current density. Importantly, chloride-containing electrolytes were deliberately avoided to prevent the formation of harmful disinfection by-products, a major concern in water treatment applications. While many previous studies have reported high degradation efficiencies using chloride-based media, such conditions limit the practical applicability of their findings.

A comprehensive identification of transformation products was achieved using LC–MS/MS, and detailed fragmentation studies were performed to distinguish between isomeric species. This analysis provided key insights into the degradation pathways of VFX. In addition, an *in silico* ecotoxicity assessment was conducted using the ECOSAR predictive model, confirming the environmental sustainability of the proposed degradation approach. Consistent with established hazard evaluation methodologies [270], this combined analytical–predictive strategy offers a more robust assessment of the treatment's environmental impact than studies limited to monitoring the removal of the parent compound.

5.3 Results

5.3.1 Evaluation of Anode Material for the Electrochemical Degradation of VFX

The choice of anode material is a critical factor affecting the electrochemical degradation efficiency of ECs. VFX, being an electroactive compound, can undergo degradation via direct AO. To determine the electrode capable of achieving the highest degradation efficiency, a preliminary study was conducted on the electrochemical behavior of VFX using platinum and GC electrodes.

GC is a structurally ordered, sp^2-hybridized, non-graphitizable form of carbon characterized by low permeability, high thermal stability, and good electrical conductivity. Its fullerene-like structure, composed of curved graphene layers enclosing closed pores, confers exceptional chemical and mechanical stability [279].

To assess VFX electrochemical behavior on GC, the voltammetric profile of a 0.1 mM VFX solution in phosphate buffer (pH 7) was recorded (**Figure 5.1 (a)**). During the anodic scan, a current peak appeared at approximately 0.74 V, corresponding to the irreversible oxidation of VFX, as no cathodic peak was observed on the reverse scan. The flat voltammetric profile obtained in the pure buffer confirmed that this peak was attributable to VFX oxidation.

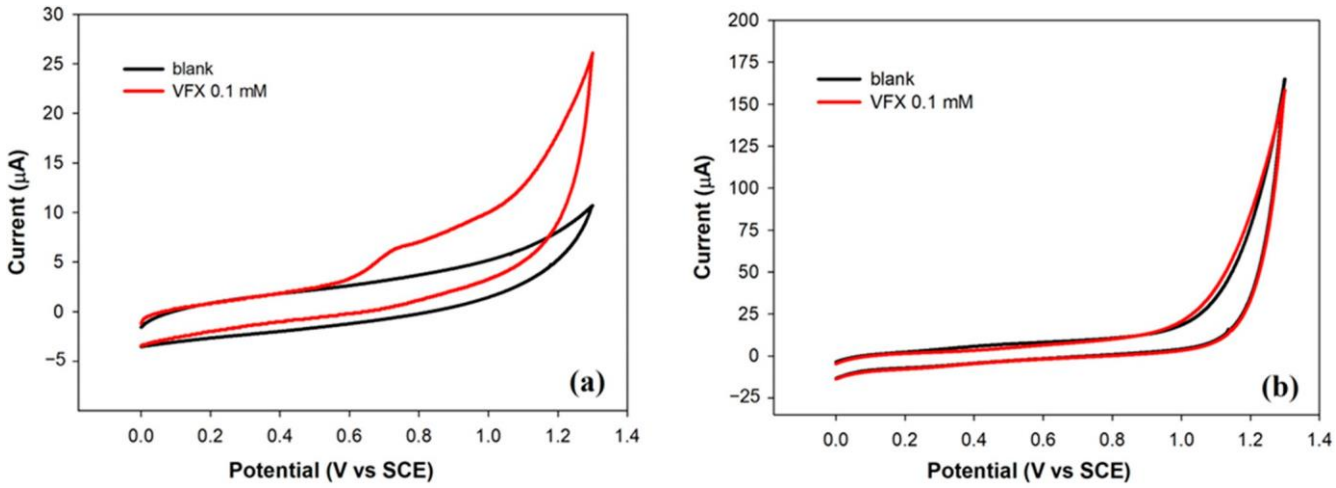

Figure 5.1 *Cyclic voltammograms acquired in phosphate buffer solution (0.1 M, pH 7) at a bare GC electrode* **(a)** *and at a bare platinum electrode* **(b)** *in the absence (black curves) and in the presence of VFX at a concentration of 0.1 mM (red curves). Scan rate: 50 mV* s^{-1}.

A similar study was conducted using a platinum electrode. Platinum is widely employed as an anode for the oxidation of organic pollutants due to its excellent electrical conductivity and chemical stability [280]. The voltammetric profile of VFX on platinum (**Figure 5.1 (b)**) closely resembled that of the pure electrolyte, with no discernible oxidation peak. This absence indicates that VFX is not electroactive on platinum within the explored potential range.

To further understand the electrochemical behavior of VFX on GC, the effect of scan rate on the voltammetric response was investigated. The relationship between peak current and scan rate provides insight into whether the electrochemical process is diffusion- or adsorption-controlled. Voltammograms recorded at scan rates ranging from 5 to 150 mV s^{-1} showed a linear relationship between peak current and scan rate (r^2 = 0.9956), characteristic of adsorption-controlled processes [268]. This behavior suggests that π–π interactions drive VFX adsorption on GC. Additionally, the anodic peak potential shifted toward more positive values with increasing scan rate, confirming the irreversibility of the oxidation process. The lack of electroactivity on platinum can be attributed to its poor affinity for VFX, which limits adsorption and, consequently, direct oxidation.

As previously noted, pharmaceutical compounds can be degraded electrochemically either through direct electron transfer or via reactive radical species generated at the electrode surface. Both GC and platinum electrodes were tested as anodes for VFX degradation, regardless of the compound's electroactivity. A graphite plate served as the cathode in all experiments.

Galvanostatic degradation was first performed at a current density of 10 mA cm^{-2} for 60 minutes using a 25 mg L^{-1} VFX solution in 0.1 M phosphate buffer (pH 7) under continuous stirring. Degradation was assessed by DPV on a conventional GC using platinum electrodes before and after electrolysis. Peak current decreased by 25% for GC and 40% for platinum, indicating greater degradation on platinum. This apparent discrepancy with CV results is explained by the predominance of indirect oxidation: although VFX did not undergo direct electron transfer on platinum, hydroxyl radicals continuously generated at the anode mediated efficient degradation.

To confirm the role of indirect oxidation, the GC experiment was repeated in the presence of 200 mM ethanol, a known •OH radical scavenger [281]. Radical-scavenging tests identify active species and their contribution to AO by allowing scavengers to compete with pollutants for reactive radicals. DPV analysis after electrolysis in the presence of ethanol showed only an 8% decrease in peak current, markedly lower than in its absence. This indicates that even on GC, VFX degradation primarily occurs through indirect mechanisms mediated by •OH radicals. While these experiments provide indirect evidence of hydroxyl radical involvement, direct confirmation could be obtained using electron paramagnetic resonance (EPR) spectroscopy.

Given the higher degradation observed on platinum, this material was selected as the anode for subsequent electrochemical experiments.

5.3.2 Optimization of the Degradation Conditions

The efficiency of EAOPs strongly depends on the electrolysis conditions, which were optimized in this study to achieve maximum removal of both VFX and its transformation products. Changes in VFX concentration during electrochemical degradation were tracked by collecting 1 mL aliquots from the electrolyte at predetermined time intervals and analyzing them by HPLC-UV. Methanol was added to each sample because it is compatible with the mobile phase and effectively quenches residual radicals during storage. It is worth noting that ethanol was used in the mechanistic experiments with GC electrodes because of its well-known selectivity for hydroxyl radicals. This approach allowed a more specific evaluation of the contribution of hydroxyl radicals to the degradation mechanism.

In electrochemical degradation processes, a supporting electrolyte is added to enhance solution conductivity and promote the formation of strong oxidizing agents. Sodium sulfate (Na_2SO_4) is considered an "active" electrolyte because it enables the generation of sulfate radicals ($SO_4^{\bullet-}$) through several pathways, most notably via reactions with hydroxyl radicals (•OH) produced during water electrolysis [282]. The availability of •OH radicals therefore constrains the rate of $SO_4^{\bullet-}$ formation. Consequently, increasing sulfate concentration does not enhance the production of reactive species nor improve pollutant removal. Excessive sulfate may also contribute to anode fouling, which diminishes electrolysis efficiency. For these reasons, a standard concentration of 0.1 M is widely used. The initial experimental conditions for VFX degradation were thus 0.1 M Na_2SO_4 at pH 7, with the supporting electrolyte.

Advanced electrochemical oxidation processes are typically operated in galvanostatic mode, where the applied current density is a critical parameter because it dictates the rate of oxidant generation. In principle, higher current densities promote the formation of radical species at the anode surface, thereby accelerating contaminant degradation. However, beyond a certain threshold, the increased voltage can induce side reactions such as oxygen evolution, leading to the formation of non-oxidizing species that do not contribute to VFX removal.

To determine this threshold, degradation experiments were conducted at current densities of 5, 10, and 25 mA cm^{-2} using a 25 mg L^{-1} VFX solution in 0.1 M Na_2SO_4 at pH 7. The resulting degradation profiles, expressed as C/C_0 versus time (where C is the VFX concentration at a given time and C_0 the initial concentration), are shown in **Figure 5.2 (a)**. After 60 minutes, the highest degradation efficiency (45.5%) was obtained at 25 mA cm^{-2}. Current densities of 5 and 10 mA cm^{-2} yielded lower efficiencies of 22% and 38.5%, respectively. No further improvement was observed at values above 25 mA cm^{-2}. Based on these results, 25 mA cm^{-2} was selected for subsequent experiments.

The influence of initial VFX concentration was also assessed using two starting levels, 25 mg L^{-1} and 1 mg L^{-1}, while keeping all other experimental parameters constant. The corresponding degradation curves are shown in Figure 5.2**(b)**. After 60 minutes, the removal efficiencies were 45.5% for the 25 mg L^{-1} solution and 54.5% for the 1 mg L^{-1} solution. The lower efficiency at higher concentrations can be attributed to the fixed amount of reactive species available under the selected operating conditions: as the pollutant concentration increases, a longer treatment time is required to achieve comparable degradation [283]. Additionally, higher concentrations of transformation products increase competition between VFX and its intermediates for reaction with radical species.

The electrolyte pH is another important factor in electrochemical degradation, particularly given the variability of wastewater pH. Previous studies have reported inconsistent trends, reflecting the complex role of pH in influencing both pollutant speciation and reactive species formation, as well as the production of species that may quench radicals [284]. In this study, VFX degradation was evaluated at pH 5, 7, and 9 using a 1 mg L-1 VFX solution in 0.1 M Na2SO4 at a current density of 25 mA cm^{-2}. The degradation curves are shown in **Figure 5.2 (c)**. After 60 minutes, a slight improvement in removal efficiency was observed at pH 9 (59%), likely due to enhanced •OH formation favored by the higher concentration of OH^- ions. Although higher pH values (e.g., ≥10–11) could potentially further improve degradation, the present study focused on conditions representative of typical wastewater. Future investigations may explore the performance of EAOPs at these higher pH levels.

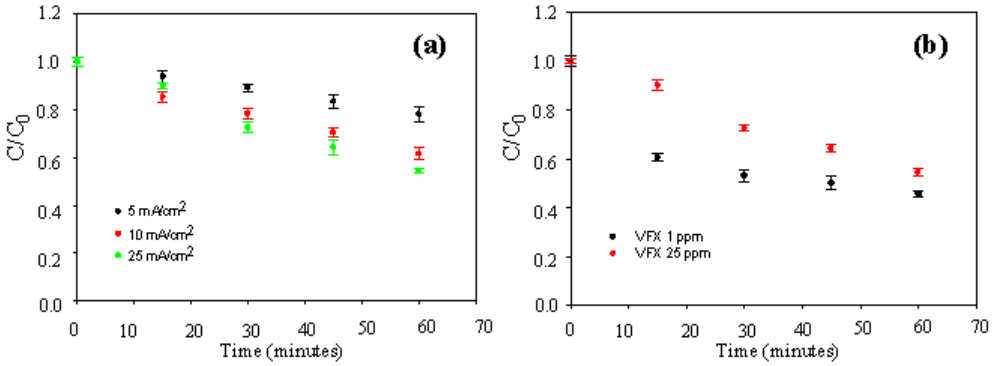

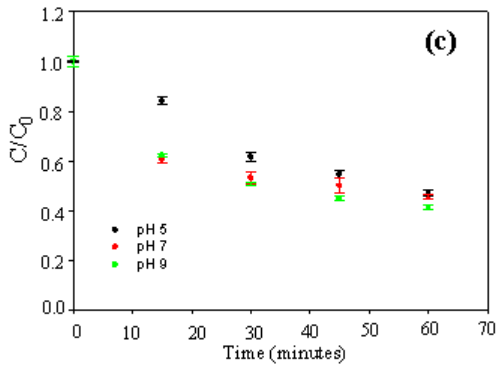

Figure 5.2 (a) *Normalized concentration–time curves for the electrochemical degradation of a 25 mg L^{-1} solution of VFX in Na_2SO_4 0.1 M at pH 7 realized by applying a current density of 5 mA cm^{-2} (black circles), 10 mA cm^{-2} (red circles) and 25 mA cm^{-2} (green circles);* **(b)** *Normalized concentration–time curves for the electrochemical degradation of a 25 mg L^{-1} (red circles) and 1 mg L^{-1} (black circles) solution of VFX in Na_2SO_4 0.1 M at pH 7 realized by applying a current density of 25 mA cm^{-2};* **(c)** *Normalized concentration–time curves for the electrochemical degradation of a 1 mg L^{-1} solution of VFX in Na_2SO_4 0.1 M at pH 5 (black circles), pH 7 (red circles) and pH 9 (green circles) realized by applying a current density of 25 mA cm^{-2}. Data points represent the mean ± standard deviation (SD) of n=3 independent experiments.*

The degradation curve for extended electrolysis was obtained under the previously optimized conditions. A VFX concentration of 25 mg L^{-1} was selected to ensure sufficient formation of degradation products for subsequent LC–MS identification. The degradation profile after 7 h (420 min) of electrolysis is shown in **Figure 5.3**. The experiment was performed in triplicate, demonstrating excellent precision attributable to the reproducible state of the platinum electrode surface (coefficients of variation: 1.04–9.77%). A high degradation efficiency of 94% was achieved. The process followed first-order kinetics (r^2=0.999), with a rate constant of 0.0084 min^{-1} and a corresponding half-life of 82.52 min.

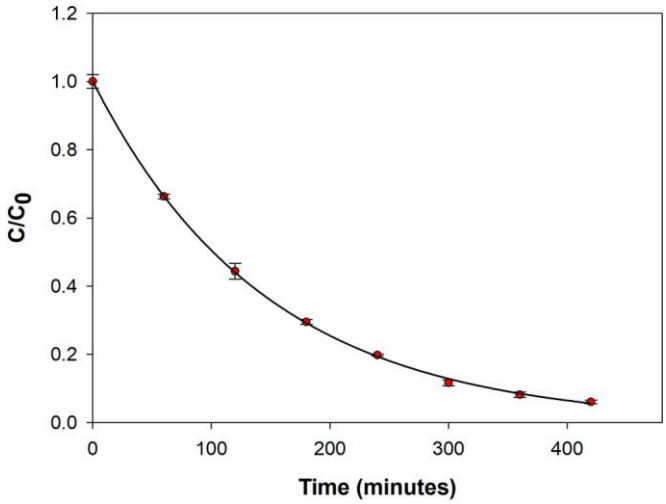

Figure 5.3 *Normalized concentration–time curve for the electrochemical degradation of a 25 mg L^{-1} solution of VFX in Na_2SO_4 0.1 M at pH 9 realized by applying a current density of 25 mA cm^{-2}. The analysis was performed in triplicate, and the results are expressed as mean ± SD.*

It is important to note that shorter degradation times and higher efficiencies have been reported in studies that added chloride ions to the electrolyte solution [271]. Those approaches also typically employ acidic pH conditions [270] and elevated current densities [272]. In contrast, the method presented here operates under milder conditions and, crucially, does not depend on accelerants such as chloride, which inevitably promote the formation of hazardous by-products.

5.3.3 Structural Elucidation of VFX and Degradation Products by LC-ESI-LIT-MS^n and LC-ESI-Orbitrap-MS

LC-DAD experiments were conducted to monitor the degradation pathway of VFX over time under various electrolysis conditions. Optimal degradation was achieved at pH 9, using a 0.1 M Na_2SO_4 electrolyte and a current density of 25 mA cm^{-2}. However, due to the limited discriminatory power of retention times and UV spectra, additional analytical techniques were required to unambiguously identify components in complex matrices, particularly unknown degradation products. Consequently, LC–MS analyses of VFX and its transformation products were performed at both low and high resolution. Electrochemical degradation was carried out under the optimized conditions using a drug concentration of 25 mg L^{-1}. Furthermore, CID-MS^n experiments were employed to elucidate the fragmentation pathways of the transformation products and to obtain more comprehensive structural information.

5.3.3.1 LC-ESI-Orbitrap-MS Studies of VFX and Its Degradation Products

The composition of the VFX degradation mixtures was elucidated using LC–ESI–Orbitrap–MS. Although TIC chromatograms were initially recorded, their interpretative value was limited by the presence of coeluting ions. Therefore, extracted ion chromatograms were employed to improve selectivity. XICs represent ion intensities within a narrow mass-to-charge window of $[M+H]^+ \pm 5.0$ mDa, enabling the detection of individual compounds, including low-abundance transformation products, while minimizing spectral interference. This approach was applied to degradation mixtures collected at different electrolysis times, enabling clear separation of the resulting products. **Figure 5.4** presents the XICs of protonated VFX and its transformation products after 100 min of electrochemical degradation at pH 9, a time point at which product concentrations were notably high.

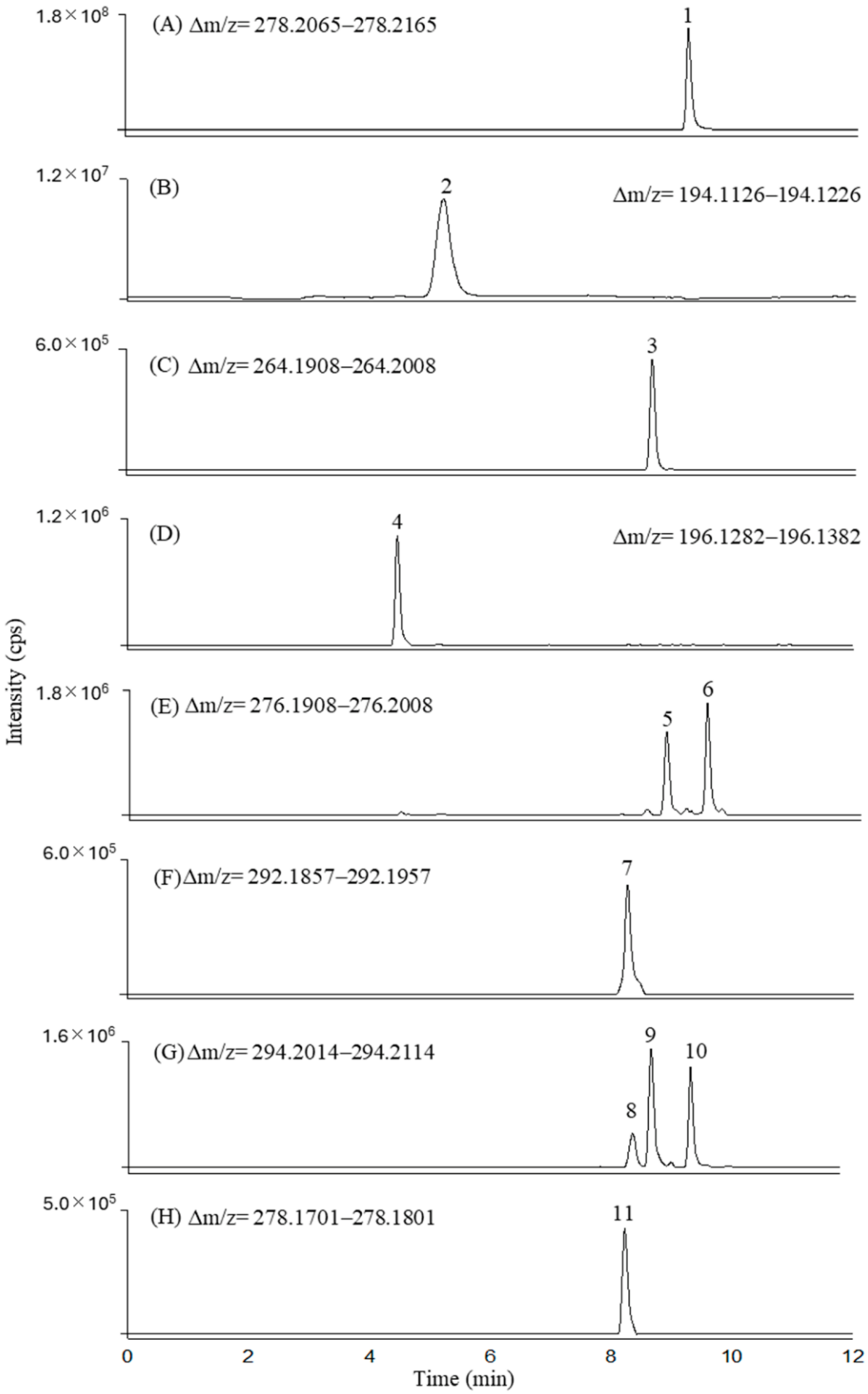

Figure 5.4 *Extracted ion chromatograms (XICs) acquired for the following compounds: VFX (**A**); V194 (**B**); V264 (N-desmethylvenlafaxine) (**C**); V196 (**D**); V276a (retention time 8.80 min, peak 5) and V276b (retention time 9.48 min, peak 6) (**E**); V292 (**F**); V294a (retention time 8.49 min, peak 8), V294b (retention time 8.83 min, peak 9), V294c (retention time 9.47 min, peak 10) (**G**); V278 (peak 11) (**H**).*

All chromatographic peaks were identified by accurate mass measurements, which enabled the determination of molecular formulas and the interpretation of MS^n data in conjunction with literature reports. CID fragmentation studies were performed for each identified product, allowing confirmation of their structures by analysis of characteristic fragmentation pathways. The chromatographic and mass spectrometric data for all detected compounds are summarized in **Table 5.1**, including retention times, molecular formulas, exact and accurate *m/z* values, mass errors, and the major $[M+H]^+$ fragment ions. Notably, the mass errors associated with the accurate mass measurements were consistently below 1.6 mg L^{-1}, indicating excellent mass accuracy.

Table 5.1 *Chromatographic and mass spectrometry data for the main transformation products resulting from the electrochemical degradation of VFX, identified by LC-ESI(+)-CID-MS^n.*

N.	Compounds	Retention time (min)	Molecular formula	[1][M+H]$^+$ *m/z* Accurate	Error (mg L^{-1})	Main Fragments $[M+H]^+$ *m/z* Nominal
1	VFX	9.24	$C_{17}H_{27}O_2N$	278.2111	-1.42	260; 215; 159; 147; 121; 58
2	V276a	8.80	$C_{17}H_{25}O_2N$	276.1954	-1.47	258; 246; 213; 178; 145; 135; 121
3	V276b	9.48	$C_{17}H_{25}O_2N$	276.1956	-0.89	258; 246; 215; 159; 147; 121
4	V264 *N-desmethylvenlafaxine.*	8.65	$C_{16}H_{25}O_2N$	264.1956	-0.70	246; 215; 121
5	V196	4.46	$C_{11}H_{17}O_2N$	196.1333	-0.28	178; 163; 147; 135
6	V194	5.19	$C_{11}H_{15}O_2N$	194.1176	-0.28	149; 121; 58
7	V292	8.28	$C_{17}H_{25}O_3N$	292.1903	-1.40	274; 256; 121
8	V294a	8.49	$C_{17}H_{27}O_3N$	294.2061	-1.09	276; 258; 231; 213; 121
9	V294b	8.83	$C_{17}H_{27}O_3N$	294.2059	-1.60	276; 258; 231; 213; 145
10	V294c	9.47	$C_{17}H_{27}O_3N$	294.2060	-1.30	276; 258; 233; 215; 178; 135; 121
11	V278	8.22	$C_{16}H_{23}O_3N$	278.1749	-0.72	263; 245; 231; 178; 164; 121

[1] average value of n = 3 *m/z* measurements.

MS^n data acquired using a LIT analyzer with CID confirmed the identities of the compounds and enabled unambiguous structural elucidation. These findings are consistent with previous reports on VFX degradation, including photochemical processes and electrochemical degradation using BDD electrodes [270]. As shown in **Figure 5.4** and summarized in **Table 5.1**, ten major transformation intermediates were identified. Among them were two isomers with an exact *m/z* of 276.1958 (V276a and V276b; **Figure 5.4 (E)**) and three isomers with an exact *m/z* of 294.2064 (V294a, V294b, and V294c; **Figure 5.4 (G)**). Accurate-mass data alone could not distinguish among these isomers, as they provide only molecular formula information. Consequently, fragmentation studies were carried out by isolating the chromatographic peaks corresponding to each species. The proposed chemical structures of the transformation products are presented in **Scheme 5.1**.

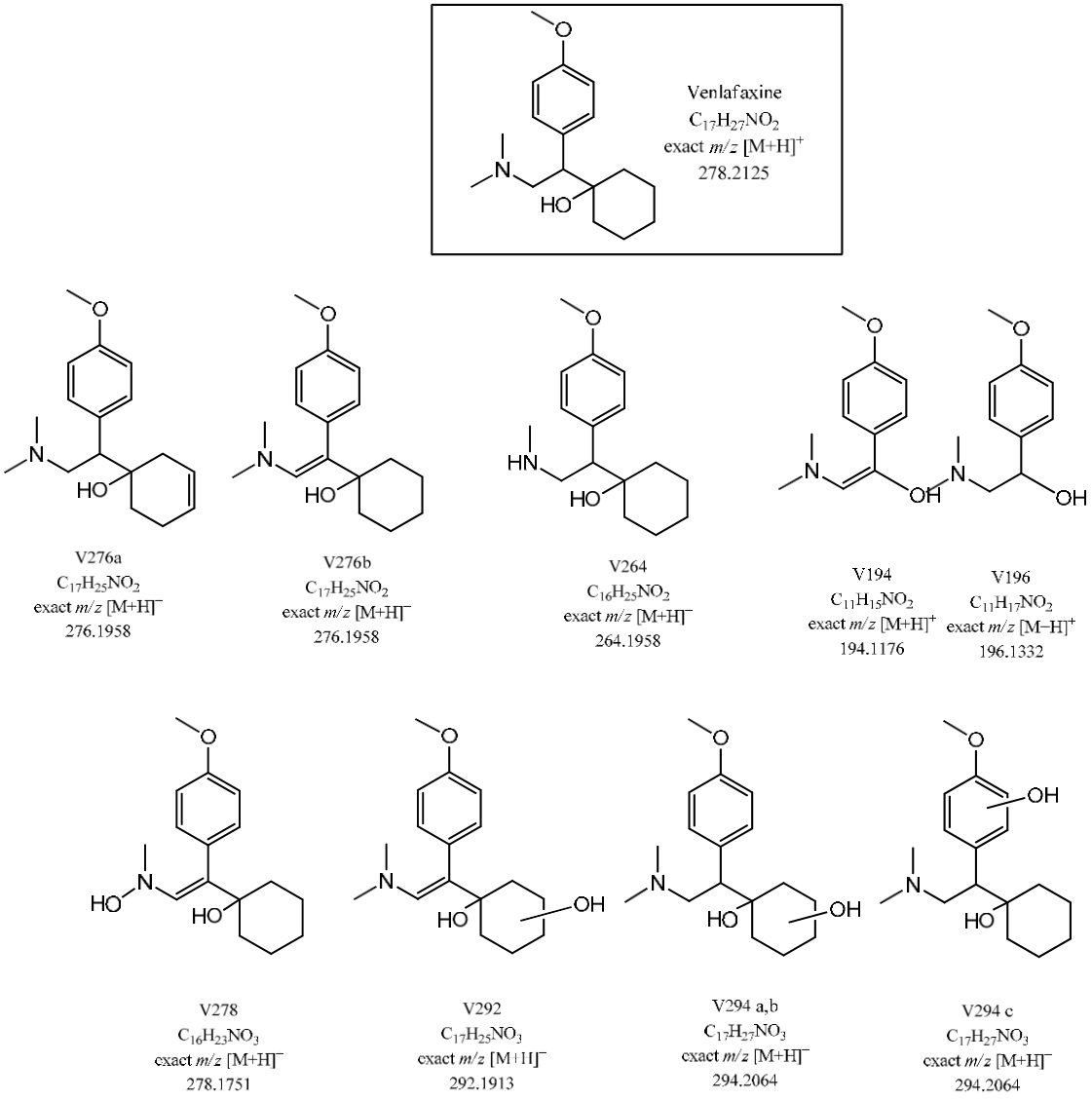

Scheme 5.1 *Proposed chemical structures, molecular formulas, and exact m/z values of VFX transformation products.*

5.3.3.2 LC-ESI-CID-MS^n Studies of VFX Degradation Products

As previously noted, VFX degradation produced two isomers with an exact *m/z* of 276.1958 (V276a and V276b; $C_{17}H_{25}NO_2^+$), eluting at 8.80 and 9.48 min, respectively. Their CID–MS^n spectra are shown in **Figure 5.5**. The 2 Da decrease relative to *m/z* 278 (VFX) is consistent with the formation of a double bond, either in the cyclohexane ring (isomer a) or along the carbon chain (isomer b).

The MS^2 spectrum of isomer V276a (**Figure 5.5 (a)**) shows that fragmentation of the molecular ion generates ions at *m/z* 258 and 213, corresponding to $C_{17}H_{23}NO^+$ and $C_{15}H_{17}O^+$, respectively. The *m/z* 258 ion forms via dehydration of V276a, followed by the creation of a second double bond within the cyclohexane ring. The ion at *m/z* 213 originates from further fragmentation of the *m/z* 258 species through loss of the dimethylamine group ($–NC_2H_7$, 45 Da). The MS^2 spectrum of isomer V276b (**Figure 5.5 (b)**) similarly shows ions at *m/z* 258 and 215, corresponding to $C_{17}H_{23}NO^+$ and $C_{15}H_{19}O^+$, respectively. As with V276a, the *m/z* 258 ion forms through dehydration, accompanied by the introduction of a conjugated double bond and conversion of the cyclohexane ring into a cyclohexene moiety. The fragment at *m/z* 215 is produced from the *m/z* 258 ion via loss of the $–NC_2H_5$ amino group (43 Da). The chemical structures of the fragments at *m/z* 213 and 215, observed in the MS^2 spectra of the two isomers (**Figures 5.5 (a)** and **5.5 (b)**, respectively), confirmed the presence of a double bond in different regions of the molecule.

The MS^3 spectrum of V276a (**Figure 5.5 (c)**), obtained from the fragmentation of the *m/z* 258 ion, revealed five fragment ions at nominal *m/z* 213, 121, 135, 145, and 178, with *m/z* 213 being the most intense. Similarly, the MS^3 spectrum of V276b (**Figure 5.5 (d)**), derived from the *m/z* 258 ion, showed four fragment ions, *m/z* 215 (most intense), 121, 147, and 159. The fragments at *m/z* 147 ($C_{10}H_{11}O^+$) and 215 ($C_{15}H_{19}O^+$) were characteristic of VFX MS^n spectra (**Table 5.1**). The ions at *m/z* 135 ($C_9H_{11}O^+$) and 178 ($C_{11}H_{16}NO^+$) were also observed. The $C_{11}H_{16}NO^+$ fragment (*m/z* 178) resulted from the loss of the hydroxy-substituted cyclohexane ring, followed by formation of a double bond, while the $C_9H_{11}O^+$ fragment originated from the *m/z* 178 ion via loss of the $–NC_2H_5$ group. These fragmentation patterns are consistent with the structures proposed in **Scheme 5.1** for both V276 isomers.

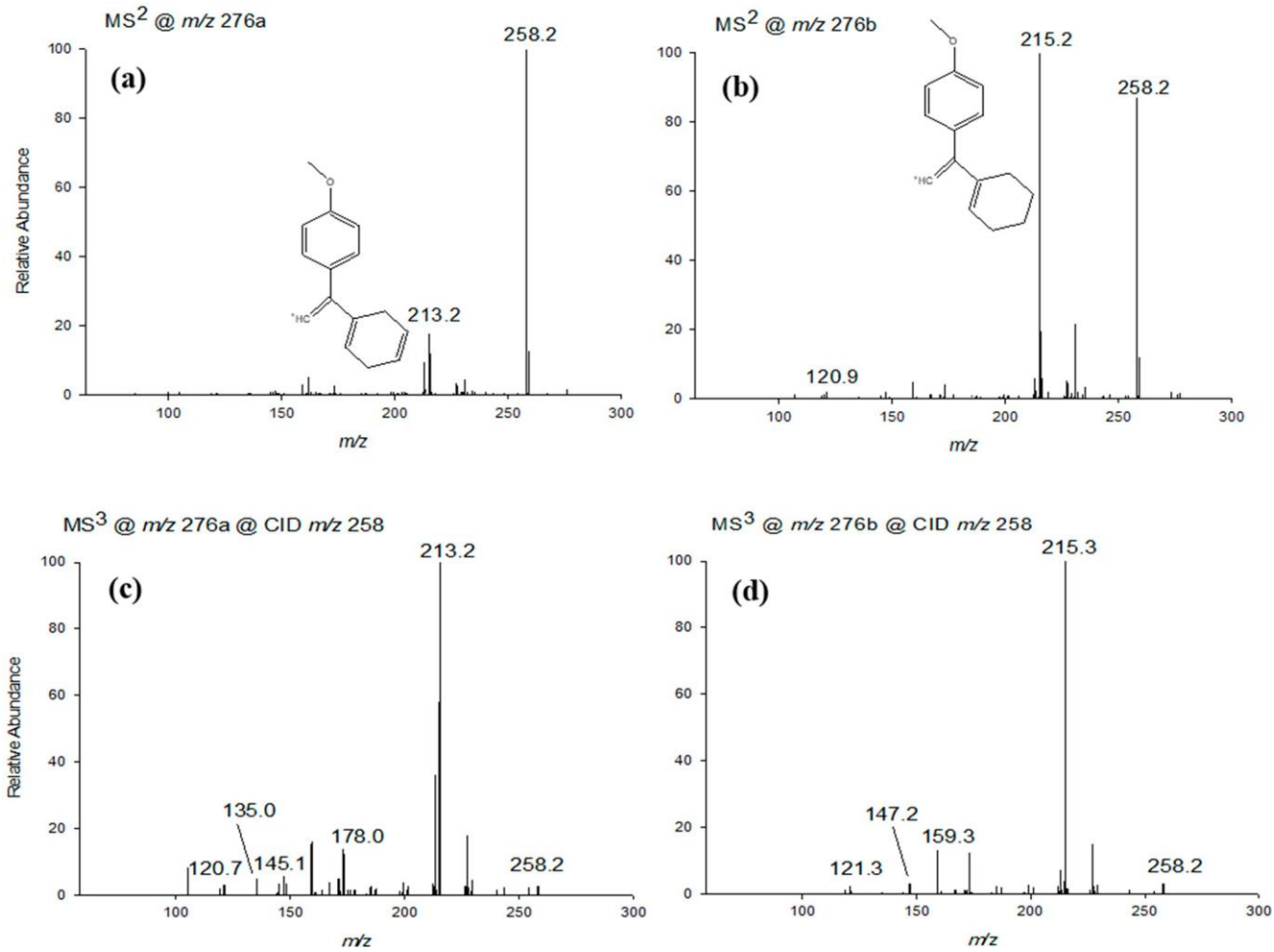

Figure 5.5 *CID-MS^n spectra* (**a**–**d**) *in positive mode of the [M+H]$^+$ ion of the two isomers at nominal m/z 276 generated by applying relative collision energies between 30% and 35%.*

Consistent with the findings of Santoke et al [285], several hydroxylated derivatives of VFX were identified, resulting from HO•/O_2•$^-$ radical attack. Five isomers with the molecular formula $C_{17}H_{28}NO_3^+$ (*m/z* 294.2063) were detected at retention times ranging from 8.49 to 9.47 min, indicating mono-hydroxylation at different positions of the parent compound. Two of these isomers were present in trace amounts, preventing MS^n fragmentation and were therefore excluded from further analysis. VFX possesses multiple potential sites for mono-oxidation, which can yield products with varying polarities, including hydroxylation of the aromatic or cyclohexane rings, the methylene carbon, or the methyl groups attached to the amine moiety. MS^n studies (**Figure 5.6(a–c)**) revealed distinct fragmentation pathways for the three major isomers, V294a, V294b, and V294c (peaks 8, 9, and 10 in **Figure 5.4**), allowing the proposal of possible –OH attack positions.

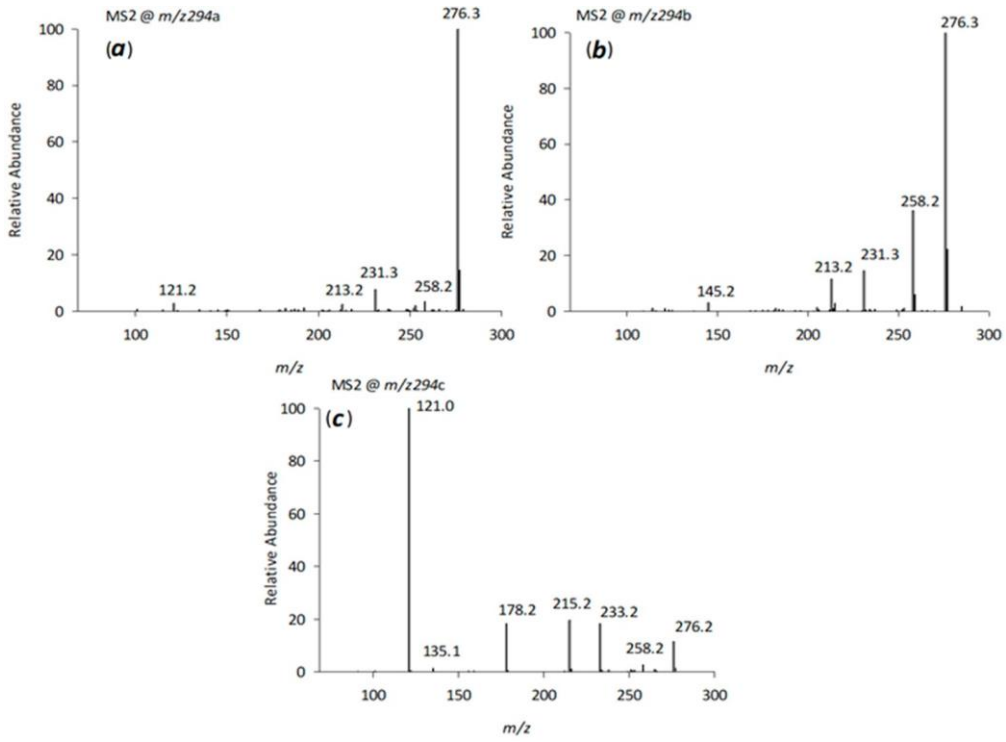

Figure 5.6 *CID-MS^n spectra* (**a**–**c**) *in positive mode of the [M+H]$^+$ ion of the isomers at m/z 294 generated by applying relative collision energies between 30% and 35%.*

MS² fragmentation of V294a and V294b showed the loss of H_2O (*m/z* 276), a feature also observed in the VFX spectrum, suggesting hydroxylation on the cyclohexane ring or the methylene group adjacent to the nitrogen atom. MS³ fragmentation of the *m/z* 276 ion produced a fragment at *m/z* 231, consistent with a modified cyclohexane ring containing an additional double bond compared with the *m/z* 215 fragment of VFX [265]. The fragment at *m/z* 213 further supported the presence of this additional double bond. However, the exact position of the –OH group within the cyclohexane ring could not be determined for these two isomers.

For isomer V294c ($C_{17}H_{28}NO_3^+$, *m/z* 294.2053), the retention time (9.47 min, immediately after VFX), a mass difference of 16 Da relative to VFX, and the elemental composition derived from accurate mass measurements indicated hydroxylation at either the methylene carbon or the aromatic ring. Observed fragments at *m/z* 276 and 215, along with a fragment at *m/z* 233 (resulting from loss of the $–NC_2H_7$ amino group, –45 Da), were consistent with monohydroxylation of the aromatic ring, likely at the ortho- or para-position relative to the methoxyl group (**Scheme 5.1**).

Electrochemical degradation of VFX likely proceeds through a combination of dehydrogenation and hydroxylation reactions. This hypothesis is supported by the identification of a transformation product with a molecular ion at *m/z* 292.1903 (peak 7 in **Figure 5.4**), consistent with the protonated molecular formula $C_{17}H_{26}O_3N^+$. This observation suggests the introduction of an oxygen atom followed by dehydrogenation. Fragment ions at *m/z* 274, 256,

and 229, which are 2 Da lower than the corresponding fragments in V276a (*m/z* 276, 258, and 231), indicate formation of an additional double bond within the cyclohexane ring. The proposed structure of V292 reflects this feature (**Scheme 5.1**).

Figure 5.7 presents the MS^2–MS^4 spectra of VFX, with the main fragment ions detailed in **Table 5.1** and their proposed structures illustrated in panels **a1–a3**. Panel **b** in **Figure 5.7** shows the MS^2 spectrum of its isomer V278 ($C_{16}H_{22}O_3N^+$, peak 11 in **Figure 5.4**), which exhibits an identical nominal mass to VFX but a distinct exact mass. The proposed structural modification involves the substitution of the nitrogen-bonded methyl group with a hydroxyl group, accounting for the absence of the *m/z* 233 fragment typically associated with dimethylamine loss (−45 Da). Instead, a fragment at *m/z* 231 is observed, corresponding to a mass loss of 47 Da, consistent with the –CH_3 to –OH substitution. Additionally, a fragment at *m/z* 263 (−15 Da), indicative of loss of the methoxy-bound methyl group ($C_{15}H_{21}O_3N^+$), is detected, aligning with previously published data [285]. The base peak at *m/z* 164.1 likely corresponds to the 4-methoxyphenyl-ethyl fragment, formed by cleavage between the cyclohexanol ring and the ethyl group, while the characteristic *m/z* 121 fragment, assigned to 1-methoxy-4-methylbenzene, is also present.

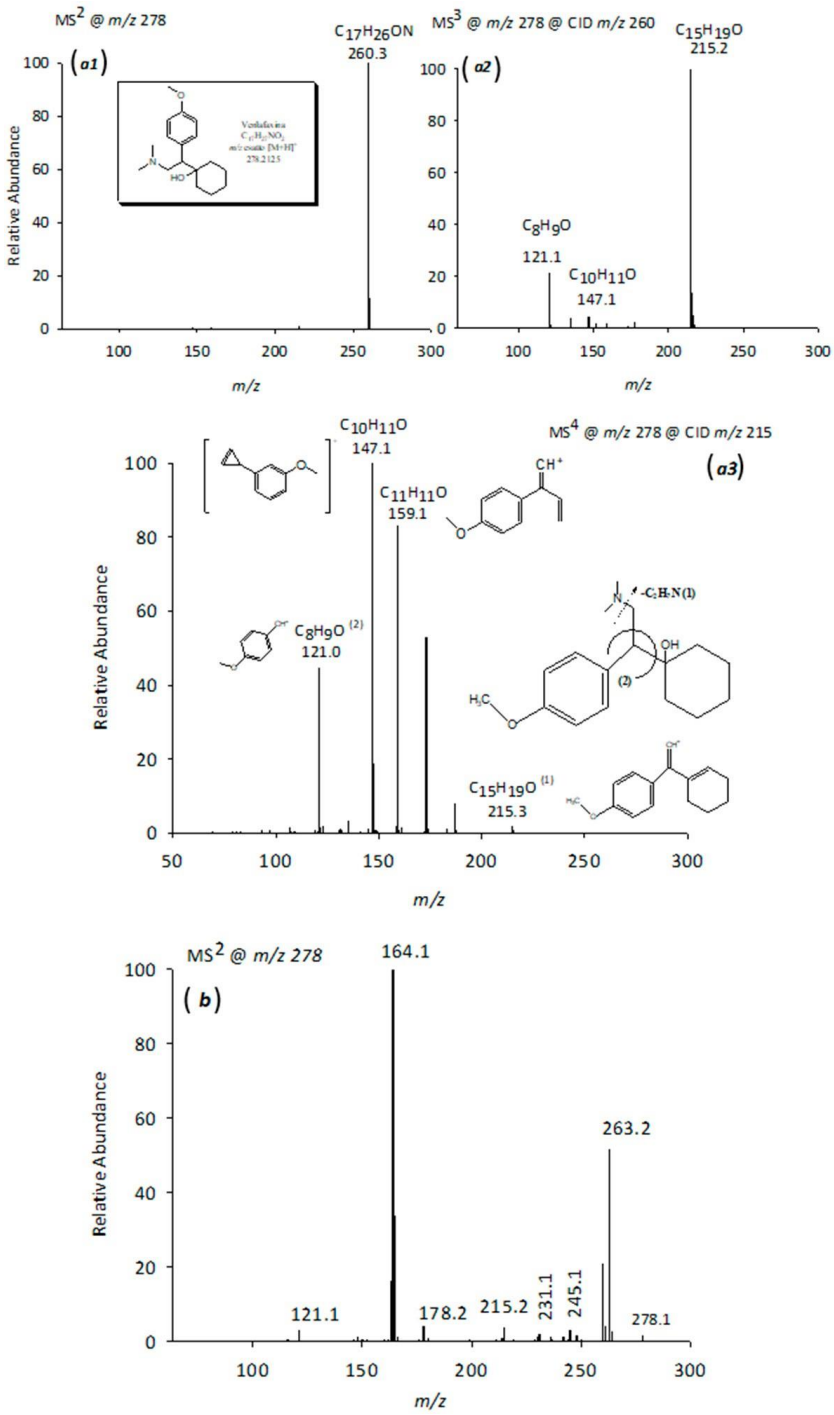

Figure 5.7 *CID–MSⁿ spectra of VFX and its isomer. Panels* **a1–a3***: Positive-mode CID–MSⁿ spectra of the [M+H]⁺ ion of VFX at m/z 278, obtained using relative collision energies of 30–35%. Panel* ***b****: Positive-mode CID–MS² spectrum of the [M+H]⁺ ion at m/z 278 corresponding to the VFX isomer, acquired under the same collision energy conditions (30–35%).*

N-desmethylvenlafaxine, resulting from N-demethylation of VFX, was identified at a retention time of 8.65 min, with an accurate *m/z* of 264.1958 and a molecular formula of $C_{16}H_{26}O_2N^+$. MS^n fragmentation of the molecular ion yielded a fragment at *m/z* 246 ($C_{16}H_{23}NO^+$), corresponding to neutral loss of 18 Da (H_2O), and the recurring *m/z* 215 ($C_{15}H_{19}O^+$) fragment supported the proposed structure (**Table 5.1**).

The study also identified V196, previously reported in the electrochemical degradation of VFX at pH 9 [283], with a retention time of 4.46 min and *m/z* of 196.1332. MS^2 fragmentation of the molecular ion produced a prominent peak at *m/z* 178 ($C_{11}H_{16}NO^+$), resulting from water loss (18 Da), and fragments at *m/z* 135 and 147, consistent with previously observed VFX fragmentation patterns. The fragment at *m/z* 163 ($C_{10}H_{13}ON^+$), attributable to N- or O-demethylation of the *m/z* 178 ion, further supported the proposed structure of V196.

V194, characterized by an accurate *m/z* of 194.1176, was identified as a key degradation product. Fragmentation of V194 yielded three distinct ions at *m/z* 58, 121, and 149. The *m/z* 121 peak, also observed in the MS^4 spectrum of VFX (panel **a3** in **Figure 5.7**), corresponds to $C_8H_9O^+$. The *m/z* 58 fragment corresponds to the dimethyl-methylene-ammonium ion ($C_3NH_8^+$), a characteristic and stable fragment of VFX and its degradation products. The *m/z* 149 fragment ($C_9H_9O_2^+$) results from loss of the dimethylamine group (−45 Da) from V194, providing strong evidence for the proposed structure.

Regarding the formation pathways of these transformation products, after 7 h of electrochemical degradation, VFX and its transformation products were reduced by more than 94% relative to the initial concentration. These products are formed through specific reaction mechanisms, including N-demethylation, dehydration, aromatic ring hydroxylation, cyclohexane ring hydroxylation, and cleavage and modification of the nitrogen moiety. Notably, electrochemical degradation at pH 9 produced three distinct mono-hydroxylated products (V294a, V294b, V294c) with *m/z* 294.2064, resulting from hydroxylation of both the aromatic and cyclohexane rings. These compounds have previously been reported only in photodegradation and AOPs [265, 285]. Other reactions produced lower-molecular-weight products, with V194 being the smallest identified. Overall, demethylation, dehydration, and subsequent hydroxylation/oxidation represent key stages in the transformation process.

Electrochemical degradation reactions are important not only for the efficiency of decontamination and removal processes but also for the generation of transformation products, which may also form in natural environments via biotic or abiotic pathways. Assessing the effectiveness and safety of a pollutant-degradation treatment, therefore, requires evaluating these transformation products, as they may exhibit higher toxicity than the parent compound. Consequently, a primary aim of this study was to determine the residual toxicity of VFX transformation products produced during electrochemical treatment.

5.3.4 Evaluation of the Ecotoxicity of Venlafaxine Degradation Products

The electrochemical degradation of pharmaceuticals can produce transformation products with toxicities that differ from those of the parent compound [29]. Therefore,

evaluating the ecotoxicity of these degradation products using *in vivo*, *in vitro*, or *in silico* methods is essential. *In vivo* assays involve live animal testing, while *in vitro* assays employ cell lines. However, due to the limited availability of commercial standards, these approaches are often impractical for assessing the ecotoxicity of pharmaceutical degradation products. In contrast, *in silico* methods use computational algorithms to predict the properties of substances, including toxicity, based on structural and experimental data from analogous compounds.

A widely used tool for this purpose is ECOSAR software [286]. ECOSAR estimates toxicity by calculating the LC_{50}, defined as the median lethal concentration (mg L^{-1}) that causes 50% mortality in test organisms. In this study, the ecotoxicity of VFX and its degradation products for *Daphnia magna*, previously identified by LC-MS and LC-MS^n, was evaluated using ECOSAR. Chemical structures were drawn in ChemDraw Ultra 12.0, and LC_{50} values for *Daphnia magna* were determined. The resulting LC_{50} values, together with the chemical structures, are presented in **Figure 5.8** using a tiered pyramid format.

The tiered pyramid provides a clear visual representation of the relative ecotoxicity of VFX and its major degradation products. Comparative analysis of molecular structures revealed a general trend: electrochemical degradation of VFX predominantly generates products with reduced toxicity relative to the parent compound. VFX itself (LC_{50} 11.1 mg L^{-1}), featuring a complex bicyclic structure and a tertiary amine group, exhibited moderate toxicity, likely due to structural characteristics that facilitate interactions with biological targets. Most degradation products displayed lower ecotoxicity; however, V276a (LC_{50} 7.8 mg L^{-1}) was an exception, showing slightly higher toxicity than the parent compound.

Compounds V194 (LC_{50} 423 mg L^{-1}) and V196 (LC_{50} 1.57×10^3 mg L^{-1}) exhibited the greatest reduction in toxicity. This effect is attributed to their simplified aromatic structures and increased oxidation, which enhance polarity and water solubility, thereby reducing bioaccumulation potential. The difference in toxicity between V194 and V196, highlighted by the increase in LC_{50} upon double-bond saturation (V194 to V196), indicates that the presence of a double bond significantly increases toxicity in lower-molecular-weight products.

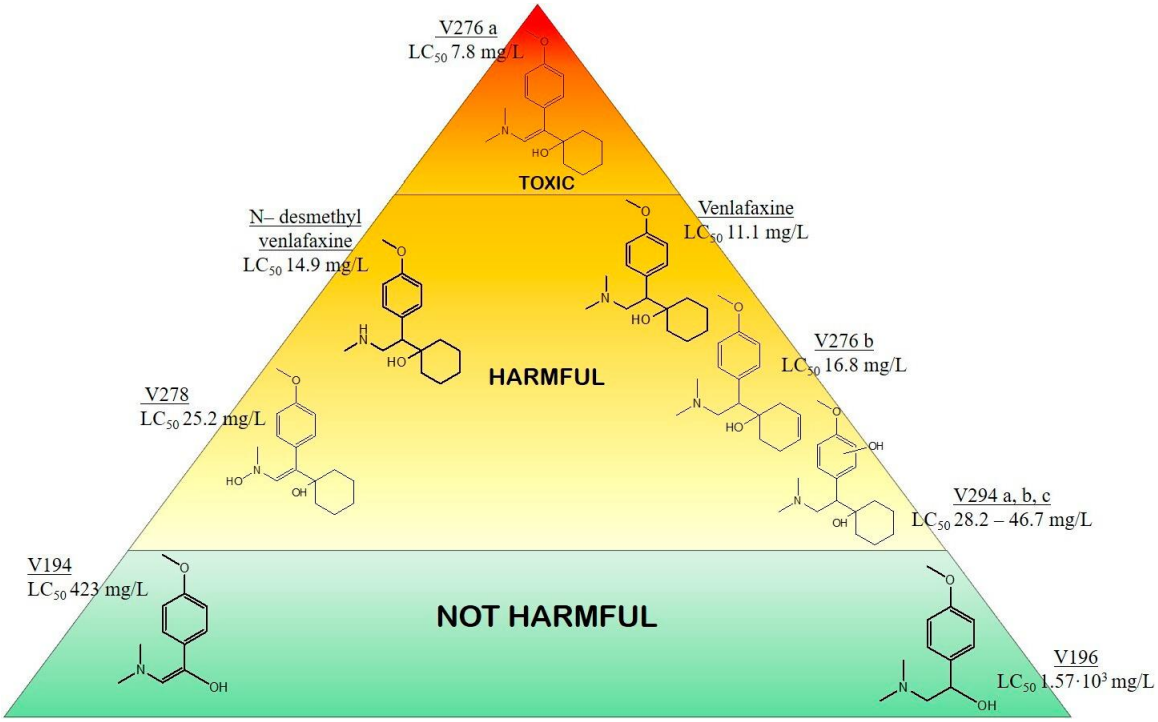

Figure 5.8 *Ecotoxicity classification of vFX and its degradation products and LC_{50} (mg L^{-1}) values calculated by ECOSAR software. Ranges (mg L^{-1}) and their respective characterization: 1 < LC_{50} < 10 toxic (red); 10 < LC_{50} < 100 harmful (orange/yellow); LC_{50} > 100 not harmful (green).*

Other degradation products, including N-desmethylvenlafaxine (LC_{50} 14.9 mg L^{-1}), V276b (LC_{50} 16.8 mg L^{-1}), V278 (LC_{50} 25.2 mg L^{-1}), and V294a–c (LC_{50} 28.2–46.7 mg L^{-1}), also exhibited lower toxicity than VFX. This reduction is likely due to increased hydroxylation and structural degradation, which enhance polarity and facilitate compound elimination.

The predominance of less toxic products, resulting from oxidation, hydroxylation, and structural simplification, highlights the efficiency of electrochemical degradation in mitigating the environmental impact of VFX. These findings are consistent with established principles of environmental toxicology, which indicate that increased polarity and simplified molecular structures generally reduce the ecotoxicity of organic compounds. In particular, this observation aligns with previous studies, such as Voigt et al. (2024), which reported that the introduction of additional hydroxyl groups decreases toxicity [270]. Overall, these results underscore the potential of electrochemical treatment as a sustainable approach for pharmaceutical waste management.

5.3.5 Electrochemical Degradation of Venlafaxine: Advantages of Platinum Electrodes

The electrochemical degradation method for VFX using platinum electrodes presents several key advantages over alternative approaches, as highlighted in **Table 5.2**. A critical factor in electrochemical applications is electrode performance, particularly operational longevity and ease of maintenance. In our study, platinum electrodes, employed with 0.1 M

Na_2SO_4 electrolyte at pH 9 and a current density of 25 mA cm^{-2}, demonstrated exceptional stability and a simple cleaning protocol. By contrast, BDD electrodes, though widely studied [269-272, 287], often pose challenges related to their specific properties and maintenance requirements. The inherent robustness of platinum electrodes contributed to enhanced experimental reproducibility and a potentially extended operational lifetime, thereby reducing procedural complexity and long-term costs.

Table 5.2 *Operational parameters and main outputs of different EAOP methods for VFX degradation.*

Electrode Material	Electrolyte Composition	pH	Current Density (mA/cm^2)	Initial VFX Concentration (mg/L)	Degradation Efficiency	Identified Transformation Products	Toxicity Data	References
Pt	0.1 M Na_2SO_4	9	25	25	94% (7 h)	10 (identified by LC-MS/MS and HRMS)	*in silico* (ECOSAR)	This study
BDD	HCl	3	Not reported	20	not detailed (deduced value: 100% after around 3 h)	4 (identified by LC-HRMS)	*in silico* (QSAR)	[270]
BDD	0.1 M Na_2SO_4, 0.02 M NaCl	6.5	100	25	98% (5 min)	16 (electrolyte NaCl) + 6 (electrolyte Na2SO4) identified by GC-MS	Toxicity test on *Chlorella Vulgaris*	[271]
BDD	0.1 M Na_2SO_4, 0.02 M NaCl	6.5	100	25	98.5% (5 min)	Not evaluated	Not evaluated	[272]
BDD	Waste water (specific electrical conductivity 1455 µS/cm)	7.2	50	1	99.9% (240 min)	3 (2 of which chlorinated) identified by LC-MS/MS and HRMS	Not evaluated	[269]

A major advantage of the platinum electrode-mediated approach employed in this study is the use of a chloride-free electrolyte (0.1 M Na_2SO_4). This is particularly important when compared to studies such as [271-272], where chloride ions (e.g., 0.02 M NaCl), although potentially accelerating degradation kinetics, introduce the risk of forming hazardous halogenated by-products. The absence of chloride in the Pt-based methodology aligns with the goals of environmentally benign remediation strategies.

As summarized in **Table 5.2**, the choice of electrode material strongly influences the formation of degradation intermediates. For example, study [272] did not identify any degradation intermediates, whereas Zhu et al. (2022) [271], using GC-MS, reported intermediates differing from those found in this study and in the study of Voigt et al. (2024)

[270], which employed LC-HRMS and identified four intermediates, while our study revealed ten transformation products. Study [269] also reported four intermediates by LC-HRMS, two of which were chlorinated due to the use of chloride-containing electrolytes. These observations highlight the critical role of electrode selection in determining the nature and diversity of transformation products.

A hallmark of responsible environmental research is thorough evaluation of potential ecological impacts. In this context, our study incorporates an *in silico* ecotoxicity assessment using ECOSAR. Notably, only two other studies have addressed ecotoxicity: Voigt et al. (2024) applied in silico QSAR analysis to four intermediates [270], while Zhu et al. (2022) conducted toxicity tests on *Chlorella vulgaris* [271]. Despite differences in methodology, these investigations provide valuable insights into the environmental fate and potential risks of electrochemical degradation products.

Although extended degradation times might be viewed as a limitation, this is offset by the enhanced stability, improved safety profile regarding by-product formation, and overall sustainability of the Pt electrode-mediated process. In addition, we calculated an energy consumption of 98 kWh m^{-3} to achieve 94% degradation of 25 mg L^{-1} VFX. Energy consumption is widely recognized as a key parameter in assessing the practical implementation of EAOPs; however, none of the other studies summarized in **Table 5.2** provided such estimates.

In summary, the electrochemical degradation of VFX using platinum electrodes represents a viable and sustainable remediation strategy. It offers distinct advantages in operational stability, environmental safety, and comprehensive ecotoxicological evaluation, supporting its potential application in sustainable pharmaceutical waste management.

5.4 Materials and methods

5.4.1 Materials

Acetonitrile (99.9%), nitric acid (70%), sodium hydroxide (98%), sodium phosphate monobasic (99%), sodium phosphate dibasic (99%), sodium sulfate (99%), ethanol (99.9%), methanol (99.8%) and venlafaxine chloridrate (Pharmaceutical Secondary Standard, certified reference material) were purchased from Sigma-Aldrich (Steinheim, Germany). Powdered alumina was supplied by Buehler (Micropolish II 0.05 μm, deagglomerated gamma alumina). Ultra-pure water used in all the experiments was obtained from a combined Elix5/Milli-Q system (Millipore, S.p.A., Milan, Italy). Platinum foil (99.9%) and graphite plate were obtained from Sigma-Aldrich (Steinheim, Germany). GC plates were purchased from HTW HochtemperaturWerkstoffe GmbH (Thierhaupten, Germany).

5.4.2 Electrochemical Experiments

5.4.2.1 CV and DPV

CV experiments were performed using a 263A potentiostat/galvanostat (EG&G Princeton Applied Research, Princeton, NJ, USA), and data acquisition was conducted with M270 software version 4.23 (EG&G). A conventional three-electrode configuration was employed, consisting of a saturated calomel electrode (SCE) as the reference, a platinum counter electrode, and a working electrode composed of either a GC disk or a platinum disk embedded in a PTFE body. DPV measurements were carried out using a CHI660B potentiostat (Shanghai CH Instrument Company, Shanghai, China).

The GC electrode was cleaned following an optimized procedure described in [288]. Briefly, the surface was mechanically polished using 0.05 μm alumina slurry and subsequently subjected to sequential sonication: first in a 1:1 (v/v) mixture of double-DW and ethanol for 2 min, then in a 1:1 (v/v) mixture of double-DW and nitric acid for 2 min, and finally in double-DW for 2 min. After each sonication step, the electrode was thoroughly rinsed with ultrapure water.

Platinum electrode cleaning was performed according to the protocol reported in [278]. The electrode surface was initially mechanically polished with 0.05 μm alumina and sonicated in double-distilled water. This was followed by chemical cleaning through brief sonication in hot nitric acid (70%). The final step consisted of electrochemical conditioning by CV in 0.5 M sulfuric acid, sweeping the potential between −0.225 V and +1.25 V (vs. SCE) at a scan rate of 100 mV s^{-1} for a sufficient number of cycles to obtain a stable and reproducible current profile.

5.4.2.2 Galvanostatic Electrolysis

Galvanostatic electrolysis experiments for VFX degradation were conducted using a 263A potentiostat/galvanostat (EG&G Princeton Applied Research, Princeton, NJ, USA). A two-electrode configuration was employed, in which a graphite plate (3 mm × 20 mm × 60 mm) served as the cathode, while either a platinum foil (0.127 mm × 25 mm × 25 mm) or a GC plate (1 mm × 20 mm × 40 mm) was used as the anode. Each anode was immersed in 0.1 M sodium sulfate electrolyte at pH 9 (unless otherwise specified), with an exposed surface area of 8 cm^2. The distance between the anode and the cathode was maintained at 2 cm. Experiments were carried out in a 100 mL reactor, and the solution was continuously stirred at room temperature throughout the electrolysis process.

5.4.3 LC-UV Conditions

LC-UV analyses were performed using an Agilent 1200 Series gradient HPLC system (Agilent Technologies, Santa Clara, CA, USA) equipped with a quaternary gradient pump, a DAD (190–950 nm), and a standard autosampler (0.1–100 μL). Separation was carried out on a C18 Supelcosil LC-ABZ column (25 cm × 3 mm, 5 μm; Supelco Inc., Bellefonte, PA, USA) maintained at room temperature. The mobile phase consisted of ultrapure water (A) and acetonitrile (B), using the following gradient program: 0 min, 90% B; 3 min, 80% B; 4–8 min, 70% B; 9 min, 80% B; 10–12 min, 90% B. The flow rate was set to 0.8 mL $min^{-1,}$ and the injection volume was 20 μL. Chromatograms were monitored at 226 nm, and full UV–VIS spectra were acquired between 190 and 400 nm.

5.4.4 LC-MS/MS Analysis

LC-MS/MS analyses of the degraded VFX solutions were performed using an Accela AS HPLC system (Thermo Fisher Scientific, Bremen, Germany) coupled to an LTQ-Orbitrap XL mass spectrometer (Thermo Fisher Scientific, Bremen, Germany) equipped with an ESI source operating in positive ion mode. The optimized source parameters were as follows: spray voltage 4.27 kV, capillary temperature 280 °C, and sheath gas flow rate 80 arbitrary units (AU). Compound identification and fragmentation were performed using full-scan acquisition (m/z 50–500) and data-dependent acquisition (DDA).

For chromatographic separation, the same column, mobile phase, and gradient employed in the LC-UV analyses were used, with a flow rate of 0.8 mL min^{-1} and a 3:1 post-column split. Low-resolution MS^n experiments were performed by CID with collision energies ranging from 30% to 35%.

Data processing was performed using Xcalibur 2.0 (Thermo Fisher Scientific). Mass spectra were imported, processed and plotted with SigmaPlot 10.0 (Systat Software, Inc., London, UK). Chemical structures of the identified compounds and fragment ions were generated using ChemDraw Ultra 12.0 (CambridgeSoft Corporation, Cambridge, MA, USA).

5.4.5 *In Silico* Toxicity Evaluation

The *in silico* toxicological evaluation of VFX and its degradation products was performed using the ECOSAR program based on the chemical structure-toxicity relationship. The degree of acute toxicity is estimated on the LC_{50} of *Daphnia Magna* after 48 h of contact [258]. The ECOSAR package, available for free download from the US EPA website [289], categorizes input compounds into one or more chemical classes. It then applies a hydrophobicity-based Structure-Activity Relationship relevant to the class(es) to predict

ecotoxicity. The logarithm of the octanol: water partition coefficient is used as the input parameter. The SARs establish a correlation between the physicochemical properties of chemicals and their aquatic toxicity. The models incorporate more than 150 SARs, covering over 50 chemical classes. The underlying assumption is that the aquatic toxicity of a compound can be predicted based on known values for similar compounds within the same class.

5.5 Conclusions

This study demonstrated the potential of advanced electrochemical oxidation processes based on galvanostatic electrolysis for purifying water from VFX, a drug included in the 4th EU Watch List due to its widespread occurrence and persistence. A platinum electrode was found to be suitable for this purpose and proved to be a good alternative to the commonly used BDD electrode. It offers the advantage of a well-established cleaning procedure, ensuring high reproducibility of its surface state, and is stable and durable over extended periods of use. The electrochemical degradation of VFX occurred through indirect oxidation by highly reactive species, specifically hydroxyl and sulfate radicals, which were electrochemically generated on the Pt anode during electrolysis.

An HPLC-UV method was used to derive the degradation curve of VFX. The experimental conditions for electrolysis, including electrolyte pH and current density, were optimized. A higher degradation yield of VFX was observed in a 0.1 M Na_2SO_4 solution at pH 9, applying a current density of 25 mA cm^{-2}. Additionally, a concentration-dependent degradation efficiency was observed, with higher efficiency at lower VFX concentrations, consistent with the derived first-order kinetics. Over longer time scales, after 7 h of electrolysis, VFX degradation was found to be satisfactory (94%), even at a concentration of 25 mg L^{-1}.

This study focused on identifying the transformation intermediates of VFX through LC-ESI-MS^n and evaluating their environmental impact. Transformation products are formed mainly through demethylation, dehydration, and hydroxylation/shortening of aromatic and cyclohexane rings. In particular, the hydroxylation reactions of the aromatic and cyclohexane rings yielded three distinct monohydroxylation products, previously identified only in photodegradation processes. Other reactions yielded lower-molecular-weight products, including N-desmethylvenlafaxine and two isomers of the V276 product.

Finally, an *in silico* ecotoxicity assessment using ECOSAR demonstrated that almost all intermediates were less toxic than VFX. Furthermore, the most abundant degradation product (V194) exhibited the lowest toxicity. Consequently, the proposed electrochemical degradation method for VFX removal from contaminated water can be considered environmentally sustainable.

The results presented in this contribution were published in the journal *Molecules* (https://doi.org/10.3390/molecules30091881).

To replace AOPs and minimize the formation of potentially toxic intermediates, adsorption onto natural materials has been explored as a complementary and sustainable strategy for VFX removal from water (Chapter 6). While electrochemical processes rely on the *in situ* generation of reactive oxidizing species, adsorption offers a simpler approach based on the physical or chemical interaction between the contaminant and the adsorbent surface. Natural materials, such as biochars, clays, and agricultural wastes, have attracted attention due to their low cost, availability, and reduced environmental impact. This approach can minimize the formation of potentially toxic transformation products and, although it does not degrade the pollutant, it provides an effective alternative for its removal, particularly in low-cost and environmentally friendly treatment systems.

6. CONTRIBUTION 4

Venlafaxine removal from water and wastewater using activated carbons from spent brewery grains produced by conventional vs. microwave pyrolysis

6.1 Abstract

The recent increase in antidepressant consumption, particularly VFX, combined with the limited effectiveness of conventional wastewater treatment processes, has led to rising environmental concentrations. Adsorption methods have emerged as effective strategies for removing persistent pharmaceuticals without generating harmful by-products. This study aimed to develop and assess two ACs derived from SBG as an efficient material for VFX removal from wastewater. Two pyrolysis methods, conventional and microwave-assisted, were evaluated to assess their influence on the adsorption properties. The materials were characterized through nitrogen physisorption and SEM to evaluate S_{BET}, porosity, and morphology. Their adsorption properties were examined through batch adsorption experiments to analyze kinetic and equilibrium behavior, and the efficacy was evaluated in both ultrapure water and real wastewater. The obtained ACs exhibited high porosity, with the S_{BET} ranging from 1080 to 1197 $m^2\ g^{-1}$. Kinetic studies indicated that adsorption followed a pseudo-second-order model, achieving equilibrium within 1 h. The equilibrium data were optimally described by the Langmuir isotherm, indicating monolayer adsorption, with the maximum adsorption capacity of microwave-assisted AC reaching 74±6 mg g^{-1}. Microwave-assisted AC has shown higher efficiency than conventionally produced AC, demonstrating that this pyrolysis technique can produce materials with enhanced adsorption properties. This study demonstrates that microwave-assisted pyrolysis of an abundant agro-industrial residue yields high-performance materials capable of efficiently removing an antidepressant included in the revised Urban Wastewater Treatment Directive from complex effluents, even at low doses, highlighting a sustainable route to mitigate pharmaceutical contamination in aquatic environments.

6.2 Introduction

Pharmaceuticals are increasingly recognized as contaminants of emerging concern due to their widespread occurrence in aquatic environments and limited removal by conventional WWTPs [104, 290-294]. Their continuous input into water bodies, coupled with biological

activity at low concentrations, has drawn increasing attention to the development of advanced, sustainable treatment strategies.

Among these compounds, the antidepressant VFX is frequently detected in surface waters and wastewater effluents and has therefore been selected as a representative target compound in this study. Its persistence through conventional treatment processes has led to its inclusion in the European Union Water Framework Directive Watch List, where it was first introduced in the 3rd Watch List in 2020 and subsequently retained in the 4th edition in 2022. More recently, it has also been considered within the broader regulatory framework addressing pharmaceutical micropollutants, such as the Urban Wastewater Treatment Directive (EU) 2024/3019 [18-19, 295].

Adsorption-based processes are widely regarded as an effective and operationally simple approach for removing pharmaceuticals from water [296-297]. In particular, ACs remain among the most efficient adsorbents, provided that their textural properties and surface chemistry are appropriately tailored [21, 298-299]. In this context, increasing emphasis has been placed on the use of agro-industrial residues as sustainable precursors for AC production, aiming to reduce both environmental impact and material costs.

SBG, the main by-product of the brewing industry, is an abundant, largely underutilized lignocellulosic biomass with an estimated global production of approximately 39 million tons per year [300]. Recent studies have demonstrated that MP constitutes an efficient alternative to conventional thermal treatments, enabling rapid and uniform heating, enhanced pore development, and reduced energy consumption [301-303].

Accordingly, this chapter investigates the synthesis of SBG-derived ACs via CP and MP using potassium carbonate as the activating agent and evaluates their adsorption performance toward VFX. The materials were systematically characterized, and their adsorption behavior was assessed through batch experiments conducted in both ultrapure water and real wastewater matrices, providing insight into the influence of pyrolysis route on adsorption efficiency and supporting the sustainable valorization of brewery residues for water treatment applications.

6.3 Materials and Methods

6.3.1 Reagents and Chemicals

The reagent used in the chemical activation process was potassium carbonate (K_2CO_3, AnalaR normapur, 99.9%). For washing the produced material, hydrochloric acid (HCl, Honeywell FLUKA, 37.0%) was employed. HCl, sodium hydroxide (NaOH, José Manuel

Gomes dos Santos, 99.3%), and sodium chloride (NaCl, Fluka, ≥99.5%) were used to determine the PZC.

Venlafaxine hydrochloride (TCI, 98%) was the pharmaceutical used for adsorption experiments. For HPLC analyses, acetonitrile and methanol (both HPLC grade) were obtained from Fisher Scientific, while HCl (37%) was supplied by Honeywell FLUKA, as previously referred. Ultrapure water was sourced from an Elga Purelab Flex 4 purification system (Veolia).

6.3.2 Carbon adsorbents production

SBG was collected from Brewery Faustino Microcervejeira, Lda (Aveiro, Portugal), dried at room temperature, and then burned for 24 hours at 100 °C. 570 g of SBG were ground using a blade mill and impregnated with K_2CO_3 at an activating agent/SBG 1:2 mass ratio, using a 0.15 g m L^{-1} solution of K_2CO_3. The mixture was then stirred in an ultrasonic bath for 1 hour and left to dry at room temperature for several days. A portion of the dried impregnated material was carbonized under a nitrogen atmosphere in a muffle furnace (Nüve, series MF 110, Turkey), heated at a rate of 10 °C min^{-1} until it reached 800 °C, with a 2-hour residence time at this temperature, resulting in the SBG-AC-CP material. The other portion was carbonized in a microwave furnace (CEM Phoenix™ AirWave) at 800 °C (heating rate of 15 °C min^{-1}) for 20 minutes, resulting in the material named SBG-AC-MP. The resulting materials were washed with approximately 1.2 M HCl, followed by distilled water, until the leachate reached a pH around 6. Finally, the produced SBG-AC-CP and SBG-AC-MP were dried overnight at 50 °C, crushed, and sieved to obtain a fine powder with a particle size ≤ 180 μm. The materials were stored in a desiccator to ensure dryness and preserve their physicochemical stability. The yield of production (η) of both carbon adsorbents produced was calculated by Eq. 6.1:

$$\eta\ (\%) = \frac{\text{final mass of carbon adsorbent (g)}}{\text{mass of precursor (g)}} \text{ x } 100 \qquad (6.1)$$

Both materials were used for VFX removal, with batch adsorption studies to evaluate kinetic and equilibrium system parameters, as described in the next sections.

6.3.3 Carbon adsorbents characterization

Both SBG-AC-CP and SBG-AC-MP samples were characterized by PZC determination, SEM, and N_2 adsorption isotherms to determine the specific surface area and pore distribution. The PZC of SBG-AC-CP and SBG-AC-MP was determined using a batch equilibration method. A series of 0.1 M NaCl solutions with pH values ranging from 2 to 11 was prepared. The initial pH (pH_i) was adjusted using 0.1 M, 0.01 M, or 0.001 M HCl and 0.1 M, 0.01 M, or 0.001 M NaOH, while maintaining a constant ionic strength. Subsequently, 30

mL of each solution was transferred into polypropylene tubes containing either 1.5 mg of SBG-AC-CP or 1.5 mg of SBG-AC-MP (corresponding to a final dosage of 50 mg L^{-1}), and the tubes were shaken at 80 rpm for 24 h. The final pH (pH_f) was then measured, and the PZC was determined by plotting ΔpH ($pH_f - pH_i$) versus pH_i. The PZC corresponds to the pH value at which the curve intercepts the x-axis ($pH_i = pH_f$).

S_{BET} of the produced materials was determined using a Micromeritics Gemini VII 2380 instrument at 77 K. Before analysis, the samples were degassed at 120 °C. Nitrogen adsorption–desorption measurements were performed using liquid nitrogen at −196 °C. The total pore volume was estimated at a relative pressure of 0.99. The BET equation [146] was applied within a relative pressure range of 0.001–0.1 to calculate S_{BET}. Microporosity (W_0) was evaluated from the low relative pressure region of the nitrogen adsorption isotherm using the D-A equation [147]. The average micropore width (L) was obtained from the Stoeckli–Ballerini equation [148]. The average pore diameter (D) was calculated according to the following equation [304]:

$$D = 2x \frac{V_p}{S_{BET}} \quad (6.2)$$

SEM images were obtained at magnifications of 700×, 15,000×, and 35,000×. A Hitachi SU70 scanning electron microscope (operated at 1, 3, and 30 kV) was employed to capture micrographs of the microstructure of the produced materials. Before analysis, the samples were dispersed onto a thin carbon film using a carbon rod coater (Emitech K950X).

6.3.4 Wastewater sampling

Wastewater samples were collected in June 2025 from a local urban WWTP in Aveiro, Portugal. The samples corresponded to the final effluent, obtained after biological treatment. Immediately after collection, to remove suspended organic matter, the effluent was filtered through 0.45 μm cellulose Supor-450 membrane disc filters under vacuum. The filtered samples were stored in the dark at 4 °C and used within 15 days. The effluent was characterized by measuring pH with a Hanna Instruments HI2020-02 pH meter, yielding a value of 7.7 ± 0.1. Other physicochemical parameters were also measured for the collected wastewater, including conductivity (2.7 mS cm^{-1}), resistivity (0.0004 MΩ ·cm), salinity (1.4 PSU), dissolved oxygen (7.8 mg L^{-1}), and redox potential (38.9 mVORP) at 21.9°C. The measured Total Organic Carbon (TOC) is 12.8 ± 0.3 mg L^{-1}, and the concentration of humic acids is 25.5 ± 0.5 mg L^{-1}, both calculated as the average of 3 replicates.

6.3.5 Adsorption experiments

6.3.5.1 Preliminary tests

To evaluate the adsorptive performance of the produced materials for VFX removal from ultrapure water and wastewater, batch adsorption experiments were conducted under controlled temperature and shaking conditions. Preliminary adsorption tests were performed to determine the optimal dose for each material for subsequent kinetic and isothermal studies. A VFX solution with an initial concentration of 5 mg L^{-1} was prepared in ultrapure water and distributed into polypropylene tubes containing three different adsorbent masses, corresponding to final doses of 25, 50, and 75 mg L^{-1}. Samples were stirred in an overhead shaker (Heidolph Reax 2) at 80 rpm for 24 h at 25.0 ± 0.1 °C.

Following shaking, aliquots of the samples were filtered through 0.22 μm PVDF filters (Whatman) and analyzed by HPLC-FLD, as described in Section 2.5. Based on the adsorption percentages obtained in the preliminary test, the adsorbent dose yielding 40–60% removal was selected for further kinetic experiments to ensure meaningful adsorption and feasible VFX analysis in the aqueous phase. All tests (preliminary, kinetic, and equilibrium) were performed in triplicate, with pharmaceutical-solution controls (without adsorbent) used as references for adsorption percentage calculations according to Eq. 6.3.

$$\text{Adsorption (\%)} = \frac{C_c - C_f}{C_c} x\ 100 \qquad (6.3)$$

where C_c (mg L^{-1}) is the concentration of pharmaceutical in the corresponding control experiments (from now on, taken as the initial pharmaceutical concentration) and C_f (mg L^{-1}) is the remaining pharmaceutical concentration in the liquid phase at the end of the adsorption experiment with each material.

Additionally, batch adsorption experiments in wastewater were conducted to evaluate the effects of matrix and competitive components in real effluents on the adsorptive performance of two materials for the removal of the antidepressant drug. Preliminary tests on wastewater were conducted in the same manner as those on ultrapure water, using higher adsorbent doses.

6.3.5.2 Adsorption kinetics

To determine the time required to reach adsorption equilibrium, a fixed adsorbent dose was contacted with 30 mL of a 5 mg L^{-1} aqueous VFX solution, prepared in either ultrapure water or wastewater. Kinetic experiments were performed as described in Section 6.3.5.1, using an adsorbent dose of 50 mg L^{-1} for both materials and matrices. Each polypropylene tube contained 30 mL of the VFX solution and 1.5 mg of SBG-AC-CP or SBG-AC-MP rigorously

weighed in a microbalance, and was shaken for varying contact times ranging from 5 to 240 min. The amount of VFX adsorbed at time *t* (q_t, mg g^{-1}) was calculated using Eq. 6.4. Experimental data were fitted to the pseudo-first order model and the pseudo-second order model [290], as depicted in Eqs. 6.5 and 6.6, respectively, to determine the kinetic parameters for each system:

$$q_t = \frac{(C_c - C_t)V}{m} \quad (6.4)$$

$$q_t = q_e(1\text{-}e^{-k_1 t}) \quad (6.5)$$

$$q_t = \frac{q_e^2 k_2 t}{1 + k_2 q_e t} \quad (6.6)$$

Where C_c (mg L^{-1}) is the initial pharmaceutical concentration, C_t (mg L^{-1}) is the concentration of pharmaceutical in solution at time *t*, *V* (L) is the volume of solution, *m* (g) is the mass of adsorbent, q_e (mg g^{-1}) refers to the amount of adsorbate per unit mass of adsorbent at equilibrium, k_1 (min^{-1}) is the pseudo-first order rate constant and k_2 (g mg^{-1} min^{-1}) is the pseudo-second order rate constant. Non-linear fittings were performed using GraphPad Prism, version 8.0.2.

6.3.5.3 Adsorption equilibrium

For adsorption isotherm determination, solutions were shaken for 240 min to ensure equilibrium, while varying the adsorbent dose and keeping the initial VFX concentration constant at 5 mg L^{-1}. Briefly, aqueous VFX solutions (5 mg L^{-1}) prepared in either ultrapure water or wastewater were combined with varying amounts of each carbon adsorbent. In ultrapure water, the dose of SBG-AC-CP ranged from 15 to 125 mg L^{-1}, whereas for SBG-AC-MP it ranged from 5 to 125 mg L^{-1}; in wastewater, the range for SBG-AC-MP was 5 to 90 mg L^{-1}. At least eight different doses were tested for each system to determine the adsorbed concentration of the adsorbate at equilibrium (q_e, mg g^{-1}), calculated according to Eq. 6.7. Experimental data were fitted to the non-linear Langmuir and Freundlich models, expressed in Eqs. 6.8 and 6.9, respectively [291-292]:

$$q_e = \frac{(C_c - C_e)V}{m} \quad (6.7)$$

$$q_e = \frac{q_m \times K_L \times C_e}{1 + K_L \times C_e} \quad (6.8)$$

$$q_e = K_F \times C_e^{(\frac{1}{N})} \quad (6.9)$$

Where C_e (mg L^{-1}) is the concentration of VFX in the solution at the equilibrium; q_m (mg g^{-1}) is the Langmuir maximum adsorption capacity of each material towards VFX; K_L (L

mg^{-1}) is the Langmuir equilibrium constant; K_F (mg g^{-1} (L $mg^{-1})^{1/N}$) is the Freundlich equilibrium constant; *N* is the degree of nonlinearity; and all the other variables are defined as in Eqs. 6.4, 6.5, and 6.6. Non-linear regression and parameter estimation for both models were performed using GraphPad Prism version 8.0.2.

6.3.6 Chromatographic analyses

The residual VFX concentration in the aqueous phase after the adsorption tests was determined by HPLC-FLD. Analyses were performed using a Shimadzu LC-20AD Prominence system (model DGU-20A5), equipped with a DGU-20A5 Prominence degasser, an LC-20AD Prominence high-pressure pump, and a CTO-10ASVP column oven, coupled to an ESA Inc. model 542 autosampler. Separation was achieved on an ACE5 C18 column (5 µm, 150 × 4.6 mm).

The mobile phase consisted of acidified water containing 0.37% (v/v) HCl and acetonitrile (60:40, v/v), delivered at a flow rate of 0.8 mL min^{-1}. The injection volume was 20 µL, and the total run time was 7 min. Both the acidified water and acetonitrile were filtered through 0.22 µm membrane filters (Whatman) before use.

VFX detection was performed using an RF-20A XS Prominence fluorescence detector equipped with an Xe lamp, with an excitation wavelength of 230 nm and an emission wavelength of 298 nm [305]. The calibration curve was constructed by analyzing standard VFX solutions with concentrations ranging from 0.10 to 5.0 mg L^{-1}, prepared in ultrapure water. All standards were filtered through 0.22 µm PVDF filters (Whatman) before injection and analyzed in triplicate. The limits of detection and quantification were calculated using Eqs. 6.10 and 6.11, respectively:

$$\text{LOD} = \frac{3.3 \cdot \sigma}{b} \tag{6.10}$$

$$\text{LOQ} = \frac{10 \cdot \sigma}{b} \tag{6.11}$$

where σ is the SD of the intercept and *b* is the slope of the calibration curve [293]. Linearity was calculated by Eq. 6.12:

$$\text{Lin}(\%) = 100 - RSD_b \tag{6.12}$$

Where RSD_b is the relative standard deviation of the curve's slope (in percentage) [294].

6.3.7 Statistical treatment of data

Statistical comparisons of adsorption data were performed using a t-test at the 95% confidence level to evaluate differences in performance among materials within the same

matrix, as well as variations in a single material's behavior across different matrices (ultrapure water and wastewater).

6.4 Results and discussion

6.4.1 Production and characterization of carbon adsorbents

The production yield was calculated using Eq. 6.1. The yields obtained for SBG-AC-CP and SBG-AC-MP were approximately 7% and 3%, respectively. Among the steps involved in material production, the washing stage inevitably resulted in material losses due to the removal of the inorganic fraction. Since this fraction does not contribute to the adsorptive performance of the materials, its removal leads to lower apparent yields when expressed per unit mass of adsorbent.

The low yields observed for both materials may also be attributed to enhanced losses of volatile organic matter resulting from the use of K_2CO_3 as a chemical activating agent. This activation agent effectively promotes the release of volatile species and the development of a porous structure, as further confirmed by S_{BET} analysis, which is highly desirable for the application considered in this study.

The PZC was determined to assess the net surface charge of the materials. A low PZC is generally associated with a high concentration of acidic surface functional groups. For SBG-AC-CP and SBG-AC-MP, the PZC values were acidic, approximately 4.0 and 3.5, respectively. This behavior is likely attributable to chemical activation with K_2CO_3, which promotes the incorporation of oxygen-containing functional groups on the carbon surface. In contrast, Sousa et al. (2020) reported neutral to slightly basic PZC values for ACs prepared from SBG via CP and chemical activation with KOH [104].

Since the surface charge of ACs depends on both solution pH and PZC, the surface is predominantly positively charged at pH values below the PZC and predominantly negatively charged at pH values above the PZC. At the working pH values employed in this study (approximately 6 for ultrapure water and 7.7 for wastewater), the surfaces of both materials are therefore mainly negatively charged. Consequently, differences in surface charge between the two materials are not expected to play a major role in their adsorption performance under the investigated conditions.

To investigate the textural properties of the materials, nitrogen adsorption isotherms and SEM analyses were performed. The main textural parameters of the produced materials, including specific surface area, total pore volume, micropore volume, average micropore width, and average pore diameter, are reported in **Table 6.1**.

Table 6.1 *Specific surface area (S_{BET}) and textural parameters of the produced ACs (SBG-AC-CP and SBG-AC-MP), including total pore volume (V_p), micropore volume (W_0), average micropore width (L), and average pore diameter (D).*

AC	S_{BET} ($m^2\ g^{-1}$)	Vp ($cm^3\ g^{-1}$)	D (nm)	Dubinin-Astakhov	
				W_0 ($cm^3\ g^{-1}$)	L (nm)
SBG-AC-CP	1080	0.48	0.88	0.43	1.47
SBG-AC-MP	1197	0.62	1.03	0.57	1.73

The S_{BET} values for SBG-AC-CP and SBG-AC-MP were 1080 and 1197 $m^2\ g^{-1}$, respectively. A similar trend was observed for the total pore volume *V*p and micropore volume W_0, both of which, although slightly, were higher for SBG-AC-MP than for SBG-AC-CP. These textural characteristics are expected to influence the adsorptive capacity of the materials positively.

SBG-AC-MP exhibited a slightly higher S_{BET} than SBG-AC-CP, indicating that MP enhances microporosity development to a greater extent than CP, as it promotes faster, more homogeneous heating of the precursor material, thereby facilitating the formation of a microporous network. The data obtained in this thesis are consistent with findings from other studies, such as that of Sousa et al. (2020), which reported that ACs were produced from CP of SBG after chemical activation with KOH, sodium hydroxide (NaOH), or phosphoric acid (H_3PO_4) [104]. Different pyrolysis temperatures and residence times were tested; at 800 °C and a 150-minute residence time, the S_{BET} values obtained with KOH, NaOH, and H_3PO_4 activation were 1090 $m^2\ g^{-1}$, 18 $m^2\ g^{-1}$, and 14 $m^2\ g^{-1}$, respectively [104]. Only the KOH-activated AC exhibited a specific surface area (1090 $m^2\ g^{-1}$) comparable to those of the ACs produced in this thesis (1080 $m^2\ g^{-1}$ for SBG-AC-CP and 1197 $m^2\ g^{-1}$ for SBG-AC-MP). The formation of microporosity in ACs derived from SBG has also been reported in previous studies [306]. Sieradzka et al. (2022) demonstrated that the brewery grains precursor in its raw form, and the biochar obtained by CP at 400 °C with and without KOH chemical activation, exhibited S_{BET} values of 0.36 $m^2\ g^{-1}$, 0.67 $m^2\ g^{-1}$, and 2619 $m^2\ g^{-1}$, respectively. These results highlight the crucial role of chemical activation in producing ACs with high specific surface areas, thereby ensuring good adsorption performance and favorable removal efficiencies. However, this high S_{BET} is generally achieved through a two-step pyrolysis process (pyrolysis followed by impregnation and pyrolysis), which has a significant impact on energy consumption during the process [306]. In the present study, milder conditions were used to pursue a more sustainable approach (e.g., microwave-assisted pyrolysis). In other studies, such as that by Fontana et al. (2016), SBG was used in its raw form - merely dried, crushed, and sieved - resulting in an S_{BET} of 0.8246 $m^2\ g^{-1}$ [307]. This further emphasizes that the precursor by itself (without chemical

activation and thermal treatment) is insufficient to yield a material with the properties of an effective adsorbent. Gómez-Delgado et al. (2025) developed ACs from SBG for the removal of azo dye Orange II by treating it with NaOH at different mass ratios (1:1 up to 3:1) and activating at temperatures from 400 to 600 °C as CP with chemical activation, achieving BET surface areas ranging from 3.46 to 466 m^2 g^{-1} [308].

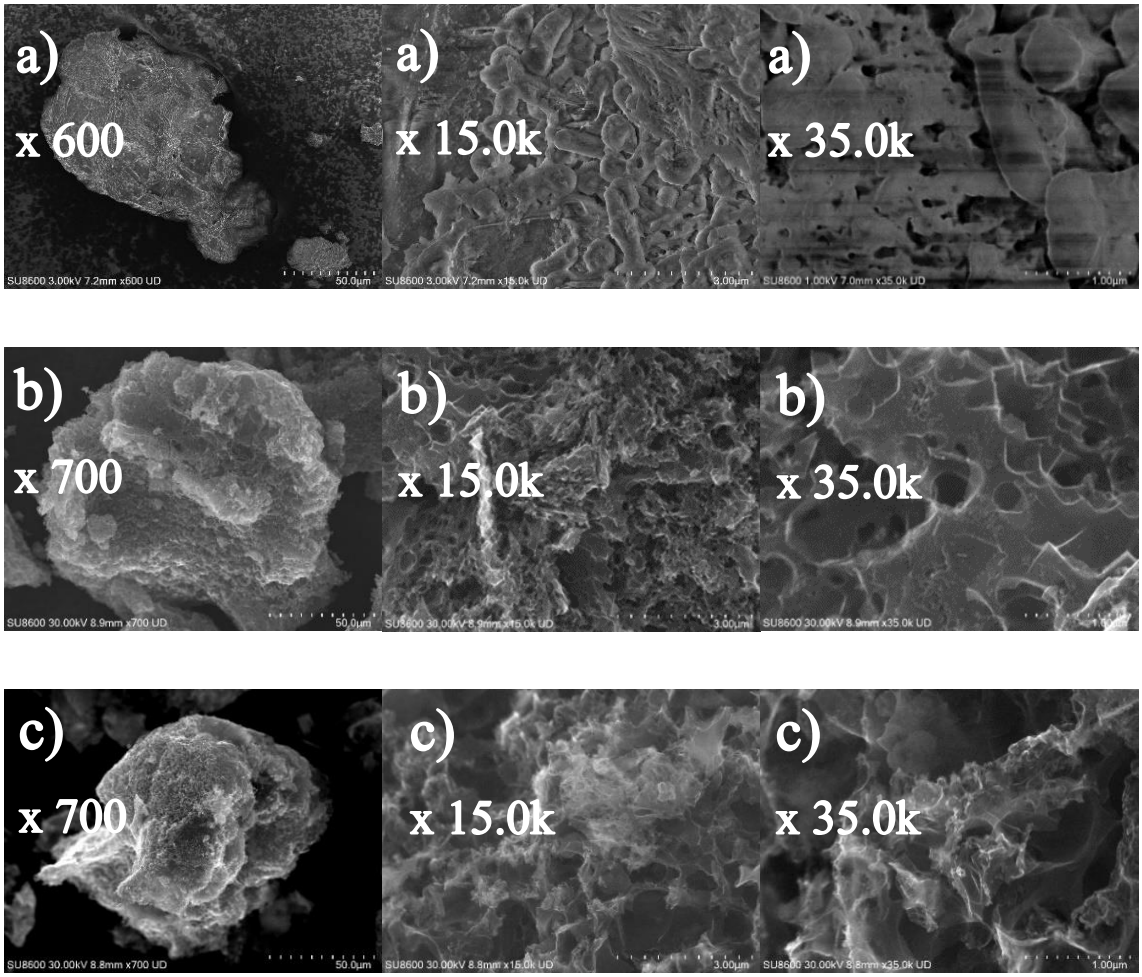

Figure 6.1 *SEM images of a) the precursor SBG, b) SBG-AC-CP, and c) SBG-AC-MP.*

SEM images obtained for the precursor and SBG-AC-CP and SBG-AC-MP (**Figure 6.1**) reveal clear differences in surface morphology among them. The surface of the precursor SBG appears homogeneous and smooth, with no evident porous structure. In contrast, both ACs display much rougher surfaces with well-developed porosity, which is favorable for effective adsorbent–adsorbate interactions, as confirmed by the high S_{BET}, Vp, and W_0 values reported in **Table 6.1**.

6.4.2 Chromatographic analyses

The quantification of VFX in the remaining water (ultrapure water and wastewater) following adsorption tests with SBG-AC-CP and SBG-AC-MP was performed by HPLC-FLD using the conditions described in Section 6.3.6. The LOD and the LOQ obtained for VFX calibration were 0.10 and 0.31 mg L^{-1}, respectively, with a linearity of 99 %.

6.4.3 Adsorption experiments

6.4.3.1 Preliminary tests

Figure 6.2 shows the histogram-like plot of the % adsorption of VFX onto two SBG-AC-CP and SBG-AC-MP in ultrapure water and wastewater, at different material doses. Both SBG-AC-CP and SBG-AC-MP demonstrated high performance even at very low adsorbent doses. After 24 h of contact between the adsorbent and VFX, in ultrapure water, the percentage removal was 63±4% for SBG-AC-CP and 62±3% for SBG-AC-MP, using an adsorbent dose of only 50 mg L^{-1} (**Figure 6.2a**). The two materials exhibited equivalent adsorptive performance in VFX removal from ultrapure water: a statistical comparison of these data (*t*-test, at 95% confidence level) revealed that there are no significant differences for adsorption of VFX onto SBG-AC-CP and SBG-AC-MP (T_{cal} (0.96) < T_{tab} (2.12), where T_{cal} represents the calculated *t* value, while T_{tab} is the tabulated value taken from the Student's *t*-table). In particular, the presence of hydroxyl and methoxy substituents in VFX's structure enables hydrogen bonding with oxygen-containing surface groups (carboxyl, hydroxyl, carbonyl) on the adsorbent. At the same time, π–π interactions can occur between the aromatic moiety of VFX and the graphitic domains of carbon materials, further enhancing adsorption [21]. Thus, the adsorption mechanism of VFX is typically governed by a combination of hydrophobic partitioning, electrostatic interactions, hydrogen bonding, and π–π stacking [309]. For both materials, a dose of 50 mg L^{-1} was selected for subsequent kinetic tests in ultrapure water.

Wastewater was also used to evaluate the adsorptive performance of the two materials under more realistic and representative conditions. To assess the adsorption capacity of the materials in wastewater, three adsorbent doses (150, 200, and 250 mg L^{-1}), higher than those used in ultrapure water, were applied, as the competitive and inhibitory effects of the real matrix must be considered, which may reduce the adsorption capacity of the materials. For SBG-AC-MP, complete VFX removal was achieved at all three doses (below LOQ), rendering the drug peak undetectable by HPLC-FLD. Consequently, the doses for SBG-AC-MP were subsequently reduced to 50, 75, and 100 mg L^{-1}.

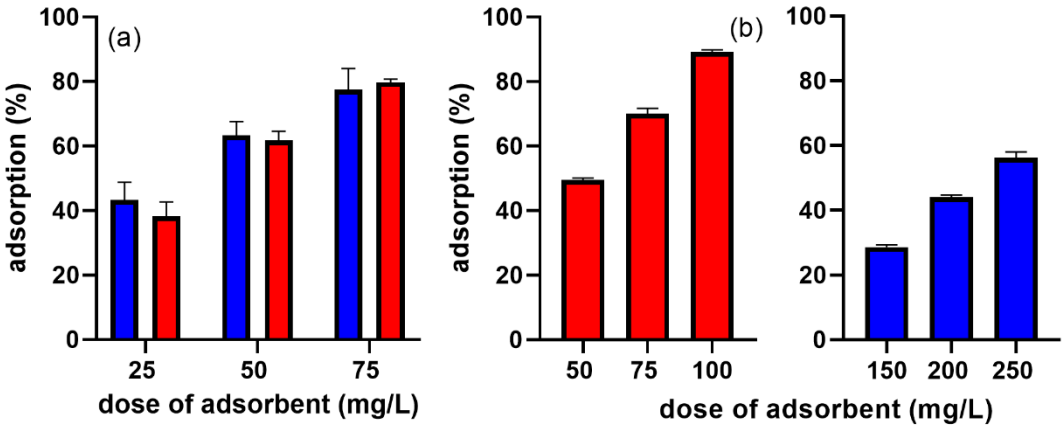

Figure 6.2 *Adsorption percentage of VFX (5 mg L⁻¹) in ultrapure water (a) and in wastewater (b) at different doses of adsorbent materials, using SBG-AC-CP (blue) and SBG-AC-MP (red).*

The adsorption percentages of the two materials for VFX in wastewater differed markedly (**Figure 6.2**): in both cases, the removal efficiency increased as the adsorbent dose increased, but for SBG-AC-MP, a dose of 50 mg L^{-1} was sufficient to achieve ~50% VFX removal, whereas SBG-AC-CP required substantially about fivefold higher doses. Thus, although the adsorption performance is similar in ultrapure water, when comparing the two materials in wastewater, the performance gap becomes evident, highlighting the importance of testing matrices relevant to the target application, as extrapolation of results can lead to erroneous conclusions.

SBG-AC-MP achieved 62±3% and 49.5±0.6% VFX removal in ultrapure water and wastewater, respectively, using the same dose of 50 mg L^{-1}. The lower removal in wastewater is due to matrix effects. A statistical comparison of these data (*t*-test, at 95% confidence level) revealed that SBG-AC-MP exhibited equivalent adsorptive performance in VFX removal from ultrapure water and wastewater: there are no significant differences for adsorption of VFX onto SBG-AC-MP in ultrapure water and wastewater (T_{cal} (1.90) < T_{tab} (2.12)). The situation is different for SBG-AC-CP: at a dose of 50 mg L-1, it achieved 63±4% removal, but an adsorbent dose of at least 200 mg L-1 was required to achieve more than 40% VFX removal in wastewater. These results highlight the better adsorption capacity of SBG-AC-MP and its superior robustness under realistic conditions.

Differences in adsorption between wastewater and ultrapure water can be explained by inhibitory and matrix effects, as well as by the interplay between VFX protonation and the materials' PZC. Because VFX has a p*K*a of 9.6, the Henderson–Hasselbalch equation indicates that at pH 6 of ultrapure water, VFX will be predominantly in its protonated form, enabling strong electrostatic attraction with the negatively charged AC surfaces, in accordance with the higher % of removal for this matrix. In wastewater (pH 7.7), a lower fraction of VFX remains

protonated, reducing potential attractive electrostatic interactions and consequently lowering adsorption, as previously demonstrated. However, the decline is less severe for SBG-AC-MP: these features enhance the accessibility and strength of adsorbate–adsorbent interactions, allowing SBG-AC-MP to perform effectively even under matrix-limited conditions. As a result, kinetic and equilibrium studies in wastewater were carried out only for SBG-AC-MP, as it showed the most promising material in terms of both adsorption performance and energy-efficient production.

6.4.3.2 Adsorption kinetics

Based on the preliminary tests (Section 6.4.3.1), a dose of 50 mg L^{-1} was selected for all kinetic experiments. To determine the time required to reach adsorption equilibrium of VFX onto SBG-AC-MP, kinetic studies were conducted in ultrapure water and wastewater, and onto SBG-AC-CP in ultrapure water. The graphical representation of the experimental kinetic results (q_t (mg g^{-1}) vs. time (min)) is shown in **Figure 6.3**, together with the fitting curves of the applied mathematical models (Eqs. 6.5 and 6.6, Section 6.3.5.2). The kinetic data for VFX adsorption onto SBG-AC-MP and SBG-AC-CP were fitted to both the pseudo-first-order and pseudo-second-order models.

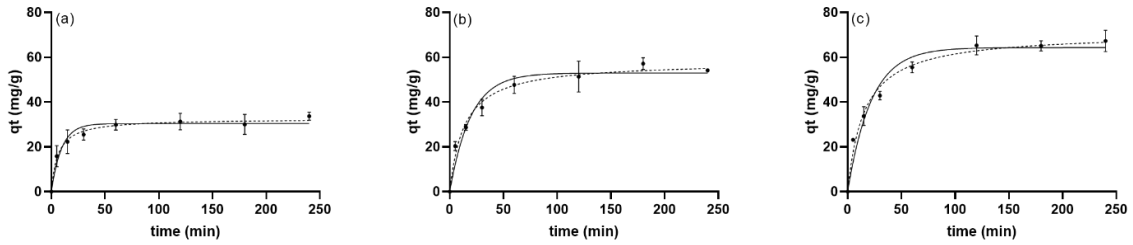

Figure 6.3 *Kinetic fittings for the experimental data of VFX adsorption onto SBG-AC-CP in ultrapure water (a), SBG-AC-MP in ultrapure water (b), and SBG-AC-MP in wastewater (c). The results were fitted to the pseudo-first-order (solid lines) and pseudo-second-order (dashed lines) kinetic models. Each data point (± SD) represents the mean of three replicates. Experimental conditions: VFX concentration 5 mg L^{-1}; adsorbent dose 50 mg L^{-1}; stirring at 80 rpm; temperature 25.0 ± 0.1 °C.*

Table 6.2 summarizes the kinetic parameters obtained from fitting the experimental data to the pseudo-first-order and pseudo-second-order models for VFX adsorption onto SBG-AC-CP and SBG-AC-MP in ultrapure water and wastewater.

Table 6.2 *Fitting parameters of the pseudo-first-order and pseudo-second-order kinetic models applied to the experimental data for VFX adsorption onto SBG-AC-CP and SBG-AC-MP in ultrapure water and wastewater. n denotes the number of data points used for the fitting.*

		Ultrapure water		Wastewater
		SBG-AC-CP	**SBG-AC-MP**	**SBG-AC-MP**
Kinetics models				
Pseudo-first-order	q_e (mg g^{-1})	30±1	53±2	64±3
	k_1 (min^{-1})	0.10±0.02	0.05±0.01	0.045±0.008
	r^2	0.9537	0.9578	0.9600
	n	8	8	8
	S_{xy}	2.584	4.387	5.193
Pseudo-second-order	q_e (mg g^{-1})	32.6±0.8	58±2	71±2
	k_2 (mg g^{-1} min)	0.0050±0.0008	0.0012±0.0002	0.0009±0.0002
	r^2	0.9877	0.9844	0.9858
	n	8	8	8
	S_{xy}	1.332	2.663	3.092

Comparing the kinetic profiles of SBG-AC-CP and SBG-AC-MP, as well as their performance in ultrapure water and wastewater systems, enables assessment of both the production process and the solution matrix on the adsorption rate. Across all systems, the pseudo-second-order model yielded a superior fit, as indicated by higher determination coefficients (r^2) and lower residual errors S_{xy} (**Table 6.2**). Although the pseudo-first-order model yields r^2 values above 0.95 for all experimental conditions, it less accurately represents the data than the pseudo-second-order model ($r^2 > 0.98$). This was further evidenced by the higher S_{xy} values obtained for the pseudo-first-order fitting (2.584, 4.387, and 5.193) relative to those for the pseudo-second-order fitting (1.332, 2.663, and 3.092). Consequently, the pseudo-second-order model was selected for further discussion. According to this model, the adsorbed concentration at the equilibrium q_e for VFX removal was 32.6±0.8 mg g^{-1} for SBG-AC-CP in ultrapure water, 58±2 mg g^{-1} for SBG-AC-MP in ultrapure water, and 71±2 mg g^{-1} for SBG-AC-MP in wastewater, all obtained under the same conditions, including material dose. As shown in **Figure 6.3** and **Table 6.2**, VFX adsorption onto both materials proceeded relatively rapidly, with equilibrium reached in 1 h. In all cases, a steep increase in q_t values was observed during the first ~30 min, in both ultrapure water and wastewater, indicating a fast initial uptake phase driven by the abundance of readily accessible active sites on the adsorbent surface. SBG-AC-CP in ultrapure water exhibited a slower approach to equilibrium and a lower q_e than SBG-AC-MP, underscoring the role of preparation method and resulting textural properties in determining the adsorption performance of the chosen materials. These findings indicate that

the chemical activation method and the thermal treatment led to favorable textural characteristics in the adsorbent, and that, together with the solution chemistry, they synergistically influence the adsorption kinetics of VFX.

For all experimental conditions investigated in this thesis, encompassing ultrapure water and actual wastewater matrices, the pseudo-second-order model yielded better outcomes. The adsorption kinetics obtained in this study for VFX are fully aligned with those reported by other studies [103, 310-312]. **Table 6.3** summarizes literature data on the adsorption kinetics of various organic contaminants from ACs derived from SBG, reporting pseudo-first-order and pseudo-second-order rate constants, correlation coefficients, and best-fit models, and provides a direct comparison with the findings of the present study. These referred studies, involving structurally diverse contaminants, such as tartrazine, acetaminophen, sulfamethoxazole, trimethoprim, ciprofloxacin, and carbamazepine, consistently indicate that adsorption onto AC is better described by the pseudo-second-order kinetic model, with reported correlation coefficients generally exceeding 0.94 [103, 310-312]. For example, Castro et al. (2022) studied the adsorption of the tartrazine yellow dye onto ACs obtained by CP. In this case as well, the pseudo-second-order model described the adsorption kinetics better than the first-order model [310]. Similarly, in a study of Araújo et al. (2020), the adsorption of acetaminophen onto KOH-activated hydrochar from SBG produced by hydrothermal carbonization was investigated. Neither raw SBG nor the corresponding non-activated hydrochar exhibited significant acetaminophen removal compared with the activated hydrochar, indicating that adsorption capacity was generated only through the activation process. In contrast, activated hydrochar derived from SBG showed high removal efficiencies, reaching 95.14% at an initial acetaminophen concentration of 50 mg L^{-1}. The adsorption kinetics of acetaminophen onto activated hydrochar from SBG revealed a rapid increase in adsorption capacity during the initial minutes, followed by a slight decrease after 30 min. After approximately 60 min, the adsorption capacity stabilized at around 20 mg g^{-1}, indicating that equilibrium had been reached. The kinetic data were well described by the pseudo-second-order model [103]. In the study of Sousa et al. (2023), sulfamethoxazole and trimethoprim adsorbed onto microwave-assisted carbons at pH 8 followed a pseudo-second-order model, with relatively low rate constants (k_2 = $3.6 \cdot 10^{-4}$ and $1.1 \cdot 10^{-4}$ $g \cdot mg^{-1} \cdot min^{-1}$, respectively), while ciprofloxacin followed a pseudo-first-order model with k_1 = 0.21 min^{-1} [311]. In the study by Apinyakul et al. (2024), carbamazepine adsorbed onto hydrothermally produced carbon at neutral pH also showed that the pseudo-second-order model provided an excellent fit (r^2 = 0.995) [312].

The overall findings from the present study provided the basis for subsequent equilibrium studies aimed at quantifying the maximum adsorption capacities.

Table 6.3 *Operating conditions, adsorption kinetics, and isotherm parameters of ACs derived from SBG: literature reports versus the SBG-AC-MP synthesized in this study. The abbreviations AMP, SMX, TMP, CFX, and CBZ mean "acetaminophen", "sulfamethoxazole", "trimethoprim", "ciprofloxacin", and "carbamazepine", respectively; the abbreviations Conv., Hydr. M-A mean "conventional", "hydrothermal", and "microwave-assisted", respectively; the abbreviations PFO and PSO mean "pseudo-first-order" and "pseudo-second-order", respectively; the abbreviation L means "Langmuir". The dose of adsorbate reported in the table refers to that used in the adsorption kinetic and isotherm tests. The dose of adsorbent reported in the table refers to that used in the adsorption kinetic tests.*

Adsorbate and dose	**Type of pyrolysis**	**Activating agent**	**S_{BET} m^2g^{-1}**	**Adsorbent dose (mg L^{-1})**	**Type of matrix (pH)**	**k_1 min^{-1}**	**r^2 PFO**	**k_2 $g \cdot mg^{-1} \cdot min^{-1}$**	**r^2 PSO**	**Best-Fit Model**	**q_m mg g^{-1}**	**Best-fit isotherm**	**r^2**	**Reference**
Tartrazine yellow dye (10 mg L^{-1})	Conv.	H_3PO_4/ SBG 1:1 ratio	769	2000	Water adjusted (pH 3)	0.12	0.88	0.04	0.94	PSO	32	L	0.89	[310]
AMP (250 mg L^{-1})	Hydr.	KOH/ SBG 4:1 ratio	1513	1000	Not specified	0.78	0.992	0.008	0.999	PSO	318	L	0.999	[103]
SMX	M-A	K_2CO_3/ SBG 1:2 ratio	929	15	Ultrapure water (pH 8)	0.11	0.959	$3.6 \cdot 10^{-4}$	0.992	PSO	434	Both	0.995	[311]
TMP						0.04	0.973	$1.1 \cdot 10^{-4}$	0.987	PSO	880		0.970	
CFX (20 µmol L^{-1})						0.21	0.974	$14 \cdot 10^{-4}$	0.939	PFO	418		0.990	
CBZ (300 mg L^{-1})	Hydr.	KOH: NaCl (1:1; w/w)	906	1000	Water adjusted (pH 7)	190	0.971	0.001	0.995	PSO	190	L	0.976	[312]
VFX (5 mg L^{-1})	M-A	K_2CO_3/ SBG 1:2 ratio	1197	50	Ultrapure water (pH~6)	0.05	0.958	0.0012	0.984	PSO	74	L	0.973	Current study

6.4.3.3 Adsorption equilibrium

Following the kinetic evaluation (Section 6.4.3.3), equilibrium adsorption studies were carried out to determine the maximum adsorption capacities of the produced ACs and to elucidate the influence of solution chemistry on VFX uptake. In fact, the adsorption isotherms represented the amount of VFX adsorbed onto SBG-AC-CP and SBG-AC-MP at equilibrium (q_e, mg g^{-1}) versus the amount of pharmaceutical remaining in solution (C_e, mg L^{-1}). These experiments allow for a deeper understanding of the interaction between the adsorbent surface and the VFX under varying conditions, complementing the kinetic analysis and providing essential parameters for practical application. The experimental equilibrium data were fitted to the Langmuir and the Freundlich isotherm models (Eqs. 6.8 and 6.9, Section 6.3.5.3). The Langmuir model assumes monolayer adsorption onto a homogeneous surface with a finite number of identical sites, whereas the Freundlich model is an empirical equation that accounts for multilayer adsorption on heterogeneous surfaces. **Figure 6.4** shows the experimental equilibrium data and the corresponding Langmuir and Freundlich isotherm fits for VFX adsorption onto SBG-AC-CP and SBG-AC-MP in ultrapure water and wastewater.

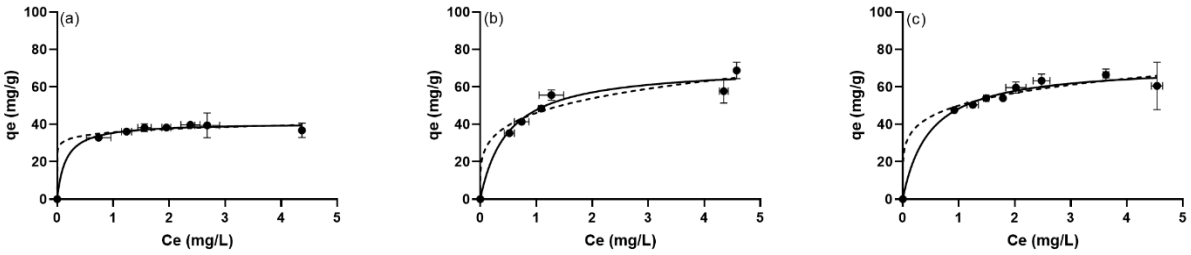

Figure 6.4 *Equilibrium adsorption for the experimental data of VFX adsorption onto SBG-AC-CP in ultrapure water (a), SBG-AC-MP in ultrapure water (b), and SBG-AC-MP in wastewater (c). The experimental data were fitted to both the Langmuir (solid lines) and the Freundlich (dashed lines) models. Each experimental point represents the mean of three replicates (± SD). Conditions: VFX at an initial concentration of 5 mg L^{-1}, adsorbent doses 5 - 125 mg L^{-1}, stirring (80 rpm), at 25.0 ± 0.1 °C.*

Table 6.4 reports the fitting parameters obtained from the Langmuir and the Freundlich isotherm models for VFX adsorption onto SBG-AC-CP and SBG-AC-MP in ultrapure water and wastewater. These parameters allow comparison of the maximum adsorption capacity and the adsorbent's affinity for VFX under different conditions, as well as the assessment of which model best describes the adsorption process.

Table 6.4 *Fitting parameters of the Langmuir and the Freundlich equilibrium models for the adsorption of VFX onto SBG-AC-CP in ultrapure water, SBG-AC-MP in ultrapure water, and SBG-AC-MP in wastewater.*

		Ultrapure water		Wastewater
		SBG-AC-CP	**SBG-AC-MP**	**SBG-AC-MP**
Equilibrium adsorption models				
Langmuir	q_m (mg g^{-1})	41±1	71±4	72±3
	K_L (L mg^{-1})	7±2	2.0±0.5	2.1±0.5
	r^2	0.9907	0.9725	0.9843
	n	8	7	9
	S_{xy}	1.394	4.048	2.671
Freundlich	K_F (mg g^{-1}(mg L^{-1})$^{-N}$)	36±1	46±2	50±2
	N	14±7	4±1	5±1
	r^2	0.9847	0.9560	0.9772
	n	8	7	9
	S_{xy}	1.791	5.118	3.218

Overall, as indicated by the r^2 and S_{xy} values reported in **Table 6.4,** the equilibrium experimental data were well fitted by both the Langmuir and the Freundlich models ($r^2 \geq 0.95$). However, the Langmuir model, which assumes monolayer adsorption on a homogeneous surface with identical adsorption sites, showed slightly higher r^2 values and lower S_{xy}, suggesting a better fit. A clearer difference was observed for VFX adsorption onto SBG-AC-MP in ultrapure water, where the Langmuir model yielded r^2 = 0.9480 and S_{xy} = 5.483, compared to r^2 = 0.9136 and S_{xy} = 7.072 for the Freundlich model. This indicates that, in this specific case, the Langmuir equation provides a noticeably better description of the equilibrium data, highlighting that VFX adsorption onto SBG-AC-CP and SBG-AC-MP occurs predominantly as a monolayer on a homogeneous surface with uniform adsorption sites. Consequently, the Langmuir model was used for subsequent discussion and interpretation of adsorption capacity parameters. The highest adsorption capacity for VFX was observed with SBG-AC-MP in ultrapure water, with a q_m value of 74±6 mg g^{-1}. In comparison, SBG-AC-CP in ultrapure water reached a q_m of 41±1 mg g^{-1}, while SBG-AC-MP in wastewater exhibited a q_m of 72±3 mg g^{-1}. Statistical analysis of these results, performed using a *t*-test at the 95% confidence level, confirmed that the adsorption capacities of SBG-AC-CP and SBG-AC-MP in ultrapure water differ significantly ($T_{cal} = 33.18 > T_{tab} = 2.15$), indicating the superior adsorption performance of the SBG-AC-MP. For SBG-AC-MP, the maximum adsorption capacity in ultrapure water is not significantly higher than in wastewater, confirming that the matrix

complexity does not adversely affect SBG-AC-MP's properties, where competitive adsorption and electrostatic interactions have negligible effects on adsorption capacity. Even the adsorption capacity of SBG-AC-MP in wastewater, despite the matrix effects inherent to real effluents, remains higher than that of SBG-AC-CP in ultrapure water: 72±3 mg g^{-1} for SBG-AC-MP in wastewater vs. 41±1 mg g^{-1} for SBG-AC-CP in ultrapure water. This finding highlights not only the intrinsic superiority of the microwave-derived AC but also its robustness under realistic environmental conditions. Moreover, MP offers additional benefits such as shorter processing times and lower energy consumption, making it a more sustainable and efficient approach to AC production.

The comparative evaluation of the equilibrium parameters obtained in this study and those reported in the literature further highlights differences in adsorption performance arising from variations in pyrolysis method, activation chemistry, and the physicochemical characteristics of each adsorbate [103, 310-312]. **Table 6.3** presents the adsorption isotherm parameters for VFX onto SBG-AC-MP, along with data for other pharmaceuticals adsorbed onto various SBG-derived ACs reported in the literature.

The equilibrium adsorption behavior of SBG-derived ACs shows that the nature of the adsorbate and solution conditions strongly influence adsorption capacity. In the study by Castro et al. (2022), tartrazine yellow dye exhibited a maximum adsorption capacity of 32 mg g^{-1} on SBG-derived AC at pH 3, with equilibrium data well described by the Langmuir isotherm [310]. In the study of Araújo et al. (2020), the activated hydrochar exhibited a very high maximum adsorption capacity (q_m = 318 mg g^{-1}) toward acetaminophen, with the equilibrium data fitting the Langmuir isotherm, indicating monolayer adsorption on uniform active sites. This high q_m (318 mg g^{-1}) is primarily attributed to the exceptionally large surface area of the hydrochar (1513 m^2 g^{-1}) generated through hydrothermal carbonization followed by KOH activation, as well as favorable interactions between acetaminophen molecules and surface functional groups [103]. The combination of a high activating agent/precursor ratio (4:1) and an intense hydrothermal process improves adsorption, but at the cost of higher processing costs and reduced sustainability.

In contrast, the SBG-AC-MP developed in this thesis was produced via MP with a lower K_2CO_3/precursor ratio (1:2), resulting in a moderately high surface area and a q_m of 71 mg g^{-1} for VFX. Although this activation is less aggressive than hydrothermal KOH treatment, it still generates sufficient porosity and surface functionality for effective adsorption at environmentally relevant pH. These results underscore that both the activating agent/precursor ratio and the type of thermal treatment directly influence carbon structure and adsorption performance, with more intensive conditions yielding higher-performing materials, albeit with

increased cost and synthesis complexity. In the study by Sousa et al. (2023), sulfamethoxazole, trimethoprim, and ciprofloxacin were adsorbed onto microwave-derived carbons obtained using the same procedure as in the present study [311]. However, these ACs exhibited lower BET surface areas (929 m^2 g^{-1}) than those of the ACs in the present study (1197 m2 g-1), and both the Langmuir and the Freundlich isotherm models provided a good fit to the experimental data. Compared to the current study, the higher adsorption capacities (q_m = 434, 880, and 418 mg g^{-1} for sulfamethoxazole, trimethoprim, and ciprofloxacin, respectively) reported by Sousa et al. (2023) are likely due to different operating conditions and stronger interaction affinity with the adsorbent surface. Similarly, carbamazepine adsorption onto hydrothermally produced carbon (activated with 1:1 KOH:NaCl, w/w) at pH 7, with SBET = 906 m2 g-1, is better described by the Langmuir isotherm than by the Freundlich or other models [311].

The equilibrium adsorption study confirmed the high efficiency of SBG-AC-MP in removing VFX, while the similar q_m values in ultrapure water and wastewater highlight its robustness under realistic conditions. The Langmuir model provided the best fit, indicating monolayer adsorption on homogeneous sites. Combined with the kinetic results, these findings demonstrate that MP activated with K2CO3 yields a material with superior adsorptive properties compared to CP, enabling high efficiency even in complex wastewater. This highlights both the strong potential of SBG-AC-MP for practical water treatment and the need to optimize operational parameters for real-world applications.

6.5 Conclusions

ACs derived from SBG were successfully produced via CP and MP using K_2CO_3 activation and evaluated for VFX removal. MP resulted in materials with superior surface properties and adsorption performance compared with CP under identical activation conditions.

High removal efficiencies were achieved in ultrapure water at low adsorbent dosages, while in wastewater, SBG-AC-MP maintained a high adsorption capacity, demonstrating greater resistance to matrix interferences than SBG-AC-CP. Adsorption kinetics followed a pseudo-second-order model, with equilibrium reached within approximately 2 h. Equilibrium data were best described by the Langmuir isotherm, indicating monolayer adsorption. Maximum adsorption capacities confirmed the superior performance of SBG-AC-MP, which retained its efficiency in wastewater despite higher pH values and inhibitory matrix effects.

Overall, MP combined with K_2CO_3 activation represents an effective strategy for producing high-performance adsorbents from agro-industrial residues. This approach offers a sustainable solution for removing pharmaceutical contaminants from complex aqueous matrices. Future research should focus on improving production yields, assessing adsorbent

regeneration, and extending the application to other contaminants and water matrices to support large-scale implementation.

The results presented in this contribution were published in the journal *Pharmaceuticals* (https://doi.org/10.3390/ph19030344).

Similarly, adsorption-based processes have been extended to other pharmaceutical contaminants, such as SILD and TAD, a potent, highly lipophilic PDE-5i that shares a similar polycyclic structure with SILD. The study reported in Chapter 7 evaluates the effectiveness of various adsorbent materials in maximizing water purification while preventing the formation of toxic transformation products, a common risk in the photochemical degradation methods previously discussed.

7. CONTRIBUTION 5

Comparative removal of erectile dysfunction pharmaceuticals from water using microwave-activated carbon derived from brewery waste and modified montmorillonite

7.1 Abstract

ED pharmaceuticals, including SILD and TAD, are increasingly recognized as ECs in aquatic environments due to their widespread consumption, environmental persistence, and incomplete removal by conventional wastewater treatment technologies. This chapter investigates the development and application of sustainable adsorbents derived from SBG via conventional and microwave-assisted pyrolysis, followed by K_2CO_3 chemical activation. The adsorption performance of these carbon-based materials is systematically compared with that of natural MMT and DDAB-MMT.

Batch adsorption experiments were conducted at an initial pharmaceutical concentration of 5 mg L^{-1}. ACs produced via microwave-assisted pyrolysis exhibited the highest adsorption efficiencies, reaching equilibrium within 2 h and achieving removal percentages of 90.3 ± 0.1% for SILD and 95 ± 2% for TAD at an adsorbent dosage of 50 mg L^{-1}. DDAB-MMT also demonstrated substantial adsorption capacity, attaining equilibrium within 60 min and removal efficiencies of 84.9 ± 0.1% for SILD and 91 ± 3% for TAD at a higher dosage of 250 mg L^{-1}.

Overall, the results emphasize the decisive role of adsorbent surface chemistry, porosity, and functionalization in controlling pharmaceutical uptake and confirm that both microwave-derived ACs and surfactant-modified clays represent effective and sustainable materials for mitigating persistent pharmaceutical contamination in water.

7.2 Introduction

The widespread occurrence of ECs in aquatic environments has emerged as a critical environmental concern, primarily due to their intrinsic chemical persistence and the insufficient removal efficiencies of conventional wastewater treatment processes [28-29, 96, 313-315]. Among these pollutants, PDE-5i such as SILD and TAD are increasingly detected in surface waters and effluents, a phenomenon directly linked to their surging global consumption and resistance to conventional biological degradation. While these compounds have not yet been formally included in any of the five European Union Watch Lists published to date, their

potential ecological impacts and bioaccumulation have necessitated an intensified scientific focus on advanced remediation technologies [29, 314-315].

Building on the results presented in the previous chapter, which demonstrated the effectiveness of MP combined with K_2CO_3 activation in producing high-performance ACs from SBG, this chapter further explores the application of these materials for the adsorption of ED pharmaceuticals. The MP approach represents a sustainable valorization pathway for agro-industrial waste, in line with circular economy principles, while providing adsorbents with enhanced surface area and tailored pore structures [104, 316-318].

In addition to carbon-based materials, this chapter also evaluates mineral-based adsorbents, specifically natural MMT and its organo-modified derivative [96, 319-320]. Mineral-based adsorbents, such as MMT, were selected for comparison with SBG-derived activated carbons due to their complementary adsorption properties and practical advantages. MMTs are naturally occurring layered silicates characterized by a lamellar structure, high cation exchange capacity, and the ability to intercalate organic and inorganic molecules between their layers. These features make them effective in removing a wide range of pollutants, including charged species, which are less efficiently adsorbed by purely carbon-based materials. Mineral-based adsorbents are abundant, cost-effective, and chemically stable, which supports their practical relevance as alternatives or complements to activated carbons. While natural MMT exhibits limited affinity for weakly polar organic molecules, surface modification via intercalation with cationic surfactants enhances its organophilic character and adsorption performance for non-polar and lipophilic compounds. In this study, natural MMT was functionalized with DDAB to increase lipophilicity.

This chapter aims to comparatively evaluate two SBG-derived ACs and clay-based adsorbents (MMT and DDAB-MMT) and elucidate the roles of synthesis pathways and surface modification in governing the removal of SILD and TAD from aqueous environments.

7.3 Materials and methods

7.3.1 Reagents and Chemicals

The reagent used in the activation process during ACs production was potassium carbonate (K_2CO_3, AnalaR normapur, 99.9%). For washing SBG-derived ACs, hydrochloric acid (HCl, Honeywell FLUKA, 37.0%) was employed. HCl (Honeywell FLUKA, 37.0%), sodium hydroxide (NaOH, José Manuel Gomes dos Santos, 99.3%), and sodium chloride (NaCl, Fluka, ≥99.5%) were used to determine the PZC of SBG-derived ACs.

Natural Na-Ca montmorillonite (beidellite) was sourced from Ward's Natural Science Establishment, Inc. (Rochester, NY, USA).

The standard sildenafil citrate and tadalafil (Certified Reference Material) were purchased from Sigma Aldrich (St. Louis, USA). Stock solutions of SILD and TAD were prepared in ultrapure water using an ultrasonic bath. Ultrapure water was sourced using an Elga Purelab Flex 4 purification system (Veolia) and a Milli-Q RG system (Millipore, Bedford, MA, USA). For HPLC analyses, acetonitrile (HPLC grade) was obtained from Fisher Scientific, and HCl (37%) was supplied by Honeywell FLUKA.

7.3.2 Production and characterization of adsorbent materials

In this study, the following materials were used: SBG-AC-CP and SBG-AC-MP as carbon-based adsorbents, MMT and DDAB-MMT as the clay components. SBG-AC-CP, SBG-AC-MP, and DDAB–MMT complexes were prepared in previous studies [1, 321]. The XPS characterization of MMT and DDAB–MMT was performed in this study.

ACs were produced and characterized according to the procedure described by Zizzamia et al. (2026) [321]. Briefly, SBG was dried, milled, and impregnated with K_2CO_3 (activating agent/SBG 1:2 mass ratio). Then, a portion of the dried impregnated material was carbonized by CP, under a nitrogen atmosphere in a muffle furnace (Nüve, series MF 110, Turkey), heating at a rate of 10 °C min^{-1} until reaching 800 °C, with a 2-hour residence time at 800 °C; the other portion was carbonized in a microwave furnace (CEM Phoenix™ AirWave) under an inert nitrogen flow, at 800 °C (heating rate of 15 °C min^{-1}), with a 20-minute residence time. After acid washing, rinsing, drying, and sieving, two ACs were obtained: SBG-AC-CP (by conventional pyrolysis) and SBG-AC-MP (by microwave pyrolysis).

DDAB–MMT complexes were prepared by Villaverde et al. according to the procedure reported in their study [1]. To obtain DDAB–MMT complexes, suspensions containing 6 mM DDAB and 5 g L^{-1} clay were stirred for 24 h, centrifuged at 25.000 g, and the supernatants discarded; the resulting complexes were lyophilized.

The elemental composition and chemical states of MMT and DDAB-MMT complexes were examined using XPS. The spectra were obtained using a PHOIBOS 100 MCD-5 (SPECS) spectrometer featuring a monochromatic Al Kα (1486.6 eV) X-ray source. The wide spectrum was acquired in Fixed Retard Ratio (FRR) mode with an energy step of 1 eV and a channel time of 0.5 s. The main signals of each sample were selected for the detailed acquisitions in Fixed Analyzer Transmission (FAT) mode, with a step energy E° = 9 eV, a channel width of 0.1 eV, and a channel time of 0.5 s, and processed with the Googly curve-fitting software for semiquantitative analysis [37].

7.3.3 Adsorption experiments

7.3.3.1 Preliminary tests

Batch adsorption experiments were conducted under controlled shaking conditions to evaluate the efficacy of SBG-AC-CP, SBG-AC-MP, MMT, and DDAB-MMT complexes in removing SILD and TAD from water. During initial screening, adsorption tests were conducted to determine the optimal adsorbent dosage for subsequent kinetic investigations, ensuring high adsorption efficiency while allowing quantifiable concentration changes over time. Distinct stock solutions of SILD and TAD (5 mg L^{-1}) were prepared in ultrapure water and aliquoted into polypropylene tubes containing varying amounts of adsorbent. The final concentrations of adsorbents were established at 25, 50, and 75 mg L^{-1} for ACs, and 100, 250, and 500 mg L^{-1} for MMT and DDAB-MMT. All samples were stirred in an overhead shaker (Heidolph Reax 2) at 80 rpm for 24 h at 25.0 ± 0.1 °C to ensure sufficient contact time for adsorption equilibrium. Following shaking, aliquots were filtered through 0.22 μm PVDF filters (Whatman) and analyzed by HPLC–UV. Based on the adsorption efficiencies obtained, the adsorbent dosage producing reliable kinetic profiles under the tested conditions was selected for subsequent kinetic studies. All experiments were conducted in triplicate. Control samples containing only the pharmaceutical solutions without adsorbent were used as references for adsorption percentage calculations, determined according to Eq. 7.1:

$$\text{Adsorption (\%)} = \frac{C_c - C_f}{C_c} x\ 100 \qquad (7.1)$$

Where C_c (mg L^{-1}) is the initial concentration in the control sample, and C_f (mg L^{-1}) represents the residual concentration after contact time.

7.3.3.2 Adsorption kinetics

Kinetic experiments were conducted at a fixed adsorbent dosage and a constant drug concentration of 5 mg L-1 to determine the contact time required to achieve adsorption equilibrium. Adsorbent concentrations were set at 50 mg L^{-1} for SBG-AC-CP and SBG-AC-MP and 250 mg L^{-1} for DDAB-MMT. Each polypropylene tube contained either 30 mL of the pharmaceutical solution and 1.5 mg of the selected AC, or 10 mL of the pharmaceutical solution and 5 mg of DDAB-MMT complexes. The suspensions were agitated at a controlled temperature for predetermined contact times ranging from 5 to 450 min for SBG-AC-CP and SBG-AC-MP, and from 5 to 240 min for DDAB-MMT.

The amount of SILD or TAD adsorbed at time t (q_t, mg g^{-1}) was calculated using Eq. 7.2. Experimental data were then fitted to the pseudo-first-order [291] and pseudo-second-order

[322] kinetic models, expressed by Eqs. 7.3 and 7.4, respectively, to evaluate the kinetic behavior and determine the model parameters for each adsorbent–pharmaceutical system.

$$q_t = \frac{(C_i - C_t)V}{m} \tag{7.2}$$

$$q_t = q_e(1\text{-}e^{-k_1 t}) \tag{7.3}$$

$$q_t = \frac{q_e^2 k_2 t}{1 + k_2 q_e t} \tag{7.4}$$

Where C_c (mg L^{-1}) is the initial pharmaceutical concentration, C_t (mg L^{-1}) is the concentration at time *t*, *V* (L) is the solution volume, and *m* (g) is the mass of adsorbent, q_e (mg g^{-1}) denotes the adsorbed concentration of adsorbate at the equilibrium, k_1 (min^{-1}) is the pseudo-first-order rate constant, and k_2 (g mg^{-1} min^{-1}) is the pseudo-second-order rate constant. Non-linear regression analyses of the kinetic models were performed using GraphPad Prism (version 8.0.2) to obtain the best-fit parameters (q_e, k_1, k_2) and to evaluate the goodness of fit based on the correlation coefficient (r^2) and residual distribution.

7.3.3.3 Adsorption equilibrium

To determine the adsorption isotherms, equilibrium batch experiments were carried out by varying the adsorbent dose while maintaining a constant initial concentration of SILD and TAD (5 mg L^{-1}). Solutions were contacted with different amounts of each AC produced and of DDAB-MMT complexes. Based on preliminary kinetic studies, the mixtures containing SBG-AC-CP, SBG-AC-MP, and DDAB-MMT complexes were agitated for 4 h, 2 h, and 1 h, respectively, to ensure equilibrium was reached. The applied adsorbent dosages ranged from 15 to 90 mg L^{-1} for SBG-AC-CP, from 15 to 80 mg L^{-1} for SBG-AC-MP, and from 25 to 500 mg L^{-1} for DDAB-MMT complexes. At least seven different concentrations were tested for each adsorbent–pharmaceutical system. These experiments allowed the determination of the materials' equilibrium adsorption capacities. The adsorbed concentration of adsorbate at the equilibrium (q_e, mg g^{-1}) was calculated according to Eq. 7.5. Experimental data were fitted to the non-linear Langmuir (homogeneous monolayer adsorption) and the Freundlich (heterogeneous adsorption) models, expressed in Eqs. 7.6 and 7.7, respectively [309].

$$q_e = \frac{(C_i - C_e)V}{m} \tag{7.5}$$

$$q_e = \frac{q_m X K_L X C_e}{1 + K_L X C_e} \tag{7.6}$$

$$q_e = K_F X C_e^{(\frac{1}{N})} \tag{7.7}$$

Where C_e (mg L^{-1}) is the equilibrium concentration of SILD or TAD in solution, q_m (mg g^{-1}) represents the maximum adsorption capacity of each material toward the two pharmaceuticals, K_L (L mg^{-1}) is the Langmuir equilibrium constant, and K_F (mg g^{-1} (L $mg^{-1})^{1/N}$) denotes the Freundlich equilibrium constant. The parameter N describes the degree of nonlinearity and reflects the heterogeneity of the adsorption sites. All other variables are defined as in Eqs. 7.2, 7.3, and 7.4. Non-linear regression and parameter estimation for both isotherm models were performed using GraphPad Prism (version 8.0.2). The fitted parameters (q_m, K_L, K_F, N) and statistical indicators (r^2 and residual errors) were used to evaluate the model suitability and describe the adsorption behavior of SILD and TAD on the investigated materials.

7.3.4 Chromatographic analyses

Analyses were performed on a Shimadzu HPLC equipped with a UV detector. The reverse-phase column used was an ACE5 C_{18} (5 µm, 150 × 4.6 mm). Measurements were performed isocratically. For both pharmaceuticals, the mobile phase used was acetonitrile/water 0.37% HCl (v/v), in a 35:65 ratio for SILD and 50:50 for TAD. The flow rate was 1.0 mL min^{-1}, the injection volume was 20 µL, and the total run time was 7 min. Both the acidified water and acetonitrile were filtered through a 0.2 µm polyamide membrane (Whatman) before use. The column was preconditioned and post-conditioned with 100% acetonitrile after each batch run to ensure consistency and avoid cross-contamination. Detection occurred at 254 nm for SILD and 290 nm for TAD. Retention times were 7.6 minutes for SILD and 8.6 minutes for TAD. Calibration curves were derived by analyzing standard solutions ranging from 0.1 to 5.0 mg L^{-1}, with each measurement conducted in triplicate. The analytical performance was assessed regarding linearity, accuracy, and sensitivity.

LOD and LOQ were determined for each curve in accordance with Eqs. 7.8 and 7.9, respectively:

$$\mathrm{LOD} = \frac{3.3 \cdot \sigma}{b} \tag{7.8}$$

$$\mathrm{LOQ} = \frac{10 \cdot \sigma}{b} \tag{7.9}$$

Where σ is the SD of the intercept and b is the slope of the calibration curve [293]. The linearity (Lin%) of the analytical method was determined using Eq. 7.10:

$$\mathrm{Lin}(\%) = 100 - RSD_b \tag{7.10}$$

Where RSD_b is the relative standard deviation of the slope (in percentage) [294].

7.4 Results and discussion

7.4.1 Characterization of natural MMT and DDAB-MMT

In **Figure 7.1a**, the XPS spectra (in wide mode) of natural MMT and the DDAB-MMT system are shown, with the photoelectron signals and the corresponding Auger signals indicated for qualitative analysis [19, 27]. To better highlight the lower-intensity signals, a magnified view of the wide-scan in the 900–1500 eV range is shown below (**Figure 7.1b**).

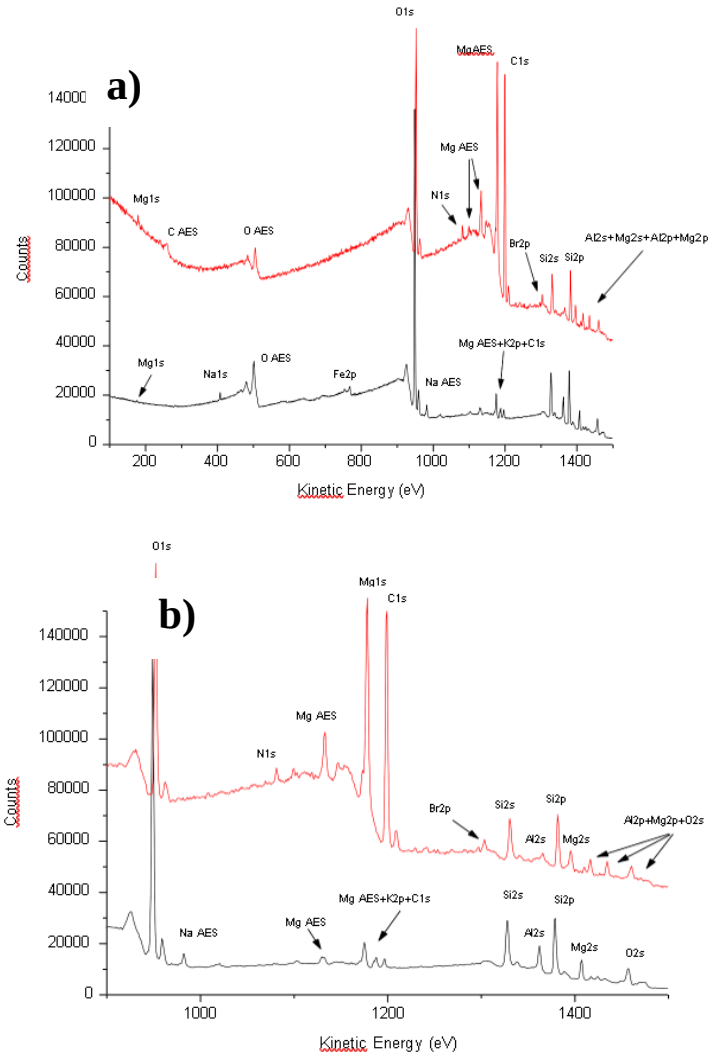

Figure 7.1 a) *XPS spectrum (in wide mode) of MMT (black) and DDAB-MMT complexes (red);* **b)** *a magnification of the wide scan in the 900–1500 eV range.*

The wide scan of natural MMT (black line in **Figure 7.1**) shows the presence of the photoelectron signals corresponding to C, K, O, Fe, Mg, Na, Al, and Si, as well as the related Auger signals for O, Mg, and Na. The wide scan of DDAB-MMT (red line in **Figure 7.1**), in addition to the photoelectron signals of C, O, Mg, Si, and Al, also shows the signals of N and Br, while those of Na, K, and Fe are absent; the Auger signals of C, O, and Mg are also present.

The presence of the signals of N and Br in the spectrum of DDAB-MMT, absent in the wide scan of raw MMT, and the increase of the signal of C1s are a confirmation of the functionalization of MMT with charged DDAB-vesicles.

7.4.2 Performance of the analysis method

To evaluate the adsorptive efficacy of the adsorbents, studies were conducted using HPLC–UV, following the chromatographic conditions described in the "Materials and methods" section. The analytical technique exhibited exceptional sensitivity and reproducibility. LOD and LOQ for SILD were 0.3 mg $L^{-1}$and 0.9 mg L^{-1}, respectively, demonstrating a linearity of 91.6%. For TAD, the LOD and LOQ were 0.3 mg L^{-1} and 1.0 mg L^{-1}, respectively, with a linearity of 97.4%. The calibration curves for both SILD and TAD are shown in Figure 7.2, and both demonstrate strong correlation coefficients across the studied concentration range, validating the linearity, accuracy, and sensitivity of the devised HPLC–UV technique for trace-level detection of these medicines in aqueous matrices.

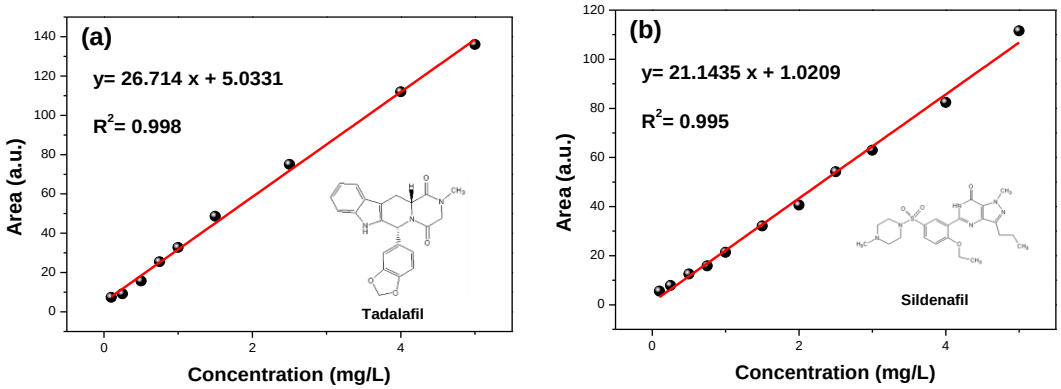

Figure 7.2 *Calibration curves of* **(a)** *TAD and* **(b)** *SILD.*

7.4.3 Adsorption experiments

7.4.3.1 Preliminary tests

Adsorption experiments were carried out to evaluate the removal efficiency of SILD and TAD from water using ACs and natural and DDAB-MMT. As shown in **Figure 7.3** and **Table 7.1**, SBG-AC-MP exhibited markedly superior performance even at low adsorbent dosages, whereas SBG-AC-CP displayed moderate adsorption efficiency. After 24 h of contact, removal of SILD and TAD reached 64 ± 3% and 62 ± 6%, respectively, using 50 mg L^{-1} SBG-AC-CP; with SBG-AC-MP, SILD removal was 90.3 ± 0.1%, and TAD removal was 95 ± 2%, at an adsorbent dose of only 50 mg L^{-1}.

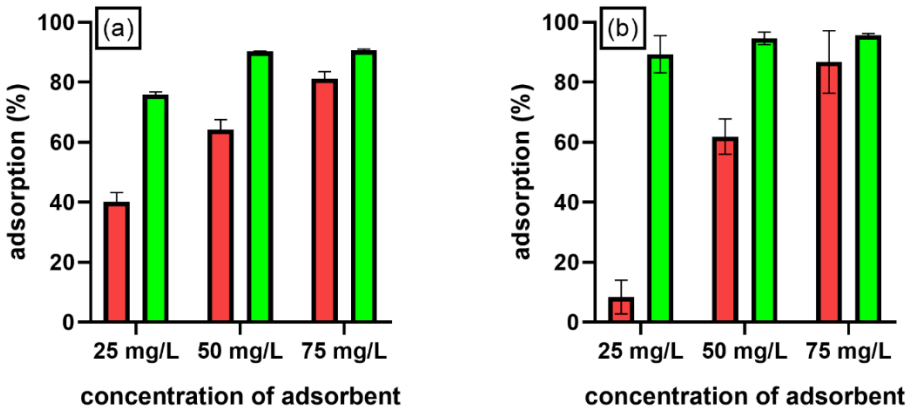

Figure 7.3 *Adsorption efficiencies of SILD (a) and TAD (b) (5 mg L^{-1}) in ultrapure water at different concentrations of adsorbent materials, using SBG-AC-CP (red) and SBG-AC-MP (green).*

The data in **Table 7.1** show that the adsorption percentage increased with increasing adsorbent dose from 25 to 75 mg L-1 for both pharmaceuticals. The higher number of available active sites at elevated doses led to greater removal percentages. SBG-AC-MP consistently outperformed SBG-AC-CP, attaining over 90% adsorption for both compounds at concentrations of 50 mg L^{-1} or higher. By contrast, SBG-AC-CP showed significantly poorer performance, with adsorption levels remaining below 50% for SILD and below 10% for TAD at a concentration of 25 mg L^{-1}. The results show that, compared to SBG-AC-CP, SBG-AC-MP is a more efficient, stable, and reproducible adsorbent for removing SILD and TAD from ultrapure water, especially at moderate to high dosages.

Table 7.1 *Adsorption efficiency and RSD of SILD 5 mg L^{-1}* **(a)** *and TAD 5 mg L^{-1}* **(b)** *in ultrapure water at different concentrations of SBG-AC-CP and SBG-AC-MP.*

(a)	**% adsorption**	
Concentration of adsorbent	**SBG-AC-CP**	**SBG-AC-MP**
25 mg L^{-1}	40±3%	76±1%
50 mg L^{-1}	64±3%	90.3±0.1%
75 mg L^{-1}	81±2%	90.6±0.4%
(b)	**% adsorption**	
Concentration of adsorbent	**SBG-AC-CP**	**SBG-AC-MP**
25 mg L^{-1}	8±6%	89±6%
50 mg L^{-1}	62±6%	95±2%
75 mg L^{-1}	87±10%	95.7±0.5%

SILD, with a p*Ka* ≈ 6.0, exists predominantly in protonated cationic form at working pH (ultrapure water exhibits a nearly neutral pH (≈ 7)), while TAD, characterized by a very high p*Ka* (~15.2), remains neutral and non-ionized under the same conditions. Both ACs

possess a PZC of 3.5-4. Thus, at pH levels above this threshold, their surfaces acquire a negative charge due to the deprotonation of hydroxyl and carboxyl groups. Under these circumstances, the adsorption of SILD is significantly enhanced by the electrostatic attraction between its cationic species and the negatively charged surface of ACs. In contrast, TAD, being neutral, is adsorbed mainly through π–π stacking, hydrogen bonding, and van der Waals interactions with the aromatic carbon framework.

The exceptional adsorption capacity of SBG-AC-MP is due to its broad microporous structure, which facilitates access to active adsorption sites. This outcome highlights the intrinsic superiority of microwave-assisted activation compared to traditional pyrolysis. As previously mentioned, microwave heating facilitates the swift and uniform formation of micropores, leading to an increased total pore volume and specific surface area, even under the same chemical activation conditions, in contrast to traditional pyrolysis. These structural changes directly improve adsorption efficiency. MP also provides operational advantages, such as reduced processing time and lower energy consumption, improving its feasibility as a more sustainable and efficient technique for producing high-performance ACs.

MMT-based materials required considerably higher doses to attain comparable removal efficiencies, owing to their lower surface area and the finite availability of active sites, in contrast to ACs [1]. Accordingly, the natural MMT and DDAB-MMT complexes concentrations tested were 100, 250, and 500 mg L^{-1} (**Figure 7.4**).

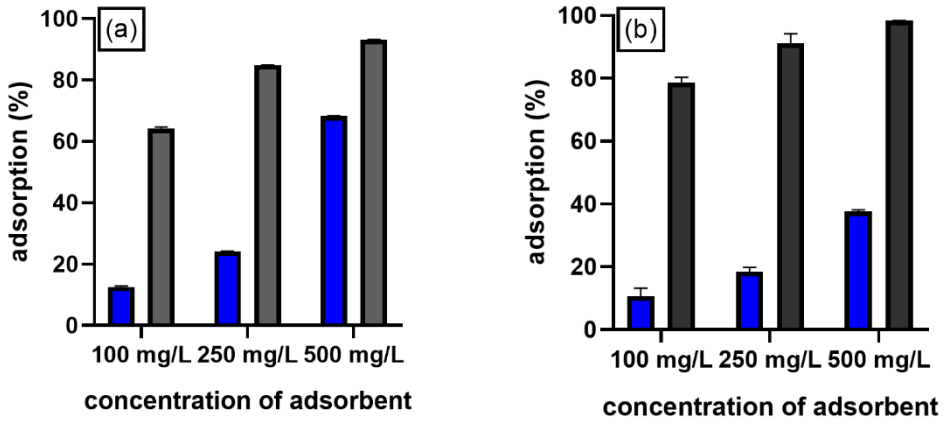

Figure 7.4 *Adsorption efficiencies of SILD (a) and TAD (b) (5 mg L^{-1}) in ultrapure water at different concentrations of adsorbent materials, using MMT (blue) and DDAB-MMT complexes (grey).*

As shown in **Table 7.2**, the removal percentage increased with the dosage of both the natural adsorbent and the DDAB-MMT. However, the DDAB-MMT complexes exhibited substantially higher adsorption percentage at all concentrations tested. For SILD, adsorption by the DDAB-MMT system exceeded 93% at 500 mg L^{-1}, compared to 68% for natural

montmorillonite. The difference was even more pronounced for TAD: the DDAB-MMT complex achieved a removal efficiency of 98.4% under the same conditions, compared to 37.7% for natural MMT. These results suggest that SILD and TAD, both lipophilic and poorly soluble in water [37, 41], are adsorbed inefficiently by natural montmorillonite. The clay's inherent hydrophilicity, coupled with its limited ability to interact with non-polar or weakly polar compounds, restricts its adsorption performance towards these pharmaceuticals. In contrast, functionalization with DDAB-vesicles enhances the surface lipophilicity of MMT and improves its affinity for hydrophobic molecules, as corroborated by XPS analyses. Consequently, unmodified MMT exhibits substantially lower adsorption capacities due to its hydrophilic nature and structurally compact framework.

Table 7.2 *Adsorption efficiency and RSD of SILD 5 mg L^{-1}* **(a)** *and TAD 5 mg L^{-1}* **(b)** *in ultrapure water at different concentrations of natural MMT and DDAB-MMT complexes.*

(a)	**% adsorption**	
Concentration of adsorbent	**MMT**	**DDAB-MMT**
100 mg L^{-1}	12.5±0.4%	64.1±0.6%
250 mg L^{-1}	24.1±0.1%	84.9±0.1%
500 mg L^{-1}	68.2±0.2%	93.1±0.1%
(b)	**% adsorption**	
Concentration of adsorbent	**MMT**	**DDAB-MMT**
100 mg L^{-1}	11±3%	79±2%
250 mg L^{-1}	18±1%	91±3%
500 mg L^{-1}	37.7±0.4%	98.4±0.1%

TAD shows slightly higher adsorption than SILD on modified MMT, mainly because of its more hydrophobic and aromatic structure. Since the surface of DDAB-MMT complexes is organophilic and hydrophobic due to the organic functionalization, it interacts more favorably with nonpolar and planar aromatic molecules like TAD through van der Waals forces and π–π stacking between aromatic rings. SILD primarily interacts through hydrogen bonds and electrostatic interactions. At pH ≈ 7, the MMT layers exhibit a permanent negative charge due to isomorphic substitution in the silicate lattice, which is counterbalanced by hydrated inorganic cations (Na^+, Ca^{2+}) present in the interlayer space. SILD may exhibit weak adsorption due to limited ion-exchange interactions; however, competition with hydrated cations and steric hindrance at the narrow interlayer spacing significantly limit uptake. For TAD, which remains neutral under these conditions, electrostatic attraction is absent. These results demonstrate that surface functionalization by the cationic double-chain surfactant DDAB markedly enhances the

adsorption performance of montmorillonite, making modified MMT a more efficient and versatile adsorbent, also for non-polar and hydrophobic molecules such as SILD and TAD.

A comparative analysis of the adsorption performance of ACs and montmorillonite-based materials reveals significant differences in efficiency and behavior. While both types of AC demonstrate effective adsorption performance at low concentrations, SBG-AC-MP achieved the highest overall adsorption percentage, exceeding 90% for both SILD and TAD with a dosage of just 50 mg L^{-1}. In contrast, although montmorillonite-based adsorbents are naturally abundant, inexpensive, and environmentally friendly, significantly higher doses (≥250 mg L-1) are required to achieve adsorption levels comparable to those of ACs. At a concentration of 250 mg L^{-1}, the DDAB-MMT system achieved 85–91% removal, whereas natural MMT remained below 25%. This highlights a significant trade-off: while MMT offers advantages in terms of sustainability, availability, economic feasibility, and functionalization potential, its reduced intrinsic surface area and fewer active sites make it a less efficient adsorbent than AC-based materials.

7.4.3.2 Adsorption kinetics

Kinetic experiments were conducted using adsorbent concentrations of 50 mg L^{-1} for ACs and 250 mg L^{-1} for the DDAB-MMT complexes. These concentrations were selected to maximize adsorption efficiency and allow quantifiable changes in concentration over time. Natural MMT was excluded from the kinetic experiments due to its poor adsorption efficiency, which prevented the development of reliable kinetic profiles under the tested conditions.

The experiments aimed to determine the time required to reach adsorption equilibrium, focusing on the adsorption characteristics of SILD and TAD on SBG-AC-CP, SBG-AC-MP, and DDAB-MMT. The experiments evaluated the adsorption rates of the carbon compounds compared with those of the clay-based adsorbent. The results were analyzed using the pseudo-first-order and pseudo-second-order kinetic models, recognized methods for characterizing adsorption on solid surfaces. The suitability of each model was assessed by comparing the experimental equilibrium adsorption capacities q_e and the corresponding correlation coefficients r^2, thereby identifying the model that best described the adsorption process for each material. The experimental kinetic profiles, expressed as the amount of SILD or TAD adsorbed per unit mass of adsorbent (q_t, mg g^{-1}) as a function of contact time, are presented in **Figures**

7.5 and **7.6**, respectively. These figures also include the fitted curves obtained from the pseudo-first-order and pseudo-second-order models.

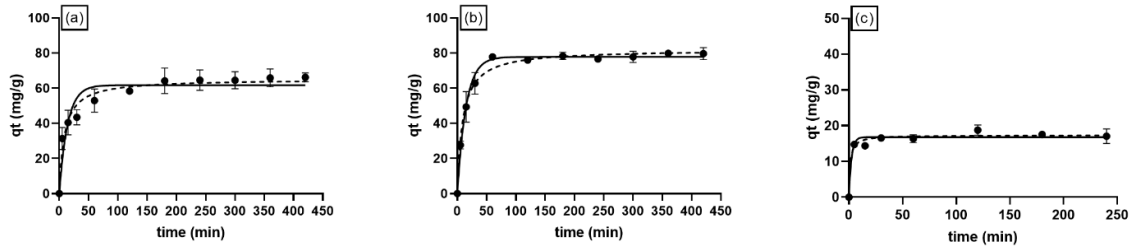

Figure 7.5 *Kinetic fittings for the experimental data of SILD adsorption onto (a) SBG-AC-CP, (b) SBG-AC-MP, and (c) DDAB-MMT complexes in ultrapure water. The results were fitted to the pseudo-first-order (solid lines) and pseudo-second-order (dashed lines) kinetic models. Each data point (± SD) represents the mean of three replicates. Points with error bars correspond to the experimental results. Experimental conditions: SILD concentration 5 mg L^{-1}; adsorbent dose 50 mg L^{-1} for both ACs and 250 mg L^{-1} for DDAB-MMT; stirring rate 80 rpm; temperature 25.0 ± 0.1 °C. Note that the y- and x-axis scales differ across the graphs to visualize the results better.*

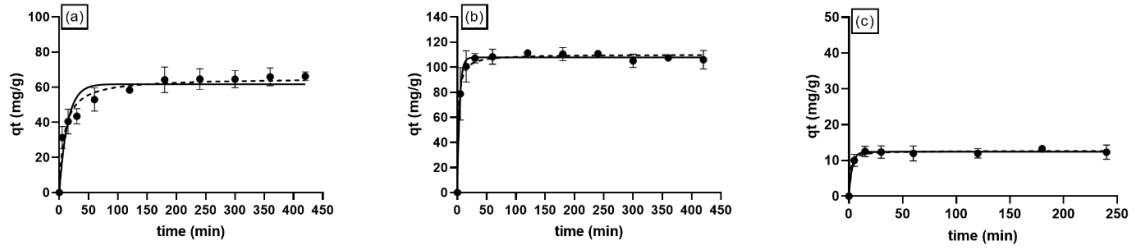

Figure 7.6 *Kinetic fittings for the experimental data of TAD adsorption onto (a) SBG-AC-CP, (b) SBG-AC-MP, and (c) DDAB-MMT complexes in ultrapure water. The results were fitted to the pseudo-first-order (solid lines) and pseudo-second-order (dashed lines) kinetic models. Each data point (± SD) represents the mean of three replicates. Points with error bars correspond to the experimental results. Experimental conditions: TAD concentration 5 mg L^{-1}; adsorbent dose 50 mg L^{-1} for both ACs and 250 mg L^{-1} for DDAB-MMT; stirring rate 80 rpm; temperature 25.0 ± 0.1 °C. Note that the y- and x-axis scales differ across the graphs to visualize the results better.*

The longer equilibrium time of 4 hours observed for SBG-AC-CP indicates that the adsorption process is slower. This is probably due to its narrower pore structure and increased microporosity, which limit the diffusion of SILD and TAD molecules into the internal adsorption sites. SBG-AC-MP (2 hours) and the DDAB-MMT system (1 hour) both exhibited faster adsorption kinetics. This can be attributed to the larger, more accessible pores of these materials and the presence of surface functional groups that enable contact with adsorbates.

Fitting the experimental data to the pseudo-first-order and pseudo-second-order models for both pharmaceuticals yielded the kinetic parameters shown in **Table 7.3**. The symbol *n* represents the number of experimental data points used in the regression analysis.

Table 7.3 *Fitting parameters of the pseudo-first-order and pseudo-second-order kinetic models applied to the experimental data for SILD* **(a)** *and TAD* **(b)** *adsorption onto SBG-AC-CP, SBG-AC-MP, and DDAB-MMT complexes in ultrapure water.*

(a)		**Ultrapure water**		
		SBG-AC-CP	SBG-AC-MP	DDAB-MMT
Kinetics models				
Pseudo-first-order	q_e (mg g^{-1})	62±3	78±1	16.8±0.5
	k_1 (min^{-1})	0.07±0.02	0.068±0.005	0.4±0.1
	r^2	0.9000	0.9906	0.9584
	n	11	11	8
	S_{xy}	6.8	2.7	1.3
Pseudo-second-order	q_e (mg g^{-1})	65±2	82±1	17.4±0.5
	k_2 (mg g^{-1} min^{-1})	0.0018±0.0004	0.0013±0.0001	0.05±0.02
	r^2	0.9646	0.9917	0.9738
	n	11	11	8
	S_{xy}	4.0	2.5	1.1

(b)		**Ultrapure water**		
		SBG-AC-CP	SBG-AC-MP	DDAB-MMT
Kinetics models				
Pseudo-first-order	q_e (mg g^{-1})	59±2	107.8±0.9	12.4±0.2
	k_1 (min^{-1})	0.027±0.003	0.25±0.02	0.33±0.04
	r^2	0.9718	0.9939	0.9913
	n	10	11	8
	S_{xy}	3.6	2.7	0.4
Pseudo-second-order	q_e (mg g^{-1})	66±1	110±1	12.7±0.3
	k_2 (mg g^{-1} min^{-1})	0.00055±0.00005	0.0050±0.0007	0.07±0.02

r^2	0.9952	0.9932	0.9870
n	10	11	8
S_{xy}	1.5	2.8	0.5

The kinetic parameters describe the adsorption behavior of SILD and TAD onto SBG-AC-CP, SBG-AC-MP, and DDAB-MMT complexes in ultrapure water. In all cases, the experimental data fitted both the pseudo-first-order and pseudo-second-order models reasonably well (r^2 > 0.90). However, the pseudo-second-order model showed a stronger correlation for SBG-AC-CP, as reflected by a higher r^2 and lower S_{xy}. SBG-AC-MP exhibited the highest q_e, compared to SBG-AC-CP and to DDAB-MMT. DDAB-MMT complexes displayed a significantly lower adsorption capacity; nonetheless, its higher apparent rate constants (k_1 = 0.4 min^{-1} and k_2 = 0.05 mg g^{-1} min^{-1} for SILD and k_1 = 0.3 min^{-1} and k_2 = 0.07 mg g^{-1} min^{-1} for TAD) indicate a faster adsorption process: equilibrium was achieved within only one hour, indicating a rapid initial uptake, consistent with surface interactions mediated by the organophilic functional groups introduced through surfactant modification. While ACs offer higher adsorption capacities, DDAB-MMT complexes exhibit rapid uptake kinetics and could serve as a complementary adsorbent for fast contaminant removal. These observations align well with previous studies. Comparable kinetic behavior has been reported for other hydrophobic pharmaceuticals adsorbed onto biochars and ACs, where surface-mediated interactions, such as π–π stacking and hydrophobic partitioning, dominate over intraparticle diffusion [325]. In a study of Alkaram et al. (2009), natural MMT exhibits very low adsorption efficiency, primarily due to its hydrophilic character and limited affinity toward nonpolar molecules [326]. However, organically modified montmorillonites, such as MMT-CTAB or MMT functionalized with long-chain surfactants, display markedly improved performance. This surface modification has also been shown to enhance adsorption kinetics and capacity in carbonaceous materials by introducing oxygen-containing functional groups that improve surface reactivity and polarity [327]. Research indicates that ACs and organically modified montmorillonites are among the most effective adsorbents for removing pharmaceuticals from aqueous environments, albeit via different mechanisms. ACs function primarily through surface chemisorption, with π–π and van der Waals interactions also contributing. In contrast, modified montmorillonites enhance performance by increasing surface affinity and hydrophobicity through organic modification.

7.4.3.3 Adsorption equilibrium

Following the kinetic evaluation, equilibrium adsorption studies were conducted to determine the maximum adsorption capacities of the tested adsorbent materials and compare them. The adsorption isotherms represented the amount of SILD or TAD adsorbed onto SBG-AC-CP, SBG-AC-MP, or DDAB-MMT complexes at equilibrium (qe, mg g^{-1}) versus the amount of pharmaceutical remaining in solution (Ce, mg L^{-1}). These tests provide a deeper understanding of the interaction between the adsorbent surface and the pharmaceutical compound, yielding essential parameters for practical application. Equilibrium adsorption experiments were performed by maintaining the initial concentration of SILD and TAD (5 mg L^{-1}) while varying the adsorbent doses. The experimental equilibrium data were fitted to the Langmuir and the Freundlich isotherm models (Eqs. 7.6 and 7.7) to describe the adsorption behavior and surface properties of SBG-AC-CP, SBG-AC-MP, and DDAB-MMT. The Langmuir model assumes monolayer adsorption onto a homogeneous surface with a finite number of identical sites, whereas the Freundlich model is an empirical equation that accounts for multilayer adsorption on heterogeneous surfaces. **Figures 7.7** and **7.8** show the experimental equilibrium data and the corresponding Langmuir and Freundlich isotherm fits for SILD and TAD adsorption, respectively, onto the SBG-AC-CP, SBG-AC-MP, and DDAB-MMT system.

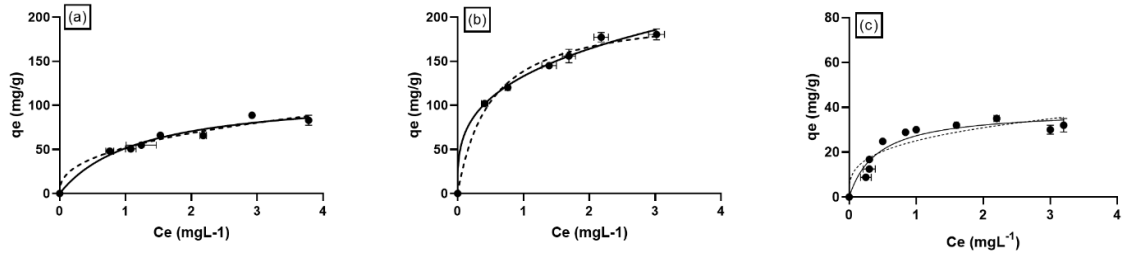

Figure 7.7 *Equilibrium adsorption isotherms of SILD onto (a) SBG-AC-CP, (b) SBG-AC-MP, and (c) DDAB-MMT systems in ultrapure water. The experimental data were fitted to both the Langmuir (solid lines) and the Freundlich (dashed lines) models. Each experimental point represents the mean of three replicates (± SD), with error bars indicating the corresponding variability. The isotherms were obtained using SILD solution at an initial concentration of 5 mg L^{-1} and adsorbent doses ranging from (a) 15 to 90 mg L^{-1}, (b) from 15 to 80 mg $L^{-1,}$ and (c) from 25 to 500 mg L^{-1}, under controlled stirring (80 rpm) at 25.0 ± 0.1 °C. Note that the y-axis scales differ across the graphs to visualize the results better.*

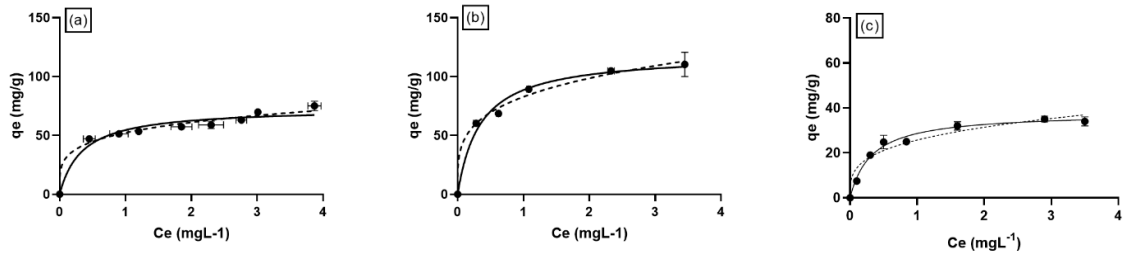

Figure 7.8 *Equilibrium adsorption isotherms of TAD onto (a) SBG-AC-CP, (b) SBG-AC-MP, and (c) DDAB-MMT systems in ultrapure water. The experimental data were fitted to both the Langmuir (solid lines) and the Freundlich (dashed lines) models. Each experimental point represents the mean of three replicates (± SD), with error bars indicating the corresponding variability. The isotherms were obtained using TAD solution at an initial concentration of 5 mg L^{-1} and adsorbent doses ranging from (a) 15 to 90 mg L^{-1}, (b) from 15 to 80 mg L^{-1} and (c) from 25 to 500 mg L^{-1}, under controlled stirring (80 rpm) at 25.0 ± 0.1 °C. Note that the y-axis scales differ across the graphs to visualize the results better.*

Table 7.4 reports the fitting parameters obtained from the Langmuir and the Freundlich isotherm models for **(a)** SILD and **(b)** TAD adsorption onto produced carbon materials, SBG-AC-CP, SBG-AC-MP, and DDAB-MMT. These parameters allow comparison of the maximum adsorption capacities and the adsorbent's affinity for SILD and TAD, as well as the assessment of which model best describes the adsorption process.

Table 7.4 *Fitting parameters of the Langmuir and the Freundlich equilibrium models applied to the experimental data for* **(a)** *SILD and* **(b)** *TAD adsorption onto SBG-AC-CP, SBG-AC-MP, and DDAB-MMT systems in ultrapure water.*

(a)		**Ultrapure water**		
		SBG-AC-CP	SBG-AC-MP	DDAB-MMT
Equilibrium models				
Langmuir	q_m (mg g^{-1})	113±12	207±10	39±3
	K_L (L mg^{-1})	0.8±0.2	2.0±0.3	2.3±0.6
	r^2	0.9667	0.9893	0.9204
	n	8	7	11
	S_{xy}	5.4	7.1	3.4
Freundlich	K_F (mg g^{-1}(mg L^{-1})$^{-N}$)	52±3	133±2	25±2
	N	2.5±0.4	3.3±0.2	3.3±0.8
	r^2	0.9672	0.9950	0.8399
	n	8	7	11
	S_{xy}	5.3	4.8	4.8
(b)		**Ultrapure water**		
		SBG-AC-CP	SBG-AC-MP	DDAB-MMT
Equilibrium models				
Langmuir	q_m (mg g^{-1})	73±4	119±6	38±1
	K_L (L mg^{-1})	2.9±0.9	2.9±0.6	3.1±0.4
	r^2	0.9546	0.9857	0.9885

	n	9	6	8
	S_{xy}	4.9	5.4	1.5
Freundlich	K_F (mg g^{-1}(mg L^{-1})$^{-N}$)	52±1	83±2	26±1
	N	4.4±0.6	4.0±0.4	3.4±0.6
	r^2	0.9814	0.9927	0.9444
	n	9	6	8
	S_{xy}	3.2	3.9	3.2

Both models adequately described the adsorption process, as evidenced by the high correlation coefficients for all systems. For adsorption onto DDAB-MMT, the Langmuir model provided a better fit to the experimental data than the Freundlich model. This suggests that adsorption on the modified clay predominantly occurs through the formation of a monolayer of adsorbate molecules on a finite number of active sites. The organomodification process likely creates a more homogeneous surface by intercalating DDAB vesicles between clay layers, thereby generating well-defined hydrophobic domains and accessible adsorption sites, and leading to a relatively ordered adsorption process consistent with Langmuir-type behavior. According to the Langmuir model, the maximum adsorption capacities *(qm) for SILD were* 113 ± 12, 207 ± 10, and 39 ± 3 mg g^{-1} for SBG-AC-CP, SBG-AC-MP, and DDAB-MMT, respectively. For TAD, the corresponding q_m values were 73 ± 4, 119 ± 6, and 38 ± 1 mg g^{-1}, following the same order. In both cases, SBG-AC-MP displayed the highest adsorption capacity, consistent with more accessible adsorption sites and stronger adsorbate–adsorbent interactions. The higher Langmuir constants (K_L) recorded for both ACs (2-3 L mg^{-1}) affirm the pronounced affinity of both medicines for the carbonaceous surfaces, influenced by π–π stacking, hydrophobic interactions, and potential hydrogen bonding with oxygenated surface groups. Conversely, the DDAB-MMT system exhibited reduced q_m values while maintaining similar KL, suggesting that, although the number of adsorption sites is constrained, the modified clay maintains a significant affinity for the analytes owing to hydrophobic and electrostatic interactions facilitated by the organic surfactant modification. The Freundlich model demonstrated a strong fit to the experimental data, indicating the presence of adsorption sites with varying affinities. The Freundlich constants for all materials demonstrate favorable adsorption characteristics. Among the adsorbents, SBG-AC-MP displayed the highest K_F values, measuring 133 ± 2 mg g^{-1}(mg L^{-1}) $^{-N}$ for SILD and 83 ± 2 mg g^{-1}(mg L^{-1}) $^{-N}$ for TAD, thereby underscoring its significant adsorption capacity. A comparison of the two pharmaceuticals indicates that SILD demonstrated greater adsorption capacity than TAD on both ACs, suggesting a stronger electrostatic attraction due to its cationic nature at neutral pH.

TAD, characterized by a neutral p*Ka* of approximately 15.2, primarily depends on hydrophobic and π–π interactions, leading to marginally reduced q_m values. The opposite trend was observed for DDAB-MMT, with TAD adsorption being marginally higher than that of SILD. The observed difference is likely due to TAD's increased hydrophobicity and larger aromatic structure, which improve its interaction with the surfactant-modified clay surface. Despite its lower capacity, the organically modified MMT demonstrates a notable affinity and accelerated kinetics, which can be attributed to the synergistic effects of hydrophobic and electrostatic interactions resulting from DDAB-modification. This makes DDAB-MMT complexes a promising, sustainable, and low-cost complementary adsorbent, especially suitable for rapid or large-scale pharmaceutical removal from aqueous environments.

7.5 Conclusions

This study provided a comprehensive evaluation of sustainable adsorption strategies for the removal of SILD and TAD from aqueous solutions, comparing the performance of SBG-derived ACs with natural MMT and its organo-modified derivative. Batch adsorption tests were conducted using 5 mg L^{-1} solutions of SILD and TAD, and the residual concentrations were measured via HPLC-UV analysis. The adsorption kinetics, equilibrium isotherms, and maximum adsorption capacities were then determined for each adsorbent. The ACs produced by MP performed exceptionally well: they reached adsorption equilibrium within 2 hours and achieved removal efficiencies of 90.3% for SILD and 95% for TAD at a low dose of 50 mg L^{-1}. DDAB-MMT was more effective than natural MMT due to its increased lipophilicity. It reached equilibrium within 60 minutes, removing 84.9% of SILD and 91% of TAD at a dose of 250 mg L^{-1}. A direct comparison revealed that, although ACs achieved high removal efficiencies at lower dosages, the DDAB-MMT system required higher dosages but had a simpler preparation process. Overall, the results suggest that waste-derived ACs strike an ideal balance between cost, efficiency, and sustainability. However, DDAB-MMT is a viable alternative for applications requiring rapid adsorption and functionalized surfaces. This research highlights the efficacy of adsorption techniques in mitigating pharmaceutical pollutants in water and promotes the use of sustainable, cost-effective materials. Future research should focus on refining synthesis parameters and functionalization techniques to improve adsorption capacity and operational viability.

8. CONCLUSIONS AND OUTLOOK

In this Ph.D. thesis, three pharmaceutical contaminants were investigated using innovative techniques to remove them from aquatic environments. The widespread use, persistence, and toxicity of these compounds pose a pressing challenge for water resource protection and environmental health, making the development of effective, sustainable, and scalable treatment solutions critical. This study explored advanced oxidation processes, electrochemical degradation, and adsorption-based approaches to provide environmentally friendly, practical remediation strategies.

Among the AOPs evaluated towards SILD, Sunlight/PMS proved the most efficient, achieving complete removal within 80–130 minutes in both DW and SWW. LC-LTQ-MS analysis identified photoproducts analogous to human metabolites, highlighting the importance of assessing transformation products. Ecotoxicity tests with *Vibrio fischeri* showed minimal adverse effects, validating the system's environmental compatibility. These results underscore the potential of Sunlight/PMS photooxidation as a cost-effective, sustainable, and scalable technique for PDE-5i removal, with future research focusing on catalyst optimization, recovery, and green alternatives.

The study on the electrochemical oxidation of VFX demonstrated that Pt electrodes are a robust, chloride-free alternative to BDD electrodes for VFX degradation. Indirect oxidation via hydroxyl and sulfate radicals enabled up to 94% removal of 25 ppm VFX after 7 hours under optimized conditions (0.1 M Na_2SO_4, pH 9, 25 mA cm^{-2}). LC-ESI-MS^n analysis revealed that transformation products formed through demethylation, hydroxylation, and ring modifications, including N-desmethylvenlafaxine and V276 isomers. *In silico* ECOSAR toxicity assessment indicated that these products were generally less toxic than VFX, confirming the environmental sustainability of this electrochemical approach, despite its higher energy requirements.

Regarding the adsorption studies, SBG-AC-MP exhibited superior physicochemical properties and adsorption performance compared to SBG-AC-CP. For VFX removal, SBG-AC-MP achieved a maximum adsorption capacity of 74 ± 6 mg g^{-1} in ultrapure water and maintained performance in wastewater without inhibitory effects. Equilibrium was reached within ~2 hours, following pseudo-second-order kinetics and Langmuir monolayer adsorption behavior.

SBG-derived ACs also effectively removed SILD and TAD, achieving high efficiencies at low doses (50 mg L^{-1}), while DDAB-MMT required higher doses (250 mg L^{-1}) but reached equilibrium faster (1 hour) due to increased lipophilicity.

Addressing the persistent challenge of ECs in aquatic environments, this thesis demonstrates that photooxidation, electrochemical oxidation, and adsorption using waste-

derived and functionalized materials can effectively mitigate the environmental burden of ECs. In particular, adsorption offers significant advantages in terms of low cost, operational efficiency, environmental compatibility, and scalability. By combining innovative technologies, sustainable materials, and circular-economy principles, it is possible to develop water-treatment solutions that are economically viable, scalable, and environmentally safe, thereby supporting global water protection, public health, and environmental sustainability.

REFERENCES

[1] J. Villaverde, T. Undabeytia, S. Nir, T. Sa, C. Maqueda, and E. Morillo, “A clay–vesicle system for water purification from organic pollutants,” *Wat. Research*, vol. 42, pp. 1211–1219, 2008, doi: 10.1016/j.watres.2007.09.004.

[2] M. Patel, R. Kumar, K. Kishor, T. Mlsna, C. U. Pittman, and D. Mohan, “Pharmaceuticals of Emerging Concern in Aquatic Systems : Chemistry, Occurrence, Effects, and Removal Methods,” *Chem. Reviews*, vol. 119, no. 6, 2019, doi: 10.1021/acs.chemrev.8b00299.

[3] D. O’Flynn *et al.*, “A review of pharmaceutical occurrence and pathways in the aquatic environment in the context of a changing climate and the COVID-19 pandemic,” *Anal. Methods*, vol. 13, no. 5, pp. 575–594, 2021, doi: 10.1039/D0AY02098B.

[4] Qater Al-Nada Ali Kanaem Al-Ibady *et al.*, " Emerging Contaminants in Water: A Review of Recent Research" on the occurrence, fate, and removal of emerging contaminants in water sources, highlighting recent developments in treatment technologies /A Review Article", *The Peerian Journal*, vol. 35, pp. 110–118, 2024.

[5] A. Yusuf *et al.*, “Monitoring of emerging contaminants of concern in the aquatic environment: a review of studies showing the application of effect-based measures,” *Anal. Methods*, vol. 13, no. 43, pp. 5120–5143, 2021, doi: 10.1039/D1AY01184G.

[6] M. Anis and S. Haydar, “Zeolite supported iron nanoparticles for the catalytic Fenton oxidative remediation of theophylline in aqueous medium,” *Desalin. and Wat. Treat.*, vol. 244, pp. 167–179, 2021, doi: 10.5004/dwt.2021.27854.

[7] J. Mbese *et al.*, “Classification, Potential Routes and Risk of Emerging Pollutants/Contaminant,” *Emer. Cont.*, Ed. London: IntechOpen, 2020, DOI: 10.5772/intechopen.94447.

[8] W. W. Carmichael, “The Cyanotoxins,” in *Classic Papers*, vol. 27, J. A. B. T.-A. in B. R. Callow, Ed. Academic Press, 1997, pp. 211–256.

[9] S. Dey, F. Bano, and A. Malik, “Pharmaceuticals and personal care product (PPCP) contamination—a global discharge inventory,” *Pharm. and Pers. Care Prod. Waste Manag. and Treat. Tech.*, 2019, pp. 1–26, https://doi.org/10.1016/B978-0-12-816189-0.00001-9.

[10] A. Yahaya *et al.*, “Analytical Methods for Determination of Regulated and Unregulated

Disinfection By-Products in Drinking Water: A Review.," *CaJoST*, vol. 2, no. 1 SE-Articles, pp. 25–36, doi: 10.4314/cajost.v2i1.34.

[11] V. Geissen *et al.*, "Emerging pollutants in the environment: A challenge for water resource management," *Int. Soil Water Conserv. Res.*, vol. 3, no. 1, pp. 57–65, 2015, doi: https://doi.org/10.1016/j.iswcr.2015.03.002.

[12] M. Letsoalo *et al.*, "Efficient detection and treatment of pharmaceutical contaminants to produce clean water for better health and environmental," *J. Clean. Prod.*, vol. 387, p. 135798, Feb. 2023, doi: 10.1016/j.jclepro.2022.135798.

[13] B. S. Rathi, P. S. Kumar, and P.-L. Show, "A review on effective removal of emerging contaminants from aquatic systems: Current trends and scope for further research.," *J. Hazard. Mater.*, vol. 409, p. 124413, May 2021, doi: 10.1016/j.jhazmat.2020.124413.

[14] D. Yadav *et al.*, "Environmental and health impacts of contaminants of emerging concerns: Recent treatment challenges and approaches," *Chemosphere*, vol. 272, p. 129492, 2021, doi: https://doi.org/10.1016/j.chemosphere.2020.129492.

[15] C. Barata, P. Alañon, S. Gutierrez-Alonso, M. C. Riva, C. Fernández, and J. V Tarazona, "A Daphnia magna feeding bioassay as a cost effective and ecological relevant sublethal toxicity test for Environmental Risk Assessment of toxic effluents.," *Sci. Total Environ.*, vol. 405, no. 1–3, pp. 78–86, Nov. 2008, doi: 10.1016/j.scitotenv.2008.06.028.

[16] O. W. On, "The Organisation for Economic Co-operation and Development," no. December, 2024.

[17] M. Cleuvers, "Aquatic ecotoxicity of pharmaceuticals including the assessment of combination effects.," *Toxicol. Lett.*, vol. 142, no. 3, pp. 185–194, May 2003, doi: 10.1016/s0378-4274(03)00068-7.

[18] G. Cortes and P. Rodriguez, *Selection of substances for the 5th Watch List under the Water Framework Directive*. 2025.

[19] L. G. Cortes *et al.*, *Selection of substances for the 3 rd Watch List under the Water Framework Directive*. 2020.

[20] D. Singh and A. Saadabadi, "Venlafaxine.," Treasure Island (FL), 2025.

[21] H. R. Ahmed, D. D. Ghafoor, N. N. M. Agha, G. A. Muhamad, P. Husamadin, and T.

M. Ali, “Advanced strategies for the removal of venlafaxine from aqueous environments: a critical review of adsorption and advanced oxidation pathways.,” *RSC Adv.*, vol. 15, no. 46, pp. 38889–38905, Oct. 2025, doi: 10.1039/d5ra06996c.

[22] A. S. Alturiqi, “Equilibrium Studies of Ternary Complexes of Cu (II) with Venlafaxine hydrochloride Drug and Some Amino Acids,” *Or. Jou. of Chem.*, 2018, https://dx.doi.org/10.13005/ojc/340170.

[23] R. Ma, H. Qu, B. Wang, F. Wang, and G. Yu, “Widespread monitoring of chiral pharmaceuticals in urban rivers reveals stereospecific occurrence and transformation,” *Environ. Int.*, vol. 138, p. 105657, 2020, doi: https://doi.org/10.1016/j.envint.2020.105657.

[24] M. del Carmen Gómez-Regalado *et al.*, “Accumulation and metabolization of the antidepressant venlafaxine and its main metabolite o-desmethylvenlafaxine in non-target marine organisms Holothuria tubulosa, Anemonia sulcata and Actinia equina,” *Mar. Pollut. Bull.*, vol. 192, p. 115055, 2023, doi: https://doi.org/10.1016/j.marpolbul.2023.115055.

[25] T. T. T. Tran, D. M. Nguyen, A. Q. Dao, V. T. Le, and Y. Vasseghian, “A state-of-the-art review on the nanomaterial-based sensor for detection of venlafaxine.,” *Chemosphere*, vol. 297, p. 134116, Jun. 2022, doi: 10.1016/j.chemosphere.2022.134116.

[26] M. Galus, J. Jeyaranjaan, E. Smith, H. Li, C. Metcalfe, and J. Wilson, “Chronic Effects of Exposure to a Pharmaceutical Mixture and Municipal Wastewater in Zebrafish,” *Aquat. Toxicol.*, vol. 132–133, Jan. 2013, doi: 10.1016/j.aquatox.2012.12.016.

[27] G. E. Agency, “Final report,” 2019.

[28] G. Bianco *et al.*, “Phosphodiesterase-5 (PDE-5) Inhibitors as Emergent Environmental Contaminants: Advanced Remediation and Analytical Methods,” *Water*, vol. 13, no. 20. 2021, doi: 10.3390/w13202859.

[29] A. R. Zizzamia *et al.*, “Efficient photooxidation processes for the removal of sildenafil from aqueous environments: A comparative study,” *Case Stud. Chem. Environ. Eng.*, vol. 9, no. February, p. 100708, 2024, doi: 10.1016/j.cscee.2024.100708.

[30] M. P. McCabe *et al.*, “Definitions of Sexual Dysfunctions in Women and Men: A Consensus Statement From the Fourth International Consultation on Sexual Medicine

2015," *J. Sex. Med.*, vol. 13, no. 2, pp. 135–143, Feb. 2016, doi: 10.1016/j.jsxm.2015.12.019.

[31] W. Ludwig and M. Phillips, "Organic causes of erectile dysfunction in men under 40.," *Urol. Int.*, vol. 92, no. 1, pp. 1–6, 2014, doi: 10.1159/000354931.

[32] M. Boolell, S. Gepi-Attee, J. C. Gingell, and M. J. Allen, "Sildenafil, a novel effective oral therapy for male erectile dysfunction.," *Br. J. Urol.*, vol. 78, no. 2, pp. 257–261, Aug. 1996, doi: 10.1046/j.1464-410x.1996.10220.x.

[33] W. S. Ahmed, A. M. Geethakumari, and K. H. Biswas, "Phosphodiesterase 5 (PDE5): Structure-function regulation and therapeutic applications of inhibitors.," *Biomed. Pharmacother.*, vol. 134, p. 111128, Feb. 2021, doi: 10.1016/j.biopha.2020.111128.

[34] M. Wanjari and S. Late, "Use of Sildenafil in young adults: a growing health problem," *Pan Afr. Med. J.*, vol. 44, 2023, doi: 10.11604/pamj.2023.44.113.39168.

[35] L. Foti *et al.*, "Comparison of sunlight-AOPs for levofloxacin removal: kinetics, transformation products, and toxicity assay on Escherichia coli and Micrococcus flavus.," *Environ. Sci. Pollut. Res. Int.*, vol. 29, no. 38, pp. 58201–58211, Aug. 2022, doi: 10.1007/s11356-022-19768-w.

[36] H. A. Ghofrani, I. H. Osterloh, and F. Grimminger, "Sildenafil: from angina to erectile dysfunction to pulmonary hypertension and beyond.," *Nat. Rev. Drug Discov.*, vol. 5, no. 8, pp. 689–702, Aug. 2006, doi: 10.1038/nrd2030.

[37] A. Hatefi, E. Rahimpour, T. Ghafourian, F. Martinez, M. Barzegar-Jalali, and A. Jouyban, "Solubility of sildenafil citrate in the binary mixtures of ethylene glycol and water at different temperatures," *J. Mol. Liq.*, vol. 299, 2020, doi: 10.1016/j.molliq.2019.112127.

[38] S. Dati, D. I. Sicurezza, S. Citrato, and S. Identificazione, "Scheda dati di sicurezza," pp. 1–12, 2025.

[39] H. Porst, H. Padma-Nathan, F. Giuliano, G. Anglin, L. Varanese, and R. Rosen, "Efficacy of tadalafil for the treatment of erectile dysfunction at 24 and 36 hours after dosing: a randomized controlled trial.," *Urology*, vol. 62, no. 1, pp. 121–126, Jul. 2003, doi: 10.1016/s0090-4295(03)00359-5.

[40] I. Eardley and J. Cartledge, "Tadalafil (Cialis) for men with erectile dysfunction.," *Int. J. Clin. Pract.*, vol. 56, no. 4, pp. 300–304, May 2002.

[41] https://pubchem.ncbi.nlm.nih.gov/compound/110635#section=LogP, last access 10/01/26.

[42] R. M. Coward and C. C. Carson, “Tadalafil in the treatment of erectile dysfunction.,” *Ther. Clin. Risk Manag.*, vol. 4, no. 6, pp. 1315–1330, Dec. 2008, doi: 10.2147/tcrm.s3336.

[43] Y. Hong *et al.*, “Contribution of sewage to occurrence of phosphodiesterase - 5 inhibitors in natural water,” *Sci. Rep.*, no. 2021, pp. 1–12, 2025, doi: 10.1038/s41598-021-89028-3.

[44] A. Nieto, M. Peschka, F. Borrull, E. Pocurull, R. M. Marcé, and T. P. Knepper, “Phosphodiesterase type V inhibitors: Occurrence and fate in wastewater and sewage sludge,” *Water Res.*, vol. 44, no. 5, pp. 1607–1615, 2010, doi: 10.1016/j.watres.2009.11.009.

[45] H. Fr. Schröder, W. Gebhardt, and M. Thevis, “Anabolic, doping, and lifestyle drugs, and selected metabolites in wastewater—detection, quantification, and behaviour monitored by high-resolution MS and MSn before and after sewage treatment,” *Anal. Bioanal. Chem.*, vol. 398, no. 3, pp. 1207–1229, 2010, doi: 10.1007/s00216-010-3958-3.

[46] A. Causanilles, E. Emke, and P. de Voogt, “Determination of phosphodiesterase type V inhibitors in wastewater by direct injection followed by liquid chromatography coupled to tandem mass spectrometry.,” *Sci. Total Environ.*, vol. 565, pp. 140–147, Sep. 2016, doi: 10.1016/j.scitotenv.2016.04.158.

[47] B. J. Venhuis, P. de Voogt, E. Emke, A. Causanilles, and P. H. J. Keizers, “Success of rogue online pharmacies: sewage study of sildenafil in the Netherlands.,” *BMJ (Clinical research ed.)*, vol. 349. England, p. g4317, Jul. 2014, doi: 10.1136/bmj.g4317.

[48] J. Shamshad and R. Ur Rehman, “Innovative approaches to sustainable wastewater treatment: a comprehensive exploration of conventional and emerging technologies,” *Environ. Sci. Adv.*, vol. 4, no. 2, pp. 189–222, 2024, doi: https://doi.org/10.1039/d4va00136b.

[49] M. Ortúzar, M. Esterhuizen, D. R. Olicón-Hernández, J. González-López, and E. Aranda, “Pharmaceutical Pollution in Aquatic Environments: A Concise Review of Environmental Impacts and Bioremediation Systems.,” *Front. Microbiol.*, vol. 13, p.

869332, 2022, doi: 10.3389/fmicb.2022.869332.

[50] K. Y. Adjei, A. Aliyu, E. Owhe-ureghe, E. A. Oriakhi, and T. Bakare-, “Biological treatment of emerging organic micropollutants in wastewater : Recent advances and perspectives,” *World Journal of Biology Pharmacy and Health Sciences*, vol. 21, no. 3, pp. 488-505, 2025, https://doi.org/10.30574/wjbphs.2025.21.3.0181.

[51] P. C. Rúa-Gómez and W. Püttmann, “Degradation of lidocaine, tramadol, venlafaxine and the metabolites O-desmethyltramadol and O-desmethylvenlafaxine in surface waters.,” *Chemosphere*, vol. 90, no. 6, pp. 1952–1959, Feb. 2013, doi: 10.1016/j.chemosphere.2012.10.039.

[52] H. Ou, R. Liu, Z. Liao, and E. Zeng, “Occurrence and fate of microplastics in urban water management systems,” *Micropl. Contam. In Aquat. Envir.*, pp. 181–228, 2024, https://doi.org/10.1016/B978-0-443-15332-7.00006-5.

[53] M. Gros, M. Petrović, and D. Barceló, “Wastewater treatment plants as a pathway for aquatic contamination by pharmaceuticals in the ebro river basin (northeast Spain).,” *Environ. Toxicol. Chem.*, vol. 26, no. 8, pp. 1553–1562, Aug. 2007, doi: 10.1897/06-495r.1.

[54] M. K. Shahid, A. Kashif, A. Fuwad, and Y. Choi, “Current advances in treatment technologies for removal of emerging contaminants from water – A critical review,” *Coord. Chem. Rev.*, vol. 442, p. 213993, Sep. 2021, doi: 10.1016/j.ccr.2021.213993.

[55] F. Al-ajmi, M. Al-marri, and F. Almomani, “A Comprehensive Review of Advanced Treatment Technologies for the Enhanced Reuse of Produced Water,” *Water*, vol.16, no. 22, p. 3306, 2024, https://doi.org/10.3390/w16223306.

[56] X. Shi, K. Y. Leong, and H. Y. Ng, “Anaerobic treatment of pharmaceutical wastewater: A critical review.,” *Bioresour. Technol.*, vol. 245, no. Pt A, pp. 1238–1244, Dec. 2017, doi: 10.1016/j.biortech.2017.08.150.

[57] X. Li, B. Wang, F. Liu, and G. Yu, “Occurrence and Removal of Pharmaceutical Contaminants in Urine : A Review,” *Water*, vol. 15, no. 8, p. 1517, 2023, https://doi.org/10.3390/w15081517.

[58] Z.-H. Liu, Y. Kanjo, and S. Mizutani, “Removal mechanisms for endocrine disrupting compounds (EDCs) in wastewater treatment - physical means, biodegradation, and chemical advanced oxidation: a review.,” *Sci. Total Environ.*, vol. 407, no. 2, pp. 731–

748, Jan. 2009, doi: 10.1016/j.scitotenv.2008.08.039.

[59] A. Naeem, T. Mahmood, R. Ali, S. Momin, and A. Khan, “Technologies for Removal of Emerging Contaminants from Wastewater,” M. Ince and O. Kaplan Ince, Eds. London: IntechOpen, 2022.

[60] R. Andreozzi, V. Caprio, A. Insola, and R. Marotta, “Advanced oxidation processes (AOP) for water purification and recovery,” *Catal. Today*, vol. 53, no. 1, pp. 51–59, 1999, doi: https://doi.org/10.1016/S0920-5861(99)00102-9.

[61] F. Lelario, M. Brienza, S. A. Bufo, and L. Scrano, “Effectiveness of different advanced oxidation processes (AOPs) on the abatement of the model compound mepanipyrim in water,” *J. Photochem. Photobiol. A Chem.*, vol. 321, pp. 187–201, 2016, doi: https://doi.org/10.1016/j.jphotochem.2016.01.024.

[62] N. R. Mirza *et al.*, “A review of the textile wastewater treatment technologies with special focus on advanced oxidation processes (AOPs), membrane separation and integrated AOP-membrane processes,” *Desalin. Water Treat.*, vol. 206, pp. 83–107, 2020, doi: https://doi.org/10.5004/dwt.2020.26363.

[63] X. Liu *et al.*, “Degradation difference of Ofloxacin and Levofloxacin by UV/H2O2 and UV/PS (persulfate): Efficiency, factors and mechanism,” *Chem. Eng. J.*, p. 123987, Dec. 2019, doi: 10.1016/j.cej.2019.123987.

[64] F. Rehman, W. Ahmad, and M. Sayed, “Mechanistic investigations on the removal of diclofenac sodium by UV/S2O82−/Fe2+, UV/HSO5−/Fe2+ and UV/H2O2/Fe2+-based advanced oxidation processes,” *Environ. Technol.*, vol. 42, no. 25, pp. 3995–4005, Nov. 2021, doi: 10.1080/09593330.2020.1770869.

[65] R. Krakowiak *et al.*, “Titanium dioxide-based photocatalysts for degradation of emerging contaminants including pharmaceutical pollutants,” *Appl. Sci.*, vol. 11, no. 18, 2021, doi: 10.3390/app11188674.

[66] R. Dhawle, Z. Frontistis, D. Mantzavinos, and P. Lianos, “Production of hydrogen peroxide with a photocatalytic fuel cell and its application to UV/H2O2 degradation of dyes,” *Chem. Eng. J. Adv.*, vol. 6, p. 100109, 2021, doi: https://doi.org/10.1016/j.ceja.2021.100109.

[67] H. Li, J. Shang, Z. Yang, W. Shen, Z. Ai, and L. Zhang, “Oxygen Vacancy Associated Surface Fenton Chemistry: Surface Structure Dependent Hydroxyl Radicals

Generation and Substrate Dependent Reactivity.," *Environ. Sci. Technol.*, vol. 51, no. 10, pp. 5685–5694, May 2017, doi: 10.1021/acs.est.7b00040.

[68] J. Wang and S. Wang, "Reactive species in advanced oxidation processes: Formation, identification and reaction mechanism," *Chem. Eng. J.*, vol. 401, p. 126158, 2020, doi: https://doi.org/10.1016/j.cej.2020.126158.

[69] C. Zaharia, D. Suteu, A. Muresan, R. Muresan, and A. Popescu, "Textile wastewater treatment by homogenous oxidation with hydrogen peroxide," *Environ. Eng. Manag. J.*, vol. 8, pp. 1359–1369, Dec. 2009, doi: 10.30638/eemj.2009.199.

[70] S. Merouani, A. Dehane, A. Belghit, O. Hamdaoui, N. El Houda Boussalem, and H. Daif, "Removal of persistent textile dyes from wastewater by Fe(ii)/H2O2/H3NOH+ integrated system: process performance and limitations††Electronic supplementary information (ESI) available. See https://doi.org/10.1039/d2va00011c," *Environ. Sci. Adv.*, vol. 1, no. 2, pp. 192–207, 2022, doi: https://doi.org/10.1039/d2va00011c.

[71] J. Wang and S. Wang, "Activation of persulfate (PS) and peroxymonosulfate (PMS) and application for the degradation of emerging contaminants," *Chem. Eng. J.*, 2017, doi: 10.1016/j.cej.2017.11.059.

[72] T. Zhang, "Heterogeneous Catalytic Oxidation of Organic Compound for Wastewater Treatment," *Advanced Oxidation Processes - Applications, Trends, and Prospects*, 2020, 10.5772/intechopen.90393.

[73] O. S. Furman, A. L. Teel, and R. J. Watts, "Mechanism of base activation of persulfate.," *Environ. Sci. Technol.*, vol. 44, no. 16, pp. 6423–6428, Aug. 2010, doi: 10.1021/es1013714.

[74] A. Ghauch and A. M. Tuqan, "Oxidation of bisoprolol in heated persulfate / H 2 O systems : Kinetics and products," *Chem. Eng. J.*, vol. 183, no. 2012, pp. 162–171, 2020, doi: 10.1016/j.cej.2011.12.048.

[75] A. Fujishima, T. N. Rao, and D. A. Tryk, "Titanium dioxide photocatalysis," *J. Photochem. Photobiol. C Photochem. Rev.*, vol. 1, no. 1, pp. 1–21, 2000, doi: https://doi.org/10.1016/S1389-5567(00)00002-2.

[76] K. Pirkanniemi and M. Sillanpää, "Heterogeneous water phase catalysis as an environmental application: a review," *Chemosphere*, vol. 48, no. 10, pp. 1047–1060, 2002, doi: https://doi.org/10.1016/S0045-6535(02)00168-6.

[77] P. R. Gogate and A. B. Pandit, “A review of imperative technologies for wastewater treatment II: hybrid methods,” *Adv. Environ. Res.*, vol. 8, no. 3, pp. 553–597, 2004, doi: https://doi.org/10.1016/S1093-0191(03)00031-5.

[78] P. R. Gogate and A. B. Pandit, “A review of imperative technologies for wastewater treatment I: oxidation technologies at ambient conditions,” *Adv. Environ. Res.*, vol. 8, no. 3, pp. 501–551, 2004, doi: https://doi.org/10.1016/S1093-0191(03)00032-7.

[79] R. Munter, S. Preis, J. Kallas, M. Trapido, and Y. Veressinina, “Advanced oxidation processes (AOPs): Water treatment technology for the twenty-first century,” *Water Science*, vol. 28, pp. 354–362, Jan. 2001.

[80] R. Andreozzi, V. Caprio, A. Insola, and R. Marotta, “Advanced oxidation processes (AOP) for water purification and recovery,” *Catal. Today*, vol. 53, no. 1, pp. 51–59, 1999, doi: 10.1016/S0920-5861(99)00102-9.

[81] P. Babay, C. A. Emilio, R. Ferreyra, E. Gautier, R. Gettar, and M. Litter, “Kinetics and mechanisms of EDTA photocatalytic degradation with TiO2,” *Water Sci. Technol.*, vol. 44, pp. 179–185, Feb. 2001, doi: 10.2166/wst.2001.0281.

[82] O. Abida *et al.*, “Degradation of 4-chlorophenol mediated by Fe(III)-NTA in homogeneous and heterogeneous systems.,” *Water Sci. Technol. a J. Int. Assoc. Water Pollut. Res.*, vol. 49, no. 4, pp. 123–128, 2004.

[83] F. Sopaj, M. A. Rodrigo, N. Oturan, F. I. Podvorica, J. Pinson, and M. A. Oturan, “Influence of the anode materials on the electrochemical oxidation efficiency. Application to oxidative degradation of the pharmaceutical amoxicillin,” *Chem. Eng. J.*, vol. 262, pp. 286–294, 2015, doi: https://doi.org/10.1016/j.cej.2014.09.100.

[84] I. Lozano, C. J. Pérez-Guzmán, A. Mora, J. Mahlknecht, C. L. Aguilar, and P. Cervantes-Avilés, “Pharmaceuticals and personal care products in water streams: Occurrence, detection, and removal by electrochemical advanced oxidation processes,” *Sci. Total Environ.*, vol. 827, p. 154348, 2022, doi: https://doi.org/10.1016/j.scitotenv.2022.154348.

[85] R. Fu, P.-S. Zhang, Y.-X. Jiang, L. Sun, and X.-H. Sun, “Wastewater treatment by anodic oxidation in electrochemical advanced oxidation process: Advance in mechanism, direct and indirect oxidation detection methods.,” *Chemosphere*, vol. 311, no. Pt 1, p. 136993, Jan. 2023, doi: 10.1016/j.chemosphere.2022.136993.

[86] M. Grassi, G. Kaykioglu, V. Belgiorno, and G. Lofrano, “Removal of Emerging Contaminants from Water and Wastewater by Adsorption Process BT - Emerging Compounds Removal from Wastewater: Natural and Solar Based Treatments,” *Emerging Compounds Removal from Wastewater: Natural and Solar Based Treatments*, Ed. Dordrecht: Springer Netherlands, pp. 15–37, 2012.

[87] S. Aziz *et al.*, “A comprehensive review of membrane - based water filtration techniques,” *Appl. Water Sci.*, vol. 14, no. 8, pp. 1–17, 2024, doi: 10.1007/s13201-024-02226-y.

[88] M. Malakootian, M. Yaseri, and M. Faraji, “Removal of antibiotics from aqueous solutions by nanoparticles: a systematic review and meta-analysis,” *Environ. Sci. Pollut. Res.*, vol. 26, no. 9, pp. 8444–8458, 2019, doi: 10.1007/s11356-019-04227-w.

[89] M. Turk Sekulic, N. Boskovic, A. Slavkovic, J. Garunovic, S. Kolakovic, and S. Pap, “Surface functionalised adsorbent for emerging pharmaceutical removal: Adsorption performance and mechanisms,” *Process Saf. Environ. Prot.*, vol. 125, pp. 50–63, 2019, doi: https://doi.org/10.1016/j.psep.2019.03.007.

[90] O. H. P. Gunawardene, C. A. Gunathilake, and K. Vikrant, *Carbon Dioxide Capture through Physical and Chemical Adsorption Using Porous Carbon Materials : A Review*. 2022.

[91] I. Langmuir, “THE ADSORPTION OF GASES ON PLANE SURFACES OF GLASS, MICA AND PLATINUM.,” *J. Am. Chem. Soc.*, vol. 40, no. 9, pp. 1361–1403, Sep. 1918, doi: 10.1021/ja02242a004.

[92] H. Freundlich, “Über die Adsorption in Lösungen,” vol. 57U, no. 1, pp. 385–470, 1907, doi: doi:10.1515/zpch-1907-5723.

[93] S. S. Alam and Y. Deng, “Modifying a Smectite using Organic Nutrients to Enhance its Efficacy at Removing Aflatoxin B1 from Corn Fermentation Solution,” *Clays Clay Miner.*, vol. 70, no. 2, pp. 196–208, 2022, doi: DOI: 10.1007/s42860-022-00179-4.

[94] T. Kananira, “Synthesis of vermiculite bio-organ clays with dimer fatty acid-based polyamide chains for oil and gas field produced water treatment,” 2025.

[95] D. H. Carrales-Alvarado, R. Ocampo-Pérez, R. Leyva-Ramos, and J. Rivera-Utrilla, “Removal of the antibiotic metronidazole by adsorption on various carbon materials from aqueous phase,” *J. Colloid Interface Sci.*, vol. 436, pp. 276–285, 2014, doi:

https://doi.org/10.1016/j.jcis.2014.08.023.

[96] K. S. D. Premarathna *et al.*, “Clay-biochar composites for sorptive removal of tetracycline antibiotic in aqueous media,” *J. Environ. Manage.*, vol. 238, pp. 315–322, 2019, doi: https://doi.org/10.1016/j.jenvman.2019.02.069.

[97] N. Z. Mohd Azmi, A. Buthiyappan, A. A. Abdul Raman, M. F. Abdul Patah, and S. Sufian, “Recent advances in biomass based activated carbon for carbon dioxide capture – A review,” *J. Ind. Eng. Chem.*, vol. 116, pp. 1–20, 2022, doi: https://doi.org/10.1016/j.jiec.2022.08.021.

[98] S. Wang *et al.*, “Development of high-performance adsorbent using KOH-impregnated rice husk-based activated carbon for indoor CO2 adsorption,” *Chem. Eng. J.*, vol. 437, p. 135378, 2022, doi: https://doi.org/10.1016/j.cej.2022.135378.

[99] F. Lelario *et al.*, “Pairing micropollutants and clay-composite sorbents for efficient water treatment: Filtration and modeling at a pilot scale,” *Appl. Clay Sci.*, vol. 137, pp. 225–232, 2017, doi: https://doi.org/10.1016/j.clay.2016.12.029.

[100] E. I. Unuabonah and A. Taubert, “Clay–polymer nanocomposites (CPNs): Adsorbents of the future for water treatment,” *Appl. Clay Sci.*, vol. 99, pp. 83–92, 2014, doi: https://doi.org/10.1016/j.clay.2014.06.016.

[101] F. Uddin, “Clays, nanoclays, and montmorillonite minerals,” *Metall. Mater. Trans. A Phys. Metall. Mater. Sci.*, vol. 39, no. 12, pp. 2804–2814, 2008, doi: 10.1007/s11661-008-9603-5.

[102] M. S. Akhtar, S. Ali, and W. Zaman, “Innovative Adsorbents for Pollutant Removal: Exploring the Latest Research and Applications.,” *Molecules*, vol. 29, no. 18, Sep. 2024, doi: 10.3390/molecules29184317.

[103] T. Araújo, H. Quesada, R. Bergamasco, D. Vareschini, and M. A. Barros, “Activated hydrochar produced from brewer’s spent grain and its application in the removal of acetaminophen,” *Bioresour. Technol.*, vol. 310, p. 123399, Apr. 2020, doi: 10.1016/j.biortech.2020.123399.

[104] A. F. C. Sousa, M. V. Gil, and V. Calisto, “Upcycling spent brewery grains through the production of carbon adsorbents—application to the removal of carbamazepine from water,” *Environ. Sci. Pollut. Res.*, vol. 27, no. 29, pp. 36463–36475, 2020, doi: 10.1007/s11356-020-09543-0.

[105] T. P. de Araújo, F. de O. Tavares, D. T. Vareschini, and M. A. S. D. Barros, "Biosorption mechanisms of cationic and anionic dyes in a low-cost residue from brewer's spent grain," *Environ. Technol.*, vol. 42, no. 19, pp. 2925–2940, Aug. 2021, doi: 10.1080/09593330.2020.1718217.

[106] M. Danish and T. Ahmad, "A review on utilization of wood biomass as a sustainable precursor for activated carbon production and application," *Renew. Sustain. Energy Rev.*, vol. 87, pp. 1–21, 2018, doi: https://doi.org/10.1016/j.rser.2018.02.003.

[107] T. M. Alslaibi, I. Abustan, M. A. Ahmad, and A. A. Foul, "A review: production of activated carbon from agricultural byproducts via conventional and microwave heating," *J. Chem. Technol. Biotechnol.*, vol. 88, no. 7, pp. 1183–1190, 2013.

[108] É. Sousa *et al.*, "Optimizing microwave-assisted production of waste-based activated carbons for the removal of antibiotics from water," *Sci. Total Environ.*, vol. 752, p. 141662, 2021, doi: 10.1016/j.scitotenv.2020.141662.

[109] C. Saucier *et al.*, "Microwave-assisted activated carbon from cocoa shell as adsorbent for removal of sodium diclofenac and nimesulide from aqueous effluents," *J. Hazard. Mater.*, vol. 289, pp. 18–27, 2015, doi: https://doi.org/10.1016/j.jhazmat.2015.02.026.

[110] S. Tongur and S. Yildiz, "Toxicological evaluation of carbamazepine active pharmaceutical ingredient with Lepidium sativum, Daphnia magna and Vibrio fischeri toxicity test methods," *Desalin. Water Treat.*, vol. 201, pp. 438–442, 2020, doi: https://doi.org/10.5004/dwt.2020.25969.

[111] S. Parvez, C. Venkataraman, and S. Mukherji, "A review on advantages of implementing luminescence inhibition test (Vibrio fischeri) for acute toxicity prediction of chemicals," *Environ. Int.*, vol. 32, no. 2, pp. 265–268, 2006, doi: https://doi.org/10.1016/j.envint.2005.08.022.

[112] M. l. Farré, M.-J. García, L. Tirapu, A. Ginebreda, and D. Barcelo, "Wastewater toxicity screening of non-ionic surfactants by Toxalert® and Microtox® bioluminescence inhibition assays," *Anal. Chim. Acta*, vol. 427, pp. 181–189, Jan. 2001, doi: 10.1016/S0003-2670(00)01022-9.

[113] M. Farré and D. Barcelo, "Toxicity Testing of Wastewater and Sewage Sludge by Biosensors, Bioassays and Chemical Analysis," *TrAC Trends Anal. Chem.*, vol. 22, pp. 299–310, Nov. 2003, doi: 10.1016/S0165-9936(03)00504-1.

[114] P. Reuschenbach, M. Silvani, M. Dammann, D. Warnecke, and T. Knacker, “ECOSAR model performance with a large test set of industrial chemicals.,” *Chemosphere*, vol. 71, no. 10, pp. 1986–1995, May 2008, doi: 10.1016/j.chemosphere.2007.12.006.

[115] “D.A. Skoog, D.M. West, F.J. Holler, S.R. Crouch ‘Fondamenti di chimica analitica’. Edises, Napoli, 2009, 30.” .

[116] “Tarrant A. W. S., Optical Measurements, Chapter 28, Instrumentation Reference Book (Fourth Edition), 2010.” .

[117] N. Mirsaleh-Kohan, W. D. Robertson, and R. N. Compton, “Electron ionization time-of-flight mass spectrometry: historical review and current applications.,” *Mass Spectrom. Rev.*, vol. 27, no. 3, pp. 237–285, 2008, doi: 10.1002/mas.20162.

[118] T. Kind and O. Fiehn, “Advances in structure elucidation of small molecules using mass spectrometry.,” *Bioanal. Rev.*, vol. 2, no. 1–4, pp. 23–60, Dec. 2010, doi: 10.1007/s12566-010-0015-9.

[119] J. B. Fenn, M. Mann, C. K. Meng, S. F. Wong, and C. M. Whitehouse, “Electrospray ionization for mass spectrometry of large biomolecules.,” *Science*, vol. 246, no. 4926, pp. 64–71, Oct. 1989, doi: 10.1126/science.2675315.

[120] V. V Laiko, M. A. Baldwin, and A. L. Burlingame, “Atmospheric pressure matrix-assisted laser desorption/ionization mass spectrometry.,” *Anal. Chem.*, vol. 72, no. 4, pp. 652–657, Feb. 2000, doi: 10.1021/ac990998k.

[121] Y. Zhang *et al.*, “In Situ Liquid Secondary Ion Mass Spectrometry: A Surprisingly Soft Ionization Process for Investigation of Halide Ion Hydration.,” *Anal. Chem.*, vol. 91, no. 11, pp. 7039–7046, Jun. 2019, doi: 10.1021/acs.analchem.8b05804.

[122] M. A. Baldwin, “Mass spectrometers for the analysis of biomolecules.,” *Methods Enzymol.*, vol. 402, pp. 3–48, 2005, doi: 10.1016/S0076-6879(05)02001-X.

[123] J. Gieniec, L. L. Mack, K. Nakamae, C. Gupta, V. Kumar, and M. Dole, “Electrospray mass spectroscopy of macromolecules: Application of an ion-drift spectrometer,” *Biomed. Mass Spectrom.*, vol. 11, no. 6, pp. 259–268, 1984.

[124] J. H. Gross, *Mass spectrometry: a textbook*. Springer Science & Business Media, 2006.

[125] M. Wilm, “Principles of electrospray ionization.,” *Mol. Cell. Proteomics*, vol. 10, no. 7, p. M111.009407, Jul. 2011, doi: 10.1074/mcp.M111.009407.

[126] A. G Marshall *et al.*, “Mass resolution and mass accuracy: how much is enough?,” *Mass Spectrom. (Tokyo, Japan)*, vol. 2, no. Spec Iss, p. S0009, 2013, doi: 10.5702/massspectrometry.S0009.

[127] A. G. Brenton and A. R. Godfrey, “Accurate mass measurement: terminology and treatment of data.,” *J. Am. Soc. Mass Spectrom.*, vol. 21, no. 11, pp. 1821–1835, Nov. 2010, doi: 10.1016/j.jasms.2010.06.006.

[128] Q. Hu, R. J. Noll, H. Li, A. Makarov, M. Hardman, and R. Graham Cooks, “The Orbitrap: a new mass spectrometer.,” *J. Mass Spectrom.*, vol. 40, no. 4, pp. 430–443, Apr. 2005, doi: 10.1002/jms.856.

[129] Y. Liang, P. Neta, X. Yang, and S. E. Stein, “Collision-Induced Dissociation of Deprotonated Peptides. Relative Abundance of Side-Chain Neutral Losses, Residue-Specific Product Ions, and Comparison with Protonated Peptides.,” *J. Am. Soc. Mass Spectrom.*, vol. 29, no. 3, pp. 463–469, Mar. 2018, doi: 10.1007/s13361-017-1842-5.

[130] R. M. Silverstein, F. X. Webster, D. J. Kiemle, and D. L. Bryce, *Identificazione spettrometrica di composti organici*. Ambrosiana, 2016.

[131] E. De Hoffmann and V. Stroobant, *Mass spectrometry: principles and applications*. John Wiley & Sons, 2007.

[132] G. L. Glish, S. A. McLuckey, T. Y. Ridley, and R. G. Cooks, “A new ‘hybrid’ sector/quadrupole mass spectrometer for mass spectrometry/mass spectrometry,” *Int. J. Mass Spectrom. Ion Phys.*, vol. 41, no. 3, pp. 157–177, 1982, doi: https://doi.org/10.1016/0020-7381(82)85032-8.

[133] R. Yost and C. Enke, “Selected ion fragmentation with a tandem quadrupole mass spectromete,” *J. Am. Chem. Soc.*, vol. 100, pp. 2274–2275, Mar. 1978, doi: 10.1021/ja00475a072.

[134] D. Douglas, “Linear quadrupoles in mass spectrometry,” *Mass Spectrom. Rev.*, vol. 28, pp. 937–960, Nov. 2009, doi: 10.1002/mas.20249.

[135] P. Wolfgang and S. Helmut, “Apparatus for separating charged particles of different specific charges," Jun. 07, 1960.

[136] I. Szabo, “New ion-optical devices utilizing oscillatory electric fields. I. Principle of operation and analytical theory of multipole devices with two-dimensional electric fields,” *Int. J. Mass Spectrom. Ion Process.*, vol. 73, no. 3, pp. 197–235, 1986, doi:

https://doi.org/10.1016/0168-1176(86)80001-5.

[137] M. H. Friedman, A. L. Yergey, and J. E. Campana, “Fundamentals of ion motion in electric radio-frequency multipole fields,” *J. Phys. E.*, vol. 15, no. 1, p. 53, 1982.

[138] C. M. Whitehouse, B. A. Andrien Jr, and E. E. Gulcicek, “Mass spectrometry with multipole ion guides," Jun. 22, 2004.

[139] A. Onzo, “Molecular cartography of the metabolome of typical food products of the Basilicata region by using high resolution mass spectrometry,” 2021.

[140] H. Andersen, L. Djuandhi, U. Mittal, and N. Sharma, “Strategies for the Analysis of Graphite Electrode Function,” *Adv. Energy Mater.*, vol. 11, Nov. 2021, doi: 10.1002/aenm.202102693.

[141] A. Ul-Hamid, *A beginners’ guide to scanning electron microscopy*, vol. 1. Springer, 2018.

[142] L. Reimer, “Scanning electron microscopy: physics of image formation and microanalysis,”1995.

[143] K. Siegbahn and K. Edvarson, “β-Ray spectroscopy in the precision range of 1: 105,” *Nucl. Phys.*, vol. 1, no. 8, pp. 137–159, 1956.

[144] D. Briggs, “Practical surface analysis,” *Auger X-Ray Photoelect. Spectroscory*, vol. 1, pp. 151–152, 1990.

[145] P. Auger, “Sur l’effet photoélectrique composé,” *J. Phys. le Radium*, vol. 6, no. 6, pp. 205–208, 1925.

[146] P. H. Emmett, “Gases i n Multimolecular Layers,” vol. 407, no. 1, 1936.

[147] M. M. DUBININ, “Physical Adsorption of Gases and Vapors in Micropores,” vol. 9, D. A. CADENHEAD, J. F. DANIELLI, and M. D. B. T.-P. in S. and M. S. ROSENBERG, Eds. Elsevier, 1975, pp. 1–70.

[148] F. Stoeckli and L. Ballerini, “Evolution of microporosity during activation of carbon,” *Fuel*, vol. 70, no. 4, pp. 557–559, 1991, doi: https://doi.org/10.1016/0016-2361(91)90036-A.

[149] A. P. Taylor, R. P. Robinson, Y. M. Fobian, D. C. Blakemore, L. H. Jones, and O. Fadeyi, “Modern advances in heterocyclic chemistry in drug discovery,” *Org. Biomol. Chem.*, vol. 14, no. 28, pp. 6611–6637, 2016, doi: 10.1039/c6ob00936k.

[150] E. Kabir and M. Uzzaman, “A review on biological and medicinal impact of heterocyclic compounds,” *Results Chem.*, vol. 4, 2022, doi: 10.1016/j.rechem.2022.100606.

[151] N. Aryal *et al.*, “Transformation products of pharmaceuticals in the environment: Their fate, (eco)toxicity and bioaccumulation potential,” *J. Environ. Manage.*, vol. 271, no. 10, pp. 1587–1594, 2020.

[152] H. B. Broughton and I. A. Watson, “Selection of heterocycles for drug design,” *J. Mol. Graph. Model.*, vol. 23, no. 1, pp. 51–58, 2004, doi: 10.1016/j.jmgm.2004.03.016.

[153] C. Lamberth and J. Dinges, “Bioactive Heterocyclic Compound Classes: Agrochemicals,” *Bioact. Heterocycl. Compd. Classes Agrochem.*, 2012, doi: 10.1002/9783527664412.

[154] L. Q. Lu, J. R. Chen, and W. J. Xiao, “Development of cascade reactions for the concise construction of diverse heterocyclic architectures,” *Acc. Chem. Res.*, vol. 45, no. 8, pp. 1278–1293, 2012, doi: 10.1021/ar200338s.

[155] R. Dua, S. Shrivastava, S. K. Sonwane, S. K. Srivastava, and others, “Pharmacological significance of synthetic heterocycles scaffold: a review,” *Adv. Biol. Res. (Rennes).*, vol. 5, no. 3, pp. 120–144, 2011.

[156] A. L. Moreno Ríos, K. Gutierrez-Suarez, Z. Carmona, C. G. Ramos, and L. F. Silva Oliveira, “Pharmaceuticals as emerging pollutants: Case naproxen an overview,” *Chemosphere*, vol. 291, 2022, doi: 10.1016/j.chemosphere.2021.132822.

[157] T. Huanyu, S. Jianghong, G. Wei, Z. Jiawei, G. Hui, and W. Yunhe, “Environmental fate and toxicity of androgens: A critical review,” *Environ. Res.*, vol. 214, 2022, doi: 10.1016/j.envres.2022.113849.

[158] Josef jampilek, “Heterocycles in Medicinal Chemistry,” *Molecules*, vol. 24, no. 3839, pp. 1–4, 2019.

[159] G. Li Petri, R. Holl, V. Spanò, M. Barreca, I. Sardo, and M. V. Raimondi, “Editorial: Emerging heterocycles as bioactive compounds,” *Front. Chem.*, vol. 11, 2023, doi: 10.3389/fchem.2023.1202192.

[160] C. Lamberth, “Heterocyclic chemistry in crop protection,” *Pest Manag. Sci.*, vol. 69, no. 10, pp. 1106–1114, 2013, doi: 10.1002/ps.3615.

[161] T. VA, “Application of Synthetic Low Molecular Weight Heterocyclic Compounds Derivatives of Pyrimidine, Pyrazole and Oxazole in Agricultural Biotechnology as a New Plant Growth Regulating Substances,” *Int. J. Med. Biotechnol. Genet.*, pp. 10–32, 2017, doi: 10.19070/2379-1020-si02002.

[162] A. Babu *et al.*, “NMI-SO2Cl2-Mediated Amide Bond Formation: Facile Synthesis of Some Dihydrotriazolopyrimidine Amide Derivatives as Potential Anti-Inflammatory and Anti-Tubercular Agents,” *Pharmaceuticals*, vol. 17, no. 5, 2024, doi: 10.3390/ph17050548.

[163] S. Brendel *et al.*, “Four selected high molecular weight heterocyclic aromatic hydrocarbons: Ecotoxicological hazard assessment, environmental relevance and regulatory needs under REACH,” *Ecotoxicol. Environ. Saf.*, vol. 163, pp. 340–348, 2018, doi: 10.1016/j.ecoenv.2018.07.035.

[164] P. González-Andrés, L. Fernández-Peña, C. Díez-Poza, C. Villalobos, L. Nuñez, and A. Barbero, “Marine Heterocyclic Compounds That Modulate Intracellular Calcium Signals: Chemistry and Synthesis Approaches,” *Mar. Drugs*, vol. 19, no. 2, 2021, doi: 10.3390/MD19020078.

[165] S. K. Khetan and T. J. Collins, “Human pharmaceuticals in the aquatic environment: a challenge to Green Chemistry.,” *Chem. Rev.*, vol. 107, no. 6, pp. 2319–2364, Jun. 2007, doi: 10.1021/cr020441w.

[166] K. V. Padoley, S. N. Mudliar, and R. A. Pandey, “Heterocyclic nitrogenous pollutants in the environment and their treatment options - An overview,” *Bioresour. Technol.*, vol. 99, no. 10, pp. 4029–4043, 2008, doi: 10.1016/j.biortech.2007.01.047.

[167] A. L. Boreen, W. A. Arnold, and K. McNeill, “Photochemical fate of sulfa drugs in then aquatic environment: Sulfa drugs containing five-membered heterocyclic groups,” *Environ. Sci. Technol.*, vol. 38, no. 14, pp. 3933–3940, 2004, doi: 10.1021/es0353053.

[168] S. M. Gupta and M. Tripathi, “A review of TiO2 nanoparticles,” *Chinese Sci. Bull.*, vol. 56, no. 16, pp. 1639–1657, 2011, doi: 10.1007/s11434-011-4476-1.

[169] M. B. Ahmed, J. L. Zhou, H. H. Ngo, W. Guo, N. S. Thomaidis, and J. Xu, “Progress in the biological and chemical treatment technologies for emerging contaminant removal from wastewater: A critical review,” *J. Hazard. Mater.*, vol. 323, pp. 274–298, 2017, doi: 10.1016/j.jhazmat.2016.04.045.

[170] T. Qadir, A. Amin, P. K. Sharma, I. Jeelani, and H. Abe, “A Review on Medicinally Important Heterocyclic Compounds,” *Open Med. Chem. J.*, vol. 16, no. 1, 2022, doi: 10.2174/18741045-v16-e2202280.

[171] I. Mushtaq and A. Ahmed, “Synthesis of biologically active sulfonamide-based indole analogs: a review,” *Futur. J. Pharm. Sci.*, vol. 9, no. 1, 2023, doi: 10.1186/s43094-023-00500-5.

[172] C. Hao, L. Lissemore, B. Nguyen, S. Kleywegt, P. Yang, and K. Solomon, “Determination of pharmaceuticals in environmental waters by liquid chromatography/electrospray ionization/tandem mass spectrometry,” *Anal. Bioanal. Chem.*, vol. 384, no. 2, pp. 505–513, 2006, doi: 10.1007/s00216-005-0199-y.

[173] M. Gaba and C. Mohan, “Development of drugs based on imidazole and benzimidazole bioactive heterocycles: Recent advances and future directions,” *Med. Chem. Res.*, vol. 25, no. 2, pp. 173–210, 2016, doi: 10.1007/s00044-015-1495-5.

[174] H. E. Hashem and Y. El Bakri, “An overview on novel synthetic approaches and medicinal applications of benzimidazole compounds: An overview on novel synthetic approaches and medicinal applications,” *Arab. J. Chem.*, vol. 14, no. 11, 2021, doi: 10.1016/j.arabjc.2021.103418.

[175] R. S. Keri, A. Hiremathad, S. Budagumpi, and B. M. Nagaraja, “Comprehensive review in current developments of benzimidazole-based medicinal chemistry,” *Chem. Biol. Drug Des.*, vol. 86, no. 1, pp. 799–845, 2015, doi: 10.1111/cbdd.12462.

[176] R. F. Costa *et al.*, “Heterocyclic Compounds: Pharmacology of Pyrazole Analogs From Rational Structural Considerations,” *Front. Pharmacol.*, vol. 12, 2021, doi: 10.3389/fphar.2021.666725.

[177] H. Kumar, D. Saini, S. Jain, and N. Jain, “Pyrazole scaffold: A remarkable tool in the development of anticancer agents,” *Eur. J. Med. Chem.*, vol. 70, pp. 248–258, 2013, doi: 10.1016/j.ejmech.2013.10.004.

[178] M. Adardour *et al.*, “Design, Synthesis, Molecular Modeling and Biological Evaluation of Novel Pyrazole Benzimidazolone Derivatives as Potent Antioxidants,” *Pharmaceuticals*, vol. 16, no. 12, 2023, doi: 10.3390/ph16121648.

[179] E. A. E. El-Helw, M. M. Gado, and A. K. El-Ziaty, “Synthesis and anti-rotavirus activity of some nitrogen heterocycles integrated with pyrazole scaffold,” *J. Iran.*

Chem. Soc., vol. 17, no. 6, pp. 1479–1492, 2020, doi: 10.1007/s13738-020-01873-7.

[180] A. K. Kabi *et al.*, "Overview on Biological Activities of Pyrazole Derivatives," *Mater. Horizons From Nat. to Nanomater.*, pp. 229–306, 2022, doi: 10.1007/978-981-16-8399-2_7.

[181] H. Z. Zhang, Z. L. Zhao, and C. H. Zhou, "Recent advance in oxazole-based medicinal chemistry," *Eur. J. Med. Chem.*, vol. 144, pp. 444–492, 2018, doi: 10.1016/j.ejmech.2017.12.044.

[182] U. A. Atmaram and S. M. Roopan, "Biological activity of oxadiazole and thiadiazole derivatives," *Appl. Microbiol. Biotechnol.*, vol. 106, no. 9–10, pp. 3489–3505, 2022, doi: 10.1007/s00253-022-11969-0.

[183] S. Joshi, M. Mehra, R. Singh, and S. Kakar, "Review on Chemistry of Oxazole derivatives: Current to Future Therapeutic Prospective," *Egypt. J. Basic Appl. Sci.*, vol. 10, no. 1, pp. 218–239, 2023, doi: 10.1080/2314808X.2023.2171578.

[184] M. Safarzaei, M. T. Maghsoodlou, E. Mollashahi, N. Hazeri, and M. Lashkari, "Synthesis of 3-aminoisoxazolmethylnaphthols via one-pot three-component reaction under solvent-free conditions," *Res. Chem. Intermed.*, vol. 44, no. 12, pp. 7449–7458, 2018, doi: 10.1007/s11164-018-3566-y.

[185] S. Pathania, R. K. Narang, and R. K. Rawal, "Role of sulphur-heterocycles in medicinal chemistry: An update," *Eur. J. Med. Chem.*, vol. 180, pp. 486–508, 2019, doi: 10.1016/j.ejmech.2019.07.043.

[186] Archna, S. Pathania, and P. A. Chawla, "Thiophene-based derivatives as anticancer agents: An overview on decade's work," *Bioorg. Chem.*, vol. 101, 2020, doi: 10.1016/j.bioorg.2020.104026.

[187] A. H. Ingall, "Thiopyrans and Fused Thiopyrans," *Compr. Heterocycl. Chem.*, vol. 3–7, pp. 885–942, 1984, doi: 10.1016/B978-008096519-2.00047-3.

[188] Z. X. Niu *et al.*, "Application and synthesis of thiazole ring in clinically approved drugs," *Eur. J. Med. Chem.*, vol. 250, 2023, doi: 10.1016/j.ejmech.2023.115172.

[189] A. Ayati, S. Emami, A. Asadipour, A. Shafiee, and A. Foroumadi, "Recent applications of 1,3-thiazole core structure in the identification of new lead compounds and drug discovery," *Eur. J. Med. Chem.*, vol. 97, no. 1, pp. 699–718, 2015, doi: 10.1016/j.ejmech.2015.04.015.

[190] M. T. Chhabria, S. Patel, P. Modi, and P. S. Brahmkshatriya, “Thiazole: A Review on Chemistry, Synthesis and Therapeutic Importance of its Derivatives,” *Curr. Top. Med. Chem.*, vol. 16, no. 26, pp. 2841–2862, 2016, doi: 10.2174/1568026616666160506130731.

[191] R. E. Khidre and I. A. M. Radini, “Design, synthesis and docking studies of novel thiazole derivatives incorporating pyridine moiety and assessment as antimicrobial agents,” *Sci. Rep.*, vol. 11, no. 1, 2021, doi: 10.1038/s41598-021-86424-7.

[192] M. F. Arshad *et al.*, “Thiazole: A Versatile Standalone Moiety Contributing to the Development of Various Drugs and Biologically Active Agents,” *Molecules*, vol. 27, no. 13, 2022, doi: 10.3390/molecules27133994.

[193] K. M. Dawood *et al.*, “Novel Bis-Thiazole Derivatives: Synthesis and Potential Cytotoxic Activity Through Apoptosis With Molecular Docking Approaches,” *Front. Chem.*, vol. 9, 2021, doi: 10.3389/fchem.2021.694870.

[194] R. Hussain *et al.*, “Imidazopyridine-Based Thiazole Derivatives as Potential Antidiabetic Agents: Synthesis, In Vitro Bioactivity, and In Silico Molecular Modeling Approach,” *Pharmaceuticals*, vol. 16, no. 9, 2023, doi: 10.3390/ph16091288.

[195] A. Majumdar and A. Pal, “Recent advancements in visible-light-assisted photocatalytic removal of aqueous pharmaceutical pollutants,” *Clean Technol. Environ. Policy*, vol. 22, no. 1, pp. 11–42, 2020, doi: 10.1007/s10098-019-01766-1.

[196] N. Masanabo, B. Orimolade, A. O. Idris, T. T. I. Nkambule, B. B. Mamba, and U. Feleni, “Advances in polymer-based detection of environmental ibuprofen in wastewater,” *Environ. Sci. Pollut. Res.*, vol. 30, no. 6, pp. 14062–14090, 2023, doi: 10.1007/s11356-022-24858-w.

[197] P. Ghosh and S. Mukherji, “Fate, detection technologies and toxicity of heterocyclic PAHs in the aquatic and soil environments,” *Sci. Total Environ.*, vol. 892, 2023, doi: 10.1016/j.scitotenv.2023.164499.

[198] M. Paut Kusturica, A. Tomas, and A. Sabo, “Disposal of unused drugs: Knowledge and behavior among people around the world,” *Rev. Environ. Contam. Toxicol.*, vol. 240, pp. 71–104, 2017, doi: 10.1007/398_2016_3.

[199] P. Karungamye, A. Rugaika, K. Mtei, and R. Machunda, “The pharmaceutical disposal practices and environmental contamination: A review in East African countries,”

HydroResearch, vol. 5, pp. 99–107, 2022, doi: 10.1016/j.hydres.2022.11.001.

[200] Q. Zhang *et al.*, "New insight into fate and transport of organic compounds from pollution sources to aquatic environment using non-targeted screening: A wastewater treatment plant case study," *Sci. Total Environ.*, vol. 863, 2023, doi: 10.1016/j.scitotenv.2022.161031.

[201] A. Kumar *et al.*, "Recent advances in nano-Fenton catalytic degradation of emerging pharmaceutical contaminants," *J. Mol. Liq.*, vol. 290, 2019, doi: 10.1016/j.molliq.2019.111177.

[202] H. Wang, H. Xi, L. Xu, M. Jin, W. Zhao, and H. Liu, "Ecotoxicological effects, environmental fate and risks of pharmaceutical and personal care products in the water environment: A review," *Sci. Total Environ.*, vol. 788, 2021, doi: 10.1016/j.scitotenv.2021.147819.

[203] C. Papaioannou, G. Geladakis, V. Kommata, C. Batargias, and G. Lagoumintzis, "Insights in Pharmaceutical Pollution: The Prospective Role of eDNA Metabarcoding," *Toxics*, vol. 11, no. 11, 2023, doi: 10.3390/toxics11110903.

[204] F. Barzegar, M. Kamankesh, and A. Mohammadi, "Heterocyclic aromatic amines in cooked food: A review on formation, health risk-toxicology and their analytical techniques," *Food Chem.*, vol. 280, pp. 240–254, 2019, doi: 10.1016/j.foodchem.2018.12.058.

[205] I. A. Khan *et al.*, "Heterocyclic amines in cooked meat products, shortcomings during evaluation, factors influencing formation, risk assessment and mitigation strategies," *Meat Sci.*, vol. 184, 2022, doi: 10.1016/j.meatsci.2021.108693.

[206] M. Bellamri, S. J. Walmsley, and R. J. Turesky, "Metabolism and biomarkers of heterocyclic aromatic amines in humans," *Genes Environ.*, vol. 43, no. 1, 2021, doi: 10.1186/s41021-021-00200-7.

[207] P. Ghosh and S. Mukherji, "Environmental contamination by heterocyclic Polynuclear aromatic hydrocarbons and their microbial degradation," *Bioresour. Technol.*, vol. 341, 2021, doi: 10.1016/j.biortech.2021.125860.

[208] Y. Geng *et al.*, "Heterocyclic Amines in Meat and Meat Products: Occurrence, Formation, Mitigation, Health Risks and Intervention," *Food Rev. Int.*, vol. 40, no. 5, pp. 1503–1519, 2024, doi: 10.1080/87559129.2023.2221346.

[209] W. Cao, J. Yuan, S. Geng, J. Zou, J. Dou, and F. Fan, “Oxygenated and Nitrated Polycyclic Aromatic Hydrocarbons: Sources, Quantification, Incidence, Toxicity, and Fate in Soil—A Review Study,” *Processes*, vol. 11, no. 1, 2023, doi: 10.3390/pr11010052.

[210] M. Honda and N. Suzuki, “Toxicities of polycyclic aromatic hydrocarbons for aquatic animals,” *Int. J. Environ. Res. Public Health*, vol. 17, no. 4, 2020, doi: 10.3390/ijerph17041363.

[211] G. Çelik, S. Stolte, and M. Markiewicz, “NSO-heterocyclic PAHs – Controlled exposure study reveals high acute aquatic toxicity,” *J. Hazard. Mater.*, vol. 460, 2023, doi: 10.1016/j.jhazmat.2023.132428.

[212] S. F. Barbuceanu *et al.*, “New Heterocyclic Compounds from Oxazol-5(4H)-one and 1,2,4-Triazin-6(5H)-one Classes: Synthesis, Characterization and Toxicity Evaluation,” *Molecules*, vol. 28, no. 12, 2023, doi: 10.3390/molecules28124834.

[213] S. Matavos-Aramyan, “Addressing the microplastic crisis: A multifaceted approach to removal and regulation,” *Environ. Adv.*, vol. 17, 2024, doi: 10.1016/j.envadv.2024.100579.

[214] M. Paut Kusturica, M. Jevtic, and J. T. Ristovski, “Minimizing the environmental impact of unused pharmaceuticals: Review focused on prevention,” *Front. Environ. Sci.*, vol. 10, 2022, doi: 10.3389/fenvs.2022.1077974.

[215] A. Samadi, A. K. Pour, and R. Jamieson, “Development of remediation technologies for organic contaminants informed by QSAR/QSPR models,” *Environ. Adv.*, vol. 5, 2021, doi: 10.1016/j.envadv.2021.100112.

[216] H. Sá, M. Michelin, T. Tavares, and B. Silva, “Current Challenges for Biological Treatment of Pharmaceutical-Based Contaminants with Oxidoreductase Enzymes: Immobilization Processes, Real Aqueous Matrices and Hybrid Techniques,” *Biomolecules*, vol. 12, no. 10, 2022, doi: 10.3390/biom12101489.

[217] G. Pérez-Lucas, A. El Aatik, M. Aliste, G. Navarro, J. Fenoll, and S. Navarro, “Removal of Contaminants of Emerging Concern from a Wastewater Effluent by Solar-Driven Heterogeneous Photocatalysis: A Case Study of Pharmaceuticals,” *Water. Air. Soil Pollut.*, vol. 234, no. 1, 2023, doi: 10.1007/s11270-023-06075-4.

[218] D. Friedmann, “A General Overview of Heterogeneous Photocatalysis as a

Remediation Technology for Wastewaters Containing Pharmaceutical Compounds," *Water (Switzerland)*, vol. 14, no. 21, 2022, doi: 10.3390/w14213588.

[219] P. R. Rout, T. C. Zhang, P. Bhunia, and R. Y. Surampalli, "Treatment technologies for emerging contaminants in wastewater treatment plants: A review," *Sci. Total Environ.*, vol. 753, 2021, doi: 10.1016/j.scitotenv.2020.141990.

[220] R. Li *et al.*, "Removal of indomethacin using UV–vis/peroxydisulfate: Kinetics, toxicity, and transformation pathways," *Chem. Eng. J.*, vol. 331, pp. 809–817, 2018, doi: 10.1016/j.cej.2017.09.025.

[221] H. Jia *et al.*, "Construction of ACNF/Polypyrrole/MIL-100-Fe composites with exceptional removal performance for ceftriaxone and indomethacin inspired by 'Ecological Infiltration System,'" *J. Colloid Interface Sci.*, vol. 650, pp. 1152–1163, 2023, doi: 10.1016/j.jcis.2023.07.050.

[222] A. R. D. Verliefde *et al.*, "Influence of membrane fouling by (pretreated) surface water on rejection of pharmaceutically active compounds (PhACs) by nanofiltration membranes," *J. Memb. Sci.*, vol. 330, no. 1–2, pp. 90–103, 2009, doi: 10.1016/j.memsci.2008.12.039.

[223] A. Kujawska, U. Kiełkowska, A. Atisha, E. Yanful, and W. Kujawski, "Comparative analysis of separation methods used for the elimination of pharmaceuticals and personal care products (PPCPs) from water – A critical review," *Sep. Purif. Technol.*, vol. 290, 2022, doi: 10.1016/j.seppur.2022.120797.

[224] J. Wang *et al.*, "Photochemical fate of β-blocker pindolol in riverine and its downstream coastal waters," *Sci. Total Environ.*, vol. 927, 2024, doi: 10.1016/j.scitotenv.2024.172236.

[225] A. Raji, K. N. Pandiyaraj, V. Kandavelu, D. Vasu, and D. Saravanan, "Efficiency evaluation of the photocatalytic degradation of telmisartan anti-hypertensive drug with Fenton, photo-Fenton and recyclable TiO2 heterogeneous catalyst," *React. Kinet. Mech. Catal.*, vol. 130, no. 2, pp. 1141–1154, 2020, doi: 10.1007/s11144-020-01806-8.

[226] D. Ljubas *et al.*, "Albendazole Degradation Possibilities by UV-Based Advanced Oxidation Processes," *Int. J. Photoenergy*, vol. 2018, 2018, doi: 10.1155/2018/6181747.

[227] S. Fukuda, Y. Sakurai, and S. Izawa, "Detoxification of the post-harvest antifungal

pesticide thiabendazole by cold atmospheric plasma," *J. Biosci. Bioeng.*, vol. 136, no. 2, pp. 123–128, 2023, doi: 10.1016/j.jbiosc.2023.05.004.

[228] J. Arcila-Saenz, G. Hincapié-Mejía, Y. A. Londoño-Cañas, and G. A. Peñuela, "Role of the hydrolytic-acidogenic phase on the removal of bisphenol A and sildenafil during anaerobic treatment," *Environ. Monit. Assess.*, vol. 195, no. 12, 2023, doi: 10.1007/s10661-023-12009-8.

[229] J. J. Jiménez, R. Pardo, M. I. Sánchez, and B. E. Muñoz, "Photochemical, thermal, biological and long-term degradation of celecoxib in river water. Degradation products and adsorption to sediment," *J. Hazard. Mater.*, vol. 342, pp. 252–259, 2018, doi: 10.1016/j.jhazmat.2017.08.037.

[230] K. Reddy, N. Renuka, M. A. Malla, B. Moodley, F. Bux, and S. Kumari, "Enhanced removal efficiency of Tetradesmus obliquus for nevirapine removal via co-substrate supplementation: removal mechanisms, relative gene expression and metabolomics," *Environ. Sci. Water Res. Technol.*, 2024, doi: 10.1039/d4ew00576g.

[231] L. M. Mahlaule-Glory, S. Mapetla, A. Makofane, M. M. Mathipa, and N. C. Hintsho-Mbita, "Biosynthesis of iron oxide nanoparticles for the degradation of methylene blue dye, sulfisoxazole antibiotic and removal of bacteria from real water," *Heliyon*, vol. 8, no. 9, 2022, doi: 10.1016/j.heliyon.2022.e10536.

[232] L. Yang *et al.*, "Biological conversion of sulfisoxazole in an autotrophic hydrogen-based membrane biofilm reactor," *J. Water Process Eng.*, vol. 51, 2023, doi: 10.1016/j.jwpe.2022.103396.

[233] A. L. Giraldo, E. D. Erazo-Erazo, O. A. Flórez-Acosta, E. A. Serna-Galvis, and R. A. Torres-Palma, "Degradation of the antibiotic oxacillin in water by anodic oxidation with Ti/IrO2 anodes: Evaluation of degradation routes, organic by-products and effects of water matrix components," *Chem. Eng. J.*, vol. 279, pp. 103–114, 2015, doi: 10.1016/j.cej.2015.04.140.

[234] E. Regulska and J. Karpińska, "Photocatalytic degradation of olanzapine in aqueous and river waters suspension of titanium dioxide," *Appl. Catal. B Environ.*, vol. 117–118, pp. 96–104, 2012, doi: 10.1016/j.apcatb.2012.01.003.

[235] M. Fedeila, Z. Hachaïchi-Sadouk, L. F. Bautista, and R. Simarro, "Biodegradation of clopidogrel bisulfate by Pseudomonas aeruginosa and Pseudomonas putida strains isolated from Algerian wastewater," *J. Contam. Hydrol.*, vol. 256, 2023, doi:

10.1016/j.jconhyd.2023.104198.

[236] D. Mansour *et al.*, “Modeling and Optimization of Electrochemical Advanced Oxidation of Clopidogrel Using the Doehlert Experimental Design Combined with an Improved Grey Wolf Algorithm,” *Water (Switzerland)*, vol. 16, no. 14, 2024, doi: 10.3390/w16141964.

[237] O. Baaloudj, N. Nasrallah, R. Bouallouche, H. Kenfoud, L. Khezami, and A. A. Assadi, “High efficient Cefixime removal from water by the sillenite Bi12TiO20: Photocatalytic mechanism and degradation pathway,” *J. Clean. Prod.*, vol. 330, no. November 2021, p. 129934, 2022, doi: 10.1016/j.jclepro.2021.129934.

[238] K. Aziz *et al.*, “High thiabendazole fungicide uptake using Cellana tramoserica shells modified by copper: characterization, adsorption mechanism, and optimization using CCD-RSM approach,” *Environ. Sci. Pollut. Res.*, vol. 29, no. 57, pp. 86020–86035, 2022, doi: 10.1007/s11356-021-16340-w.

[239] M. Hojamberdiev *et al.*, “Unveiling the origin of the efficient photocatalytic degradation of nitazoxanide over bismuth (oxy)iodide crystalline phases,” *Environ. Sci. Nano*, vol. 11, no. 1, pp. 336–350, 2023, doi: 10.1039/d3en00548h.

[240] S. A. Huang and J. D. Lie, “Phosphodiesterase-5 (PDE5) Inhibitors In the Management of Erectile Dysfunction.,” *P T*, vol. 38, no. 7, pp. 407–419, Jul. 2013.

[241] https://markwideresearch.com/sildenafil-citrate-market, last access 10/01/26.

[242] D. Chen, X. Deng, and S. Jin, “A Review on Epigenetic Toxicological Mechanisms of Sildenafil and Its Metabolites, the Emerging Pollutants,” *Rev. Environ. Contam. Toxicol.*, vol. 261, Oct. 2023, doi: 10.1007/s44169-023-00050-0.

[243] Y. Hong *et al.*, “Contribution of sewage to occurrence of phosphodiesterase-5 inhibitors in natural water,” *Sci. Rep.*, vol. 11, no. 1, p. 9470, 2021, doi: 10.1038/s41598-021-89028-3.

[244] M. O. Barbosa, N. F. F. Moreira, A. R. Ribeiro, M. F. R. Pereira, and A. M. T. Silva, “Occurrence and removal of organic micropollutants: An overview of the watch list of EU Decision 2015/495,” *Water Res.*, vol. 94, pp. 257–279, 2016, doi: https://doi.org/10.1016/j.watres.2016.02.047.

[245] J.-Q. Jiang, Z. Zhou, and V. K. Sharma, “Occurrence, transportation, monitoring and treatment of emerging micro-pollutants in waste water — A review from global

views," *Microchem. J.*, vol. 110, pp. 292–300, 2013, doi: https://doi.org/10.1016/j.microc.2013.04.014.

[246] R. Kumar *et al.*, "A review on emerging water contaminants and the application of sustainable removal technologies," *Case Stud. Chem. Environ. Eng.*, vol. 6, no. May, p. 100219, 2022, doi: 10.1016/j.cscee.2022.100219.

[247] P. Eichhorn, S. Pérez, J. Aceña, P. Gardinali, J. L. Abad, and D. Barceló, "Identification of phototransformation products of sildenafil (Viagra) and its N-demethylated human metabolite under simulated sunlight," *J. Mass Spectrom.*, vol. 47, no. 6, pp. 701–711, 2012, doi: 10.1002/jms.2998.

[248] L. P. Herbert, D. B. Becker-Krail, and W. C. Cory, "Persistent phototransformation products of vardenafil (Levitra®) and sildenafil (Viagra®)," *Chemosphere*, vol. 134, pp. 557–562, 2015, doi: 10.1016/j.chemosphere.2014.12.011.

[249] C. Medana *et al.*, "Horse metabolism and the photocatalytic process as a tool to identify metabolic products formed from dopant substances: the case of sildenafil," *Drug Test. Anal.*, vol. 3, no. 10, pp. 724–734, Oct. 2011, doi: https://doi.org/10.1002/dta.334.

[250] P. M. Chapman, "Whole effluent toxicity testing - Usefulness, level of protection, and risk assessment," *Environ. Toxicol. Chem.*, vol. 19, no. 1, pp. 3–13, 2000, doi: 10.1002/etc.5620190102.

[251] P. Sharma, N. Singh, and S. Sharma, "ATP binding cassette transporters and cancer: revisiting their controversial role," *Pharmacogenomics*, vol. 22, no. 18, pp. 1211–1235, Nov. 2021, doi: 10.2217/pgs-2021-0116.

[252] M. I. Polo-López *et al.*, "Mild solar photo-Fenton: An effective tool for the removal of Fusarium from simulated municipal effluents," *Appl. Catal. B Environ.*, vol. 111–112, pp. 545–554, 2012, doi: https://doi.org/10.1016/j.apcatb.2011.11.006.

[253] J. Aceña *et al.*, "Structure elucidation of phototransformation products of unapproved analogs of the erectile dysfunction drug sildenafil in artificial freshwater with UPLC-Q Exactive-MS," *J. Mass Spectrom.*, vol. 49, no. 12, pp. 1279–1289, 2014, doi: 10.1002/jms.3461.

[254] S. Ahn *et al.*, "Structural determination of sildenafil and its analogues in dietary supplements by fast-atom bombardment collision-induced dissociation tandem mass

spectrometry," *Rapid Commun. Mass Spectrom.*, vol. 23, no. 19, pp. 3158–3166, Oct. 2009, doi: https://doi.org/10.1002/rcm.4238.

[255] M. G. Montalbán, J. M. Hidalgo, M. Collado-González, F. G. Díaz Baños, and G. Víllora, "Assessing chemical toxicity of ionic liquids on Vibrio fischeri: Correlation with structure and composition," *Chemosphere*, vol. 155, pp. 405–414, 2016, doi: https://doi.org/10.1016/j.chemosphere.2016.04.042.

[256] M. C. C. Maior, R. Carpa, R. Fetke, and V. Muntean, "Determination of the inhibitory effect of water samples on the light emission of Vibrio fischeri: TUE-282," *FEBS Journal*, vol. 281, p. 525, 2014.

[257] M. Abbas *et al.*, "Vibrio fischeri bioluminescence inhibition assay for ecotoxicity assessment: A review," *Sci. Total Environ.*, vol. 626, pp. 1295–1309, 2018, doi: https://doi.org/10.1016/j.scitotenv.2018.01.066.

[258] J. C. Madden, S. J. Enoch, M. Hewitt, and M. T. D. Cronin, "Pharmaceuticals in the environment: Good practice in predicting acute ecotoxicological effects," *Toxicol. Lett.*, vol. 185, no. 2, pp. 85–101, 2009, doi: 10.1016/j.toxlet.2008.12.005.

[259] A. Polanco-Rodriguez, *Emerging Pollutants in Water and Wastewater: UNESCO-Sida Project Case-Studies". Case-Study from Latin America: Mexico - Maya Area. Sweden 2016*, 2016.

[260] C. Castillo-Zacarías *et al.*, "Antidepressant drugs as emerging contaminants: Occurrence in urban and non-urban waters and analytical methods for their detection," *Sci. Total Environ.*, vol. 757, 2021, doi: 10.1016/j.scitotenv.2020.143722.

[261] L. P. de Souza *et al.*, "Photochemical environmental persistence of venlafaxine in an urban water reservoir: A combined experimental and computational investigation," *Process Saf. Environ. Prot.*, vol. 166, pp. 478–490, 2022, doi: https://doi.org/10.1016/j.psep.2022.08.049.

[262] J. H. Bisesi Jr, L. E. Sweet, P. van den Hurk, and S. J. Klaine, "Effects of an antidepressant mixture on the brain serotonin and predation behavior of hybrid striped bass," *Environ. Toxicol. Chem.*, vol. 35, no. 4, pp. 938–945, Apr. 2016, doi: 10.1002/etc.3114.

[263] P. K. Pandis *et al.*, "Key Points of Advanced Oxidation Processes (AOPs) for Wastewater, Organic Pollutants and Pharmaceutical Waste Treatment: A Mini

Review," *ChemEngineering*, vol. 6, no. 1, 2022, doi: 10.3390/chemengineering6010008.

[264] I. M. D. Gonzaga, C. V. S. Almeida, and L. H. Mascaro, "A Critical Review of Photo-Based Advanced Oxidation Processes to Pharmaceutical Degradation," *Catalysts*, vol. 13, no. 2, 2023, doi: 10.3390/catal13020221.

[265] D. Lambropoulou, E. Evgenidou, V. Saliverou, C. Kosma, and I. Konstantinou, "Degradation of venlafaxine using TiO2/UV process: Kinetic studies, RSM optimization, identification of transformation products and toxicity evaluation," *J. Hazard. Mater.*, vol. 323, pp. 513–526, 2017, doi: https://doi.org/10.1016/j.jhazmat.2016.04.074.

[266] P.-S. Konstas, C. Kosma, I. Konstantinou, and T. Albanis, "Photocatalytic Treatment of Pharmaceuticals in Real Hospital Wastewaters for Effluent Quality Amelioration," *Water*, vol. 11, no. 10, 2019, doi: 10.3390/w11102165.

[267] K. Hellauer *et al.*, "Advancing Sequential Managed Aquifer Recharge Technology (SMART) Using Different Intermediate Oxidation Processes," *Water*, vol. 9, no. 3, 2017, doi: 10.3390/w9030221.

[268] F. C. Moreira, R. A. R. Boaventura, E. Brillas, and V. J. P. Vilar, "Electrochemical advanced oxidation processes: A review on their application to synthetic and real wastewaters," *Appl. Catal. B Environ.*, vol. 202, pp. 217–261, 2017, doi: https://doi.org/10.1016/j.apcatb.2016.08.037.

[269] E. Mordačíková *et al.*, "Influence of boron doped diamond electrodes properties on the elimination of selected pharmaceuticals from wastewater," *J. Electroanal. Chem.*, vol. 862, p. 114007, 2020, doi: https://doi.org/10.1016/j.jelechem.2020.114007.

[270] M. Voigt, J. M. Dluziak, N. Wellen, V. Langerbein, and M. Jaeger, "Comparison of photoinduced and electrochemically induced degradation of venlafaxine," *Environ. Sci. Pollut. Res.*, vol. 31, no. 9, pp. 13442–13454, 2024, doi: 10.1007/s11356-024-32018-5.

[271] Y. Zhu, B. Chang, X. Sun, H. Luo, W. Wang, and C. Li, "Chloride-mediated electrochemical degradation of the venlafaxine antidepressant," *Environ. Technol. Innov.*, vol. 25, p. 102189, 2022, doi: https://doi.org/10.1016/j.eti.2021.102189.

[272] B. Yu, Q. Han, C. Li, Y. Zhu, X. Jin, and Z. Dai, "Influencing factors of venlafaxine degradation at boron-doped diamond anode," *Arab. J. Chem.*, vol. 15, no. 1, p. 103463,

2022, doi: https://doi.org/10.1016/j.arabjc.2021.103463.

[273] Y. He, H. Lin, Z. Guo, W. Zhang, H. Li, and W. Huang, “Recent developments and advances in boron-doped diamond electrodes for electrochemical oxidation of organic pollutants,” *Sep. Purif. Technol.*, vol. 212, Nov. 2018, doi: 10.1016/j.seppur.2018.11.056.

[274] P. Brosler, A. Girão, R. Silva, J. Tedim, and F. Oliveira, “In-house vs. commercial boron-doped diamond electrodes for electrochemical degradation of water pollutants: A critical review,” *Front. Mater.*, vol. 10, Mar. 2023, doi: 10.3389/fmats.2023.1020649.

[275] R. Bogdanowicz and J. Ryl, “Structural and electrochemical heterogeneities of boron-doped diamond surfaces,” *Curr. Opin. Electrochem.*, vol. 31, p. 100876, 2022, doi: https://doi.org/10.1016/j.coelec.2021.100876.

[276] B. Chaplin, I. Wylie, H. Zeng, J. Carlisle, and J. Farrell, “Characterization of the performance and failure mechanisms of boron-doped ultrananocrystalline diamond electrodes,” *J. Appl. Electrochem.*, vol. 41, Nov. 2011, doi: 10.1007/s10800-011-0351-7.

[277] X.-R. Lu, M.-H. Ding, C. Zhang, and W.-Z. Tang, “Comparative study on stability of boron doped diamond coated titanium and niobium electrodes,” *Diam. Relat. Mater.*, vol. 93, pp. 26–33, 2019, doi: https://doi.org/10.1016/j.diamond.2019.01.010.

[278] M. E. Carbone, R. Ciriello, A. Guerrieri, and A. M. Salvi, “XPS investigation on the chemical structure of a very thin, insulating, film synthesized on platinum by electropolymerization of o-aminophenol (oAP) in aqueous solution at neutral pH,” *Surf. Interface Anal.*, vol. 46, no. 10–11, pp. 1081–1085, Oct. 2014, doi: https://doi.org/10.1002/sia.5438.

[279] H. Diaf *et al.*, “Revisiting thin film of glassy carbon,” *Phys. Rev. Mater.*, vol. 4, no. 6, p. 66002, Jun. 2020, doi: 10.1103/PhysRevMaterials.4.066002.

[280] D. M. Heard and A. J. J. Lennox, “Electrode Materials in Modern Organic Electrochemistry,” *Angew. Chemie Int. Ed.*, vol. 59, no. 43, pp. 18866–18884, Oct. 2020, doi: https://doi.org/10.1002/anie.202005745.

[281] J. Xie, C. Zhang, and T. D. Waite, “Hydroxyl radicals in anodic oxidation systems: generation, identification and quantification,” *Water Res.*, vol. 217, p. 118425, 2022, doi: https://doi.org/10.1016/j.watres.2022.118425.

[282] L. Chen, C. Lei, Z. Li, B. Yang, X. Zhang, and L. Lei, “Electrochemical activation of sulfate by BDD anode in basic medium for efficient removal of organic pollutants,” *Chemosphere*, vol. 210, pp. 516–523, 2018, doi: https://doi.org/10.1016/j.chemosphere.2018.07.043.

[283] L. Kemmou, Z. Frontistis, J. Vakros, I. D. Manariotis, and D. Mantzavinos, “Degradation of antibiotic sulfamethoxazole by biochar-activated persulfate: Factors affecting the activation and degradation processes,” *Catal. Today*, vol. 313, pp. 128–133, 2018, doi: https://doi.org/10.1016/j.cattod.2017.12.028.

[284] N. Rabaaoui and M. S. Allagui, “Anodic oxidation of salicylic acid on BDD electrode: variable effects and mechanisms of degradation.,” *J. Hazard. Mater.*, vol. 243, pp. 187–192, Dec. 2012, doi: 10.1016/j.jhazmat.2012.10.016.

[285] H. Santoke, W. Song, W. J. Cooper, and B. M. Peake, “Advanced oxidation treatment and photochemical fate of selected antidepressant pharmaceuticals in solutions of Suwannee River humic acid.,” *J. Hazard. Mater.*, vol. 217–218, pp. 382–390, May 2012, doi: 10.1016/j.jhazmat.2012.03.049.

[286] M. la Farré, M. J. García, L. Tirapu, A. Ginebreda, and D. Barceló, “Wastewater toxicity screening of non-ionic surfactants by Toxalert® and Microtox® bioluminescence inhibition assays,” *Anal. Chim. Acta*, vol. 427, no. 2, pp. 181–189, 2001, doi: 10.1016/S0003-2670(00)01022-9.

[287] J. R. Dominguez, T. González, S. E. Correia, and M. M. Núñez, “Emerging Contaminants Decontamination of WWTP Effluents by BDD Anodic Oxidation: A Way towards Its Regeneration,” *Water*, vol. 15, no. 9. p. 1668, 2023, doi: 10.3390/w15091668.

[288] G. Cembalo *et al.*, “An Amperometric Biosensor Based on a Bilayer of Electrodeposited Graphene Oxide and Co-Crosslinked Tyrosinase for L-Dopa Detection in Untreated Human Plasma,” *Molecules*, vol. 28, no. 13. p. 5239, 2023, doi: 10.3390/molecules28135239.

[289] https://www.epa.gov/tsca-screening-tools/ecological-structure-activity-relationships-ecosar-predictive-model, last access 10/01/26.

[290] Y. S. Ho, J. C. Y. Ng, and G. McKay, “KINETICS OF POLLUTANT SORPTION BY BIOSORBENTS: REVIEW,” *Sep. Purif. Methods*, vol. 29, no. 2, pp. 189–232, Oct. 2000, doi: 10.1081/SPM-100100009.

[291] E. E. Jasper, V. O. Ajibola, and J. C. Onwuka, “Nonlinear regression analysis of the sorption of crystal violet and methylene blue from aqueous solutions onto an agro-waste derived activated carbon,” *Appl. Water Sci.*, vol. 10, no. 6, 2020, doi: 10.1007/s13201-020-01218-y.

[292] A. Acharya *et al.*, “Adsorption of arsenic and fluoride: Modeling of single and competitive adsorption systems,” *Heliyon*, vol. 10, no. 11, 2024, doi: 10.1016/j.heliyon.2024.e31967.

[293] R. Kaviani, “ Comparison of Different Approaches for Calculating LOD and LOQ in an HPLC-Based Analysis Method ,” *Pharm. Sci.*, vol. 31, no. 1, pp. 106–109, 2024, doi: 10.34172/ps.024.40452.

[294] E. J. Díaz-Montaña, M. Barbero-López, R. Aparicio-Ruiz, D. L. García-González, and M. T. Morales, “Optimization of Calibration Strategies for the Quantification of Volatile Compounds in Virgin Olive Oil,” *Foods*, vol. 14, no. 19, 2025, doi: 10.3390/foods14193439.

[295] D. Papagiannaki, S. Morgillo, G. Bocina, P. Calza, and R. Binetti, “Occurrence and human health risk assessment of pharmaceuticals and hormones in drinking water sources in the metropolitan area of turin in Italy,” *Toxics*, vol. 9, no. 4, 2021, doi: 10.3390/toxics9040088.

[296] N. Bagotia, “Regeneration strategies for exhausted adsorbents used in water treatment - A critical review,” *J. Water Process Eng.*, vol. 69, p. 106560, 2025, doi: https://doi.org/10.1016/j.jwpe.2024.106560.

[297] A. K. Badawi, M. Abd Elkodous, and G. A. M. Ali, “Recent advances in dye and metal ion removal using efficient adsorbents and novel nano-based materials: an overview,” *RSC Adv.*, vol. 11, no. 58, pp. 36528–36553, 2021, doi: 10.1039/d1ra06892j.

[298] D. Fatta-Kassinos, M. I. Vasquez, and K. Kümmerer, “Transformation products of pharmaceuticals in surface waters and wastewater formed during photolysis and advanced oxidation processes - degradation, elucidation of byproducts and assessment of their biological potency.,” *Chemosphere*, vol. 85, no. 5, pp. 693–709, Oct. 2011, doi: 10.1016/j.chemosphere.2011.06.082.

[299] A. A. Ioannidi *et al.*, “Effective Degradation of Venlafaxine via Biochar Activated Persulfate: Kinetics, Transformation Products, and Toxicity Assessment,” *Molecules*, vol. 30, no. 18, 2025, doi: 10.3390/molecules30183720.

[300] S. I. Mussatto, G. Dragone, and I. C. Roberto, “Brewers’ spent grain: Generation, characteristics and potential applications,” *J. Cereal Sci.*, vol. 43, no. 1, pp. 1–14, 2006, doi: 10.1016/j.jcs.2005.06.001.

[301] Y. Fernandez, A. Arenillas, and J. Angel, “Microwave Heating Applied to Pyrolysis,” *Adv. Induction Microw. Heat. Miner. Org. Mater.*, 2011, doi: 10.5772/13548.

[302] I. Fernández, S. F. Pérez, J. Fernández-Ferreras, and T. Llano, “Microwave-Assisted Pyrolysis of Forest Biomass,” *Energies*, vol. 17, no. 19, 2024, doi: 10.3390/en17194852.

[303] P. S. Selvaraj *et al.*, “Hydrothermal carbonization approach for transforming biomass waste to value added hydrochar and its applications in water remediation,” *Desalin. Water Treat.*, vol. 322, 2025, doi: 10.1016/j.dwt.2025.101199.

[304] V. Calisto, C. I. A. Ferreira, S. M. Santos, M. V. Gil, M. Otero, and V. I. Esteves, “Production of adsorbents by pyrolysis of paper mill sludge and application on the removal of citalopram from water,” *Bioresour. Technol.*, vol. 166, pp. 335–344, 2014, doi: 10.1016/j.biortech.2014.05.047.

[305] R. Mandrioli, L. Mercolini, R. Cesta, S. Fanali, M. Amore, and M. A. Raggi, “Analysis of the second generation antidepressant venlafaxine and its main active metabolite O-desmethylvenlafaxine in human plasma by HPLC with spectrofluorimetric detection,” *J. Chromatogr. B*, vol. 856, no. 1, pp. 88–94, 2007, doi: https://doi.org/10.1016/j.jchromb.2007.05.046.

[306] M. Sieradzka, C. Kirczuk, I. Kalemba-rec, A. Mlonka-mędrala, and A. Magdziarz, “Pyrolysis of Biomass Wastes into Carbon Materials,” *Energies*, vol. 15, no. 5, pp. 1–12, 2022, doi: 10.3390/en15051941.

[307] K. B. Fontana, E. S. Chaves, J. D. S. Sanchez, E. R. L. R. Watanabe, J. M. T. A. Pietrobelli, and G. G. Lenzi, “Textile dye removal from aqueous solutions by malt bagasse: Isotherm, kinetic and thermodynamic studies,” *Ecotoxicol. Environ. Saf.*, vol. 124, pp. 329–336, 2016, doi: https://doi.org/10.1016/j.ecoenv.2015.11.012.

[308] E. Gomez-Delgado, D. Morales-Urrea, J. Alean, and A. López-Córdoba, “Activated carbons from brewers spent grain improve Orange II removal through combined adsorption and enzymatic oxidation.,” *Sci. Rep.*, vol. 15, no. 1, p. 22487, Jul. 2025, doi: 10.1038/s41598-025-05061-6.

[309] O. Baaloudj *et al.*, “Efficient biochar regeneration for a circular economy: Removing emerging contaminants for sustainable water treatment,” *Colloids Surfaces A Physicochem. Eng. Asp.*, vol. 705, p. 135730, 2025, doi: 10.1016/j.colsurfa.2024.135730.

[310] L. E. N. Castro, R. R. Mançano, D. A. J. Battocchio, and L. M. S. Colpini, “Adsorption of food dye using activated carbon from brewers’ spent grains,” *Acta Scientiarum - Technology*, vol. 45. 2023, doi: 10.4025/actascitechnol.v45i1.60443.

[311] É. M. L. Sousa, M. Otero, M. V. Gil, P. Ferreira, V. I. Esteves, and V. Calisto, “Insights into matrix and competitive effects on antibiotics removal from wastewater by activated carbon produced from brewery residues,” *Environ. Technol. Innov.*, vol. 30, 2023, doi: 10.1016/j.eti.2023.103074.

[312] N. Apinyakul, S. Chanpee, N. Kaewtrakulchai, N. Khemasiri, A. Eiad-ua, and P. Assawasaengrat, “Synthesis of nanoporous carbon from brewer waste by hydrothermal carbonization assisted chemical activation for carbamazepine adsorption,” *Case Stud. Chem. Environ. Eng.*, vol. 9, p. 100716, Apr. 2024, doi: 10.1016/j.cscee.2024.100716.

[313] F. Wang *et al.*, “Emerging contaminants: A One Health perspective,” *Innovation*, vol. 5, no. 4, 2024, doi: 10.1016/j.xinn.2024.100612.

[314] Official Journal of the European Union, “REGULATION (EU) 2020/741 OF THE EUROPEAN PARLIAMENT AND OF THE COUNCIL of 25 May 2020 on minimum requirements for water reuse,” *L177*, pp. 32–55, 2020.

[315] G. Knopp, C. Prasse, T. A. Ternes, and P. Cornel, “Elimination of micropollutants and transformation products from a wastewater treatment plant effluent through pilot scale ozonation followed by various activated carbon and biological filters,” *Water Res.*, vol. 100, pp. 580–592, 2016, doi: 10.1016/j.watres.2016.04.069.

[316] J. Saleem, U. Bin Shahid, M. Hijab, H. Mackey, and G. McKay, “Production and applications of activated carbons as adsorbents from olive stones,” *Biomass Convers. Biorefinery*, vol. 9, no. 4, pp. 775–802, 2019, doi: 10.1007/s13399-019-00473-7.

[317] P. Nowicki, J. Kazmierczak-Razna, P. Skibiszewska, M. Wiśniewska, A. Nosal-Wiercińska, and R. Pietrzak, “Production of activated carbons from biodegradable waste materials as an alternative way of their utilisation,” *Adsorption*, vol. 22, no. 4, pp. 489–502, 2016.

[318] T. Tay, S. Ucar, and S. Karagöz, “Preparation and characterization of activated carbon from waste biomass,” *J. Hazard. Mater.*, vol. 165, no. 1–3, pp. 481–485, 2009.

[319] M. Al Kausor, S. Sen Gupta, K. G. Bhattacharyya, and D. Chakrabortty, “Montmorillonite and modified montmorillonite as adsorbents for removal of water soluble organic dyes: A review on current status of the art,” *Inorg. Chem. Commun.*, vol. 143, p. 109686, 2022.

[320] O. Baaloudj *et al.*, “Biochar-based Downflow Fixed-Bed Adsorption Systems for Water Treatment: Process Optimization, Reusability, and Techno-Economic Evaluation,” *Sep. Purif. Technol.*, vol. 377, 2025, doi: 10.1016/j.seppur.2025.134347.

[321] A.R. Zizzamia, A. Almeida, M.V. Gil, F. Lelario, and V. Calisto, “Venlafaxine removal from water and wastewater using activated carbons from spent brewery grains produced by conventional vs. microwave pyrolysis“, *Pharm.*, vol.19, no. 344, pp. 1-21, 2026, doi.org/10.3390/ph19030344.

[322] M. C. Dal and N. Onursal, “Two new linearized equations derived from a pseudo-second-order kinetic model,” *Desalin. Water Treat.*, vol. 308, pp. 183–189, 2023, doi: 10.5004/dwt.2023.29992.

[323] J. Comyn, “Practical surface analysis: Volume 1: Auger and X-ray photoelectron spectroscopy Edited by: D. Briggs and MP Seah John Wiley & Sons, 1990, 657+ xiv pp.” Elsevier, 1992.

[324] J. E. Castle and A. M. Salvi, “Chemical state information from the near-peak region of the X-ray photoelectron background,” *J. Electron Spectros. Relat. Phenomena*, vol. 114–116, pp. 1103–1113, 2001, doi: https://doi.org/10.1016/S0368-2048(00)00305-4.

[325] C. Peiris, S. R. Gunatilake, T. E. Mlsna, D. Mohan, and M. Vithanage, “Biochar based removal of antibiotic sulfonamides and tetracyclines in aquatic environments: A critical review,” *Bioresour. Technol.*, vol. 246, pp. 150–159, 2017, doi: 10.1016/j.biortech.2017.07.150.

[326] U. F. Alkaram, A. A. Mukhlis, and A. H. Al-Dujaili, “The removal of phenol from aqueous solutions by adsorption using surfactant-modified bentonite and kaolinite,” *J. Hazard. Mater.*, vol. 169, no. 1–3, pp. 324–332, 2009, doi: 10.1016/j.jhazmat.2009.03.153.

[327] P. Chingombe, B. Saha, and R. J. Wakeman, “Surface modification and

characterisation of a coal-based activated carbon," *Carbon N. Y.*, vol. 43, no. 15, pp. 3132–3143, 2005, doi: 10.1016/j.carbon.2005.06.021.

PUBBLICATIONS

Articles

Second year

1. *Efficient photooxidation processes for the removal of sildenafil from aqueous environments: A comparative study*, **A.R. Zizzamia**, C. Tesoro, G. Bianco, S.A. Bufo, R. Ciriello, M. Brienza, L. Scrano, and F. Lelario, *Case Studies in Chemical and Environmental Engineering* **2024**, 9, February: 100708, doi: 10.1016/j.cscee.2024.100708.
2. *Efficient biochar regeneration for a circular economy: Removing emerging contaminants for sustainable water treatment*, O. Baaloudj, S. Chiron, **A.R. Zizzamia**, V. Trotta, D. Del Buono, D. Puglia, M. Rallini, and M. Brienza, *Colloids Surfaces A: Physicochemical and Engineering Aspects* **2025**, 705: 135730, doi: 10.1016/j.colsurfa.2024.135730.
3. *Environmental Fate, Ecotoxicity, and Remediation of Heterocyclic Pharmaceuticals as Emerging Contaminants: A Review of Long-Term Risks and Impacts*, O. Baaloudj, L. Scrano, S.A. Bufo, L.A. Sade Modley, F. Lelario, **A.R. Zizzamia**, L. Emanuele, and M. Brienza, *Organics* **2025**, 1-18, doi: org/10.3390/org6010001.

Third year

1. *Electrochemical Degradation of Venlafaxine on Platinum Electrodes : Identification of Transformation Products by LC-MS / MS and In Silico Ecotoxicity Assessment*, **A.R. Zizzamia**, V. Pasquariello, F. Lelario, C. Tesoro, and R. Ciriello, *Molecules* **2025**, 1-24, doi: org/10.3390/molecules30091881.
2. *Venlafaxine Removal from Water and Wastewater Using Activated Carbons from Spent Brewery Grains Produced by Conventional vs. Microwave Pyrolysis*, **A.R. Zizzamia**, Â. Almeida, M.V. Gil, F. Lelario, and V. Calisto, *Pharmaceuticals* **2026**, 19, 344, doi.org/10.3390/ph19030344.

Oral and Poster Communications

First year

1. **A.R. Zizzamia**, C. Tesoro, G. Bianco, S.A. Bufo, R. Ciriello, L. Scrano, M. Brienza, and F. Lelario *"Comparison of advanced oxidation processes for the degradation of sildenafil in water"* 4th International Conference of Risk Assessment of Pharmaceuticals in the Environment, 9-10 October **2023**, Barcelona (Spain), **POSTER** communication.
2. **A.R. Zizzamia**, C. Tesoro, S.A. Bufo, M. Brienza, G. Bianco, R. Ciriello, L. Scrano, and F. Lelario *"Fotodegradazione di tadalafil e sildenafil in soluzioni acquose: efficacia di rimozione, cinetiche e fotoprodotti"* SICA (Società Italiana Chimica Agraria), 12-15 September **2023**, Palermo (Italy), **POSTER** communication.

Second year

1. **A.R. Zizzamia**, C. Tesoro, G. Bianco, S.A. Bufo, R. Ciriello, M. Brienza, L. Scrano, and F. Lelario *"Innovative methods to remove PDE5 inhibitors from polluted water"* 5th International Conference of Risk Assessment of Pharmaceuticals in the Environment, 24-25 June **2024**, Anacapri (Italy), **ORAL** communication.
2. **A.R. Zizzamia**, C. Tesoro, G. Bianco, S.A. Bufo, R. Ciriello, M. Brienza, L. Scrano, and F. Lelario *"Efficient photooxidation processes for the removal of sildenafil from aqueous environments: A comparative study"* SCI XXVIII National Congress, 26-30 August **2024**, Milano (Italy), **POSTER** communication.
3. **A.R. Zizzamia**, C. Tesoro, S.A. Bufo, F. Lelario, L. Scrano, M. Brienza, O. Baaloudj, and Z. Krinii *"Innovative methods to remove phosphodiesterase 5 inhibitors from polluted water"* VIII Convegno della rete CUCS, 12-14 September **2024**, Firenze (Italy), **ORAL** communication.

Third year

1. **A.R. Zizzamia**, A. Almeida, M.V. Gil, F. Lelario, and V.M. Amaro Calisto *"Removal of venlafaxine from water through carbon adsorbents produced from spent brewery grains"* 6th International Conference of Risk Assessment of Pharmaceuticals in the Environment, 20-21 October **2025**, Aveiro (Portugal), **ORAL** communication.

2. **A.R. Zizzamia**, A. Almeida, M.V. Gil, F. Lelario, and V.M. Amaro Calisto *"Removal of sildenafil and tadalafil from water through carbon adsorbents produced from spent brewery grains"* 6th International Conference of Risk Assessment of Pharmaceuticals in the Environment, 20-21 October **2025**, Aveiro (Portugal), **POSTER** communication.
3. I. Rosco, A. Almeida, **A.R. Zizzamia**, F. Lelario, and V.M. Amaro Calisto *"Activated carbon from spent coffee grounds for efficient removal of venlafaxine from ultrapure water and wastewater"* 6th International Conference of Risk Assessment of Pharmaceuticals in the Environment, 20-21 October **2025**, Aveiro (Portugal), **POSTER** communication.
4. **A.R. Zizzamia**, V. Pasquariello, F. Lelario, I. Rosco, C. Tesoro, and R. Ciriello *"Evaluation of electrochemical degradation using a platinum anode for venlafaxine removal"* 6th International Conference of Risk Assessment of Pharmaceuticals in the Environment, 20-21 October **2025**, Aveiro (Portugal), **POSTER** communication.

ATTENDED WORKSHOP AND SCHOOLS

First year

"Scuola in comunicazione della chimica SCI*C 2023", III edition. November 12-13 2023, Hotel Sporting, Rimini (Italy).

Second year

28esimo Corso di Spettrometria di Massa 2024, "Spettrometria di Massa- teoria e applicazioni in vari ambiti". March 11-15 2024, Certosa of Pontignano, Siena (Italy).

EXPERIENCE ABROAD

From 09/01/2025 to 11/07/2025, at Departamento de Química, Universidade de Aveiro, 3810-193 Aveiro, Portugal, under the supervision of Professor Vânia Maria Amaro Calisto.

ACKNOWLEDGEMENTS

This Ph.D. thesis would not have been possible without the support of many people. I would like to thank my supervisor, Prof. Filomena Lelario, for believing in me and for guiding me with rigor, passion, and dedication. She has been able to combine scientific rigor with profound humanity, demonstrating that academic excellence arises from listening, leading by example, and fostering others' growth. She has been a constant point of reference both professionally and personally: her support, kindness, and integrity have left a mark that goes far beyond this work.

I express my deepest gratitude to my co-supervisors, Prof. Aurelio Sabino Bufo and Prof. Giuliana Bianco, for their professionalism, availability, and the care with which they followed and enriched this research path.

I thank the coordinator, Prof. Patrizia Falabella, and the department director, Prof. Giacomo Prosser, for their support and availability.

I sincerely thank my host supervisor, Prof. Vânia Maria Amaro Calisto, for welcoming me to her institution and for her invaluable scientific supervision. Her professionalism, combined with extraordinary human generosity, contributed significantly to the development of this work. And thanks to Dr. Ângela Almeida, who followed and helped me a lot during this period abroad.

I would also like to thank Prof. Rosanna Ciriello, Prof. Laura Scrano, Dr. Monica Brienza and Dr. Oussama Baaloudj for their help, scientific support and for the constructive dialogue that accompanied the various stages of this work.

Finally, I thank my Ph.D. colleagues Giuseppe, Pierantonio, Marilena, Francesca, Francesco and Cağdaş, companions on this long journey, for sharing both the challenges and the satisfactions.

A thank you to Incoronata, my thesis student, with whom I shared my experience in Portugal: over time, she has also became an important friend.

My deepest thanks go to my family, Francesco and my friends for the patience, love and trust they have never failed to give me.